

# Computational modelling of brain energy metabolism and circulation in the neonatal animal model

Tracy Moroz \*

Thesis submitted for the degree of  
Doctor of Philosophy (PhD) at UCL

Supervisors:  
Dr Ilias Tachtsidis <sup>†</sup>  
Professor Chris E Cooper<sup>‡</sup>

---

\*Center for Mathematics and Physics in the Life Sciences and Experimental Biology, University College London

<sup>†</sup>Department of Medical Physics and Bioengineering, University College London

<sup>‡</sup>School of Biological Sciences, University of Essex

I, Tracy Moroz confirm that the work presented in this thesis is my own. Where information has been derived from other sources, I confirm that this has been indicated in the thesis.

Tracy Moroz

## Abstract

Hypoxic-ischaemic (HI) encephalopathy is a common cause of brain injury in neonates. The physiological processes occurring in the brain during asphyxia and in recovery are complex, and many aspects are not well understood. Piglets are often used as experimental models when investigating HI and testing new treatments.

This thesis focuses on the development and application of a mathematical model of blood flow and energy metabolism in the piglet brain during oxygen deprivation. The model consists of differential and algebraic equations which aim to describe the relevant cerebral physiology. The multiscale nature of the model, and its level of simplification, arise from its aim of helping to interpret experimental non-invasive measurements from near-infrared spectroscopy (NIRS) and magnetic resonance spectroscopy (MRS).

NIRS uses light to determine concentration changes of oxy and deoxyhaemoglobin in tissue. It can also detect changes in the oxidation of cytochrome-c-oxidase (CCO), an important marker of aerobic metabolism. This complements the information gained from MRS, which can measure the concentrations of key metabolites in tissue such as ATP, phosphocreatine and lactate. Multimodal monitoring with NIRS and MRS simultaneously gives a more complete picture of the metabolic state of the brain.

The model has been compared with extensive multimodal data from piglets: both averaged, from brief anoxia studies, and individual datasets, from HI studies. Morris sensitivity analysis was implemented in order to systematically investigate the effects of altering all parameters. Optimisation of important parameters was also implemented. Simulations of anoxia lead to the suggestion that autoregulation in the newborn piglets was impaired. The consequences of cell death in the brain caused by HI were also investigated with simulations. The model is a novel tool which can be used to help test physiological hypotheses of clinical importance and increase understanding of the mechanisms of HI.

# Acknowledgements

First of all, I would like to thank my supervisors Ilias Tachtsidis and Chris Cooper for their help and advice. I would also like to thank Murad Banaji, whose work laid the foundations for this project, and Tharindi Hapuarachchi for the useful discussions we had. Finally I would like to thank Tom for his help with programming, and my family and friends.

# Publications

## Journal Papers

- T. Moroz, M. Banaji, N. J. Robertson, C. E. Cooper and I. Tachtsidis. Computational modelling of the piglet brain to simulate near-infrared spectroscopy and magnetic resonance spectroscopy data collected during oxygen deprivation. *J. R. Soc. Interface*, 9:1499–1509, 2012.
- T. Moroz, T. Hapuarachchi, A. Bainbridge, D. Price, E. Cady, E. Baer, K. Broad, M. Ezzati, D. Thomas, X. Golay, N. J. Robertson, C. E. Cooper and I. Tachtsidis. Modelling blood flow and metabolism in the piglet brain during hypoxia-ischaemia: simulating brain energetics. *Adv. Exp. Med. Biol.*, 789:339–344, 2013.
- T. Hapuarachchi, T. Moroz, A. Bainbridge, D. Price, E. Cady, E. Baer, K. Broad, M. Ezzati, D. Thomas, X. Golay, N. J. Robertson and I. Tachtsidis. Modelling blood flow and metabolism in the piglet brain during hypoxia-ischaemia: simulating pH changes. *Adv. Exp. Med. Biol.*, 789:331–337, 2013.
- T. Moroz, M. Banaji, M. Tisdall, C. E. Cooper, C.E. Elwell and I. Tachtsidis. Development of a model to aid NIRS data interpretation: results from a hypercapnia study in healthy adults. *Adv. Exp. Med. Biol.*, 737:293–300, 2012.
- C. Kolyva, I. Tachtsidis, A. Ghosh, T. Moroz, C. E. Cooper, M. Smith and C. E. Elwell. Systematic investigation of changes in oxidized cerebral cytochrome *c* oxidase concentration during frontal lobe activation in healthy adults. *Biomed. Opt. Express*, 3(10):2550–2556, 2012.
- T. Moroz, T. Hapuarachchi, A. Bainbridge, D. Price, E. Cady, E. Baer, K. Broad, M. Ezzati, D. Thomas, X. Golay, N. J. Robertson, C. E. Cooper and I. Tachtsidis. Modelling blood flow and metabolism in the preclinical neonatal brain during physiological insults (Submitted to *PLoS Comput. Biol.*)

## Conference abstracts

- T. Moroz, T. Hapuarachchi, M. Banaji, N. J. Robertson, C. E. Cooper and I. Tachtsidis. Modelling blood flow and metabolism in the piglet brain during hypoxic-ischaemia: simulating brain energetics. ISOTT 2012, Bruges, Belgium
- T. Hapuarachchi, T. Moroz, N. J. Robertson and I. Tachtsidis. Modelling blood flow and metabolism in the piglet brain during hypoxic-ischaemia: simulating pH changes. ISOTT 2012, Bruges, Belgium
- T. Hapuarachchi, T. Moroz, N. J. Robertson and I. Tachtsidis. Modelling blood flow and metabolism in the preclinical neonatal brain during physiological insults. Virtual Physiological Human 2012, London, UK
- T. Moroz, M. Banaji, N. J. Robertson, C. E. Cooper and I. Tachtsidis. Computational modelling of oxygen deprivation in the neonatal piglet brain. International Conference on Systems Biology 2011, Mannheim, Germany
- T. Moroz, M. Banaji, N. J. Robertson, C. E. Cooper and I. Tachtsidis. Computational modelling of oxygen deprivation in the neonatal piglet brain. ISOTT 2011, Washington DC, USA
- T. Moroz, M. Banaji, C. E. Cooper, N. J. Robertson and I. Tachtsidis. Computational modelling of the piglet brain to simulate near infrared spectroscopy and magnetic resonance spectroscopy data collected during physiologic insults. UCL computation in predictive life and medical sciences symposium 2011, London, UK
- T. Moroz, M. Banaji, C. E. Cooper, N. J. Robertson and I. Tachtsidis. Computational modelling of the piglet brain to simulate near infrared spectroscopy and magnetic resonance spectroscopy data collected during physiologic insults. UCL neuroscience symposium 2011, London, UK
- T. Moroz, M. Banaji, C. E. Cooper, N. J. Robertson and I. Tachtsidis. Computational modelling of the piglet brain to simulate near infrared spectroscopy and magnetic resonance spectroscopy data collected during physiologic insults. Brain 2011, Barcelona, Spain
- T. Moroz, M. Banaji, C. E. Cooper, C. E. Elwell and I. Tachtsidis. Computational modelling of the NIRS brain tissue oxygenation signal in healthy adults during a CO<sub>2</sub> challenge. ISOTT 2010, Ascona, Switzerland

# Contents

<b>1</b>	<b>Introduction</b>	<b>18</b>
1.1	Motivation . . . . .	18
1.1.1	Aims . . . . .	19
1.2	Physiology . . . . .	20
1.2.1	Circulation . . . . .	21
1.2.2	Blood flow regulation . . . . .	22
1.2.3	Metabolism . . . . .	24
1.2.4	Hypoxia-Ischaemia . . . . .	33
1.3	Measurements . . . . .	34
1.3.1	NIRS . . . . .	35
1.3.2	MRS . . . . .	42
1.3.3	TCD . . . . .	44
1.3.4	Systemic measurements . . . . .	45
1.3.5	Piglet experiments . . . . .	48
1.3.6	Current research at UCL . . . . .	50
1.4	Summary . . . . .	51
<b>2</b>	<b>Modelling biological systems</b>	<b>52</b>
2.1	Methods used in biological modelling . . . . .	53
2.1.1	Chemical reactions . . . . .	53
2.1.2	Transport . . . . .	55
2.2	Overview of circulation and metabolism models . . . . .	55
2.2.1	Models of circulation . . . . .	61
2.2.2	Models of oxygen delivery . . . . .	63
2.2.3	Models of metabolism . . . . .	63
2.3	Models combining circulation and metabolism . . . . .	65
2.3.1	Models by Aubert <i>et al.</i> . . . . .	66
2.3.2	Model by Simpson <i>et al.</i> . . . . .	68
2.3.3	Model by Cloutier <i>et al.</i> . . . . .	69
2.3.4	Model by Beard . . . . .	70

2.3.5	Model by Vatov <i>et al.</i> . . . . .	73
2.3.6	BrainCirc . . . . .	73
2.3.7	BrainSignals . . . . .	75
2.3.8	Comparison between models . . . . .	81
2.4	Summary . . . . .	82
<b>3</b>	<b>Methods</b>	<b>84</b>
3.1	The BRAINCIRC modelling environment . . . . .	84
3.1.1	Describing the model . . . . .	84
3.1.2	Running a simulation . . . . .	87
3.1.3	Markup languages for modelling . . . . .	88
3.1.4	Reasons for using BRAINCIRC . . . . .	92
3.2	Comparison of model with data . . . . .	93
3.3	Optimisation . . . . .	94
3.3.1	Powell's method . . . . .	95
3.3.2	PSwarm . . . . .	96
3.3.3	Bayesian methods . . . . .	98
3.4	Sensitivity analysis . . . . .	98
3.5	Summary . . . . .	101
<b>4</b>	<b>Hypercapnia in healthy adults</b>	<b>102</b>
4.1	CO <sub>2</sub> and brain physiology . . . . .	102
4.2	Previous NIRS studies . . . . .	103
4.3	Method and results . . . . .	107
4.3.1	Experimental protocol . . . . .	107
4.3.2	Data analysis and modelling . . . . .	107
4.3.3	Initial optimisations . . . . .	109
4.3.4	Model extensions . . . . .	111
4.4	Discussion . . . . .	116
4.5	Conclusions . . . . .	120
<b>5</b>	<b>The BrainPiglet model and anoxia in piglets</b>	<b>122</b>
5.1	The BrainPiglet model . . . . .	122
5.1.1	Circulation . . . . .	123
5.1.2	Metabolism . . . . .	126
5.2	Steady state simulations . . . . .	131
5.3	Modelling anoxia . . . . .	134
5.3.1	Methods . . . . .	134
5.3.2	Results . . . . .	136
5.3.3	Discussion . . . . .	144

5.4	Conclusions . . . . .	146
<b>6</b>	<b>Hypoxia-ischaemia in piglets</b>	<b>148</b>
6.1	Sensitivity analysis . . . . .	148
6.2	Modelling carotid artery occlusion . . . . .	150
6.3	Experimental protocol . . . . .	151
6.4	Methods and results . . . . .	154
6.4.1	Experimental results . . . . .	154
6.4.2	Data analysis . . . . .	157
6.4.3	Parameter optimisation . . . . .	157
6.4.4	Effect of total haemoglobin concentration . . . . .	161
6.4.5	Cell death . . . . .	165
6.5	Discussion . . . . .	171
6.5.1	Sensitivity analysis . . . . .	171
6.5.2	Parameter optimisation . . . . .	172
6.5.3	Cell death . . . . .	174
6.6	Conclusions . . . . .	176
<b>7</b>	<b>Discussion</b>	<b>178</b>
7.1	Summary . . . . .	178
7.2	Future work . . . . .	182
7.2.1	Mathematical and computational techniques . . . . .	182
7.2.2	Representation of physiology . . . . .	186
7.2.3	Spatial resolution . . . . .	187
7.2.4	Comparison with new measurements . . . . .	187
7.2.5	Adaptation to humans . . . . .	189
7.2.6	Secondary energy failure and treatment . . . . .	190
7.3	Summary . . . . .	190
<b>A</b>	<b>Piglet data</b>	<b>192</b>
<b>B</b>	<b>Error Calculations</b>	<b>205</b>
<b>C</b>	<b>BrainSignals model equations, variables and parameters</b>	<b>207</b>
C.1	Differential Equations . . . . .	207
C.2	Algebraic Equations . . . . .	208
C.3	Chemical Reactions . . . . .	208
C.4	Variables . . . . .	208
C.5	Temporary Variables . . . . .	209
C.6	Parameters . . . . .	213

C.7	Derived Parameters . . . . .	217
<b>D</b>	<b>BrainPiglet model equations, variables and parameters</b>	<b>224</b>
D.1	Differential Equations . . . . .	224
D.2	Algebraic Equations . . . . .	225
D.3	Chemical Reactions . . . . .	226
D.4	Variables . . . . .	227
D.5	Temporary Variables . . . . .	228
D.6	Parameters . . . . .	236
D.7	Derived Parameters . . . . .	242
	<b>Bibliography</b>	<b>251</b>

# List of Figures

1.1	Brain Structure . . . . .	21
1.2	Brain blood supply . . . . .	21
1.3	Autoregulation . . . . .	24
1.4	CBF vs $P_aO_2$ in rats . . . . .	24
1.5	CBF vs $CO_2$ in rhesus monkeys . . . . .	25
1.6	Glycolysis . . . . .	27
1.7	TCA cycle . . . . .	28
1.8	Oxidative Phosphorylation . . . . .	29
1.9	Absorption spectrum of water . . . . .	36
1.10	Absorption spectra for Hb and $HbO_2$ in the near-infrared region . . . . .	37
1.11	Difference extinction spectrum of cytochrome oxidase . . . . .	38
1.12	TOI and CCO during hypocapnia . . . . .	42
1.13	Example $^1H$ MRS spectrum . . . . .	44
1.14	Example $^{31}P$ MRS spectrum . . . . .	45
1.15	Transcranial doppler ultrasound . . . . .	46
1.16	A typical capnograph . . . . .	47
2.1	Michaelis Menten reaction rate . . . . .	54
2.2	Electrical circuit analog of the model by Ursino and Lodi . . . . .	62
2.3	Schematic diagram of the 2001 model by Aubert and Costalat . . . . .	66
2.4	Schematic diagram of the 2005 model by Aubert and Costalat . . . . .	67
2.5	Schematic diagram of the model by Simpson <i>et al.</i> . . . . .	68
2.6	Schematic diagram of the model by Cloutier <i>et al.</i> . . . . .	69
2.7	Simulation of HI using the model by Cloutier <i>et al.</i> . . . . .	71
2.8	Schematic diagrams of the model by Beard . . . . .	72
2.9	Overview of the BrainCirc model . . . . .	74
2.10	Schematic diagram of the BrainSignals model . . . . .	75
2.11	CBF vs arterial pressure in the BrainSignals model . . . . .	77
2.12	Electron transfer chain and proton pumping in the BrainSignals model . . . . .	79
3.1	Flow diagram of modelling process . . . . .	85

3.2	Modified Powell's method optimisation trajectory . . . . .	96
4.1	Instrumentation error in the EtCO <sub>2</sub> signal . . . . .	107
4.2	Modelling and optimisation process for TOS and V <sub>mca</sub> . . . . .	109
4.3	V <sub>mca</sub> response error vs TOI response error for initial optimisations . . .	111
4.4	V <sub>mca</sub> response error vs TOI response error for all optimisations . . . . .	115
4.5	Example TOS, V <sub>mca</sub> and ΔoxCCO from a volunteer during hypercapnia	117
4.6	ΔoxCCO <sub>d</sub> response vs ΔoxCCO <sub>m</sub> response for different optimisations .	118
4.7	CCO mean square errors after optimisations . . . . .	118
4.8	Modelled and measured ΔoxCCO for two subjects . . . . .	119
5.1	Schematic diagram of the BrainPiglet model . . . . .	124
5.2	Circulation in the BrainPiglet model . . . . .	124
5.3	Effect of the steady state assumption on arterial radius changes . . . . .	127
5.4	Metabolic processes relating to glycolysis, lactate and the TCA cycle . .	127
5.5	Metabolic processes relating to ATP use, synthesis and buffering . . . . .	129
5.6	Steady state plots vs oxygen saturation for the BrainPiglet model . . . . .	132
5.7	Steady state plots vs P <sub>a</sub> for the BrainPiglet model . . . . .	133
5.8	Steady state plots vs P <sub>a</sub> CO <sub>2</sub> for the BrainPiglet model . . . . .	134
5.9	Experimental results from anoxia experiments in piglets . . . . .	135
5.10	Inputs for modelling anoxia . . . . .	136
5.11	Comparison of modelled and measured signals during anoxia with de- fault parameter values . . . . .	137
5.12	Effect of changing autoregulation capacity on the BrainPiglet model . .	138
5.13	Comparison of modelled and measured signals during anoxia with al- tered parameter values . . . . .	139
5.14	Modelled lactate during anoxia . . . . .	139
5.15	Steady state plots vs oxygen saturation with parameter changes . . . . .	141
5.16	Steady state plots vs blood pressure with parameter changes . . . . .	142
5.17	Steady state plots vs CO <sub>2</sub> with parameter changes . . . . .	142
5.18	ΔoxCCO during anoxia . . . . .	143
5.19	Modelled [Py] and [NAD]/[NADH] during anoxia . . . . .	146
5.20	Reduction of ΔoxCCO during anoxia . . . . .	146
6.1	μ <sup>*</sup> vs σ for [ATP] in steady state simulations. . . . .	149
6.2	CBF vs occlusion in the BrainPiglet model . . . . .	152
6.3	Pressure drop through model compartments at different levels of occlusion	153
6.4	Measured NIRS and H-MRS signals from a HI insult on one piglet . . .	155
6.5	Measured NIRS and <sup>31</sup> P-MRS signals from a HI insult on one piglet . .	156
6.6	μ <sup>*</sup> and σ from sensitivity analysis for fitting of hypoxia ischaemia data .	158

6.7	Modelled and measured NIRS and H-MRS signals before and after parameter optimisation for a HI insult on one piglet . . . . .	162
6.8	Modelled and measured NIRS and <sup>31</sup> P-MRS signals before and after parameter optimisation for a HI insult on one piglet . . . . .	163
6.9	Variation of rms error between modelled and measured $\Delta\text{oxCCO}$ . . . . .	164
6.10	Variation of rms error between modelled and measured <sup>31</sup> P-MRS variables	164
6.11	Measured Hb changes during HI . . . . .	166
6.12	Simulated $\Delta\text{HbT}$ and $\Delta\text{Hb}_{\text{diff}}$ vs [Hbtot] at different $\text{S}_a\text{O}_2$ . . . . .	167
6.13	Calculation of the recovery fraction . . . . .	167
6.14	Relationship between recovery of CCO and NTP and PCr following HI	168
6.15	Modelled and measured results from a piglet which did not recover after HI with and without simulated cell death . . . . .	170
6.16	Effect of uncoupling on the model . . . . .	176
7.1	Example of $P_a\text{CO}_2$ , $\text{S}_a\text{O}_2$ and $P_a$ measurements with added noise . . . . .	184
7.2	Example of ABC parameter estimation . . . . .	185
7.3	Comparison of measured and modelled pH . . . . .	189
A.1	Measured data for Piglet LWP158 . . . . .	192
A.2	Measured data for Piglet LWP164 . . . . .	193
A.3	Measured data for Piglet LWP167 . . . . .	194
A.4	Measured data for Piglet LWP168 . . . . .	195
A.5	Measured data for Piglet LWP169 . . . . .	196
A.6	Measured data for Piglet LWP170 . . . . .	196
A.7	Measured data for Piglet LWP173 . . . . .	197
A.8	Measured data for Piglet LWP175 . . . . .	198
A.9	Measured data for Piglet LWP179 . . . . .	199
A.10	Measured data for Piglet LWP180 . . . . .	200
A.11	Measured data for Piglet LWP183 . . . . .	201
A.12	Measured data for Piglet LWP185 . . . . .	202
A.13	Measured data for Piglet LWP186 . . . . .	203
A.14	Measured data for Piglet LWP188 . . . . .	204

# List of Tables

2.1	A summary of some of the models of brain circulation and metabolism .	60
2.2	Number of compartments, variables and parameters in models of energy metabolism and circulation . . . . .	82
4.1	A summary of NIRS studies of CO <sub>2</sub> challenges . . . . .	105
4.2	Hypercapnia data . . . . .	108
4.3	Initial optimisation results . . . . .	110
4.4	Details of optimisation methods and results . . . . .	114
5.1	Parameters that were changed from their BrainSignals values in the BrainPiglet model . . . . .	123
5.2	Parameters that were changed to improve the simulations of anoxia. . .	136
6.1	Steady state sensitivity analysis . . . . .	150
6.2	Most influential parameters in fitting HI data as determined by sensitivity analysis . . . . .	159
6.3	Parameter values after optimisation to HI data . . . . .	161
6.4	Results of optimisations of $\Delta\text{oxCCO}$ and <sup>31</sup> P-MRS variables including a fraction of dead cells . . . . .	169

# Acronyms

**ABC** approximate Bayesian computation.

**ADP** adenosine diphosphate.

**AMP** adenosine monophosphate.

**ANLS** astrocyte-neuron lactate shuttle.

**ATP** adenosine triphosphate.

**CBF** cerebral blood flow.

**CBV** cerebral blood volume.

**CCO** cytochrome-c-oxidase.

**CMRO<sub>2</sub>** cerebral metabolic rate of oxygen consumption.

**CO<sub>2</sub>** carbon dioxide.

**CSF** cerebrospinal fluid.

**DAE** differential algebraic equation.

**EEG** electroencephalography.

**EPP** exchangeable phosphate pool.

**EtCO<sub>2</sub>** end tidal carbon dioxide (CO<sub>2</sub>).

**FAD** flavin adenine dinucleotide.

**FiO<sub>2</sub>** fractional inspired oxygen.

**GDP** guanosine diphosphate.

**GTP** guanosine triphosphate.

**ΔHb<sub>diff</sub>** change in difference in brain tissue concentration between oxy and deoxy-haemoglobin.

**ΔHbO<sub>2</sub>** change in brain tissue concentration of oxyhaemoglobin.

**ΔHbT** change in total brain tissue haemoglobin concentration.

**HCO<sub>3</sub><sup>-</sup>** bicarbonate ions.

**ΔHHb** change in brain tissue concentration of deoxyhaemoglobin.

**HI** hypoxia ischaemia.

**ICP** intracranial pressure.

**JSON** javascript object notation.

**MABP** mean arterial blood pressure.

**MCMC** Markov chain Monte Carlo.

**MCT** monocarboxylate transporter.

**MRS** magnetic resonance spectroscopy.

**MSE** mean square error.

**NAA** N-acetyl aspartate.

**NAD** nicotinamide adenine dinucleotide.

**NIRS** near-infrared spectroscopy.

**NMDA** N-methyl-D-aspartate.

**NO** nitric oxide.

**NOS** nitric oxide synthase.

**NTP** nucleotide triphosphate.

**O<sub>2</sub>** oxygen.

**OAT** one at a time.

**ΔoxCCO** change in concentration of oxidised cytochrome-c-oxidase (CCO).

**P<sub>a</sub>CO<sub>2</sub>** partial pressure of carbon dioxide in the arterial blood.

**P<sub>a</sub>O<sub>2</sub>** partial pressure of oxygen in the arterial blood.

**P<sub>i</sub>** inorganic phosphate.

**PCO<sub>2</sub>** partial pressure of carbon dioxide.

**PCr** phosphocreatine.

**PET** positron emission tomography.

**PEt** phosphoethanolamine.

**rms** root mean square.

**ROS** reactive oxygen species.

**S<sub>a</sub>O<sub>2</sub>** arterial oxygen saturation.

**SBML** Systems Biology Markup Language.

**SpO<sub>2</sub>** oxygen saturation of haemoglobin in the pulsatile component of the blood.

**TCA** tricarboxylic acid.

**TCD** transcranial doppler.

**TOI** tissue oxygenation index.

**TOS** tissue oxygen saturation.

**UQ** ubiquinone.

**V<sub>mca</sub>** velocity of blood in the middle cerebral artery.

**VSM** vascular smooth muscle.

# Chapter 1

## Introduction

### 1.1 Motivation

Most of the work described in this thesis is concerned with hypoxia ischaemia (HI) in neonates. HI caused by birth asphyxia is a major cause of perinatal brain injury. In developed countries, its incidence is 1 to 2 per 1000 live births, and asphyxia is estimated to account for 23 % of worldwide neonatal deaths [1]. HI leads to long term problems in up to 25 % of survivors [2]. These include conditions such as cerebral palsy, epilepsy and mental retardation [3].

It is believed that much of the damage to the brain caused by HI occurs as a result of metabolic disruptions during the recovery period. This is known as secondary, or delayed energy failure. Measurements of brain function often return to normal after a hypoxic-ischaemic episode but show an impairment again after several hours [4]. The severity of secondary energy failure has been shown to be correlated with outcome [5]. Treatment given during the crucial hours before this has the potential to reduce the severity of damage and improve outcome.

A number of therapies have been investigated, one of the most promising and widely used being hypothermia. Hypothermia has been shown to be beneficial [6, 7]; and its benefit may be increased if it is used together with neuroprotective drugs. It is thought hypothermia may increase the window during which such drugs can have an effect. Drugs used include erythropoietin, melatonin, magnesium sulphate and xenon [8].

Some of the difficulties in the treatment of HI include identifying which individuals are at risk of long-term damage and could therefore benefit from treatment, and monitoring

progress during treatment. Magnetic resonance spectroscopy (MRS) has been used to predict outcome in infants [9, 10] but cannot be used for continuous monitoring for practical reasons. Both near-infrared spectroscopy (NIRS) and electroencephalography (EEG) have also been used to follow the progress of asphyxiated infants [11]. NIRS can measure brain oxygenation and metabolism (see Section 1.3.1) and can be used safely for extended periods.

Mathematical modelling could help to bring together measurements from these different modalities, giving a fuller picture of the state of the brain. It could also be used to predict quantities that cannot be measured. Ultimately, the aim is to develop a model of the human neonatal brain which can be used clinically. The process of developing the model and its predictions may also help increase understanding the physiological processes involved in birth asphyxia and subsequent cellular damage. A successful model could also be used to suggest new treatments or predict their effects by simulation.

As a first step towards this goal, a mathematical model of the neonatal piglet brain, which is often used as a model of the neonatal human brain, has been developed. This model, which will be referred to as BrainPiglet, is the first of this kind which has been used to investigate HI in piglets. The model has been used to simulate oxygen challenges in the piglet brain and has been compared with both individual and averaged measured data. The experimental data with which the model is compared is drawn from NIRS and MRS. The BrainPiglet model is the first physiological model to combine measurements from these two modalities. It has been used to help investigate associations between their measurements, and has also been used to help generate hypotheses concerning the vascular and chemical process occurring in HI.

The BrainPiglet model was created by adapting and extending a model of the adult brain (BrainSignals [12]). Before beginning the development of BrainPiglet, this model was used to investigate a hypercapnia challenge in healthy adult brain. This work is of interest in its own right (see Section 4.1) but also serves as an introduction to the NIRS measurements and the use of the model to interpret them.

### **1.1.1 Aims**

The aims of this thesis are:

- To use the BrainSignals model to simulate NIRS signals during hypercapnia.
- To extend and adapt the BrainSignals model to simulate circulation and

metabolism in the brain of a neonatal piglet.

- To use this model to simulate NIRS and MRS signals during anoxia and HI in piglets.
- To use the simulations to help generate and evaluate physiological hypotheses, and to understand NIRS and MRS measurements.

## 1.2 Physiology

The brain makes up only about 2 % of human body weight, but is responsible for about 20 % of the body's oxygen consumption and 25 % of glucose consumption. It also receives about 15 % of resting cardiac output [13]. This results in a cerebral blood flow (CBF) of around  $50 \text{ ml min}^{-1} 100 \text{ g}_{\text{brain}}^{-1}$ .

Brain tissue is made up of neurons, blood vessels and glial cells. Neurons are the cells that carry the nerve impulses. An average human brain contains an estimated 100 billion of them, each with approximately 10 000 connections to other neurons [14]. A neuron is made up of a cell body and an axon. The brain is separated into grey matter, which contains mostly cell bodies, and white matter, which contains mostly axons. There are at least as many glial cells in the brain as neurons. They support the neurons structurally, supply nutrients and oxygen, help to insulate neurons and to destroy dead neurons.

The brain is surrounded by three membranes, or meninges, which protect the brain, called the pia mater, arachnoid mater and dura mater. Between the arachnoid mater and the pia mater is the subarachnoid space. This is filled with cerebrospinal fluid (CSF), a fluid similar in composition to blood plasma. It is also found in the ventricles of the brain. Its functions are to protect the brain mechanically, to clear metabolic waste and provide nutrients, and to help regulate intracranial pressure.

The basic structure of the brain is shown in Figure 1.1. It is divided into three main parts, the cerebrum, the cerebellum and the brain stem. The brain stem controls basic functions such as breathing and blood pressure. The cerebellum controls balance and coordination. The cerebrum controls higher level thinking. It is the largest part of the brain and is divided into four lobes.

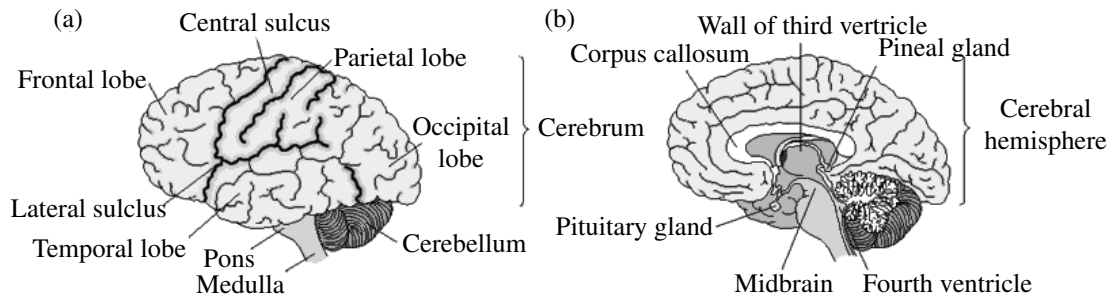


Figure 1.1: Structure of the brain [14]

## 1.2.1 Circulation

The brain is supplied by the internal carotid and the vertebral arteries. These join at the base of the brain to form the circle of Willis which allows blood flow to the brain to continue if the supply from one of the arteries is interrupted. Blood travels to the brain tissue through the cerebral arteries. This is illustrated in Figure 1.2. The middle cerebral artery is important for blood flow measurements, since it passes under a thin part of the skull. Doppler ultrasound can be used to measure the speed of blood in this artery.

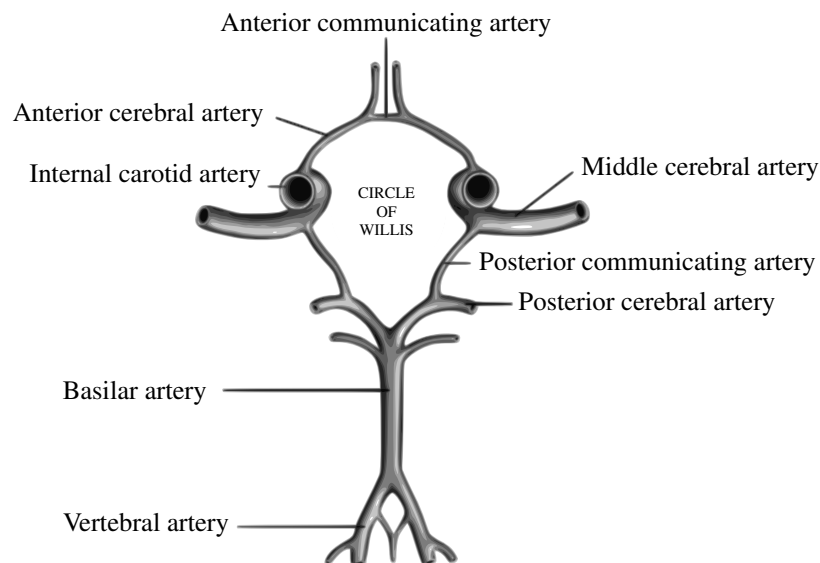


Figure 1.2: Diagram showing the blood supply to the brain [15]

Blood vessels are classified as arteries, arterioles, capillaries, venules and veins. Arteries are vessels that carry blood away from the heart. In the brain, this means they carry oxygenated blood. Haemoglobin in the arteries is usually about 96–100 % saturated with oxygen. Arteries have a layer of smooth muscle and elastic tissue. The elastic tissue allows the vessels to respond passively to changes in pressure. The smooth muscle can contract or relax in response to certain stimuli to change the rate of blood flow. Vasodilation and constriction can be caused by many different chemicals, for example

nitric oxide. Physiological conditions which lead to vasodilation include hypoxia and hypercapnia. Conversely, hyperoxia and hypocapnia lead to vasoconstriction. This is discussed further below.

Capillaries are vessels connecting arterioles and venules the diameters of which are comparable to the diameter of a red blood cell. Their wall is a single layer, which allows substances to pass between the blood and the surrounding tissue. In the brain, the endothelial cells lining the capillaries are packed more tightly than in other tissues. This forms what is called the blood brain barrier, because it separates the circulating blood from the brain tissue and CSF. Substances such as bacteria and large hydrophilic molecules, which are normally able to pass through capillary walls, are unable to do so in the brain. Glucose is actively transported across the barrier, as are other important substrates. Small molecules including oxygen and carbon dioxide are able to diffuse across the barrier. Cerebral capillaries are surrounded by astrocytes, a type of glial cell whose functions include helping to maintain the blood brain barrier.

Blood from the capillaries flows into the veins. Veins contain blood which is usually about 60 % saturated with oxygen. Veins in the brain have no muscular tissue and have no valves. Most veins drain into the venous sinuses. These drain into the jugular vein. Roughly three quarters of the brain blood volume is venous blood.

### **1.2.2 Blood flow regulation**

It is crucial that the brain has a constant supply of metabolites, in particular oxygen. If the flow of blood to the brain is stopped, neuronal electrical activity stops within seconds, and irreversible cell damage occurs after a few minutes [16]. It is therefore important that blood flow to the brain is matched to demand.

#### **Mechanisms**

The mechanisms by which cerebral blood flow regulation occurs are complex, but are generally divided into three classes: myogenic, metabolic and neurogenic [13].

**Myogenic** refers to the direct response of the vessel wall to changes in the transmural pressure gradient. The vascular smooth muscle cells contain stretch-activated ion channels. When activated, these allow the influx of cations, which causes membrane depolarisation. This leads to an influx of calcium ions, causing muscle constriction. The endothelium is also thought to have mechanoreceptor proper-

ties, and respond to changes in transmural pressure and flow velocity [17].

**Metabolic** describes the process by which the vessels respond to changes in concentrations of certain metabolites. For example, an increase in carbon dioxide ( $\text{CO}_2$ ) causes an increase in hydrogen ions, which stimulates vasodilation. The mechanism by which changes in oxygen concentration are coupled to flow are not fully understood, but adenosine is known to play a role [17].

**Neurogenic** mechanisms can also cause changes in vascular tone. This is thought to be more important for larger arterioles, since they are more densely innervated [18].

### **Autoregulation**

Cerebral autoregulation is the ability of the brain to maintain a constant blood flow, despite changes in perfusion pressure [19]. Cerebral perfusion pressure is defined as the pressure difference that drives blood flow through the brain. It is a function of the arterial and venous pressures, as well as the intracranial pressure, and is between 70 and 90 mmHg under normal conditions in a healthy adult human. The CBF is determined by the perfusion pressure and the cerebrovascular resistance, which varies with the radius of the blood vessels. The process of autoregulation involves changes in vessel radius, mainly of the small arteries, to counteract the effect of perfusion pressure changes on CBF. Usually, normal CBF can be maintained for blood pressures in the range of about 60–140 mmHg as illustrated in Figure 1.3. This range is shifted in patients with chronic hyper- or hypotension [20]. The blood pressure CBF curve is less well defined in newborns [21], but the lower threshold appears to be below 30 mmHg [22] and absent autoregulation has been observed following severe birth asphyxia [23].

### **O<sub>2</sub>**

The normal partial pressure of oxygen in the arterial blood ( $\text{P}_a\text{O}_2$ ) is around 100 mmHg. A reduced concentration of oxygen in the blood is known as hypoxia. When this occurs, the cerebral blood vessels dilate, thus increasing CBF, and the amount of oxygen available. An increased concentration is called hyperoxia, and leads to a constriction of the cerebral arteries, and therefore to a reduced CBF. The relationship between  $\text{P}_a\text{O}_2$  and CBF in adult rats is shown in Figure 1.4.

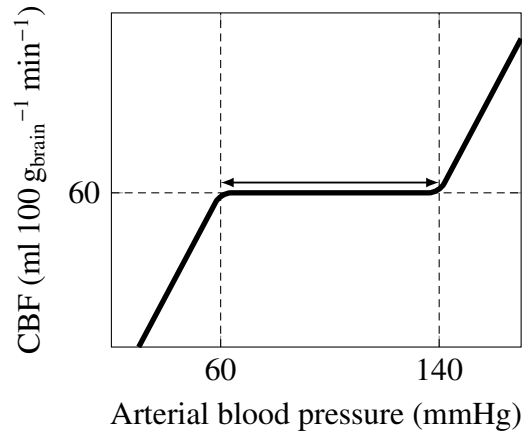


Figure 1.3: Diagram illustrating autoregulation in adult humans adapted from Folino [15]. The arrow shows the idealised autoregulation plateau.

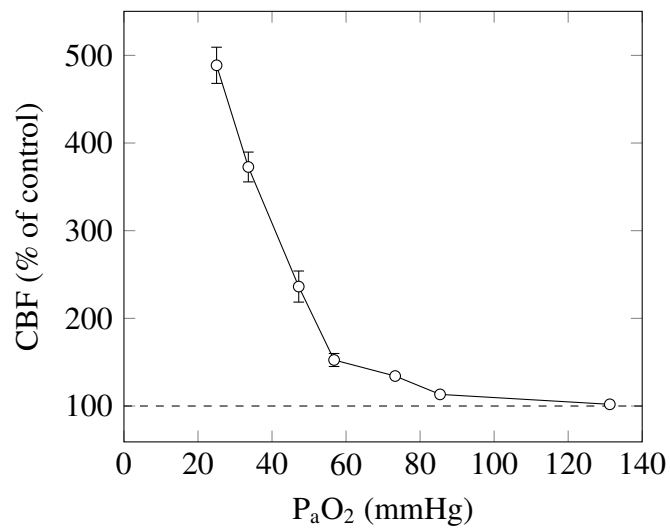


Figure 1.4: Effect of  $P_{aO_2}$  on CBF in rats [24]

## CO<sub>2</sub>

Increased levels of CO<sub>2</sub> in the blood lead to brain blood vessel dilation, and decreased levels lead to constriction. Figure 1.5 shows the results of an experiment carried out on eight rhesus monkeys, to investigate the relationship between blood CO<sub>2</sub> levels and CBF [25]. Also shown is the line of fit proposed by the authors.

### 1.2.3 Metabolism

One of the most important metabolic process that takes place in the brain is respiration. Respiration involves the conversion of glucose and oxygen to CO<sub>2</sub> and water, and produces energy in the form of adenosine triphosphate (ATP) which can be used in the

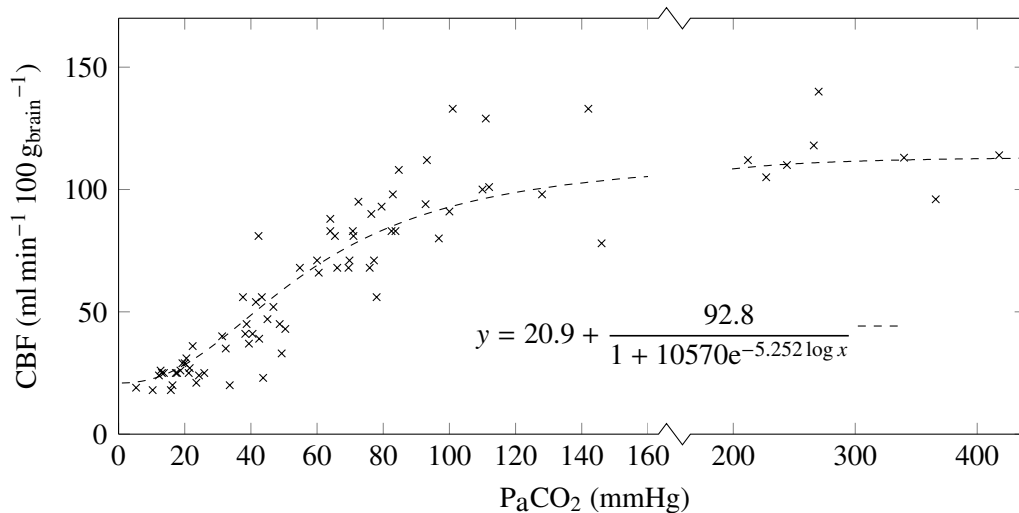


Figure 1.5: CBF vs  $P_a\text{CO}_2$  in rhesus monkeys. The dotted line shows the best fit proposed by the author [25].

cell. In other tissues, substrates other than glucose are sometimes used. However, the brain uses almost exclusively glucose, because fatty acids cannot cross the blood brain barrier. Respiration is divided into three stages. The first is glycolysis, which takes place in the cell cytoplasm. This is followed by the Krebs cycle and then oxidative phosphorylation, both of which are carried out in the mitochondria. These processes are explained below. More detail can be found in Siesjö [26].

## Glycolysis

Glycolysis is the name given to the set of reactions that result in the break down of glucose to pyruvate. Two molecules of three carbon pyruvate are formed for each six carbon glucose molecule. In the process, two adenosine diphosphate (ADP) molecules are phosphorylated and two nicotinamide adenine dinucleotide (NAD) molecules are reduced. The overall reaction is



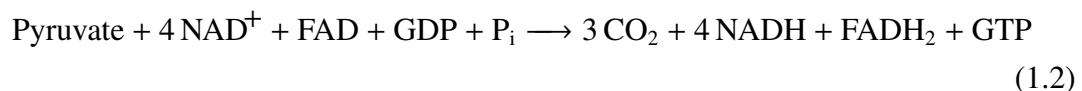
Glycolysis takes place in ten steps as shown in Figure 1.6. These can be considered in two stages, each consisting of five steps. During the first stage, known as the investment stage, energy from two ATP molecules is used. The first ATP is used in an irreversible phosphorylation of glucose, which is the first step of glycolysis. The second is used in a step important to the control of glycolysis, a phosphorylation catalysed by phosphofruktokinase. At the end of the first stage, two three carbon molecules have been

formed. In the second stage, or generation stage, these molecules are rearranged to form pyruvate, and energy is regained by the phosphorylation of four ADP molecules. The reduction of  $\text{NAD}^+$  also occurs in the second stage. The NADH produced cannot cross the mitochondrial inner membrane. However, it is effectively transported into the mitochondrial matrix by the malate-aspartate shuttle.

In the brain, the main function of glycolysis is to produce pyruvate. Under normal conditions, glycolysis produces only a small fraction of the ATP used by the cell. In anaerobic conditions however, it becomes more important. The pyruvate produced by glycolysis can be converted into lactate. This regenerates the  $\text{NAD}^+$  necessary for glycolysis to continue, and keep producing ATP. The conversion of pyruvate to lactate also produces a proton. This is a major cause of the acidosis that occurs in hypoxia or ischaemia. Lactate can be converted back to pyruvate, or transported to the liver.

### **Krebs cycle**

In aerobic respiration, the pyruvate produced by glycolysis is transported into the mitochondria and further metabolised. The set of reactions known as the Krebs, tricarboxylic acid (TCA) or citric acid cycle involves the oxidation of pyruvate to  $\text{CO}_2$ . It takes place in the mitochondrial matrix. For each molecule of pyruvate oxidised, one molecule of guanosine diphosphate (GDP) is phosphorylated, and four molecules of NAD and one molecule of flavin adenine dinucleotide (FAD) are reduced to NADH and  $\text{FADH}_2$  respectively. The overall reaction is shown below; a more detailed reaction scheme is illustrated in Figure 1.7



The NADH produced function as electron donors in the electron transport chain. The step of the cycle involving the oxidation of succinate to fumarate is coupled to the reduction of ubiquinone to ubiquinol, which also takes part in the electron transport chain. Whilst aerobic respiration is the main function of the cycle, its intermediates also have a number of other functions in the cell.

### **Oxidative phosphorylation**

The chemiosmotic theory of oxidative phosphorylation was proposed by Mitchell in 1961 [27]. It states that ATP synthesis is coupled to electron transfer by a proton elec-

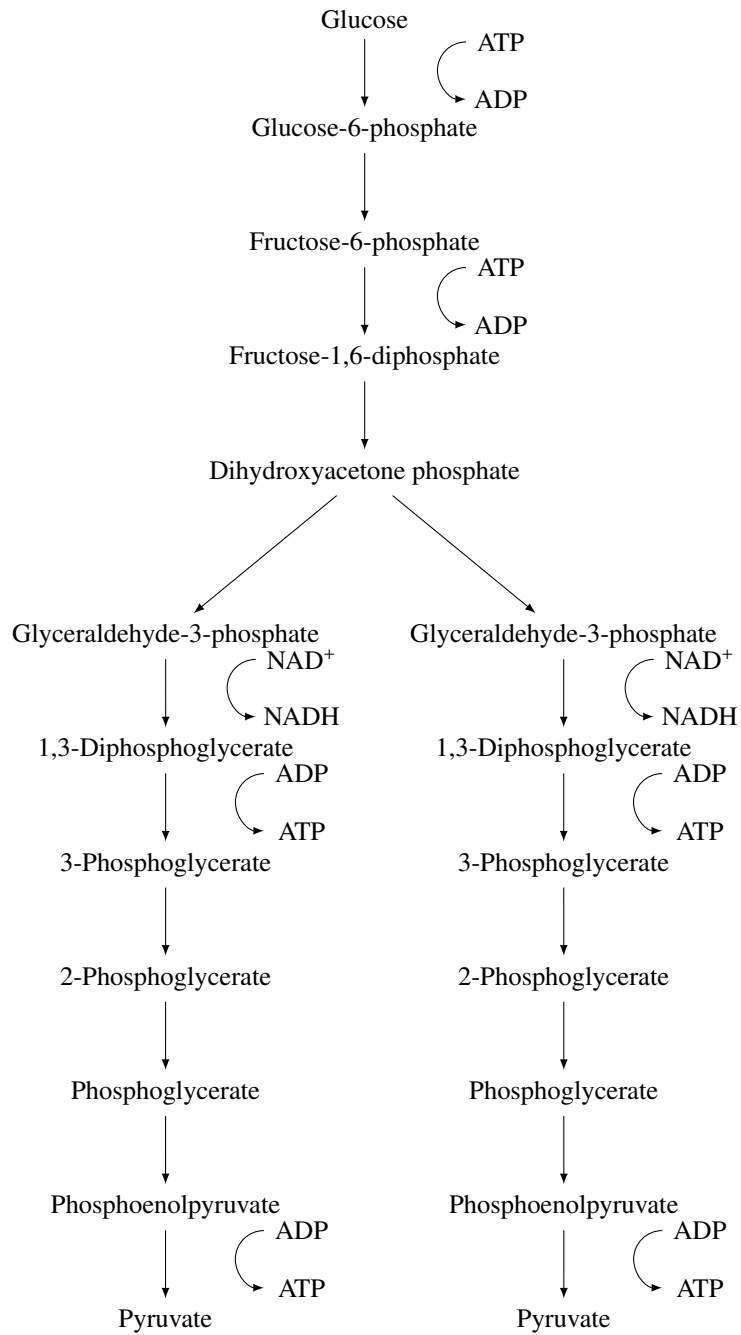


Figure 1.6: Intermediates of glycolysis

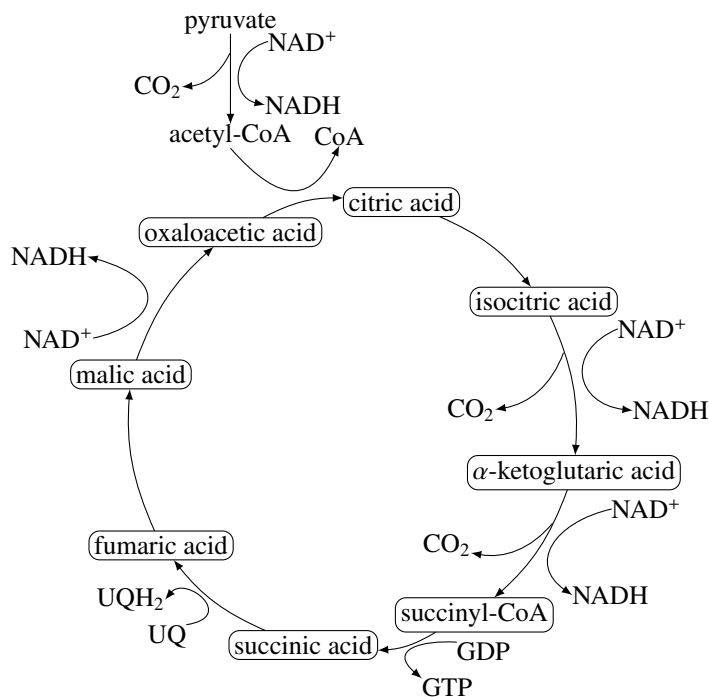


Figure 1.7: The TCA cycle

trochemical gradient. The electron transport chain involves the passage of electrons between donors and acceptors down an energy gradient. The initial electron donor is the NADH produced by the TCA cycle. The electrons pass through Complex I which oxidises the NADH and reduces ubiquinone to ubiquinol, and also pumps protons across the inner mitochondrial membrane. Ubiquinone is also reduced by succinate dehydrogenase (Complex II) coupled to a step in the TCA cycle. Electrons pass from ubiquinol to cytochrome c via Complex III which is also coupled with a net transport of protons out of the mitochondrial matrix. The final donor is the cytochrome-c-oxidase (CCO) complex (Complex IV), which passes electrons to oxygen to form water. Four electrons and four protons are needed to reduce oxygen to water. CCO has three redox centres. Electrons are first transferred from cytochrome c to the CuA and haem a centres. They are then transferred to the haem a<sub>3</sub>-CuB centre and from there to oxygen [28]. The oxidation state of the CuA centre can be measured by near-infrared spectroscopy (see Section 1.3.1).

As electrons pass from NADH to oxygen, their energy decreases. This energy is used to pump protons from the mitochondrial matrix into the intermembrane space. This creates an electrochemical gradient, combining a concentration gradient and an electrical potential. The molecular motor ATP synthase is found in the inner mitochondrial membrane. It couples the movement of protons into the mitochondrial matrix, down their energy gradient, to the phosphorylation of ATP. Under certain conditions, it also operates in reverse, using energy from ATP hydrolysis to pump protons. It is thought that

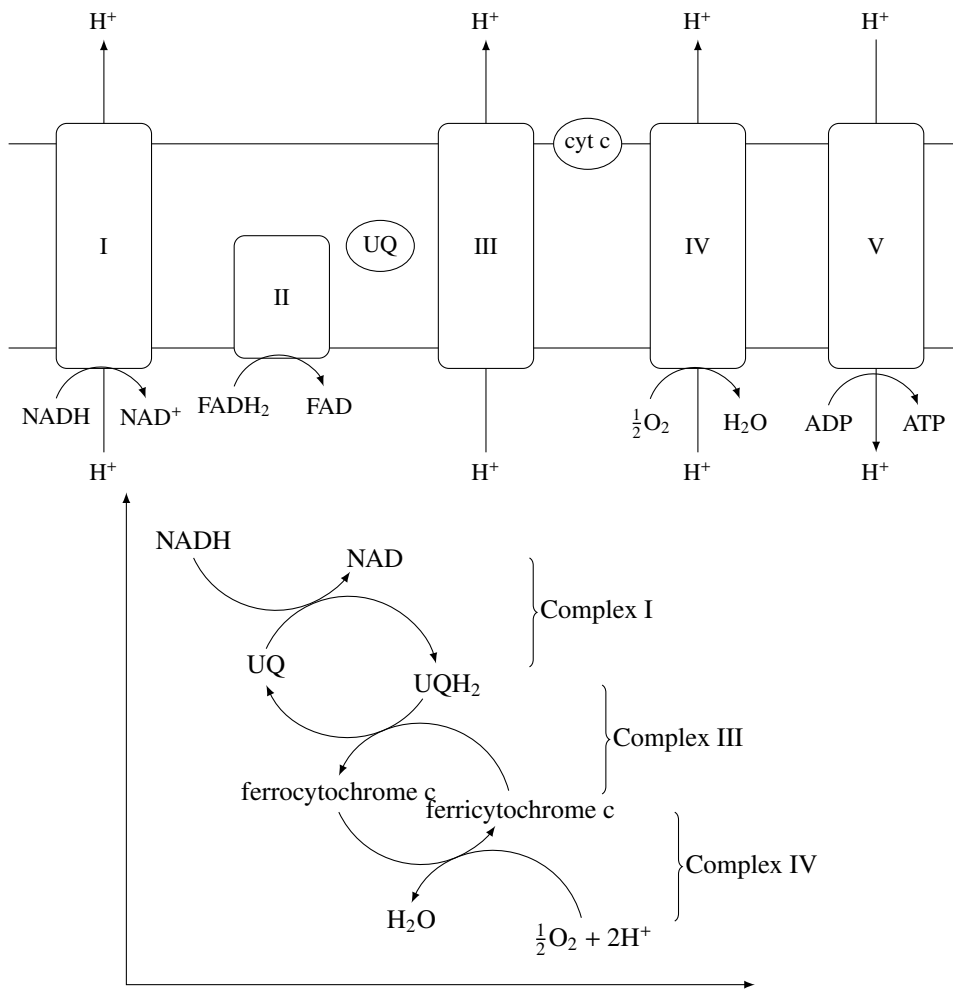


Figure 1.8: Diagrams of Oxidative Phosphorylation. The top diagram shows the complexes involved in the inner mitochondrial membrane. The bottom diagram shows the path of electrons through the chain, during which they flow through a cascade of redox centres within each complex.

the translocation of between three and four protons is coupled to the phosphorylation of one ATP molecule [29]. The newly synthesised ATP must also be transported out of the mitochondrial matrix, and the ADP must be transported in. This is done by an enzyme called ADP/ATP translocase. Since in the cell ATP exists as  $\text{ATP}^{4-}$  and ADP as  $\text{ADP}^{3-}$ , this is equivalent to the transport of a proton across the membrane. Phosphate is also transported across the membrane by a specialized transporter; this is a neutral process.

Not all the protons pumped by the electron transport chain return to the matrix via ATP synthase. The electrochemical gradient is also used to drive other processes, such as transport processes. Protons also travel through leak channels. The proportion of protons travelling through these channels varies with the tissue. In the brain it is thought to be between 10 and 40 % [30]. This decreases when the rate of energy generation increases. The overall efficiency of oxidative phosphorylation is often quantified by the P:O ratio. This is the number of moles of ATP phosphorylated per mole of oxygen consumed. The maximum for this ratio (if all protons are used for ATP synthesis) is around 2.5 [31].

### Energy and metabolic regulation

The energy required to phosphorylate ATP depends on the standard Gibbs free energy of the reaction, and also the relative concentrations of metabolites in the cell.

$$\Delta G = \Delta G_0 + RT \ln \left( \frac{[\text{ATP}]}{[\text{ADP}][\text{P}_i]} \right) \quad (1.3)$$

This  $\Delta G$  is known as the phosphorylation potential, although this term is sometimes used to describe the ratio  $[\text{ATP}]/([\text{ADP}][\text{inorganic phosphate (P}_i)])$ . The standard Gibbs energy for the reaction ( $\Delta G_0$ ) is  $30.5 \text{ kJ mol}^{-1}$ . Typical concentrations in the cytoplasm for ATP and ADP are 3 mM and 0.3 mM. Inorganic phosphate is present at concentrations of around 1.5 mM [26]. This gives a  $\Delta G$  of about  $52 \text{ kJ mol}^{-1}$ . However, the situation is complicated by the fact that the concentrations of metabolites are different inside and outside the mitochondria. Also, ATP, ADP and  $\text{P}_i$  can all exist bound to metal ions, most importantly magnesium. Most of the ATP in the cell is bound to  $\text{Mg}^{2+}$  ions, whereas most of the ADP is not [26]. In the mitochondria, bound forms participate in the ATP synthesis reaction, and unbound forms are transported across the membrane [32]. Another variable that has been suggested as a useful measure of the energy state of the cell is the ‘energy charge’ [33].

$$\text{Energy charge} = \frac{[\text{ATP}] + 0.5[\text{ADP}]}{[\text{ATP}] + [\text{ADP}] + [\text{AMP}]} \quad (1.4)$$

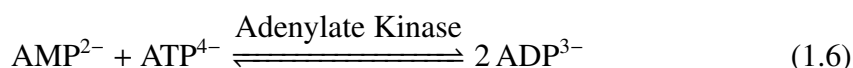
These measures are useful because it is important that ATP concentration is kept high, so that the many cellular reactions relying on ATP can continue. In order to keep ATP concentration constant there are many methods of regulation, although the full details of regulation are not known.

An important step in the control of glycolysis is the reaction catalysed by phosphofruktokinase. The activity of this enzyme is reduced by allosteric ATP binding, but increased by adenosine monophosphate (AMP) binding.

Two reactions are important for buffering ATP levels in the cytoplasm. The first is the phosphocreatine system. Phosphocreatine exists mainly in the cytoplasm of the cell. Its concentration can be measured with magnetic resonance spectroscopy (see Section 1.3.2). In conditions where ATP synthesis cannot meet demand, a phosphate can be transferred from phosphocreatine (PCr) to ATP, catalysed by creatine kinase.



This reversible reaction is fast, so it is usually considered to always be in equilibrium. The reaction also involves a proton, which means that it is pH sensitive. The second reaction is the conversion of two molecules of ADP to one each of ATP and AMP. This is catalysed by the enzyme adenylate kinase.



Again, it is a fast reaction and is usually considered to always be at equilibrium.

Oxidative phosphorylation is regulated by ADP concentration. It has also been suggested that CCO is regulated allosterically at ADP/ATP binding sites [34]. ATP synthesis rate could also be increased by a greater substrate (NADH) supply. Several enzymes involved in the TCA cycle have been suggested as regulatory sites. The oxygen concentration is another important factor. If there is not enough oxygen to receive electrons, the components of the electron transport chain will become more reduced, and the rate of proton pumping across the membrane will decrease. It has been shown in mitochondrial suspensions that cerebral metabolic rate of oxygen consumption ( $\text{CMRO}_2$ ) begins to decrease when the oxygen concentration falls below  $20 \mu\text{M}$  [35]. The concentration at which metabolism is impaired is often called the critical oxygen concentration.

## Metabolite transport

In order for respiration to occur, metabolites need to be transported from the blood into the cell. Glucose and lactate are transported by facilitated diffusion. The family of transporters responsible for glucose transport are the GLUT transporters. There are twelve of these proteins, but GLUT1 and GLUT3 are responsible for the majority of glucose transport in the brain. GLUT1 is found at the blood-brain barrier, and (in the brain) GLUT3 is found almost exclusively in neurons [36]. The kinetics of these transporters have been studied in red blood cells [37].

The proteins responsible for transporting lactate are the monocarboxylate transporter (MCT) proteins. They also transport other monocarboxylates such as pyruvate. There are four types of MCTs that are known to transport metabolites and all of these have been found in the brain, although MCT3 has a limited distribution. MCT2 is found only in neurons in the brain; it is widely expressed in rats, but not in humans. The kinetics and rate constants of the different MCTs for lactate varies, for example, the kinetics of MCT1 are sensitive to pH, whereas those of MCT2 are not. Because the different MCTs are expressed differently in astrocytes and neurons, the lactate transport properties of the two cell types differ, with the transporters of astrocytes having on average a greater affinity for lactate [36].

These different lactate and glucose transport behaviours are important when considering the astrocyte-neuron lactate shuttle (ANLS). This is a hypothesis concerning the coupling of neuronal activity and glucose use [38]. It states that the increase in glutamate (a neurotransmitter) caused by neuronal activity leads to an increase in glucose uptake and glycolysis in astrocytes. This means that lactate production is increased, and lactate is released from the astrocytes and taken up by neurons where it is used to fuel the TCA cycle to produce ATP. Since it was first suggested, there has been a considerable amount of experimental evidence collected which is consistent with the theory [39]. There has also been a lot of mathematical modelling investigating ANLS. The concept of ANLS is not universally accepted, and some mathematical models have been used to argue that neurons meet their energy needs in rested and activated states almost exclusively by the uptake and metabolism of glucose (see Jolivet *et al.* [40] and Mangia *et al.* [41] for an overview of the disagreement).

### 1.2.4 Hypoxia-Ischaemia

Hypoxia at birth is usually caused by insufficient placental or pulmonary gas exchange. Ischaemia follows from cardiac depression. The lack of oxygen reaching the cells leads to energy failure, which in time, leads to cell death. A large part of what is known about the biochemistry of HI has been discovered from experiments on rats.

In general, cell death can be divided into three types: necrosis, apoptosis and phagocytosis. Necrosis is death caused by external factors. The cell membrane is damaged, and the cellular contents are released into the extracellular space causing inflammation. Apoptosis is a type of programmed cell death. It is important for development, and is a highly regulated process. It occurs in response to a variety of signals and results in cell fragments which are engulfed by other cells. Phagocytosis occurs when a signal from the cell causes the cell to be phagocytosed (engulfed and destroyed by another cell) and it has not undergone cell death by another method [42]. All three forms contribute to the cell death caused by HI. The relative importance of the three is not precisely known, but it varies based on the severity of the insult, the time after the insult, and the area of the brain. It has also been observed that the apoptosis caused by HI is different from apoptosis that occurs as a normal part of development, and hybrid necrotic-apoptotic cell deaths are seen. In fact, when considering HI it may be more accurate to consider necrosis and apoptosis as two ends of a continuum [43].

During the insult itself, necrosis is the leading cause of cell death. The lack of oxygen causes a reduction in pH, an increase in lactate, and a decrease in ATP concentration. The cell may no longer be able to pump sufficient  $\text{Na}^+$  out of the cell causing water to enter, and the cell membrane to depolarise [44].

There are several ways in which cell damage and death following HI during secondary energy failure is thought to occur. Glutamate is an excitatory neurotransmitter which requires energy for its reuptake. The reduction in available energy caused by HI therefore leads to a build up of glutamate in the extracellular space. This build up, known as excitotoxicity, causes over-activation of N-methyl-D-aspartate (NMDA) receptors which leads to a high level of calcium ions entering the cell. This can affect biochemical pathways in the brain leading to apoptosis, and can also cause depolarisation leading to necrosis [45]. It is possible that the immature brain is more sensitive to glutamate excitotoxicity, since NMDA receptors are present in greater numbers, as glutamate plays an important role in growth and development [2]. It has been observed in rats that those areas of the brain most sensitive to HI are also more sensitive to glutamate toxicity [46].

Another factor contributing to cell damage in HI is oxidative stress [47]. The term re-

active oxygen species (ROS) describes molecules containing oxygen with an unpaired electron, which are therefore highly reactive. Examples include superoxides and peroxides. Under normal conditions, cells are protected against ROS by antioxidants. However, if there is increased production, they can cause damage, particularly to mitochondria, and this can trigger apoptosis. This is known as oxidative stress. The immature brain is more vulnerable to oxidative stress because it has a lower antioxidant capacity. In addition, there is a high concentration of iron present which is involved in the formation of free radicals and damage to membrane proteins.

One contributor to oxidative stress is nitric oxide (NO). NO has many different functions in the brain. These include acting as a potent vasodilator, and as a neurotransmitter. It is synthesised by nitric oxide synthase (NOS) which exists in different forms. In neurons, NO is mainly produced by neuronal NOS (nNOS). The process is  $\text{Ca}^{2+}$  dependent, and so the  $\text{Ca}^{2+}$  influx caused by HI leads to increased NO production [48]. Excess NO can lead to cell damage in a number of ways, including reacting with the superoxide ion to form peroxynitrite, an inhibitor of mitochondrial function. It has been found in mice, that disruption of the nNOS gene reduces neuron damage from HI [49]. However, some studies have found inhibition of NOS is not beneficial for HI. This may be because an increase in epithelial NOS activity causes dilation of the blood vessels and increased blood flow which decreases the damage caused by HI. In fact, this vasodilation effect makes NO a potential treatment for ischaemia, and NO inhalation has recently been shown to reduce damage from ischaemia following traumatic brain injury in adult mice [50].

A number of therapies have been investigated for HI. Many of these are intended to disrupt the pathways of the biochemical processes discussed above. One of the most promising therapies is hypothermia. Rather than acting on a particular target, hypothermia is thought to decrease damage from all of the above causes via a reduction in the metabolic rate [7]: it decreases the rate of glutamate release, decreases the activity of NMDA receptors and decreases the rate of production of free radicals. Studies in human neonates show an overall positive effect of hypothermia [6]. Many studies have also been carried out in animal models, including in piglets (see Section 1.3.5).

### **1.3 Measurements**

There are many different ways of making measurements of the brain. The technique used depends on what is being measured. One measurement that is often of interest is the CBF. The first quantitative measurements of this were made by Kety and Schmidt in

1948 using a technique involving nitrous oxide and measurements of blood gases [51]. Other ways of monitoring cerebral blood flow or its changes include MRI arterial spin labelling, NIRS techniques and Doppler ultrasound. The latter measures the speed of blood flow through major arteries supplying the brain.

Information about the activity of the brain can also be obtained using a variety of methods. NIRS uses the difference in the absorption properties between oxygenated and deoxygenated haemoglobin to measure changes in brain oxygenation, which may be related to changes in brain activity. Functional MRI (fMRI) uses the different magnetic properties to detect the decrease in deoxygenated haemoglobin that accompanies an increase in electrical activity. Direct measurements of the electrical activity of the brain can be made by electroencephalography (EEG), however this does not offer the spatial resolution of MRI.

NIRS can also be used for monitoring oxygen metabolism, by measuring the oxidation state of CCO. MRS is another way to measure metabolic changes. It uses similar principles to MRI, but measures the concentration of a greater range of compounds, with a much lower spatial resolution [52]. Nuclei used for MRS include  $^1\text{H}$ ,  $^{31}\text{P}$ ,  $^{19}\text{F}$ ,  $^{13}\text{C}$  and  $^{23}\text{Na}$ . This allows measurement of concentrations of metabolites including ATP, PCr and lactate. Positron emission tomography (PET) is another technique which can give useful metabolic information [53]. It involves the use of radioactive tracers which can be used to label almost any biological compound. This makes PET a very flexible technique, however it involves exposure to ionising radiation. If invasive measurements are possible, microdialysis can be used to measure metabolite concentrations in extracellular fluid [54].

This work involves comparing the outputs of a mathematical model with physiological data, particularly data from NIRS and MRS. These techniques and their measurements are explained in more detail below.

### **1.3.1 NIRS**

When light travels through a solution it is absorbed by coloured compounds called chromophores. Tissue can be thought of a solution of these chromophores. Visible light cannot travel far through tissue, since it is strongly absorbed and scattered. Near-infrared describes light of wavelength 650–1000 nm. In this range of wavelengths, absorption by water is lower, as shown in Figure 1.9, which allows light to travel further through tissue. Near-infrared spectroscopy can be used to make quantitative measurements of the chromophore concentrations in tissue [56]. The three main absorbing chromophores

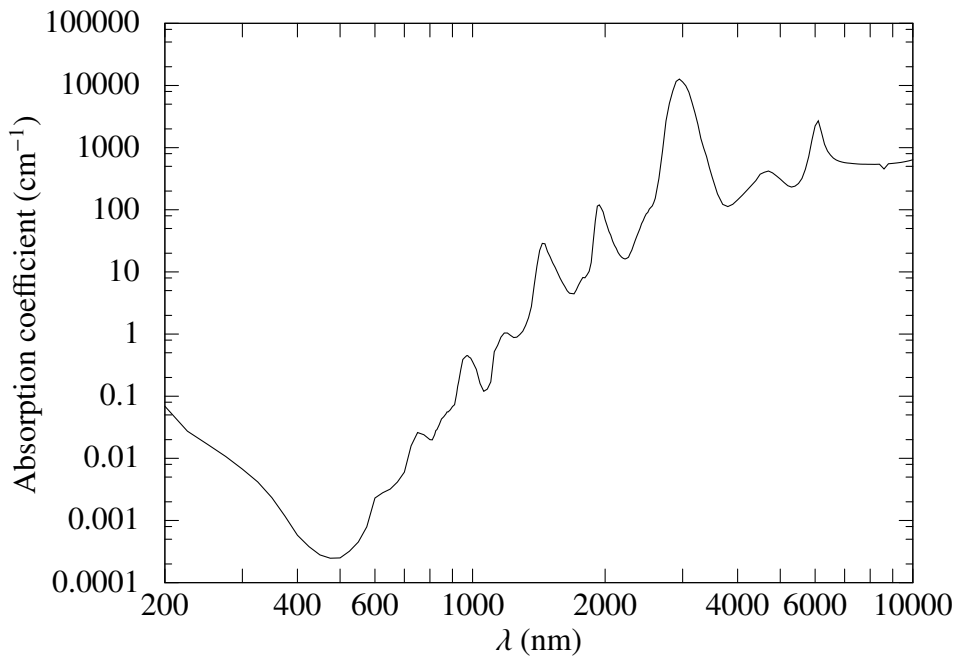


Figure 1.9: Absorption spectrum of water in the wavelength range 200–10 000 nm [55]

in the near infrared wavelength range are oxyhaemoglobin, deoxyhaemoglobin and oxidised cytochrome c oxidase (see 1.2.3). The absorption spectra for haemoglobin and oxyhaemoglobin are shown in Figure 1.10.

The Beer-Lambert law can be used to calculate the concentrations of absorbers in a solution, by measuring the absorption of light at known wavelengths. However, the effects of scattering in tissue mean that total concentrations of the chromophores cannot be measured, and a modified Beer-Lambert must be used which can only determine their concentration changes [56].

NIRS is most often used to measure blood flow and metabolism in the brain and in muscles [57]. It is especially useful for situations where other types of monitoring are not practical. It is often used on infants because their thinner skulls allow for greater penetration of the light. This means that NIRS measurement will cover a larger area of the brain. In some cases, the light is detected having passed through the head, whereas in adults, reflected light must always be used. Its uses include identifying cerebral hypoxia and monitoring during procedures [58]. One of its main advantages over other measurement techniques is that it can detect changes in the oxidation state of CCO. NIRS is also used for animal studies [59].

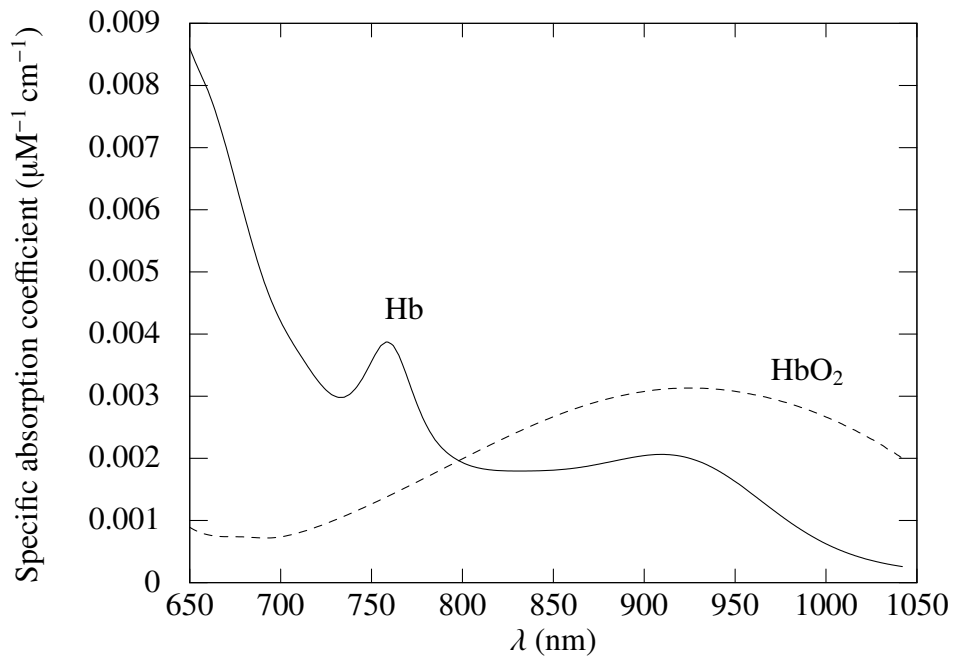


Figure 1.10: Absorption spectra for Hb and HbO<sub>2</sub> in the near-infrared region

## Haemoglobin

Haemoglobin and oxyhaemoglobin changes can be measured by NIRS. It is possible to measure the change in brain tissue concentration of oxyhaemoglobin ( $\Delta\text{HbO}_2$ ) and the change in brain tissue concentration of deoxyhaemoglobin ( $\Delta\text{HHb}$ ). These measurements are affected by volume changes and by oxygen saturation changes. The two signals can be added to give the change in total brain tissue haemoglobin concentration ( $\Delta\text{HbT}$ ), and subtracted to give the change in difference in brain tissue concentration between oxy and deoxyhaemoglobin ( $\Delta\text{Hb}_{\text{diff}}$ ).  $\Delta\text{Hb}_{\text{diff}}$  is considered a more reliable signal since some sources of noise will be removed by the subtraction. Changes in  $\Delta\text{HbT}$  can be used to estimate changes in cerebral blood volume (CBV). Techniques exist by which these haemoglobin signals can be used to make absolute CBF [60] and CBV [61] measurements.

## Cytochrome c oxidase

CCO plays an important role in mitochondrial respiration (see Section 1.2.3). Monitoring of oxidation changes at its  $\text{Cu}_A$  centre with NIRS was first proposed by Jöbsis [62]. The  $\text{Cu}_A$  centre is strongly absorbing in the near infrared region. Whilst the overall concentration of CCO does not change over short periods of time, the fraction of  $\text{Cu}_A$  that is oxidised does. The difference extinction spectrum of the oxidised and reduced forms

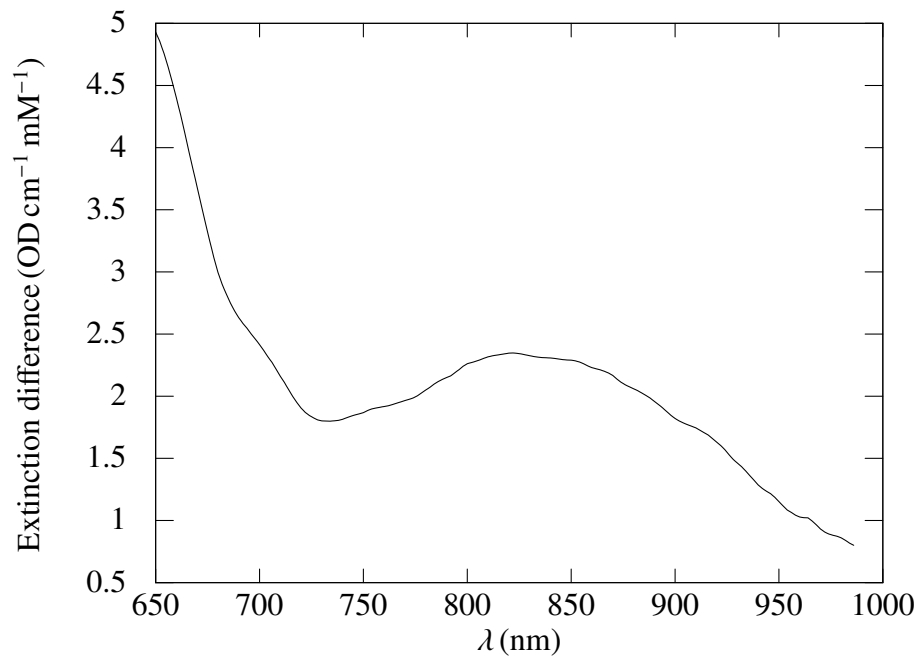


Figure 1.11: Difference extinction spectrum of cytochrome oxidase

of cytochrome oxidase (Figure 1.11) can be used to measure these changes. The spectrum shown includes a small contribution from other forms of cytochrome oxidase, but is mainly due to cytochrome c oxidase. Because the concentration of CCO in tissue is only about 10 % that of haemoglobin, it is more difficult to measure. Consequently, one of the main difficulties in measuring CCO is ensuring that the changes seen are actually CCO changes, and not artefacts from haemoglobin. Multiple methods have been used to calculate  $\text{Cu}_A$  oxidation changes from optical measurements. Gagnon *et al.* compared 13 algorithms and found a general agreement in their calculated  $\text{Cu}_A$  oxidation changes [63]. Matcher *et al.* [64] compared algorithms used by four different groups. They found that some of the algorithms showed more interference from the haemoglobin measurements than others. The main determinant of the oxidation state of  $\text{Cu}_A$  is the concentration of oxygen in the mitochondria. It is also affected by changes in substrate concentration and protonmotive force. NIRS measurement of CCO has advantages over direct methods of oxygen concentration measurement such as microelectrodes, because it is non-invasive and sensitive to the concentration at the mitochondria, which is where oxygen is used [65]. When oxygen concentration is low, electrons cannot be transferred to oxygen, and so  $\text{Cu}_A$  becomes more reduced.

**CCO measurements in vivo** The first measurements of CCO redox changes in vivo were reported by Jöbsis in 1977 [62]. CCO was seen to become more reduced during episodes of anoxia and ischaemia in anaesthetised cats. It became more oxidized during stimulated activity in the cortex, and also when  $\text{CO}_2$  or  $\text{P}_a\text{O}_2$  were increased.

A later study also using cats [66] found that CCO became more reduced when oxygen delivery was decreased, but that no changes were seen if the changes in oxygen ( $O_2$ ) delivery were only small. This experiment used blood-fluorocarbon exchanged cats thus removing the possibility of haemoglobin contamination in the signal.

The same pattern has been observed in other animals. For example, Hoshi *et al.* [67] lowered fractional inspired oxygen ( $FiO_2$ ) in adult rats from 100 % to 10 % and, although changes in  $\Delta HbO_2$  and  $\Delta Hb$  were seen, there was no change in change in concentration of oxidised CCO ( $\Delta oxCCO$ ). When  $FiO_2$  was lowered further, CCO became reduced. The point at which no further reduction of CCO was seen coincided with the flattening of the EEG measurement. Experiments involving blood-fluorocarbon exchanged rats have also confirmed that NIRS is sensitive to  $Cu_A$  oxidation changes [68, 69] and again shown that a lowered  $FiO_2$  leads to a reduction of CCO [70]. Similarly, Cooper *et al.* [71] found a linear relationship between the cerebral  $O_2$  delivery rate and the decrease in  $\Delta HbO_2$  in adult rats. CCO redox state did not change until the  $O_2$  delivery rate had reached half its normal value. They estimated that CCO was 82 % oxidised under baseline conditions. In another study, Cooper *et al.* used cyanide to completely reduce the CCO in piglets [72]. When afterwards, the piglets were subjected to anoxia, no further changes were seen in the  $\Delta oxCCO$  confirming that NIRS can be used to measure changes in CCO redox state in piglets.

In experiments with foetal lambs, an oxidation of CCO has been observed in the brain during decreased oxygen delivery [73, 74]. In one of these studies, a reduction was measured simultaneously in the leg, suggesting there may be mechanisms in the brain which help to protect it against hypoxia.

In summary, the majority of studies of CCO during hypoxia have shown that, unlike  $\Delta HbO_2$  and  $\Delta Hb$ , CCO redox state is not sensitive to small changes in oxygen delivery, and  $Cu_A$  becomes reduced during hypoxia only after a delay. This may be because CCO has a high affinity for oxygen [75]. Edwards *et al.* found similar results in human infants, with no changes in CCO observed in arterial oxygen saturation ( $S_aO_2$ ) range 85–99 % [76], but an increase in  $\Delta oxCCO$  was seen when  $P_aCO_2$  was increased. An earlier study in human infants [61] also found an oxidation of CCO in response to an increase in  $P_aCO_2$ . However, an oxidation was also observed when  $S_aO_2$  was increased.

The situation in adult humans is different: changes in CCO oxidation are seen with small changes in  $S_aO_2$ . Tisdall *et al.* found a linear correlation between  $\Delta oxCCO$  and cerebral oxygen delivery [77].  $\Delta oxCCO$  changes were also found to correlate with  $S_aO_2$  changes during sleep apnea [78]. CCO redox changes have also been observed during functional activation, for example during visual stimulation [79, 80]. Some functional

activation studies have used Monte Carlo simulations to show that changes measured in  $\text{Cu}_A$  oxidation could not be attributed to cross talk from haemoglobin alone [81]. A recent study involving an anagram task in healthy adults found that whilst the majority of subjects showed a significant oxidation of CCO during the task, some subjects showed a reduction [82]. Finally,  $\Delta\text{oxCCO}$  changes have also been observed during hypercapnia in healthy adults [83].

Aside from differences in experimental methods and algorithms, the differences in CCO redox state changes during hypoxia between animals, infant humans and adult humans may be caused by the differing resting metabolic rates of these groups. In the majority of animal studies, anaesthesia is used, which may affect the metabolic rate and the baseline redox state of CCO.

## TOS

In this thesis, the term tissue oxygen saturation (tissue oxygen saturation (TOS)) will be used to describe the percentage of haemoglobin that is oxygenated in a volume of tissue.

$$\text{TOS} = \frac{[\text{HbO}_2]}{[\text{HbO}_2] + [\text{HHb}]} \times 100\% \quad (1.7)$$

TOS can be measured by spatially resolved spectroscopy.

There is a variety of approaches to measuring TOS. Different instruments have different measurement techniques and different algorithms for calculating the estimate of TOS. There are several commercially available spectrometers which measure TOS [84]. Some are listed below, along with the specific name given to the measurement of TOS from that particular instrument, where this exists.

- NIRO by Hamamatsu, Japan measures tissue oxygenation index (TOI)
- INVOS by Somanetics, USA measures regional oxygen saturation ( $\text{rSO}_2$ )
- TRS-20 by Hamamatsu, Japan
- FORE-SIGHT by Casmed, USA measures cerebral tissue oxygen saturation ( $\text{SctO}_2$ )
- NIMO by NIROX, Italy measures tissue oxygen saturation ( $\text{StO}_2$ )
- O2C by LEA, Germany measures the oxygen saturation of haemoglobin ( $\text{SO}_2$ )

- OxiplexTS by ISS, USA
- T.Ox by ViOptix, USA
- EQUANOX, Nonin, USA measures rSO<sub>2</sub>
- InSpectra by Hutchinson, USA measures tissue oxygen saturation (StO<sub>2</sub>)

TOI [85] (a measurement of TOS from the NIRO spectrometers) is used in this work for comparison with TOS from the model. There have been several comparisons between the experimental methods, for example TOI and rSO<sub>2</sub> (INVOS) have been compared many times [86, 87, 88, 89]. In general the comparisons have shown that whilst the two measurements do not always agree numerically, they show similar changes in response to certain stimuli.

In principle, TOS is a simple measurement: the percentage of haemoglobin in tissue which is saturated with oxygen. However, in practice it can be difficult to interpret, because there are several physiological variables involved. It is most sensitive to venous oxygenation, because venous blood makes up approximately 75 % of the blood in the brain. One way of expressing TOS during steady state conditions is

$$\text{TOS} = \text{SaO}_2 - \left( \frac{V_{\text{ven}}}{V_{\text{art}} + V_{\text{ven}}} \right) \frac{\text{CMRO}_2}{k \text{ CBF} [\text{Hbtot}]} \quad (1.8)$$

where  $k$  is the oxygen carried per haemoglobin (about 1.3 ml g<sup>-1</sup>) [90]. From this expression, it can be seen that TOS can be affected by a number of variables. An increase in arterial saturation (with all other variables constant) would increase TOS, as would an increase in arterial volume. A decrease in CMRO<sub>2</sub> or an increase in CBF would lead to a lower oxygen extraction fraction and therefore a higher venous oxygenation, which again would increase TOS.

TOS measurements vary between individuals, and between different sites of measurement [91]. It is not fully known which factors contribute most to these differences. In general, the algorithms for calculating TOS attempt to give a measurement originating mainly from the deeper tissue, so that when used on the brain the signal comes mainly from the cerebral tissue, rather than from the overlying layers. However, there is concern that the measurements may be subject to extracerebral contamination. There is some evidence from theory and experiment to suggest that TOI is sensitive to changes in brain tissue, as opposed to extracranial tissue [92, 93].

The measurement of TOS has been used to study the injured brain [94]. For example, to monitor patients after traumatic brain injury [95] or during coronary bypass [96].

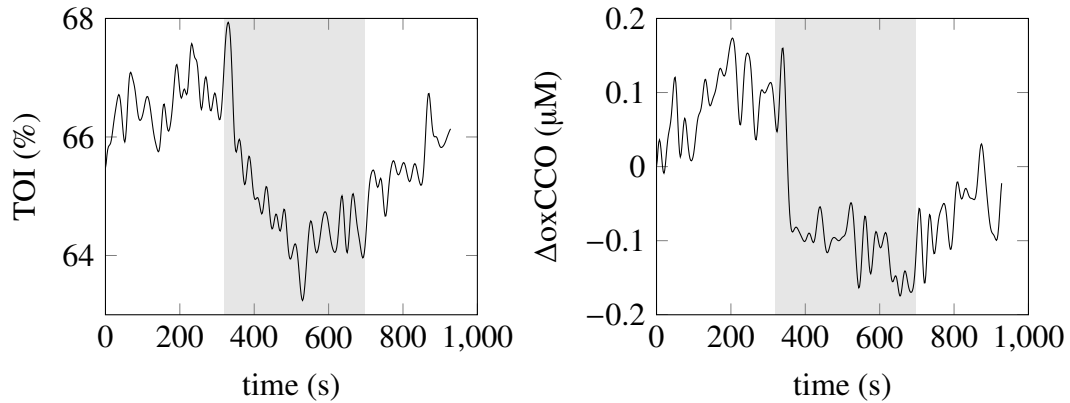


Figure 1.12: Example of TOI and CCO measurements by near-infrared spectroscopy during a hypocapnia challenge in a healthy adult. The hypocapnia period is indicated by the shaded area.

Despite results showing its monitoring can improve treatment, the clinical usage of TOS has been impeded by the lack of a well defined range of normal values, and the difficulty in validating the NIRS measurements. TOS has also been used to investigate responses in healthy subjects. TOI decreases have been observed during hypoxia and hypocapnia and increases during hyperoxia and hypocapnia [97, 88]. The TOI signal for a healthy adult during hypocapnia is shown in Figure 1.12.

### 1.3.2 MRS

Magnetic resonance spectroscopy uses the principle of nuclear magnetic resonance (NMR). This depends on the magnetic properties of the nucleus. A nucleus with a magnetic moment placed in a strong magnetic field, has a resonant frequency. This frequency depends on the properties of the nucleus and on the strength of the magnetic field. By applying a pulse of RF magnetic field matched to the resonant frequency, nuclei can be made to transition into an excited state for a short time. Whilst in this state, they give rise to a measurable, oscillating magnetic field. In a biological sample, this field will be made up of several components with slightly different frequencies. These correspond to the different molecules in the sample, since the resonant frequency of a nucleus is altered slightly by its chemical environment. By taking a Fourier transform of the measured field, the different molecules can be identified. The strength of the signal depends on the number of nuclei present, and therefore on the concentration of the substance.

The area of a peak in a spectrum is proportional to the concentration of that metabolite in the sampled region. Concentrations are often expressed as ratios. This allows cancelling

of unknowns relating to the measurement, however it can be more difficult to interpret. An alternative is to use a phantom with known concentrations as a reference. The main nucleus used in biological applications is  $^1\text{H}$ .  $^{31}\text{P}$  is also used and is discussed here. Only metabolites with concentrations greater than about 1 mM are detectable, although this depends on the system being used.

Figure 1.13 shows an example of an  $^1\text{H}$  spectrum from a normal human frontal lobe. The position of the peaks is expressed in parts per million (ppm). This is the shift in frequency from a given reference compound. The main peaks that can be distinguished in the  $^1\text{H}$  spectrum are described below.

**NAA** N-acetyl aspartate (NAA) is a molecule which is found in neurons, but not in glial cells. It is synthesised in mitochondria, and is thought to play a role in myelinogenesis and in fluid balance [98]. NAA is used as marker for neuron number and function. A decreased concentration is seen in diseases which cause neuron loss or damage, such as Alzheimer's disease and multiple sclerosis, and also in tumours.

**Lactate** In a healthy human brain, lactate is present at concentrations of around 0.5 mM, and so is not normally detectable. However, increases in lactate commonly occur when aerobic metabolism is compromised. Under these conditions, a lactate peak becomes detectable. Lactate peaks are visible in hypoxia, ischaemia, mitochondrial disorders, and some tumours. It is difficult to quantify the change in lactate concentration relative to baseline during an experiment, since this can depend strongly on the estimate of baseline concentration [99].

**Choline** Choline is generally found in compounds involved in membrane synthesis. Once it is incorporated into the membrane, choline cannot be seen by MRS. Therefore, an increased choline signal indicates increased membrane turnover or cell breakdown. This occurs in conditions such as tumours and multiple sclerosis.

**Creatine** Creatine is involved in cellular energy generation as discussed in Section 1.2.3. Here, it is the total creatine concentration ( $[\text{Cr}] + [\text{PCr}]$ ) that is measured. This is not likely to change significantly over the course of an experiment. However, regional variations in creatine concentration can sometimes be seen in the brain, and the signal may change with age or disease [100].

**Myo-inositol** mIns is a sugar synthesised in glial cells. It can be used as a glial marker and increased mIns is seen in inflammation, and disorders such as Alzheimer’s disease [101].

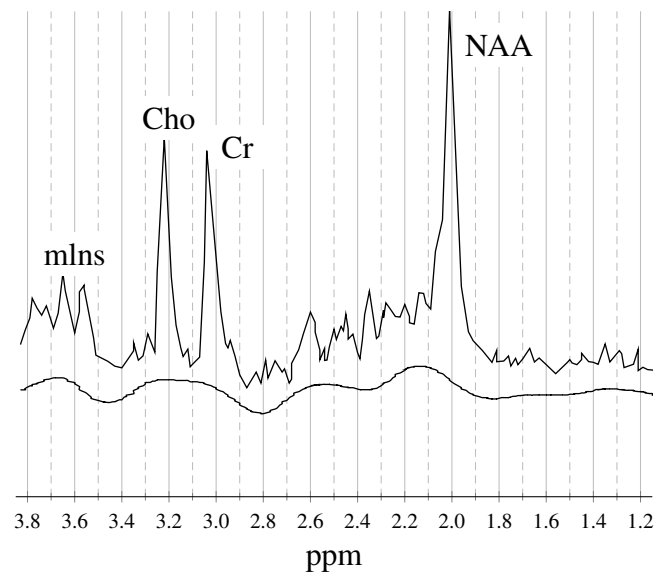


Figure 1.13: An example  $^1\text{H}$  MRS spectrum from a normal human frontal lobe taken from [52]

Figure 1.14 shows an example  $^{31}\text{P}$  spectrum from a healthy brain taken from [102]. The main peaks that can be distinguished are PCr,  $\text{P}_i$  and  $\alpha$ ,  $\beta$  and  $\gamma$  nucleotide triphosphate (NTP), which mostly originate from ATP. Also visible are peaks from phospho-monoesters (PME) and phosphodiester (PDE). These are groups of compounds the concentrations of which are reduced in neurodegenerative diseases. Individual metabolites from these groups can be identified with more advanced MRS techniques [103]. ADP concentration is often inferred from the creatine kinase equilibrium.  $^{31}\text{P}$  MRS can also be used to determine pH, from the shift in one or more of the peaks relative to the PCr peak as indicated by  $\delta$  in Figure 1.14. It is considered to be a reliable estimate of intracellular pH [104].

### 1.3.3 TCD

Transcranial doppler (TCD) is a technique which uses ultrasound to measure the velocity of blood through cerebral blood vessels. It uses the Doppler effect: an effect by which the frequency of a wave is altered by motion between the source and detector. The observed frequency shift can be used to calculate the relative velocity between the source and the detector in the direction of wave travel. In the case of TCD, the source is the reflection of ultrasound waves from the moving blood cells, and the detector is the

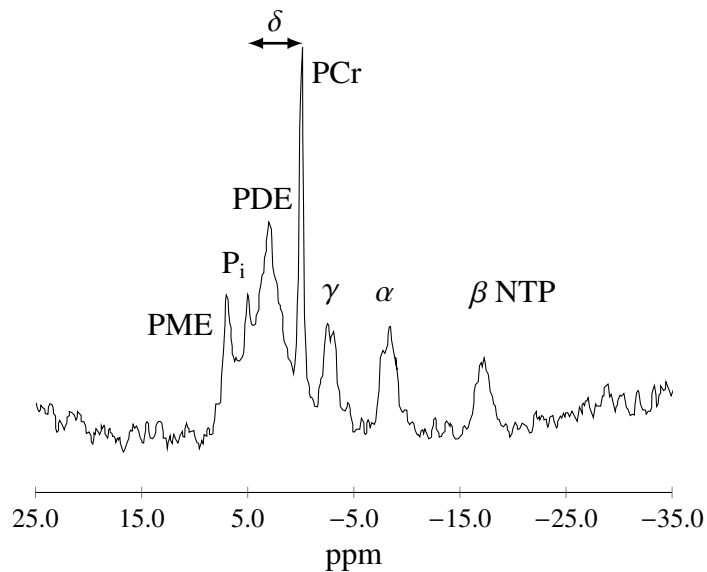


Figure 1.14: An example of a typical  $^{31}\text{P}$  MRS spectrum taken from [102].

stationary ultrasound probe. The use of Doppler ultrasound for cerebral measurements was first proposed in 1982 by Aaslid *et al.* [105]. Its main use is for monitoring CBF. Blood flow cannot be measured directly, since it depends on the radius of a vessel as well as the speed of flow through it. However, TCD can be used to monitor changes in CBF, since it can often be assumed that the radius of the insonated vessel is constant. Low frequencies must be used to allow enough ultrasound to pass through the skull. This means the technique has a poor spatial resolution, so is not suitable for imaging. However, the temporal resolution is good [106]. TCD relies on acoustic windows: areas of the skull where the bone is thinner than elsewhere. The blood vessels shown in Figure 1.15 can be investigated through the several available windows. These are the transtemporal, transorbital, transformial and submandibular windows [107]. However, approximately 10 % of people lack an acoustic window altogether, meaning TCD is not possible. The most commonly used window is the transtemporal window. One important vessel that can be insonated through this window is the middle cerebral artery. This measurement is known as the velocity of blood in the middle cerebral artery ( $V_{\text{mca}}$ ). Clinically, the uses of TCD include monitoring CBF after traumatic brain injury, and intra-operative monitoring [108]. It is also used to monitor autoregulation, including the cerebrovascular response to  $\text{CO}_2$ .

### 1.3.4 Systemic measurements

There are several systemic measurements that can be made simply and non-invasively which are relevant to the circulation and metabolism of the brain. These include heart

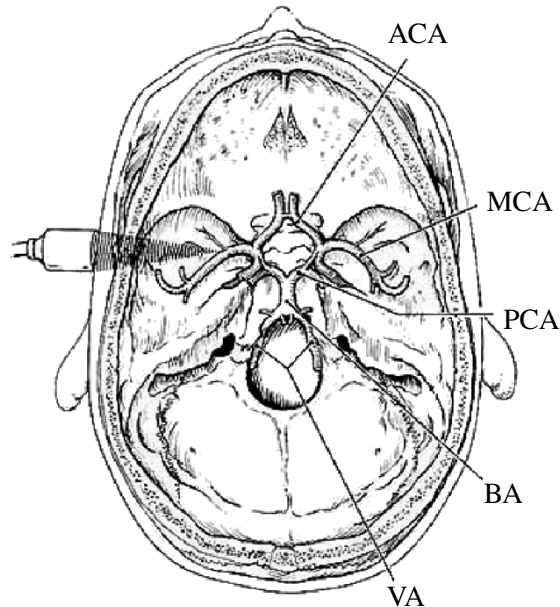


Figure 1.15: A diagram illustrating the use of TCD through the temporal window [108]. The vessels marked are the anterior cerebral artery (ACA), middle cerebral artery (MCA), posterior cerebral artery (PCA), basilar artery (BA) and both vertebral arteries (VA).

rate, blood pressure, CO<sub>2</sub> levels and arterial oxygen saturation.

### **Pulse oximetry**

Pulse oximetry was first developed in 1974 [109]. It was based on oximeters used to detect hypoxia in pilots in the 1940s [110]. Like NIRS, it measures the absorption of known wavelengths of light to determine blood oxygenation. However, unlike NIRS and the early oximeters, pulse oximetry measures the variation in light attenuation across the cardiac cycle. If two wavelengths are used, the oxygen saturation of haemoglobin in the pulsatile component of the blood (SpO<sub>2</sub>) can be calculated [111]. If it is assumed that pulsatile volume changes are entirely caused by arterial volume changes, SpO<sub>2</sub> will be equivalent to S<sub>a</sub>O<sub>2</sub>. Pulse oximetry measurements are usually made on the ear or the finger because of the ease of measurement.

Pulse oximetry is now very common in clinical use. It has been shown to produce accurate results for saturations above 80 % [112]. Below this, measurements are less accurate, in part because there is less data from other methods available to compare with. However, clinically, it is not usually necessary to have an accurate saturation measurement below 80 %. Other limitations of pulse oximetry include being unable to distinguish HbCO from HbO<sub>2</sub>.

## CO<sub>2</sub> measurements

Carbon dioxide produced during respiration is removed from the body by transport in the blood, followed by diffusion into the lungs. The partial pressure of carbon dioxide (PCO<sub>2</sub>) in the airways at the end of expiration is known as end tidal CO<sub>2</sub> (EtCO<sub>2</sub>). Under normal conditions, an equilibrium is quickly reached between the blood in the pulmonary capillaries and the gas in the alveoli. Therefore, EtCO<sub>2</sub> is equal to the partial pressure of carbon dioxide in the arterial blood (P<sub>a</sub>CO<sub>2</sub>) [113]. The measurement of PCO<sub>2</sub> in the airways is known as capnometry, and its visualisation over time as capnography.

A typical capnograph is shown in Figure 1.16. During inhalation, and at the beginning of exhalation PCO<sub>2</sub> is effectively zero. There is a rapid increase when exhalation of alveolar air begins, followed by a more gradual increase, at the end of which EtCO<sub>2</sub> is measured. A normal EtCO<sub>2</sub> measurement is around 35–40 mmHg. Finally, there is a rapid decrease back to zero at the start of inhalation.

EtCO<sub>2</sub> can be measured in a number of ways, the most common being with an infrared capnometer [114]. It is often used clinically during anaesthesia to monitor ventilation.

CO<sub>2</sub> levels in the blood can also be measured transcutaneously [115]. This involves warming the skin under the sensor, to dilate the capillaries, making their blood composition more similar to arterial blood. CO<sub>2</sub> concentration is determined by measuring pH in an electrode separated from the skin by a CO<sub>2</sub> permeable membrane. Alternatively, PCO<sub>2</sub> can be measured optically in a small sample of gas adjacent to the skin.

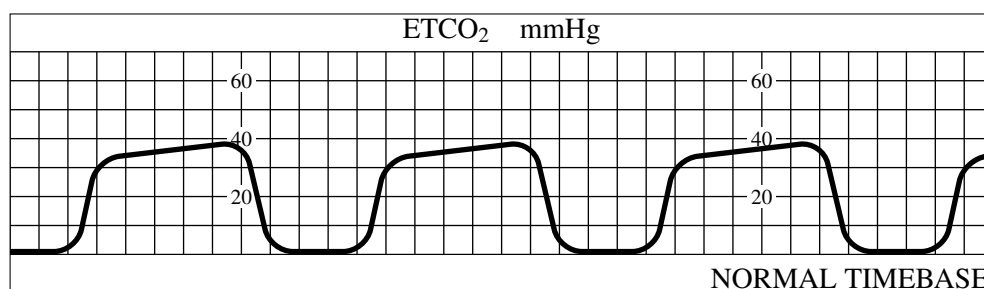


Figure 1.16: A typical capnograph [113]

## Blood pressure

The most common method of measuring blood pressure is to use a sphygmomanometer [116]. The measurement involves using an inflatable cuff to determine the pressure necessary to occlude the arteries. The site of measurement is usually the upper arm,

since it is at the same height as the heart, but measurements are also frequently made at the wrist or the finger. Blood pressure is typically quoted as two values: the maximum (systolic) and minimum (diastolic) arterial pressures in the cardiac cycle. Their normal values are around 120 and 80 mmHg respectively, although there is a wide variation between people, with age, and in response to situations such as stress or exercise [14].

Sometimes, it is the mean arterial blood pressure (MABP), the time average of arterial pressure, that is of interest. The shape of the blood pressure curve means that MABP is closer to diastolic pressure. It can be estimated as the diastolic pressure plus one third of the systolic to diastolic pressure difference, although more accurate estimates exist [117].

### 1.3.5 Piglet experiments

Several animal models have been used to investigate perinatal hypoxia-ischaemia, including rats, mice, rabbits, sheep, non-human primates and piglets [118]. Piglets have commonly been used for investigating HI. Animal models are useful, because it is difficult to make measurements on humans during hypoxia-ischaemia, and animal models allow for controlled conditions. However, animal models have the disadvantage that the findings in the animal may not be applicable to humans, and that long term measurements are more difficult [119]. A 1997 review by Rooney *et al.* [120] found that of 292 animal studies related to perinatal hypoxic ischaemic encephalopathy, 23% used piglets. A newborn piglet is similar in size to a newborn human, however its brain matures faster. Another difference is that piglets are usually anaesthetised during the experiments.

<sup>31</sup>P-MRS has often been used to study both birth-asphyxiated human infants [121, 9] and piglet models. Lorek *et al.* [122] developed a piglet model of secondary energy failure which they monitored with MRS. The piglets were subjected to temporary bilateral carotid artery occlusion and hypoxia, and then studied for 48 h during recovery. During the insult phase the concentration ratios PCr/P<sub>i</sub> and NTP/EPP fell to almost zero but returned to their baseline values soon after the insult. Both ratios then began to decline again around 24 h later despite no changes in P<sub>a</sub>O<sub>2</sub> or blood pressure. The magnitude of the changes seen during secondary energy failure was related to the severity of the initial energy depletion. The same model was also used by Mehmet *et al.* [123] to show that the time integral of the fall in NTP/exchangeable phosphate pool (EPP) was directly related to the fraction of cells undergoing apoptosis 48 h following the insult, as identified by light and electron microscopy and DNA fragmentation. In another study

$^{31}\text{P}$ -MRS and  $^1\text{H}$ -MRS spectra were acquired alternately [124]. The  $^1\text{H}$ -MRS lactate peak was observed to rise during the insult, then return to baseline, and then rise again over the following 48 h. The NAA peak was reduced in height, but appeared broader after 48 h. The maximum in the Lac/NAA ratio during delayed energy failure was positively related to the severity of the insult as measured by the integral of the NTP/EPP fall.

One of the first investigations into the relationship between NIRS measurements and MRS measurements in hypoxic piglets was done by Tsuji *et al.* [125]. They used four week old anaesthetised piglets, which were subjected to four increasingly severe hypoxic episodes with recovery in between. The  $\text{FiO}_2$  was reduced from 25 % to 12 %, 8 %, 6 %, or 4 % for 10 min and then returned to 25 % for a recovery period of approximately 30 min before the next hypoxia. The  $\Delta\text{HbO}_2$  decreased and the  $\Delta\text{HHb}$  increased at all levels of hypoxia, however there was no significant decrease of  $\Delta\text{oxCCO}$  until  $\text{FiO}_2$  reached 6 %. No significant decrease in NTP and PCr concentrations were seen at  $\text{FiO}_2$  levels of 12 % and 8 % but a decrease was seen at  $\text{FiO}_2$  of 6 %. A correlation was seen between the values of  $\Delta\text{oxCCO}$  and both NTP and PCr at the end of hypoxia. However, no correlation was seen between NTP or PCr with either  $\Delta\text{HbO}_2$  or  $\Delta\text{HHb}$ . The authors attributed this to the changes in systemic blood pressure which were observed and would have affected the CBF. The findings were in agreement with an earlier study which found a correlation between  $\Delta\text{oxCCO}$  and the  $\text{PCr}/\text{P}_i$  ratio in hypoxic dogs and cats [126].

Cooper and Springett [75] used NIRS and MRS to investigate HI in piglets caused by occlusion of the carotid arteries and a reduction in  $\text{FiO}_2$ . They found an excellent correlation between the fall in  $\Delta\text{oxCCO}$  and the fall in NTP concentration during the period of delayed energy failure. A correlation was not seen between the  $\Delta\text{oxCCO}$  signal and the  $\text{PCr}/\text{P}_i$  ratio. However, the authors point out that some of this correlation may be explained by changes in the optical properties of the brain (for example increased water content of the cells) giving misleading values for  $\Delta\text{oxCCO}$ .

Tichauer *et al.* [127] used NIRS to measure CBF and  $\text{CMRO}_2$  in newborn piglets following HI. The measurement of CBF was made using a intravascular tracer (indocyanine green).  $\text{CMRO}_2$  was calculated from the CBF measurement combined with a measurement of absolute haemoglobin concentration (also measured by NIRS). They found that immediately following HI, CBF was around 70 % greater than at baseline and  $\text{CMRO}_2$  was 30 % lower than baseline.  $\text{CMRO}_2$  remained decreased for several hours following the insult, whilst the other measurements returned to their baseline values. The method of estimating  $\text{CMRO}_2$  assumes a constant arterial to venous volume ratio, which means that the estimates may be inaccurate during the insult itself. Other studies

in neonatal animals have also found a  $CMRO_2$  reduction following HI [128, 129], but some studies found no changes [130, 131]. An increased  $CMRO_2$  has been observed in human infants with brain injuries, including those caused by HI, compared with healthy infants in the first few days of life [132].

NIRS has also been used together with EEG to monitor piglets subjected to HI. This was first done by Ioroi *et al.* [133] using the previously described piglet model of secondary energy failure [122]. They recorded a decrease in the amplitude integrated EEG (aEEG) signal during HI and during the reperfusion period. Similar to previous studies, a drop in  $\Delta HbO_2$  and a rise in  $\Delta HHb$  were seen during HI which quickly returned to baseline in the first minutes of reperfusion. The aEEG signal, although it showed recovery during the reperfusion phase, recovered more slowly, and did not reach baseline levels after 2 h. This appears to be consistent with the reduced  $CMRO_2$  suggested by the work of Tichauer *et al.*. Studies of human asphyxiated infants have found that aEEG in the first 3 h of life could be used to predict the severity of outcome [134].

### **1.3.6 Current research at UCL**

NIRS and MRS are two non-invasive methods for monitoring the brain which are currently being used at UCL. NIRS is used for adults, babies and animals. In adults, it is being used for patients with brain injuries, to add to current monitoring methods. NIRS studies are also being carried out on healthy volunteers to validate the measurements and help to understand how to interpret them. These studies include hypercapnia experiments, which are the subject of Chapter 4. Whilst there has been extensive work carried out on modelling light transport in tissue to understand the measurements, there has been less work on physiological modelling to help to interpret the measurements and investigate their compatibility with current knowledge of brain circulation and metabolism.

NIRS is used for animal models simultaneously with MRS at UCL to monitor piglets subjected to HI. One of the aims of these experiments is to establish if the NIRS measurement of  $\Delta oxCCO$  can be used to predict outcome and to monitor treatment. Combining NIRS with the more widely used MRS helps to validate the measurements and can also be used to gain an insight into metabolism and pathology following HI.

## 1.4 Summary

The brain requires a constant supply of oxygen and glucose from its circulation. This is metabolised to generate the ATP necessary to carry out the brain's vital functions. Cerebral autoregulation ensures that the supply is maintained despite systemic changes. However, if the changes are too large, the autoregulation mechanisms can no longer compensate and damage can occur. HI in neonates is one example of this, and is a significant cause of brain injury. Although several mechanisms responsible for the damage caused by HI are known, there are many questions remaining. Detecting these mechanisms at an early stage to help inform treatment is a particular challenge.

Two tools which can help with this are NIRS and MRS, both non-invasive modalities that can safely be used to monitor the brains of newborns. The two are complementary, with NIRS using light to monitor changes in tissue oxygenation and mitochondrial metabolism, and MRS using magnetic fields to monitor pH and the concentration of certain metabolites, the most relevant being ATP, PCr,  $P_i$  and lactate. The two modalities can be used simultaneously.

Piglets are often used as models of human neonates to investigate HI. There have been many previous studies where the brains of piglets subjected to HI have been monitored using either MRS or NIRS, and several where both have been used. Many of these have focused on one or two specific measurements as markers of outcome. Whilst this is valuable from a clinical perspective, it is important to try to understand the measurements together, at the level of the individual. This is where computational modelling could help. A model could help with the understanding of complex, non-linear relationships between the measurements, and help to link them to the biochemical mechanisms occurring at the cellular level. The form and content of the model will be strongly influenced by the experimental measurements available. However, it is important to allow for measurements which are not performed in the particular experiments used, but may be used by others or become available in future. A physiological approach will help to give the model the flexibility necessary for this. Chapter 2 discusses the use of mathematical modelling to investigate biological systems, and reviews some common approaches and some of the existing models relevant to the applications in this thesis.

## Chapter 2

# Modelling biological systems

Mathematical modelling is a powerful tool for investigating biological systems. Physiological modelling in particular, is a useful way to collate knowledge about a system and make explicit the assumptions that are being made. There is a long history of applying mathematics to biological problems. However, computational advances have led to an ability to solve complex sets of equations in short spaces of time. Also, developments in experimental biology have made available large amounts of data with which to develop and validate models. This creates the opportunity to use sophisticated mathematical models in medicine. The development of such models relies upon, and also informs, a biological understanding of the systems involved. The ultimate aim of this type of modelling is to have a set of integrated models covering all aspects and scales of human physiology, which can be tailored to individuals. Projects with the objective of achieving these aims already exist [135, 136]. These projects will only be possible with the development of mathematical models of many different systems. Therefore biological modelling and systems biology are growing fields [137].

A model has been defined as an abstract representation of a complex system in mathematical form [138]. The formulation of a model usually requires some simplifying assumptions, and the accuracy of the model relies on the validity of these assumptions. A mathematical model representing an entire human is a huge challenge. Hunter and Borg [139] pointed out that the range of scales required in such a model would stretch from 1 nm to 1 m on the spatial scale and from 1  $\mu$ s to  $10^9$  s on the temporal scale. Southern *et al.* [138] classify biological models in terms of ‘levels of biological organisation’. These range from environmental to quantum, and also include (among others) organ, cellular and molecular. Multiscale models include a mixture of these levels and must include interactions between them.

The nature of the model will depend on the scale (or scales) that it represents. Models on the cellular scale deal with chemical reactions, whereas models on the organ or tissue scale tend to involve physical properties of the system. The models used in this thesis are concentrated on these scales, and involve both physical modelling of the blood flow in the brain, and modelling of chemical reactions taking place at the cellular level.

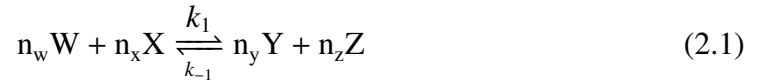
This chapter contains background information relating to biological modelling. The first section introduces some of the standard methods used to model biological processes which are relevant to this work. The following section concerns existing models in the areas of cerebral blood flow and metabolism.

## 2.1 Methods used in biological modelling

### 2.1.1 Chemical reactions

#### Mass action

The rate of a reaction obeying the law of mass action depends only on the concentration of the reactants and products. For example, in the reaction.



the rate of formation of the product is given by

$$[\dot{Y}] = k_1 [W]^{n_w} [X]^{n_x} - k_{-1} [Y]^{n_y} [Z]^{n_z}. \quad (2.2)$$

At equilibrium the forwards and backwards rates are equal, therefore the ratio of the rate constants is given by

$$\frac{k_1}{k_{-1}} = \frac{[Y]_{eq}^{n_y} [Z]_{eq}^{n_z}}{[W]_{eq}^{n_w} [X]_{eq}^{n_x}} = K_{eq} \quad (2.3)$$

where  $K_{eq}$  is the equilibrium constant for the reaction. At equilibrium the Gibbs free energy change for the reaction is zero. Away from equilibrium it can be calculated as

$$\Delta G = RT \left[ -\ln K_{eq} + \ln \left( \frac{[Y]^{n_y} [Z]^{n_z}}{[W]^{n_w} [X]^{n_x}} \right) \right]. \quad (2.4)$$

## Michaelis Menten

The Michaelis Menten equation describes a simple enzyme mediated reaction. For the conversion of a substrate S to a product P catalysed by an enzyme E, the reaction scheme is



where ES is the enzyme substrate complex. The formation of the complex is reversible, but dissociation of the product from the enzyme is assumed to be fast and irreversible. Total enzyme concentration is constant.

$$[E_T] = [ES] + [E]. \quad (2.6)$$

In steady state, the fraction of enzyme bound to the substrate is also constant

$$[ES] = k_1[S]([E_T] - [ES]) - (k_{-1} + k_2)[ES] = 0. \quad (2.7)$$

The rate of formation of product can then be calculated.

$$[\dot{P}] = k_2[ES] = \frac{v_{\max}[S]}{k_M + [S]}, \quad k_M = \frac{k_{-1} + k_2}{k_1}, \quad v_{\max} = k_2[E_T] \quad (2.8)$$

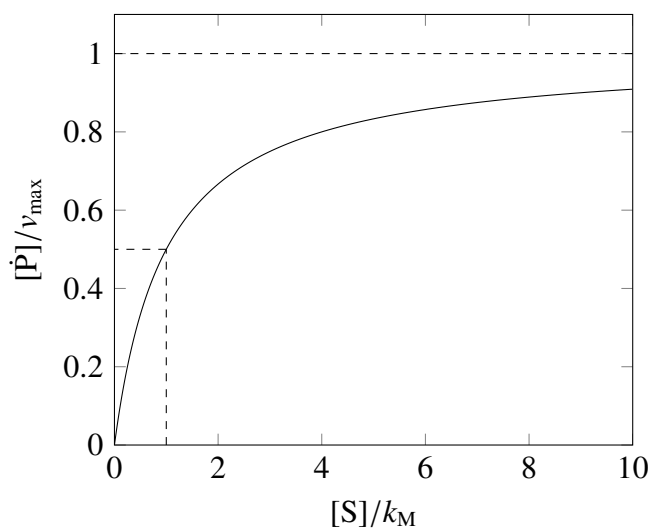


Figure 2.1: Reaction rate vs substrate concentration for a reaction obeying Michaelis Menten kinetics

The relationship has two parameters:  $v_{\max}$  the maximum reaction rate, which is limited by the enzyme concentration, and  $k_M$ , the substrate concentration at which the reaction rate is half maximal. The relationship between rate and substrate concentration is illustrated in Figure 2.1. This equation is very commonly used in the description of biological reactions which show saturation kinetics.

### 2.1.2 Transport

Passive diffusion of a substance across a barrier, between two compartments with concentrations  $c_1$  and  $c_2$  can be modelled as a mass action process.

$$\frac{\partial c_1}{\partial t} = -k(c_1 - c_2) \quad (2.9)$$

where  $k$  is a constant relating to the properties of the barrier. Transport of substances across a biological membrane is often controlled by membrane proteins. In these cases the movement of the substances can be described as a more complex chemical reaction, for example, a Michaelis-Menten reaction catalysed by the membrane protein.

## 2.2 Overview of circulation and metabolism models

The rest of this chapter is devoted to discussing existing models of circulation and metabolism. In the case of models of blood flow, only models of the brain will be discussed, since these are the most relevant. On the other hand, energy metabolism is very similar across cell types, so some of the models discussed are general models, or models of different cell types. Some of the more recent models of brain circulation and energy metabolism are summarised in Table 2.1 and are discussed below. In this section, models which describe only cerebral circulation, oxygen delivery, or specific aspects of metabolism are described. These models are focused relative to the scope required to simulate brain circulation and metabolism as a whole, and to simulate measurements from a variety of modalities. Many of them have been included in, or used to help construct more general models, which are the subject of the Section 2.3.

Paper and year	Main Aspect	Summary	Situation modelled
Korzeniewski and Froncisz [32] 1991	Oxidative phosphorylation	Dynamic model of respiration in isolated cells including substrate dehydrogenation, respiratory chain, CCO, ATP synthesis and use.	Oxygen concentration, CCO oxidation and ATP concentrations in cellular suspensions.
Czosnyka <i>et al.</i> [140] 1993	Circulation	Cerebrovascular resistance and compliance as a function of cerebral perfusion pressure and arterial CO <sub>2</sub> pressure	Interhemispheric asymmetry of CBF reactivity to arterial CO <sub>2</sub> in patients with carotid artery stenosis.
Hyder <i>et al.</i> [141] 1998	Oxygen delivery	Oxygen concentration and transport, CBF, oxygen extraction and CMRO <sub>2</sub>	Relationship between CBF and CMRO <sub>2</sub> for graded anaesthesia in rats and humans and functional activation in humans.
Ursino and Lodi [142] 1998	Circulation	Interaction between CBF, CBV, ICP and autoregulation.	ICP dynamics and cerebral dynamics in response to CO <sub>2</sub> changes.

Table 2.1: A summary of some of the models of brain circulation and metabolism

Paper and year	Main Aspect	Summary	Situation modelled
Aubert <i>et al.</i> [143] 2001	Functional activation	Neuronal energy metabolism, brainhaemodynamics and blood-brain barrier exchange, sodium mebrane transport and Na/K ATPase.	Function imaging by fMRI and MRS obtained during prolonged stimulations.
Korzeniewski and Zoladz [144] 2001	Oxidative phosphorylation	Oxidative phosphorylation in mammalian skeletal muscle. Extension of previous models including the creatine kinase system.	Used to demonstrate that CK does not significantly affect the kinetics oxidative phosphorylation. Suggests parallel activation of different steps of oxidative phosphorylation at higher work intensities.
Gjedde [145] 2002	Oxygen delivery	Oxygen tension in mitochondria and capillaries, oxygen diffusion, blood flow and oxygen consumption.	Regional cerebral blood flow and metabolism as functions of arterial oxygen saturation.

Table 2.1: A summary of some of the models of brain circulation and metabolism

Paper and year	Main Aspect	Summary	Situation modelled
Cortassa <i>et al.</i> [146] 2003	Metabolism	ODE model of cardiac mitochondrial energy metabolism including TCA cycle, oxidative phosphorylation and $\text{Ca}^{2+}$ .	Mitochondrial bioenergetic data, $\text{Ca}^{2+}$ dynamic and respiratory control.
Aubert and Costalat [147] 2005	Astrocytes & neurons	Model of compartmentalised energy metabolism in neurons and astrocytes.	Theoretical testing of the ANLS hypothesis.
Jung <i>et al.</i> [148] 2005	Circulation	Cerebral circulation and oxygen supply and autoregulation	Relationship between blood pressure and CSF production. Correlation between arterial oxygen concentration and blood pressure with impaired autoregulation.
Beard [149] 2006	Oxygen transport and metabolism	Oxygen transport and metabolism including ATP, ADP, PCr and oxidative phosphorylation and ATP synthase.	Based on data from isolated mitochondria. Compared with ATP, ADP, PCr and $\text{P}_i$ data at different workloads during coronary hypoperfusion.

Table 2.1: A summary of some of the models of brain circulation and metabolism

Paper and year	Main Aspect	Summary	Situation modelled
Vatov <i>et al.</i> [150] 2006	Metabolism	Cerebral blood flow, oxygen pressure, mitochondrial NADH redox state and extracellular potassium.	Pathological conditions including complete and partial ischaemia and cortical spreading depression.
Simpson <i>et al.</i> [36] 2007	Astrocytes & neurons	Brain glucose and lactate levels during neuronal activation, including kinetic description of transporter proteins.	Concludes neurons are primarily responsible for glucose uptake and the generation of lactate transients.
Alastruey <i>et al.</i> [151] 2008	Circulation	One dimensional non-linear model of pulsatile blood flow and arterial haemodynamics and autoregulation.	Effects of anatomical variation in the circle of Willis on blood flow after sudden carotid artery occlusion.
Cloutier <i>et al.</i> [152] 2009	Astrocytes & neurons	Based on Aubert and Costolat [147] but including glutamate cycling, an expanded description of glycolysis, and glycogen dynamics.	Calibrated from in vivo data from freely moving rats. Verified by data from a restraint simulation.

Table 2.1: A summary of some of the models of brain circulation and metabolism

Paper and year	Main Aspect	Summary	Situation modelled
Linninger <i>et al.</i> [153] 2009	Circulation	Blood, CSF, parenchyma and spinal canal model to predict intracranial pressure gradients and blood and CSF flow.	CSF flow velocities in normal subjects and subjects with hydrocephalus.
DiNuzzo <i>et al.</i> [154] 2010	Astrocytes & neurons	Unification of models by Aubert and Costolat [147] Simpson <i>et al.</i> [36] and Mangia <i>et al.</i> [155].	Modelling of metabolite trafficking in the brain during functional activation. Concludes neuronal metabolism is controlled through glucose uptake.
Orlowski <i>et al.</i> [156] 2011	Metabolism	Addition of pH dynamics to the model of Cloutier <i>et al.</i> [152], including pH buffering and proton transport channels.	pH changes following ischaemic stroke to help understand tissue damage.

Table 2.1: A summary of some of the models of brain circulation and metabolism

### 2.2.1 Models of circulation

Many compartment models of cerebral circulation have been published since the work of Monro and Kellie [157]. These models are made up of several compartments, usually including the arteries and veins. Other commonly modelled compartments include capillaries, CSF and venous sinuses. In general, this type of models aim to predict variables such as CBF or intracranial pressure (ICP) from measurements such as arterial blood pressure and  $P_a\text{CO}_2$ . They assume laminar flow of incompressible fluid along the cerebral blood vessels, and use a variety of different methods to relate changes in the resistance and volumes of the vessels, and the flow through them to changes in pressure. A common way of representing such models is as an electrical circuit. Flow is analogous to current, perfusion pressure to voltage, resistance of the vessel walls to electrical resistance and changes in volume of the vessels are related to capacitance. An example is shown in Figure 2.2.

These types of models do not, in general, involve spatial resolution or modelling of flow in individual vessels. This would increase the complexity of the model and make it more computationally intensive to solve. Models of this kind do exist [158, 159] and it would be helpful to use this kind of model if comparing with measurements from modalities offering spatial information such as MRI.

An aspect of particular importance in models of cerebral circulation is autoregulation. Most mathematical analyses of autoregulation fall into two categories: transfer function analysis and physiological models. The former involves formulating functions which map the input (in this case the arterial blood pressure) to the output (in this case some measure of CBF such as  $V_{mca}$ ) [160, 161]. Transfer function analysis assumes a linear, time invariant system. Therefore, if a system cannot be approximated well by these assumptions, a physiological approach is often used. This involves creating a mathematical representation of the autoregulatory system. The two approaches have also been combined [162].

One well-established model that takes a physiological approach is the model by Ursino and Lodi [142] which has been used to investigate autoregulation and  $\text{CO}_2$  response. Another model with a similar approach is that of Jung *et al.* [148]. This model was developed specifically to investigate measurements from patients in neurosurgical intensive care, and it also includes a model of oxygen diffusion from the capillaries. These models concentrate on changes in steady state, or changes over relatively long time scales, but other models focus on pulsatile flow. Examples include the models by Alastruey *et al.* [151] and Linninger *et al.* [153] and the model by Czosnyka *et al.* [140]

which investigates the relationship between cerebral perfusion pressure and CO<sub>2</sub> levels with the pulse wave of CBF. The models of circulation used in this work are based on the model by Ursino and Lodi [142] and this is therefore described in more detail below.

### Model by Ursino and Lodi

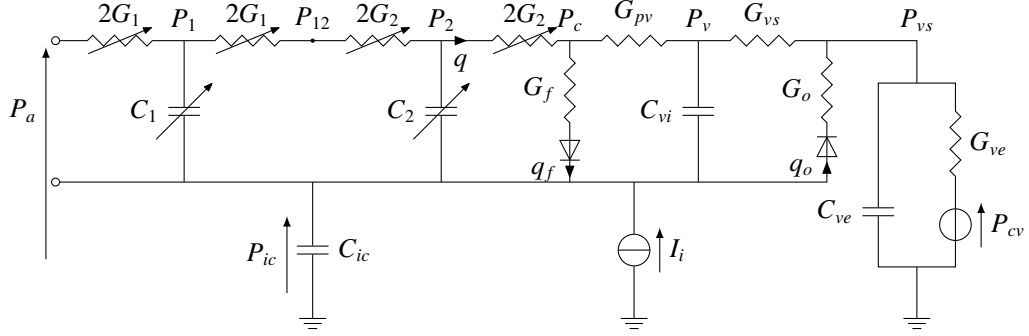


Figure 2.2: Electrical circuit analog from Ursino and Lodi [142]

The model by Ursino and Lodi [142] is a model of cerebral blood flow, intracranial pressure and volume, and CSF, illustrated by an analogous electrical circuit in Figure 2.2. The total intracranial volume  $V$  is related to the intracranial pressure  $P_{ic}$  by the compliance  $C_{ic}$ . The compliance itself is inversely proportional to the intracranial pressure and a constant  $k_E$ .

$$C_{ic} \left( \frac{dP_{ic}}{dt} \right) = \frac{dV}{dt}, \quad C_{ic} = \frac{1}{k_E P_{ic}} \quad (2.10)$$

There are four compartments with variable volume: the large pial arteries, small pial arteries, veins and CSF. The arteries are modelled as a parallel arrangement of vessels with equal (inner) radius  $r$ . Blood volume is proportional to  $r^2$  and the conductance of the vessels to  $r^4$ . The radius is determined by intravascular pressure  $P$ , intracranial pressure, and the tension  $T$  in the arterial walls.

$$P_a r - P_{ic}(r + h) = T_e + T_m + T_v \quad (2.11)$$

$T_e$ ,  $T_m$  and  $T_v$  are the elastic, muscular and viscous tensions, which are summed to give the total tension. The wall thickness  $h$  is calculated from the inner radius, assuming that the vessel wall is incompressible. The elastic and viscous tensions are functions of  $r$ . Muscular tension is also a function of  $r$ , but additionally depends on a parameter that changes in response to CO<sub>2</sub> levels and to represent autoregulation.

The venous part of the model is divided into three compartments. The first represents vessels from the capillary venules to the large cerebral veins, and the second represents

the final part of the large cerebral veins up to the dural sinuses. The pressure in the first compartment is always higher than the ICP, and therefore this compartment does not collapse. Its conductance is considered to be constant i.e. the effect of small changes in diameter are ignored. The second compartment is assumed to collapse before entering the dural sinuses, where the pressure in the vessels equals the ICP. The total volume of these two venous compartments ( $V_v$ ) varies according to

$$P_v - P_{ic} = P_{v0} \exp(K_v (V_v - V_{v0})) + P_{v1} \quad (2.12)$$

where  $P_v$  is the venous pressure,  $P_{ic}$  is the intracranial pressure and  $P_{v0}$ ,  $P_{v1}$ ,  $K_v$  and  $V_{v0}$  are constants. The final venous compartment represents the dural sinuses to the heart and has a fixed conductance and compliance.

CSF is produced from the capillaries, and drains into the venous sinuses. The rates of these processes are proportional to the transmural pressure differences. However, they are assumed to only occur in one direction, and their rates become zero if the pressure gradient changes direction.

## 2.2.2 Models of oxygen delivery

Other models concentrate on oxygen delivery and the relationship between flow and oxygen consumption. One such model is that by Gjedde *et al.* [145]. It was used to investigate oxygen delivery during neuronal activation and show that experimental results could be consistent with a negligible reserve of oxygen in brain mitochondria. Another model of this sort was developed by Hyder *et al.* [141]. It was created to investigate the relationship between CBF and CMRO<sub>2</sub> seen in data from a range of experiments. It differs from an earlier model by Buxton and Frank [163] by allowing a variable diffusivity of the capillary bed. Although these models have been successful at reproducing data from experiments such as functional activation, they do not model cellular metabolism and therefore cannot, in general, model concentration changes of metabolites.

## 2.2.3 Models of metabolism

The scope of models of energy metabolism ranges from the whole process of energy metabolism to modelling oxygen binding with CCO [164]. The models in this thesis need to cover the whole of energy metabolism in order to simulate the necessary ex-

perimental signals. However, to limit the complexity of the model, most stages are represented by a single reaction. More detailed models are useful for helping to develop simplified expressions, and in the future could be included in a modular way into a larger model.

There are several models of glycolysis which include all the reactions and stages. Glycolysis has particularly been modelled in yeast [165, 166] and red blood cells [167, 168]. There is a large amount of experimental data available for these cell types and the biochemical pathways are well known. In yeast, models have been able to reproduce glycolytic oscillations seen in these cells [166]. Detailed models of the TCA cycle also exist [169]. A comprehensive model of the TCA cycle was developed by Wu *et al.* [170]. The model includes 42 flux expressions, of which 11 are TCA cycle fluxes and most of the remaining fluxes are related to transport. It draws on the earlier work of Kohn *et al.* [171] and it can simulate the concentrations of 34 biochemical reactants. The rate constants were taken from experimental values where possible and the rest were estimated based on data from isolated mitochondria. The model was used to predict how the TCA cycle is regulated. The authors concluded that the most important regulator is the mitochondrial redox state i.e. the NAD/NADH ratio, but that ADP concentration is also an important factor.

Models concentrating on oxidative phosphorylation include the models by Korzeniewski in isolated mitochondria and in muscle, and the model of cardiac metabolism by Cortassa *et al.* [146]. The Korzeniewski models are discussed in more detail below, since aspects of the models in this thesis are taken from them. The Cortassa model, in addition to oxidative phosphorylation, describes the TCA cycle and other processes in the mitochondrial matrix. The form of the equation describing ATP synthesis is based on a model by Magnus and Keizer [172]. The rate equation is derived from a six stage cycle. Different paths around this cycle are evaluated and combined to give an overall rate. Some of these paths represent incomplete coupling; i.e. transfer of protons can occur without ATP synthesis or vice versa. This also leads to the rate depending differently on the two components of the protonmotive force. The constants in the expression are derived by fitting to data from isolated mitochondria.

### **Models by Korzeniewski**

Korzeniewski and co-workers have developed dynamic models of oxidative phosphorylation, initially for mitochondria in cellular suspensions [32], and then extended to muscle [144].

The models include the main reactions involving ATP, ADP,  $P_i$  and phosphocreatine. The total exchangeable phosphate pool is a constant and equal to

$$3[\text{ATP}] + 2[\text{ADP}] + [\text{AMP}] + [P_i] + [\text{PCr}]. \quad (2.13)$$

ATP and ADP exist in free and magnesium bound forms. The relative concentrations of these forms depends on the  $Mg^{2+}$  concentration and the relevant dissociation constant. In addition, ATP and ADP are considered separately in the mitochondria and in the cytosol. The rate of transfer between these is dependent on the mitochondrial and cytoplasmic concentrations of free ATP and ADP, and on the protonmotive force. The form of the kinetics is complex and was derived from experimental data.

The ATP synthesis rate is calculated by assuming the rate limiting step is the dissociation of ATP from the enzyme ATPase. ATPase exists in two states: bound to the substrate, and bound to the product. The dissociation rates of these two states are equal. The ratio between the concentrations of substrate-enzyme state and product-enzyme state is equal to the displacement of the synthesis reaction from equilibrium. With these assumptions, ATP synthesis rate  $v_{s,\text{ATP}}$  can be calculated as

$$v_{s,\text{ATP}} = k_s \frac{e^{\Delta G} - 1}{e^{\Delta G} + 1} \quad (2.14)$$

where  $k_s$  is a constant and  $\Delta G$  is the Gibbs free energy change for the reaction resulting in the synthesis of one molecule of ATP in the mitochondria. Hydrolysis of ATP takes place in the cytoplasm and is modelled as a single Michaelis-Menten process. The constant  $k_M$  is set so that ATP use is almost saturated at physiological ATP concentrations. The reactions catalysed by creatine kinase and adenylate kinase are modelled as mass action reactions.

## 2.3 Models combining circulation and metabolism

Below, several models are described that aim to represent multiple aspects of energy metabolism, circulation and oxygen delivery in a number of compartments or cell types. All are models of the brain except that of Beard [149]. This models cardiomyocytes and focuses on mitochondrial metabolism which is similar between cell types.

### 2.3.1 Models by Aubert *et al.*

The models of brain energy metabolism by Aubert *et al.* have been widely used and adapted since the first model was published in 2001 [143]. This is a model of electrical activity, energy metabolism and haemodynamics made up of 17 variables and 49 parameters and is illustrated in Figure 2.3.

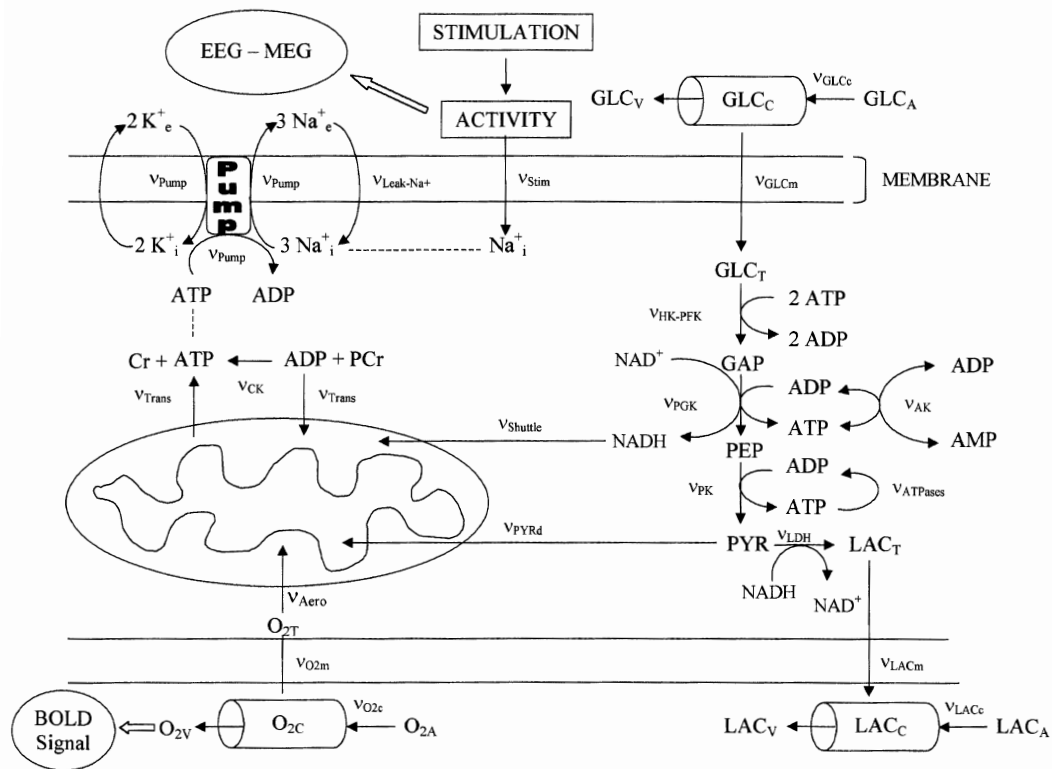


Figure 2.3: Schematic diagram of the 2001 model by Aubert *et al.* [143]

There are two compartments representing the capillaries and the intracellular contents of the neurons. ATP is consumed mainly by the Na<sup>+</sup>/K<sup>+</sup> pumps, and this process is modelled with a Michaelis-Menten relationship to ATP. It is also consumed by other ATPases which are grouped into a single process occurring at a constant rate. ATP is regenerated by glycolysis, oxidative phosphorylation and by phosphocreatine. The creatine kinase reaction is modelled as a mass action reaction, with no dependence on pH. The description of glycolysis is taken from a model of metabolism in erythrocytes by Heinrich and Rapoport [173], and parameter values are also taken from the model of erythrocyte metabolism by Joshi and Palsson [168]. The description of glycolysis involves four stages. Conversion between pyruvate and lactate is modelled as a mass action reaction. Lactate, glucose and oxygen are all transported between the blood and the intracellular space: lactate and glucose by facilitated diffusion, and oxygen by

simple diffusion.

Mitochondrial respiration is modelled as a single step, which means this model cannot simulate CCO redox state. Two different rates are given based on alternative hypotheses. In the first, the rate is dependent on pyruvate concentration and oxygen concentration following the Michaelis-Menten relation, and on the ATP/ADP ratio following the Hill equation. In the second, the rate depends on the oxygen concentration, and on a second messenger which is proposed to be present during activation. The rate of mitochondrial respiration is directly proportional to the rate of ATP transport out of the mitochondria (and this also determines the rate of transport of ADP into the mitochondria). The rate of oxygen consumption is also directly proportional to the respiration rate.

The model was created to investigate the BOLD response seen during activation in fMRI. It does not attempt to model blood flow, and activation is represented by an increase in blood flow (as an input) and an increase in sodium ions entering the intracellular compartment.

An updated version of the model was published in 2002 [174], this time made up of 15 variables and 51 parameters. The main difference in this version of the model was the introduction of a venous compartment based on the balloon model of Buxton *et al.* [175].

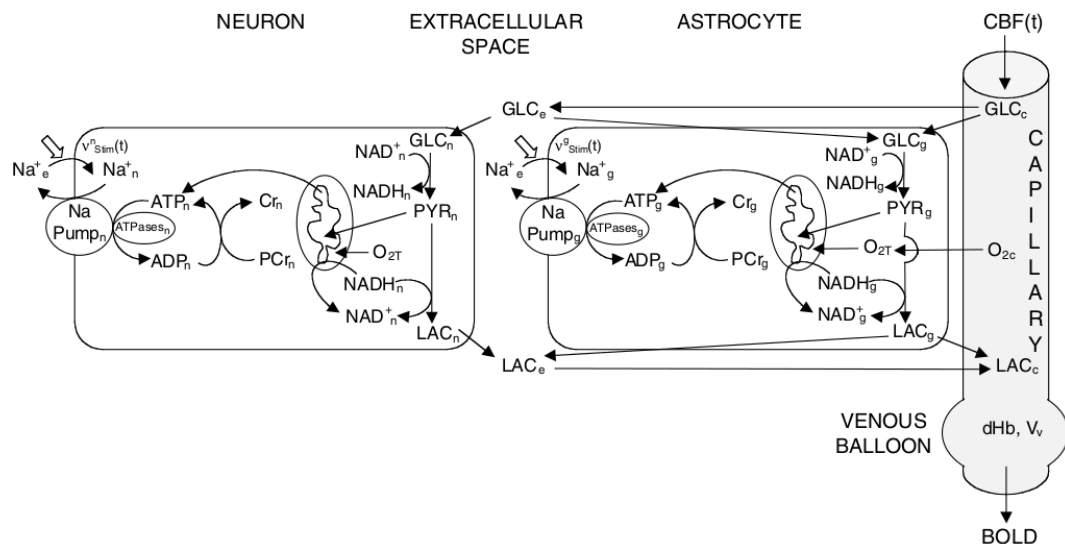


Figure 2.4: Schematic diagram of the 2005 model by Aubert and Costalat [176]

This model was later adapted to investigate the ANLS by adding more compartments to differentiate between the astrocytes, neurons and extracellular space [147] as illustrated in Figure 2.4. Five compartments are included: the intracellular spaces of the astrocytes

and neurons, the extracellular space, and capillaries and veins. The intracellular reactions in the neurons and astrocytes were taken from the previous homogeneous models, and most of the parameters have the same value in the two compartments. The main difference between them is that a lactate efflux from astrocytes at rest was assumed, whilst for neurons there was neither production or consumption. The model has 20 differential equations and around 85 parameters.

### 2.3.2 Model by Simpson *et al.*

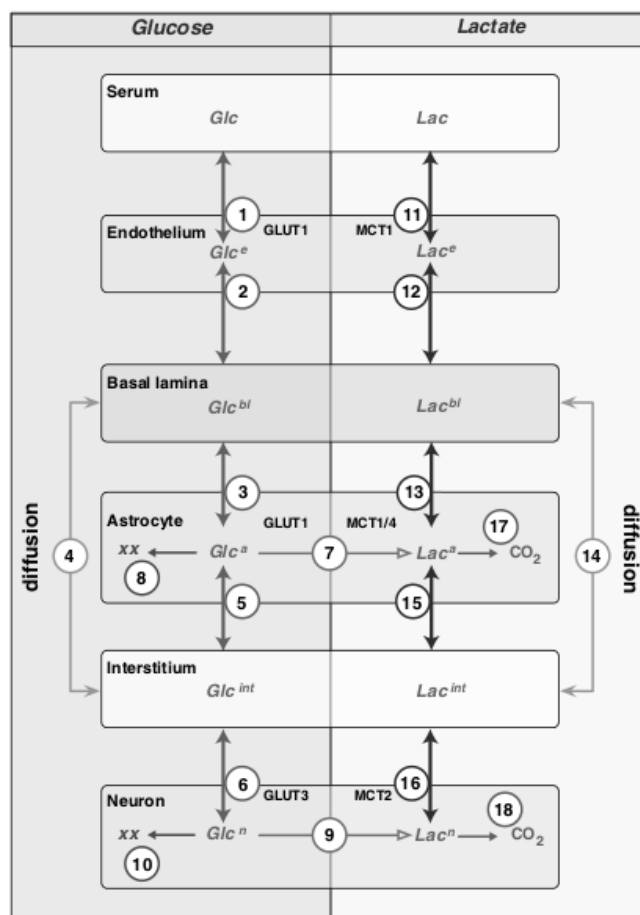


Figure 2.5: Schematic diagram of the model by Simpson *et al.* [36]

The model by Simpson *et al.* [36] concentrates on glucose and lactate transport between six compartments: serum, endothelial cells, basal lamina, interstitium, astrocytes and neurons. The flows of lactate and glucose between these compartments are illustrated in Figure 2.5. It was created with the aim of helping to test the ANLS hypothesis and differs from other models with this aim by considering the transport of substrates across the blood brain barrier. As it concentrates on transport, it does not contain a detailed description of oxidative metabolism. It instead contains one equation repre-

senting conversion of glucose to lactate, and another representing conversion of lactate to  $\text{CO}_2$ . There are several parameters controlling the rate of the flows shown in Figure 2.5, whose values are set from a knowledge of the properties of the different MCT and GLUT proteins expressed in the different cell types (see Section 1.2.3). The model has 10 variables, representing the concentrations of glucose and lactate in each of the compartments except the serum, and around 50 parameters.

The model simulations did not demonstrate the ANLS, but instead suggested that neurons are the main site of glucose uptake and use. The same model was later used to demonstrate a neuron-to-astrocyte lactate shuttle (the opposite of the ANLS) [155].

### 2.3.3 Model by Cloutier *et al.*

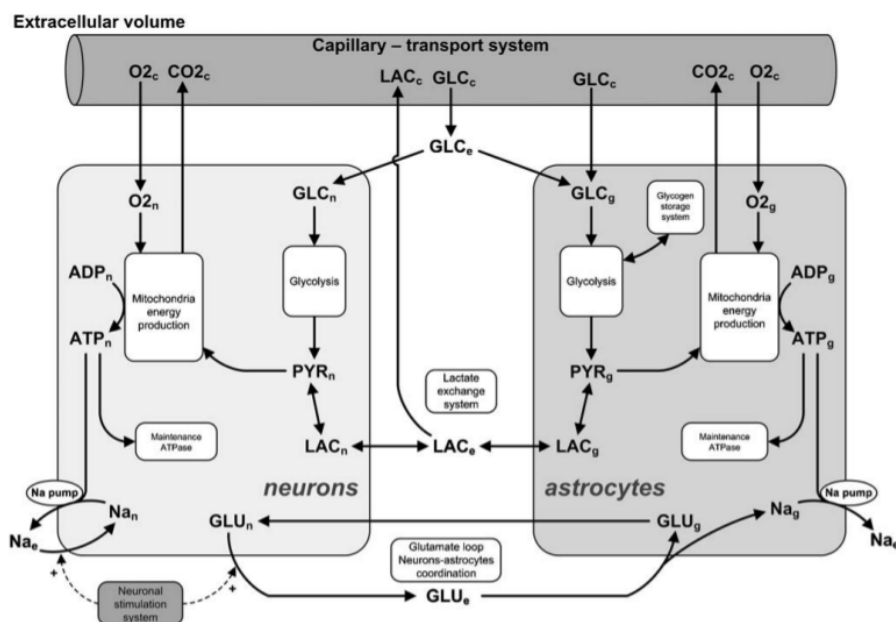


Figure 2.6: Schematic diagram of the model by Cloutier *et al.* [152]

The compartmentalised model by Aubert and Costalat [147] was modified and used by Cloutier *et al.* [152], again to investigate the ANLS, but this time comparing with *in vivo* data from freely moving rats under different stimuli. A schematic diagram of this model is shown in Figure 2.6.

The model includes several modifications with the aim of better simulating the metabolic response to stimulation. Firstly, the model of glycolysis was expanded to contain five reactions rather than three. Secondly, the cycling of the neurotransmitter glutamate between astrocytes and neurons was added to the model. The cycle is represented by three equations, and glutamate has the effect of influencing astrocyte metabolism dur-

ing stimulation. Thirdly, simulation of glycogen dynamics in astrocytes was added, with glycogen acting as an additional substrate supply. Finally, the single equation representing mitochondrial metabolism was altered to include inhibition at high ATP/ADP ratios.

The model has 34 differential equations, 89 parameters, and an additional 9 parameters describing the stimulation input. The parameter values were set by comparison with steady state data, and dynamic data from a tail pinch experiment in rats. The model was then validated by comparing with a restraint stimulus in rats, and was found to match the experimentally measured glucose and lactate concentrations well.

The model has also been further extended by Orlowski *et al.* [156] to simulate pH with the aim of understanding pH changes during stroke. This model was itself expanded to include cellular oedema and diffusion in the extracellular space, which allows three-dimensional simulations of stroke damage [177].

Figure 2.7 shows a simulation with the model by Cloutier *et al.*, downloaded in SBML format from the Biomedels database [178], and carried out using the BRAINCIRC modelling environment (see Section 3.1). Hypoxia-ischaemia was simulated by halving the arterial oxygen concentration from 8.34 mM to 4.17 mM after 100 s for 300 s. At the same time, blood flow entering the capillaries was also halved from  $0.012 \text{ s}^{-1}$  to  $0.006 \text{ s}^{-1}$ . All other parameter values were left unchanged. The model shows a fall in ATP and PCr concentration in neurons, and a much smaller drop in the astrocytes. The difference is likely to be caused by the higher rate of oxygen consumption in the neurons. Both astrocytes and neurons display a drop in glucose concentration and a rise in lactate concentration, with the astrocytes being slower to recover. The overall rate of glucose transport into the cells  $v_{\text{GLC}}$  and lactate transport out of the cells  $v_{\text{LAC}}$  are shown in the bottom two graphs of Figure 2.7. At rest, lactate flows out of the astrocytes and into neurons, indicative of the ANLS. When oxygen levels are low, the rate of glycolysis in the neurons increases leading to lactate flowing out and more glucose entering.

### 2.3.4 Model by Beard

Beard developed a model to represent oxidative phosphorylation and oxygen transport in cardiac muscle [149] which is shown in Figure 2.8. The model is made up of five compartments: the capillaries, interstitial space, and the cellular cytoplasm, mitochondrial matrix and mitochondrial intermembrane space. Unlike the other models described here, this model uses a distributed one dimensional representation of oxygen transport i.e. the oxygen concentration of the compartments varies along the length of the capil-

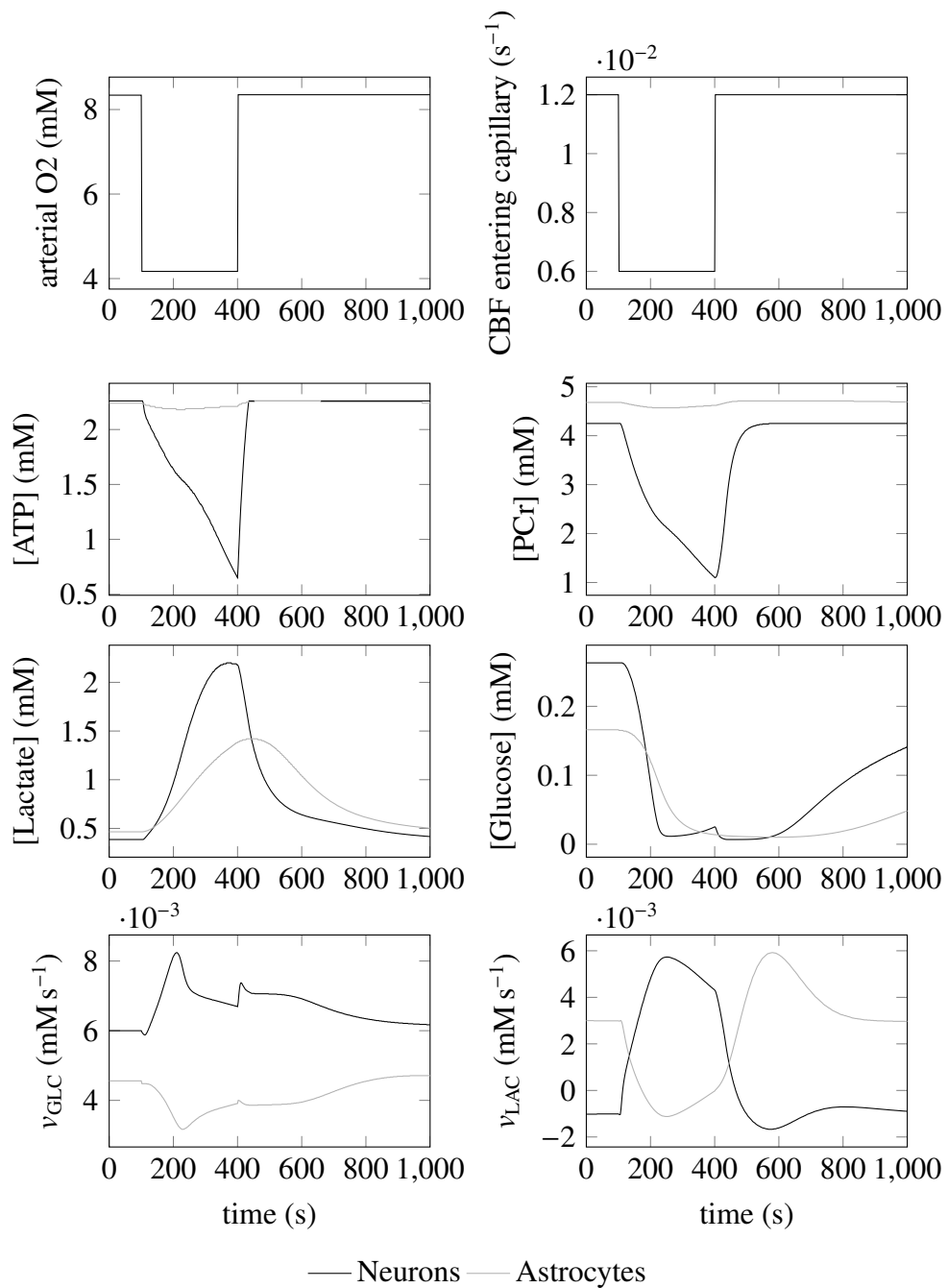


Figure 2.7: Simulation of hypoxia-ischaemia using the model by Cloutier *et al.* [152]. The top two graphs show the inputs and the other graphs show the model predictions for concentration and flow rate changes in the neurons and astrocytes.

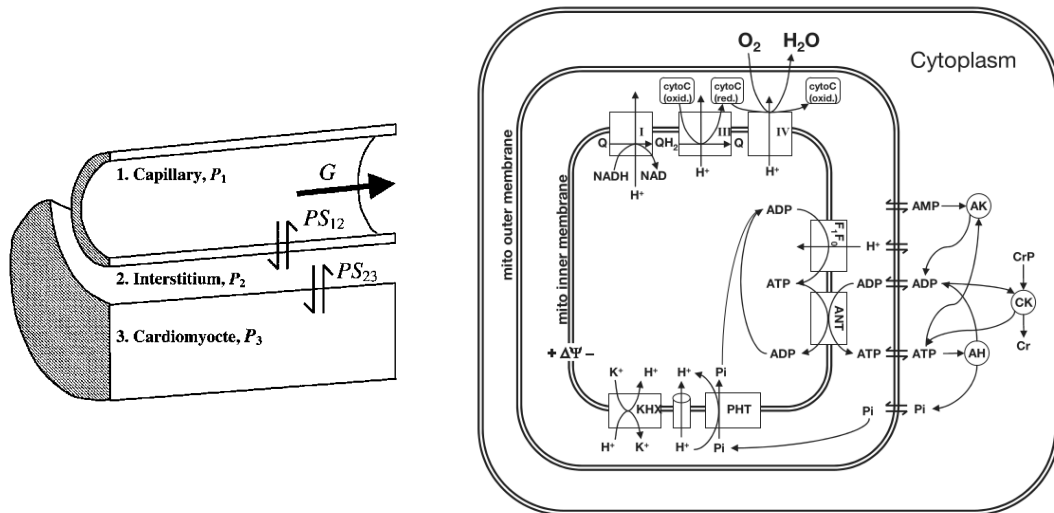


Figure 2.8: Schematic diagram of the 2006 model by Beard [149]. The diagram on the right is taken from Wu *et al.* [179] which uses a slightly changed version of the same model.

lary. There are 34 variables in the model and around 65 parameters.

The aim of this model was to investigate how mitochondrial metabolism is regulated, and it therefore contains more detail in the mitochondrial part of the model. Glycolysis and the TCA cycle are not explicitly modelled, instead there is a modelled rate of NAD reduction which is dependent on  $P_i$  concentration. The fluxes through complexes I, III and IV of the electron transport chain are modelled separately. The expressions for these fluxes have a similar form to one another which is derived by considering thermodynamic equilibrium. The flux through complex IV (CCO) includes a factor of

$$\frac{1}{1 + k/[O_2]} \quad (2.15)$$

where  $k$  is a constant that is present to account for the observed dependence of the rate of oxygen consumption on oxygen concentration. This factor is relevant to the oxidation state of CCO which is discussed in Chapter 5. ATP synthesis is also modelled and depends on the concentrations of  $P_i$  and magnesium bound ATP and ADP. Magnesium binding of ATP and ADP is modelled in both the mitochondrial matrix and the intermembrane space.

Simulations were compared with data from canine hearts and the model predicted that cytoplasmic inorganic phosphate is an important regulator of mitochondrial respiration, allowing ATP rates in cardiac muscle to remain almost constant despite large variations of metabolic rate.

### 2.3.5 Model by Vatov *et al.*

The model by Vatov *et al.* [150] was created in order to use measurable variables to estimate variables that are not measured, in a clinical setting in real time. The model is simpler than many of the others discussed here, because speed of solution was a primary concern. It is made up of six differential equations, and its variables include extracellular potassium concentration and measurable NADH concentration. It is not explicitly separated into compartments, but it includes simulation of blood flow and a simple representation of autoregulation. It has been used to simulate ischaemia and cortical spreading depression.

### 2.3.6 BrainCirc

The BrainCirc model (Banaji *et al.* [180]) published in 2005 was developed in conjunction with the BRAINCIRC modelling environment (see Section 3.1) with which it consequently shares its name. The primary aim in its development was to investigate autoregulation. An overview of the main sites and processes is shown in Figure 2.9. The ten compartments of the model can be grouped into blood vessels, brain tissue and vascular smooth muscle (VSM).

The circulatory part of the model is similar to the model by Ursino and Lodi [142] (Section 2.2.1). The blood vessels are subdivided into five compartments: proximal arteries, distal arteries, capillaries, veins and venous sinuses. Venous volume depends on transmural pressure, and intracranial pressure is variable.

The radius of the arterial compartments is controlled by the VSM. There are two VSM sites, corresponding to the proximal and distal arteries. The response of the VSM to signalling molecules is important for autoregulation. Contraction is determined by the concentrations of  $\text{Ca}^{2+}$ , and of NO.  $\text{Ca}^{2+}$  concentration depends on the conductance of potassium ion channels. Four types of these channels are modelled. Their combined conductance is a function of the concentrations of  $\text{Ca}^{2+}$ ,  $\text{K}^+$ , ATP,  $\text{H}^+$ , adenosine and NO, and also of the membrane potential.

Brain tissue is divided into three compartments: extracellular space, cytoplasm, and mitochondrial matrix. It is the extracellular space that exchanges substances with the VSM. It also exchanges substances with the blood in the capillaries, and with the cytoplasm. The most important chemicals exchanged are oxygen and glucose.

The cytoplasm is the site of energy usage. During neural activity  $\text{K}^+$  is expelled from

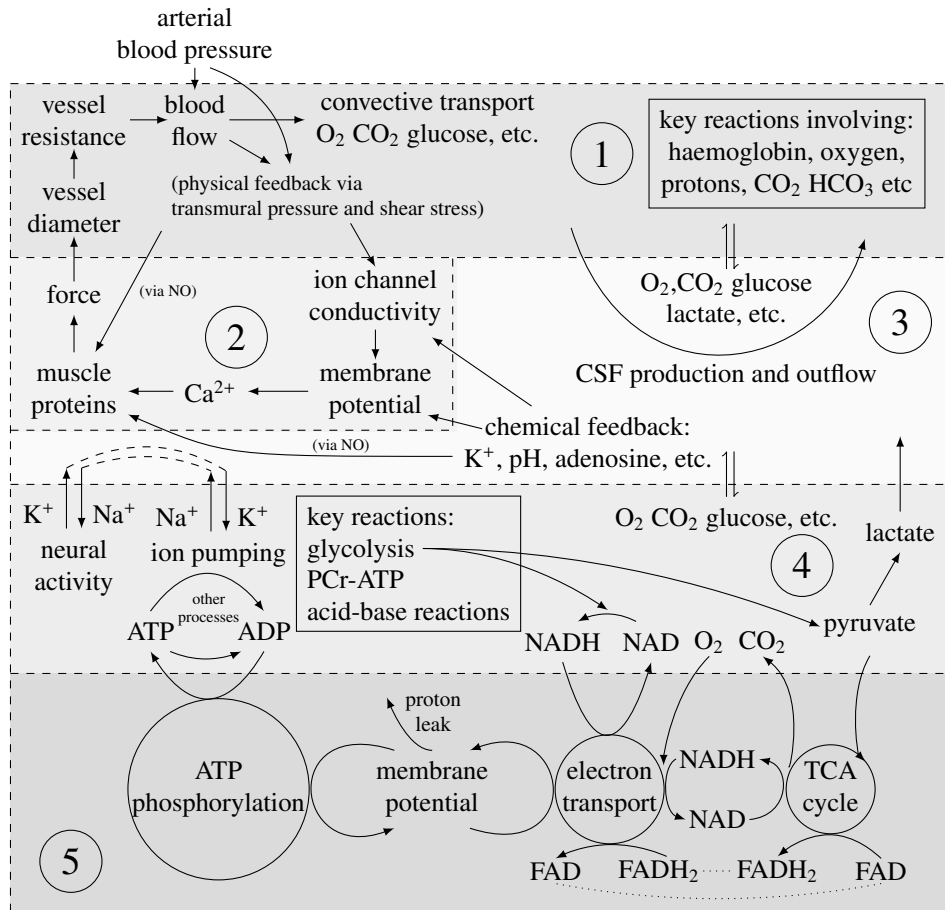


Figure 2.9: The main processes and sites of the BrainCirc model reproduced from Banaji *et al.* [180]. The sites are 1. Vascular system 2. Vascular smooth muscle 3. Extracellular space 4. cytoplasm and 5. mitochondrial matrix.

the cytoplasm and  $\text{Na}^+$  enters. ATP is needed to restore the balance. ATP is also used for other processes, which are combined into a single Michaelis-Menten process. The phosphocreatine system and adenylate kinase system are also modelled. These reactions are treated as mass action reactions, with rate constants set such that they are nearly always at equilibrium. Glycolysis in the cytoplasm is modelled as a one step irreversible Michaelis-Menten process. It involves the production of four protons. The  $v_{\max}$  of the reaction is regulated by the AMP/ATP ratio. Pyruvate can be converted to lactate, and lactate is transported into the extracellular space, and then into the blood.

The cytoplasm exchanges substances with the mitochondrial matrix. Oxygen and  $\text{CO}_2$  diffuse across the membrane, whilst NADH, ATP/ADP,  $\text{P}_i$  and pyruvate are associated with specific transport processes. The most important mitochondrial process is the TCA cycle. This is modelled as a three stage process. The electron transport chain is modelled in a single step. The return of three protons to the matrix is coupled to the phosphorylation of one ADP molecule. The rate of ATP synthesis is taken from the model by Korzeniewski [144] (see 2.2.3). Some protons return to the matrix via

leak channels, and the size of the leak current has an exponential dependence on the protonmotive force.

### 2.3.7 BrainSignals

The BrainSignals model [12] is a model of cerebral blood flow and metabolism in the adult human brain. It was developed with the intention of helping to predict, interpret and validate NIRS measurements, in particular the oxidation of CCO. A schematic diagram of the model showing the four compartments and the main processes modelled within them is shown in Figure 2.10. The model is described here in detail, since it forms the basis for all the modelling in this thesis.

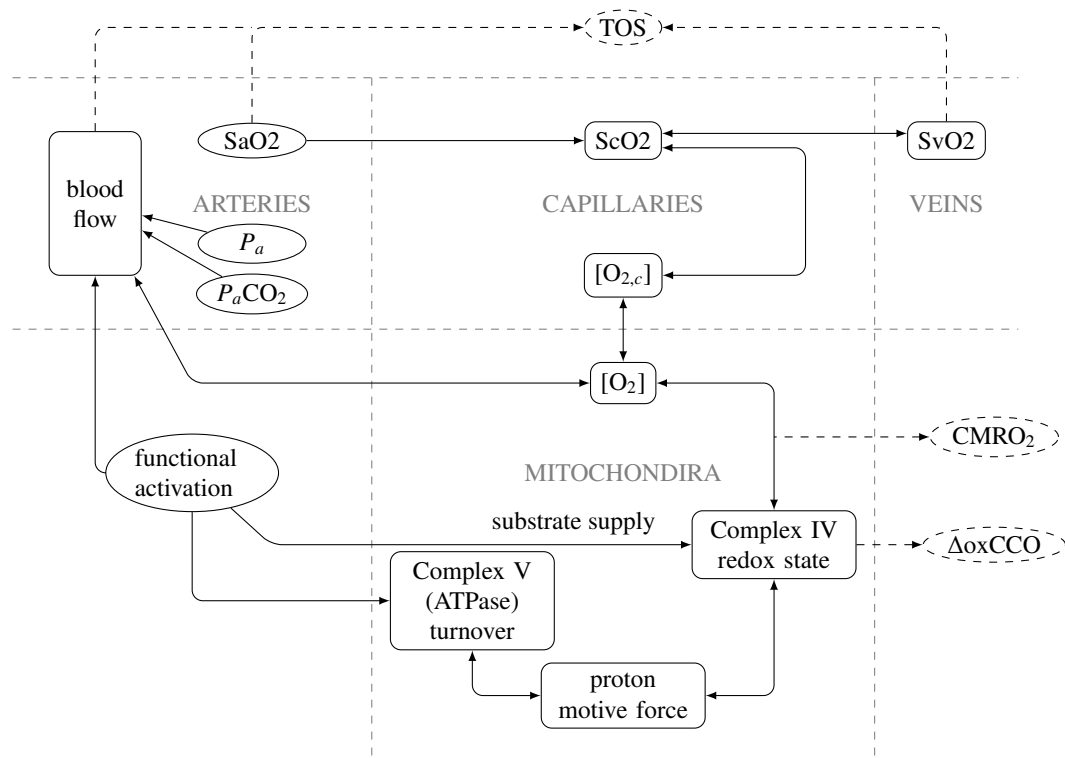


Figure 2.10: Schematic diagram of the BrainSignals model

### Circulation

The circulatory part of the model is based on the model by Ursino and Lodi [142], but has been simplified. There are three circulation compartments representing the arteries and arterioles, the capillaries and the veins. The volumes of the veins is assumed to be constant, and the volume of the capillaries is considered negligible. The arterial volume  $V_a$  is proportional to the square of the arterial compartment radius  $r$ , which along with

blood pressure determines CBF by

$$\text{CBF} = G(P_a - P_v), \quad G = K_G r^4 \quad (2.16)$$

where  $G$  is the conductance of the cerebral artery compartment,  $K_G$  is a constant, and  $P_a$  and  $P_v$  are the blood pressures at the start of the arterial and venous compartments respectively.

The arterial radius  $r$ , and therefore the conductance  $G$  is determined by the balance of pressure, and elastic wall tension  $T_e$  and muscular wall tension  $T_m$  (force per unit length) generated in the artery walls

$$T_e + T_m = \left( \frac{P_a + P_v}{2} - P_{ic} \right) r \quad (2.17)$$

where  $P_{ic}$  is the intracranial pressure which is assumed to be constant. The elastic tension depends only on  $r$ .

$$T_e = h \left( \sigma_{e0} \left( \exp \left( \frac{K_\sigma (r - r_0)}{r_0} \right) - 1 \right) - \sigma_{coll} \right) \quad (2.18)$$

where  $\sigma_{e0}$ ,  $K_\sigma$ ,  $r_0$  and  $\sigma_{coll}$  are constants and  $h$  is the vessel wall thickness, which is given by

$$h = -r + \sqrt{r^2 + 2r_0 h_0 + h_0^2} \quad (2.19)$$

The muscular tension is also a function of  $r$

$$T_m = T_{\max} \exp \left( - \left| \frac{r - r_m}{r_t - r_m} \right|^{n_m} \right) \quad (2.20)$$

where  $T_{\max}$  is the maximum tension,  $r_m$  is the radius at which this occurs and  $r_t$  and  $n_m$  determine the shape of the function. Autoregulation is represented in the model by having  $T_{\max}$  vary with arterial pressure  $P_a$ : an increase in arterial pressure leads to an increase in  $T_{\max}$  and so a decrease in  $r$ .  $T_{\max}$  also depends on three other parameters in the same way,  $\text{SaO}_2$ ,  $P_a\text{CO}_2$  and energy demand ( $u$ ). These four parameters are combined to give a single parameter  $\eta$

$$\eta = R_P \left( \frac{v_{P_a}}{v_{P_a,n}} - 1 \right) + R_O \left( \frac{v_{\text{O}_2}}{v_{\text{O}_2,n}} - 1 \right) + R_u \left( 1 - \frac{v_u}{v_{u,n}} \right) + R_C \left( 1 - \frac{v_{\text{CO}_2}}{v_{\text{CO}_2,n}} \right) \quad (2.21)$$

where  $R_x$  is a sensitivity constant associated with parameter  $x$ , and  $v_x$  is a time filtered version of the parameter  $x$

$$\frac{dv_x}{dt} = \frac{1}{\tau_x} (x - v_x) \quad (2.22)$$

where  $\tau_x$  is a time constant. The variable  $\eta$  determines  $T_{\max}$  by a sigmoidal relationship

$$T_{\max} = T_{\max 0}(1 + k_{\text{aut}}\mu), \quad \mu = \frac{\mu_{\min} + \mu_{\max}e^{\eta}}{1 + e^{\eta}} \quad (2.23)$$

where  $k_{\text{aut}}$  is a parameter to allow for simulation of loss of autoregulation, and  $\mu_{\min}$  and  $\mu_{\max}$  are the lower and upper limits of  $\mu$ . The steady state relationship between CBF and  $P_a$  with autoregulation present ( $k_{\text{aut}} = 1$ ) and absent ( $k_{\text{aut}} = 0$ ) is shown in Figure 2.11.

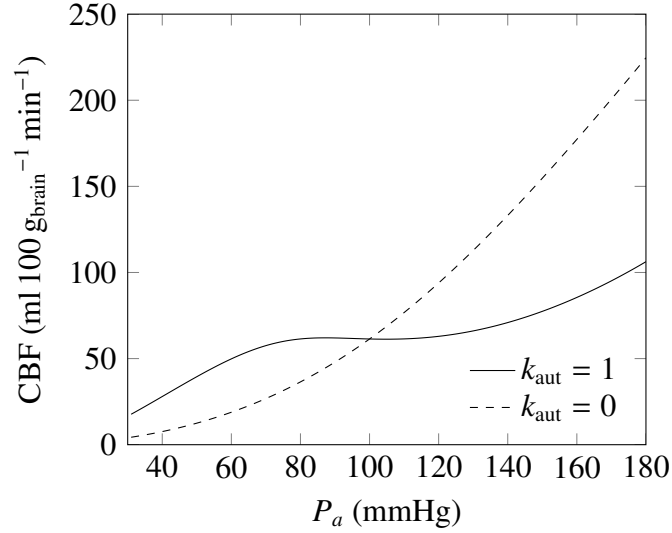


Figure 2.11: Steady state relationship between arterial pressure and blood flow in the circulation part of the BrainSignals model with and without autoregulation

## Oxygen transport

The blood compartments in the model contain oxyhaemoglobin ( $\text{HbO}_2$ ) and deoxyhaemoglobin (HHb). The sum of their concentrations ( $[\text{Hbtot}]$ ) is fixed, and equal in all compartments, i.e.

$$[\text{HbO}_{2,a}] + [\text{HHb}_a] = [\text{Hbtot}] \quad (2.24)$$

$$[\text{HbO}_{2,v}] + [\text{HHb}_v] = [\text{Hbtot}] \quad (2.25)$$

where a subscript  $a$  or  $v$  indicates haemoglobin in the arterial or venous compartment. Arterial oxygen saturation ( $\text{SaO}_2$ ) is often measured, and so is an important input parameter. Arterial haemoglobin concentration can be calculated from it by

$$[\text{HbO}_{2,a}] = \text{SaO}_2[\text{Hbtot}]. \quad (2.26)$$

Capillary oxygen saturation  $\text{ScO}_2$  is an average of the arterial and venous saturations. Dissolved oxygen concentration in the capillaries ( $[\text{O}_{2,c}]$ ) depends only on the capillary

saturation and is calculated by

$$[O_{2,c}] = \phi \left( \frac{ScO_2}{1 - ScO_2} \right)^{\frac{1}{n_h}} \quad (2.27)$$

where  $\phi$  is the concentration of oxygen at half maximal saturation and  $n_h$  is the Hill coefficient for the dissociation of oxygen from haemoglobin which is assumed to be constant, i.e. the Bohr effect is ignored.

Transport of oxygen from the capillaries to the mitochondria is a simple diffusion process which takes place at rate

$$J_{O_2,min} = D_{O_2}([O_{2,c}] - [O_2]) \quad (2.28)$$

where  $[O_2]$  and  $[O_{2,c}]$  are the oxygen concentrations in the mitochondria and the capillary, and  $D_{O_2}$  is a diffusion constant set so that, under normal conditions, the rate of oxygen delivery to the mitochondria equals the rate of oxygen usage ( $CMRO_2$ ). The oxygen transfer rate must also satisfy

$$J_{O_2,min} = CBF([HbO_{2,a}] - [HbO_{2,v}]). \quad (2.29)$$

By combining the above equations, the oxygen saturations in veins and capillaries and  $J_{O_2,min}$  can be calculated.

## Metabolism

The metabolic part of the model concentrates on oxidative phosphorylation in the mitochondria. This involves the pumping of protons into the mitochondria, which then return to the cytoplasm via ATP synthase. The electrochemical potential for protons is

$$\Delta p = \Delta \Psi + Z(pH_m - pH_o), \quad (2.30)$$

where  $\Delta \Psi$  is the membrane potential,  $pH_m$  is the mitochondrial pH,  $pH_o$  is the cytoplasmic pH and the constant  $Z$  is given by

$$Z = \frac{RT}{\log_{10}(e)F}, \quad (2.31)$$

where  $R$  is the ideal gas constant,  $T$  is the temperature and  $F$  is the Faraday constant. The modelled cytoplasmic pH is fixed and the mitochondrial pH is calculated from the proton concentration. However, in order to simulate buffers, an effective mitochondrial

volume for protons is modelled as  $R_{\text{Hi}} V_{\text{mit}}$  where  $V_{\text{mit}}$  is the mitochondrial volume and the scaling factor  $R_{\text{Hi}}$  is

$$R_{\text{Hi}} = \frac{C_{\text{buffi}}}{(10^{-\text{pH}_m} - 10^{-(\text{pH}_m - \text{dpH})})/\text{dpH}} \quad (2.32)$$

where  $C_{\text{buffi}}$  and  $\text{dpH}$  are constants.

The proton pumping occurs by the electron transport chain, which is modelled as three reactions summarised in Figure 2.12.

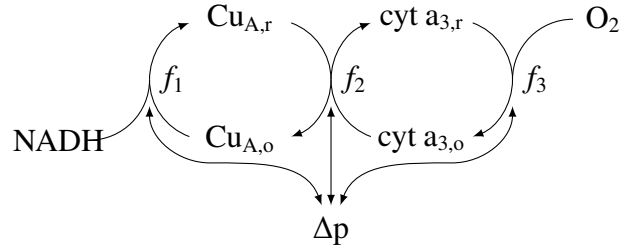


Figure 2.12: Electron transfer chain and proton pumping in the BrainSignals model

The first reaction combines Complexes I–III and describes the transfer of four electrons from NADH to the CuA centre of CCO. This reaction is coupled to the transport of  $p_1$  protons across the membrane. It is considered to be reversible, and its rate is given by

$$f_1 = k_1 \text{Cu}_{\text{A},0} - k_{-1} \text{Cu}_{\text{A},r} \quad (2.33)$$

The forward rate  $k_1$  is given by

$$k_1 = k_{1,0} \exp(-c_{k1} (\Delta p - \Delta p_n)) \quad (2.34)$$

where  $k_{1,0}$  depends on the ratio of NAD to NADH,  $\Delta p_n$  is the normal value of  $\Delta p$  and  $c_{k1}$  is a constant. The ratio of the rate constants is given by

$$\frac{k_1}{k_{-1}} = \text{Keq}_1 = \frac{\text{Cu}_{\text{A},\text{req}}}{\text{Cu}_{\text{A},\text{oeq}}} \quad (2.35)$$

The free energy for this reaction is

$$\Delta G_1 = -4 \left( E_1 + Z \log \left( \frac{\text{Cu}_{\text{A},0}}{\text{Cu}_{\text{A},r}} \right) \right) + p_1 \Delta p. \quad (2.36)$$

When the reducing substrate is NADH

$$E_1 = \mathcal{E}_0(\text{Cu}_A) - \mathcal{E}_0(\text{NADH}) + \frac{Z}{2} \log \left( \frac{1}{[\text{NAD}]/[\text{NADH}]} \right) \quad (2.37)$$

where  $\mathcal{E}_0$  refers to a standard redox potential. At equilibrium,  $\Delta G_1 = 0$ , which can be used to give an expression for the equilibrium constant.

$$\text{Keq}_1 = 10^{-(p_1\Delta p/4 - E_1)/Z} \quad (2.38)$$

The second reaction describes the transfer of the four electrons to the haem  $a_3$ /CuB centre, and the pumping of  $p_2$  protons. Again, it is considered reversible and its rate is given by

$$f_2 = k_2 \text{Cu}_{A,r} \text{cyt } a_{3,o} - k_{-2} \text{Cu}_{A,o} \text{cyt } a_{3,r}. \quad (2.39)$$

The forward rate is

$$k_2 = k_{2,n} \exp(-c_{k2} (\Delta p - \Delta p_n)) \quad (2.40)$$

where  $k_{2,n}$  and  $c_{k2}$  are constants. Their ratio is set in the same way as for the first reaction, with the free energy given by

$$\Delta G_2 = -4 \left( \mathcal{E}_0(\text{cyt } a_3) - \mathcal{E}_0(\text{Cu}_A) + Z \log \left( \frac{\text{Cu}_{A,r} \text{cyt } a_{3,o}}{\text{Cu}_{A,o} \text{cyt } a_{3,r}} \right) \right) + p_2 \Delta p \quad (2.41)$$

and equilibrium constant

$$\frac{k_2}{k_{-2}} = \text{Keq}_2 = 10^{-(p_2\Delta p/4 - \mathcal{E}_0(\text{cyt } a_3) + \mathcal{E}_0(\text{Cu}_A))/Z}. \quad (2.42)$$

The final reaction describes the reduction of oxygen by cytochrome  $a_3$ , and the pumping of  $p_3$  protons. This reaction is modelled as irreversible, and its rate is given by

$$f_3 = k_3 [\text{O}_2] \text{cyt } a_{3,r} \left( \frac{e^{-c3(\Delta p - \Delta p_{30})}}{1 + e^{-c3(\Delta p - \Delta p_{30})}} \right) \quad (2.43)$$

where  $\Delta p_{30}$ ,  $c3$  and  $k_3$  are constants. This reaction sets the rate of oxygen consumption

$$\text{CMRO}_2 = V_{\text{mit}} f_3. \quad (2.44)$$

The rates of the three reactions ( $f_1$ ,  $f_2$  and  $f_3$ ) are equal under normal conditions. When they differ there is a change in the oxidation state of the redox centres. The membrane potential  $\Delta\Psi$  varies according to

$$\frac{d\Delta\Psi}{dt} = \frac{p_1 f_1 + p_2 f_2 + p_3 f_3}{C_{im}}, \quad (2.45)$$

where  $C_{im}$  is the capacitance of the inner mitochondrial membrane. The potential  $\Delta p$  is used to drive ATP synthesis, although this is not explicitly modelled. The flow rate of

protons through Complex V is

$$L_{CV} = L_{CV,\max} \left( \frac{1 - e^{-\theta}}{1 + r_{CV} e^{-\theta}} \right), \quad \theta = k_{CV} (\Delta p + Z \log(u) - \Delta p_{CV0}) \quad (2.46)$$

The parameter  $r_{CV}$  accounts for a bias between the forward and backward reaction rates, and  $\Delta p_{CV0}$  is the protonmotive force at which there would be no net flow of protons.  $L_{CV,\max}$  is the maximum rate of proton flow through the membrane. It is set from the normal rate of proton flow which is determined by the normal  $CMRO_2$ . Any different effects of  $\Delta\Psi$  and  $\Delta pH_n$  are ignored. Under normal conditions, 25 % of protons return through leak channels. This percentage varies with  $\Delta p$  according to

$$L_{lk} = k_{unc} L_{lk0} (\exp(k_{lk2} \Delta p) - 1) \quad (2.47)$$

where  $L_{lk0}$  and  $k_{lk2}$  are constants and  $k_{unc}$  is a parameter representing uncouplers, which under normal conditions is set to one.

### 2.3.8 Comparison between models

The models described in Section 2.3 have many aspects in common. One way in which to compare models is by their level of complexity. The number of compartments, variables or equations and parameters of the different models are compared in Table 2.2. Two models stand out in this table. The model by Vatov *et al.* [150] has fewer variables and parameters than the other models, and it is not explicitly divided into compartments. This makes it suitable only for simulating particular signals, and limits its flexibility and its similarity to the underlying physiology. The BrainCirc model (Banaji *et al.* 2005 [180]) stands out for the opposite reason: it has many more parameters, and variables than the other models. This can make it difficult to understand the behaviour of the model and also means it takes longer to solve the model equations.

The models also concentrate on different aspects of physiology. The model by Simpson *et al.* [36] is specifically a model of glucose and lactate transport between compartments and is therefore unsuitable for modelling other aspects of metabolism. However parts of the model and its parameter values may be included in other models, for example, the model by Cloutier *et al.* takes some parameter values from this model. It has also been combined with the model by Aubert and Costalat [154].

In order to simulate both the NIRS and MRS signals, the circulation, the cellular cytoplasm and mitochondria must be modelled. None of these existing models contain enough detail in all these areas. The models by Beard [149] and the BrainSignals model

Paper and Year	Number of compartments	Number of equations / variables	Number of parameters (approx for some models)
Aubert <i>et al.</i> [143] 2001	2	17	49
Aubert <i>et al.</i> [174] 2002	3	15	51
Aubert and Costalat [147] 2005	5	20	85
Banaji <i>et al.</i> [180] 2005	10	168	237
Beard [149] 2006	5	34	65
Vatov <i>et al.</i> [150] 2006		6	10
Simpson <i>et al.</i> [36] 2007	6	10	50
Banaji <i>et al.</i> [12] 2008	4	12	80
Cloutier <i>et al.</i> [152] 2009	4	34	89

Table 2.2: Number of compartments, variables and parameters in models of energy metabolism and circulation

(Banaji *et al.* 2008 [12]) have more detail relating to mitochondrial metabolism and oxidative phosphorylation, whilst the others concentrate on cytoplasmic metabolism. Only the two models by Banaji *et al.* have sufficient detail in the circulatory part of the model to simulate the NIRS haemoglobin signals. Many of the models differentiate between astrocytes and neurons. This significantly increases the complexity of the model and is not essential if the differences between these compartments are not of particular interest. It may, however, lead to improved simulations of lactate concentration.

None of these models is specialised to the neonatal brain. The majority of the metabolic processes occurring are the same in neonates as in adults. However, the appropriate values for model parameters may differ, and processes may have different levels of importance.

## 2.4 Summary

There is a long history of both compartment models of cerebral circulation, and models of cellular energy metabolism. Integrative, multi-scale models combining the two have only begun to be developed recently. In particular, the models by Aubert and co-workers [143, 147] are early examples of this type, and have been the starting point for several other models. Since 2005, a major application of this type of modelling has been to investigate the ANLS, thus requiring the compartmentalisation of the models into astrocytes and neurons. The Braincirc model [180] takes a similar approach to these models, but is focused on autoregulation, and contains a large number of pa-

rameters and variables, and is therefore more complex. The BrainSignals model [12] is smaller and was developed to simulate NIRS signals, and so contains more detail relating to mitochondrial metabolism to allow simulation of the  $\Delta\text{oxCCO}$  signal.

The aim of this thesis is to simulate signals from both NIRS and MRS. The BrainSignals model is therefore a good starting point, but it must be expanded to include more reactions occurring in the cytoplasm, to allow simulation of MRS measured variables. In addition, none of these existing models are specialised to the neonatal brain, which is necessary for this work. A new model has been developed, starting from the BrainSignals model, to simulate HI in newborn piglets. This new model (referred to as the BrainPiglet model) is described in Chapter 5 and it is applied to experimental data in Chapters 5 and 6. The computational and mathematical techniques used to carry out this modelling are the subject of the next chapter.

# Chapter 3

## Methods

This chapter describes the methods used in the modelling process, which begins with specifying the model equations and using them to run simulations. Subsequent steps include comparison of the model output with measured data, sensitivity analysis and parameter optimisation. A flow diagram illustrating the process is shown in Figure 3.1 and the steps are described in the following sections.

### 3.1 The BRAINCIRC modelling environment

All the simulations were carried out using the open source BRAINCIRC modelling environment [181] developed by Banaji. The model specification, generation, and the solving of the resulting differential algebraic equations (DAEs) have been used unchanged in this work. New methods for output and analysis of the results have been developed and used.

#### 3.1.1 Describing the model

Models in the BRAINCIRC environment are specified in several plain text files. Before describing these files, the terminology used throughout this thesis to describe different types of quantities in the model is clarified.

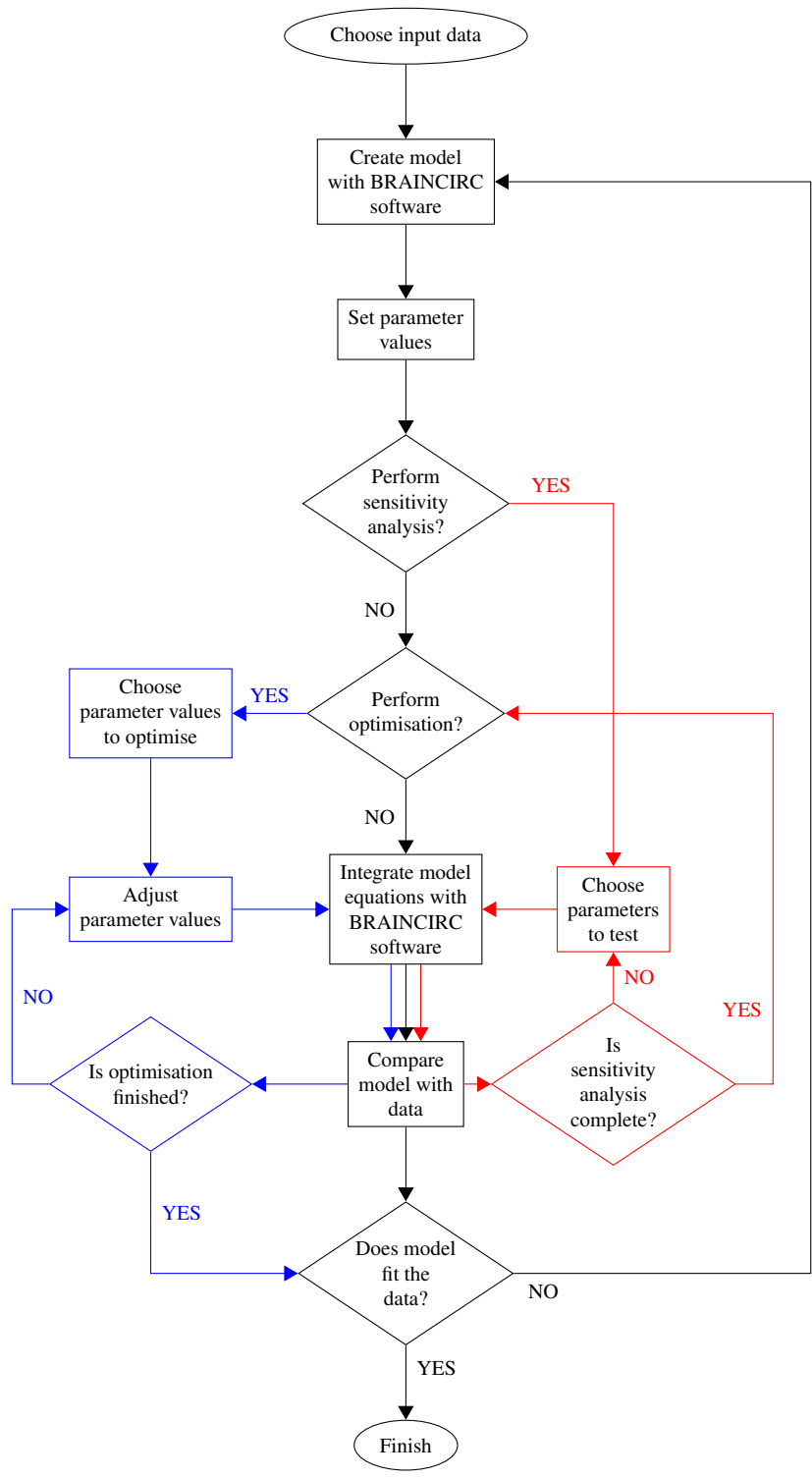


Figure 3.1: Flow diagram illustrating the modelling process. Red arrows represent the path followed during sensitivity analysis, and blue arrows represent the path followed during optimisation. The diagram illustrates the process in general: the specific processes followed in each chapter are described within the chapter.

## Model quantities

The term parameter is used to describe any quantity in the model that has a given numerical value, and is therefore an input to the model. A parameter's value will only change throughout a simulation if it (or a parameter on which it depends) is explicitly changed in a model input file (see Section 3.1.2). Parameters are further divided into those that are settable i.e. those for which a numerical value must be given, and those that are derived i.e. those calculated from settable and/or other derived parameters.

The term variable is used to describe any quantity in the model whose value is determined by solving the model, and is therefore an output. Variables are divided into true variables and temporary variables. True variables are those that are explicitly solved for in the model, whereas temporary variables are functions of true variables and parameters.

Temporary variables and derived parameters are used in order to allow the model equations to be expressed more naturally, and thus make them more readable. In many cases, the outputs of interest are temporary variables rather than true variables. The use of temporary variables therefore makes it easier to compare model outputs with data.

## Model files

A model is made up of three types of files. Examples of these are available to download with the software.

**Module files** These are the files in which the equations and processes of the model are specified. A model can include any number of module files. Each file is split into several sections, including those which define parameters, variables, temporary variables and chemical reactions. Expressions describing derived parameters and temporary variables are given in C syntax using the names of the appropriate parameters/variables. Chemical reactions can be written in a particular format by declaring the reactants and products and the stoichiometry. If the reaction is declared to be of a Michaelis-Menten or mass action type, the rate expression is automatically generated from given constants. Alternatively the rate expression can be defined explicitly. Differential equation terms are then generated for the reactants and products from the reaction rate and stoichiometry. An example of a chemical reaction definition with explanatory comments is shown below

```

\\Name to use as identifier
name: PCrtoATP
\\Reaction type is two-way Mass Action
type: MA2
\\reactants and their stoichiometry
left: 1.0, _PCr, 1.0, _ADP, 1.0, _Hy
\\products and their stoichiometry
right: 1.0, _ATP, 1.0, _Cr
\\number of compartments in the reaction
comps: 2
\\compartment volume for each reactant
compsleft: 1.0, 1.0, R_Hic
\\compartment volume for each reactant
compsright: 1.0, 1.0
\\required rates, for reaction type MA2 these are
\\rate constants for the forward and backward reactions
rates: k_PCrATP, k_nPCrATP

```

Module files also have sections for specifying algebraic relations, differential equations, and individual terms in differential equations.

**Descriptor files** These files state which processes are used in the model. They allow different reactions or equations to be included without rewriting the whole model. A BRAINCIRC ‘model’ can therefore be thought of as a family of models, with each different descriptor file specifying an individual model.

**Parameter files** These are the files which contain the values for the settable parameters. All settable parameters used in the model must have a value given in a single parameter file which is specified when a simulation is run.

### 3.1.2 Running a simulation

Running a simulation requires an input file. These files specify changes in parameter values over time. They can be used to input experimental data. They also usually contain, for convenience, the experimental data which will be compared with simulation outputs.

The DAEs are solved with the RADAU5 fortran solver, which uses a Runge-Kutta method of order 5 with step size control and continuous output. The time between the output points therefore depends on the time step that is chosen by the solver which can vary throughout the simulation. The BRAINCIRC program outputs the results in plain text files. However, these files are large, and writing them limits the speed of simulations, and therefore this has been replaced with files in the HDF5 format [182] in order to speed up running large numbers of simulations for optimisation and sensitivity analysis.

### 3.1.3 Markup languages for modelling

Markup languages are popular formats for exchanging information. The two commonly used markup languages for biological modelling are Systems Biology Markup Language (SBML) and CellML. SBML is a XML based format for representing reaction networks [183, 184]. CellML [185] is a similar project, but has less of a focus on chemical reactions, and concentrates more on reusing models in a modular way. Other XML based formats exist for exchanging different types of information, including FieldML for representing mathematical fields such as the distribution of biochemical compounds, and Simulation Experiment Description Markup Language (SED-ML) for encoding simulation details. Only SBML and CellML will be further discussed here, since these are the most well-established, and the most relevant to the BRAINCIRC software.

Online databases exist to share models in both the SBML and CellML formats. The BioModels database [178] is the largest of these, the latest version (June 2013) contains 143 013 models, however only 963 of these are published models with the remainder generated from reaction pathways. The database accepts models in both SBML and CellML formats. The CellML model repository [186] is specifically for CellML models and (accessed August 2013) contains 458 models. Both of these repositories consist mainly of models concentrating on specific aspects of biochemistry, although they also contain larger and organ scale models. The CellML model repository is divided into categories; there are 33 models in the ‘Neurobiology’ category. Only one of these, the model by Cloutier *et al.* [152] is a general model of brain metabolism. The ‘Metabolism’ category contains 78 models, including several of the models mentioned in Chapter 2 [152, 146, 166, 144, 170]. The BioModels database is not divided into categories in a similar way, however a search for ‘brain’ returns 144 models including, again the model by Cloutier *et al.* [152] and also the Braincirc model by Banaji *et al.* [180] described in Section 2.2.

There are many different pieces of software for creation, analysis and use of SBML and CellML models. The SBML website [187] contains a software matrix to compare different software tools, of which there are currently 254 listed including BRAINCIRC. The CellML website lists around 40 software tools, including two main multi-purpose modelling environments, OpenCell [188] and OpenCOR [189].

Given the popularity of these two XML formats, it is important that the BRAINCIRC environment is capable of importing and exporting models encoded in SBML and CellML. BRAINCIRC can import SBML models and convert them to the BRAINCIRC format, however it has no export facilities. Therefore, an SBML exporter for models in the BRAINCIRC format has been developed. The details of this, and the differences between the two formats is discussed in the following section. Adding similar capabilities for CellML is a future priority. There are tools that allow conversion between CellML and SBML in both directions. However, these currently have limited functionality, although they are likely to be improved in the future.

### Comparison between BRAINCIRC format and SBML

The SBML exporter is written in python using the libSBML python API [190]. There are several differences in the way SBML and BRAINCIRC specify models that can render the import and export processes imperfect; the main problem being that chemical reactions are not preserved. The current export method translates all BRAINCIRC parameters and variables into SBML ‘parameters’. Reactions are translated into terms in the differential equations that govern the rate of change of these SBML parameters, rather than into SBML reactions. This reason for this arises from the different way in which chemical reactions are represented in the two formats, which may stem from the fact that SBML is more oriented towards reaction networks than BRAINCIRC.

In SBML, quantities taking part in reactions must be defined as species. Each species must reside within a defined compartment. The rate of chemical reactions must be given per amount of species, rather than (as is more usual) per change in concentration. This is so that reactions between species in different compartments, such as transport reactions, are handled correctly. To illustrate this, consider the reaction  $R_1$  described by



where  $S_1$  and  $S_2$  are species in the same compartment. The rate of the reaction is given by

$$\frac{d[S_2]}{dt} = -\frac{d[S_1]}{dt} = k[S_1] \quad (3.2)$$

where  $k$  is a constant. In SBML, the reaction would be represented as

```
<reaction id="R_1">
  <listOfReactants>
    <speciesReference species="S_1" stoichiometry="1" />
  </listOfReactants>
  <listOfProducts>
    <speciesReference species="S_2" stoichiometry="1" />
  </listOfProducts>
  <kineticLaw>
    <math xmlns="http://www.w3.org/1998/Math/MathML">
      <apply>
        <times /> <ci> k </ci> <ci> S_2 </ci> <ci> c_1 </ci>
      </apply>
    </math>
  </kineticLaw>
</reaction>
```

where  $c_1$  is the volume of the compartment containing  $S_1$  and  $S_2$ . The kineticLaw element describes the rate of change of the amount of  $S_1$  and  $S_2$  in moles ( $A_{S_1}$  and  $A_{S_2}$ ) and it is then assumed that

$$\frac{dA_{S_2}}{dt} = - \frac{dA_{S_1}}{dt} = kc_1[S_1] \quad (3.3)$$

$$\frac{d(c_1[S_2])}{dt} = - \frac{d(c_1[S_1])}{dt} = kc_1[S_1] \quad (3.4)$$

which is equivalent to Equation 3.2. If  $S_2$  is instead defined to reside in a different compartment from  $S_1$  which has a volume  $c_2$ , Equation 3.2 is no longer valid. The above SBML reaction definition does remain valid however, because the rates are now considered to be

$$\frac{d(c_2[S_2])}{dt} = - \frac{d(c_1[S_1])}{dt} = kc_1[S_1]. \quad (3.5)$$

BRAINIRC does not have a global concept of compartments, and neither does it distinguish between a species, and a non-chemical variable. Reaction rates are specified in the more usual way, as relative to concentrations of the chemicals involved. The reaction above, with the two substances in one compartment, would be represented in BRAINIRC as

```
name: R_1
type: MA1
```

```
left: 1.0, S_1
right: 1.0, S_2
rates: k
```

and the rate terms in Equation 3.2 would be automatically generated when the model is compiled. If a reaction includes chemicals in more than one compartment, this must be made explicit in its definition by specifying, for each chemical involved, the volume of the compartment relative to the volume of the native compartment of the reaction. In the second case therefore, with the two substances in different compartments, the reaction definition must be changed to

```
name: R_1
type: MA1
left: 1.0, S_1
right: 1.0, S_2
rates: k
comps: 2
compsleft: 1.0
compsright: (c_2 / c_1)
```

in order for the correct rate equations to be generated.

The BRAINCIRC method is simpler than the SBML method for models with only one compartment. It also gives greater flexibility; but in practice this flexibility is rarely taken advantage of, and can lead to mistakes. In its current form therefore, the method for specifying chemical reactions in BRAINCIRC is better thought of as a short-cut for writing differential equations rather than a comprehensive specification of reactions. An improvement would be to adopt a system more similar to SBML in which the compartment of a chemical is defined.

Also, currently in BRAINCIRC, every variable involved in a chemical reaction is taken to be a true variable, even if (as is commonly the case) some can be expressed in terms of others as temporary variables. Identifying sets of true variables and temporary variables, would simplify the simulation process. This is not straightforward however, because the stoichiometry may be expressed in terms of parameters, the values of which are not defined until runtime. A proper analysis of the reactions would therefore require symbolic mathematics.

Another difficulty in translating BRAINCIRC models into SBML models is the feature of BRAINCIRC that allows a parameter to be defined using a function written in C.

Mathematical expressions in SBML are defined using a restricted subset of Content MathML. MathML is a recommendation of the W3C group for describing mathematics [191]. It can be used for describing both the presentation of displayed mathematics, and the content of mathematical expressions. It is not possible to translate any C function which can be used in BRAINCIRC into MathML. For example, reading and writing to files is possible in BRAINCIRC parameter functions. There is currently very limited support for translating these explicitly defined C functions into MathML (where this is possible) and this could be improved. However, the BrainPiglet model does not use these functions at all, and BrainSignals uses them only for very simple conditional statements, which can be translated by the exporter.

The final difference between SBML and BRAINCIRC that will be discussed is units. The use of units in SBML is optional. However, if a model involves quantities with units, describing them is useful for avoiding mistakes, and vital if the model is to be understood by others. BRAINCIRC does not have any methods of dimensional analysis, but does allow for optional descriptions of each model quantity, which can include units. The exporter has an option to include SBML units.

The libSBML library has functions to check the consistency of models, which can include checking units are dimensionally consistent. To make it easier to achieve consistent dimensions, SBML allows a unit attribute to be added to numbers in mathematical expressions. This is useful for numbers in expressions which are not dimensionless, such as multiplying by 100 to convert between metres and centimetres. The alternative, to define these numbers as parameters, would in general overcomplicate the model. There is no equivalent to this in BRAINCIRC, and so these units must be added manually to an exported SBML model to create a model with consistent units. This was carried out for both the BrainSignals and BrainPiglet models, and the units were checked for consistency.

### **3.1.4 Reasons for using BRAINCIRC**

Using the BRAINCIRC environment was the natural choice for this work, since the BrainSignals model was created in BRAINCIRC format, and the environment was being used by others in the group. But the software also offers advantages over other popular alternatives. MATLAB®[192] or packages based on MATLAB (e.g. PottersWheel [193] and SimBiology [194]) are often used. BRAINCIRC has a major advantage over these packages in that it is free software [195] available to be used and modified by anyone, and only depends on other software available without charge. The plain text format

in which BRAINCIRC stores models is easy to read and edit directly, whereas XML files are more difficult to read and edit. Software packages that store models in SBML and CellML formats therefore usually require an interface to edit and examine models. The flexibility of using different descriptor files and parameter files as described above is another strength of BRAINCIRC. Finally, many software packages for systems biology have limited or no support for solving DAEs, for example the Systems Biology Workbench does not support DAEs and OpenCell has only experimental support.

In general, although maintaining custom software is time-consuming, it allows greater control of the modelling process. Provided adequate import and export functionality to and from SBML and CellML formats exists, models can still be shared with others using different software.

## 3.2 Comparison of model with data

Both measured and modelled signals are resampled to one point per second before comparison. All analysis is carried out using NumPy [196]. In most cases, comparison involves calculating the mean square error (MSE) between the measured signal and the (potentially modified) modelled signal. Four types of comparisons are used, depending on how the modelled signal is modified. For a modelled signal  $X$  and a measured signal  $Y$  with  $N$  equally spaced data points, the four types are (using the notation  $\bar{A} = \sum_i A_i/N$ ):

**Unmodified** The MSE between the measured and unmodified modelled signal

$$\text{MSE}_u = \frac{1}{N} \sum_i (X_i - Y_i)^2. \quad (3.6)$$

**Offset** The modelled signal is offset such that its mean matches that of the measured signal

$$\text{MSE}_o = \frac{1}{N} \sum_i \left( X_i - (\bar{X} - \bar{Y}) - Y_i \right)^2. \quad (3.7)$$

**Scale** The modelled signal is scaled

$$\text{MSE}_s = \frac{1}{N} \sum_i \left( X_i \frac{\overline{XY}}{\overline{X^2}} - Y_i \right)^2. \quad (3.8)$$

**Scale and Offset** Both a scaling factor and an offset are applied to the modelled signal

$$\text{MSE}_{so} = \frac{1}{N} \sum_i \left( aX_i - (a\bar{X} - \bar{Y}) - Y_i \right)^2 \quad a = \frac{\overline{XY} - \bar{X} \cdot \bar{Y}}{\overline{X^2} - \bar{X}^2}. \quad (3.9)$$

For each case, the offset and scaling factors are calculated to give the minimum possible error. A derivation of these factors can be found in Appendix B. The root mean square (rms) error ( $\sqrt{\text{MSE}}$ ) may also be calculated for each of the four forms above.

Although the offset and scaling factors are used because the measurement may contain an arbitrary offset or scaling, it is the modelled signal that is altered in all cases. This is because the magnitude of the modelled signal may depend on the model parameters. Therefore, modifying the measured signal to match it would have unintended consequences when performing parameter optimisation.

### 3.3 Optimisation

The goal of optimisation is to minimise some aspect of the model output. Usually, this is the rms distance between a modelled signal and a measured signal across part or all of the trace. A new graphical interface has been developed to perform optimisation for a BRAINCIRC model of any number of settable parameters (subject to the constraints of the particular optimisation algorithm used). Any aspect of the model output can be minimised that can be written as an expression in NumPy [196], and there are shortcuts for generating expressions which minimise the four errors between a modelled and a measured signal described in Section 3.2. The program allows plotting of the results as the optimisation is running to follow its progress. Alternatively, optimisations can be run without using the interface, in which case multiple optimisations can be run simultaneously, provided they use the same module and descriptor files. The details of the optimisation, and the results, are saved in the javascript object notation (JSON): a plain text format which is supported by many different programming languages.

The optimisation itself is performed using OpenOpt [197]. This is an open-source optimisation framework that has many features. Here, it is used because it provides a common interface to many different open-source optimisation algorithms. Optimisation methods can be broadly divided into global and local methods. Local methods attempt to find any minimum point, and the minimum found can often depend on the starting position or details of the algorithm.

Local methods usually require many fewer evaluations of the objective function, and may also have more reliable convergence properties. There are many different methods, some make use of function derivatives and some do not. Local methods can be used where it is known that there is only one minimum point, or if there is more than one, but it does not matter which is found. However, for functions resulting from complex models such as those used in this thesis, there may be multiple minima, and the possibility of converging to one which is not the overall minimum cannot be ignored.

Global methods attempt to find the overall minimum over the whole of a given parameter space. Methods of global optimisation are often based on natural phenomena. Examples include simulated annealing, inspired by the thermodynamics of cooling [198], evolutionary algorithms such as the genetic algorithm, inspired by natural selection [199] and particle swarm methods, inspired by the flocking of animals such as birds or fish [200]. Of course, it can never be guaranteed that the overall minimum has been found, unless every possible point is tested.

Two methods have been used in this thesis: one local and one global. The local method chosen was the modified Powell's method implemented in SciPy [201]. The global method used was the PSwarm solver [202] developed by Vaz and Vicente [203]. These methods were chosen because they are linked to the OpenOpt framework and were found to give good results in preliminary optimisations. They are described below.

### 3.3.1 Powell's method

This algorithm for finding a local minimum was originally proposed by Powell [204]. It is a popular method because it is efficient, and since it does not make use of derivatives, it can be used for complex functions. The implementation described here is that of the SciPy package [201] which is a modified version of the original method.

To minimise a function  $f(\mathbf{x})$ , a starting point  $\mathbf{x}_0$  is chosen, and  $f(\mathbf{x}_0)$  is evaluated. For all optimisations in this thesis, the starting point is chosen at the default parameter values. The function is then minimised in the direction of change of the first parameter, starting from  $\mathbf{x}_0$ . Brent's method [205] is used for the one-dimensional minimisations. This is a commonly used method which is both efficient and reliable. The resulting best position in this direction is denoted  $\mathbf{x}_1$ , and the decrease in the objective function ( $f(\mathbf{x}_0) - f(\mathbf{x}_1)$ ) is recorded as  $\Delta_1$ . The function is then minimised in the direction of change of the second parameter starting from  $\mathbf{x}_1$ , the resulting best position denoted  $\mathbf{x}_2$ , and the decrease  $f(\mathbf{x}_1) - f(\mathbf{x}_2)$  recorded as  $\Delta_2$ . This process is then repeated for each of the  $N$  parameters, giving a final position  $\mathbf{x}_N$ .

The search direction which gave rise to the largest  $\Delta$  is then replaced with the direction from  $\mathbf{x}_0$  to  $\mathbf{x}_N$  provided two conditions are met. Firstly,  $f_E = f(2\mathbf{x}_N - \mathbf{x}_0)$  must be smaller than  $f(\mathbf{x}_0)$ . This condition indicates that further improvements in the direction  $\mathbf{x}_N - \mathbf{x}_0$  may be possible. Secondly, the  $\Delta$  in the direction of greatest decrease ( $\Delta^*$ ) must account for a large enough proportion of the total decrease, assessed by

$$2(f(\mathbf{x}_0) - 2f(\mathbf{x}_N) + f_E)(f(\mathbf{x}_0) - f(\mathbf{x}_N) - \Delta^*)^2 < \Delta^*(f(\mathbf{x}_0) - f_E)^2. \quad (3.10)$$

If these conditions are satisfied, and the direction set is therefore updated, a further one-dimensional minimisation is carried out in the new search direction ( $\mathbf{x}_0 - \mathbf{x}_N$ ).

Another iteration is then carried out by setting  $\mathbf{x}_0$  to  $\mathbf{x}_N$ , and again searching for a minimum consecutively in each of the set of search directions. The algorithm continues until the required accuracy of the function value has been reached (or the maximum number of permitted function evaluations is reached). An example of the progress of the algorithm whilst minimising a simple function of two parameters

$$f(p_1, p_2) = \sqrt{4.0(p_1 - p_2)^2 + (1 - p_1 - p_2)^2} \quad (3.11)$$

starting from  $p_1 = p_2 = 0$  is shown in Figure 3.2.

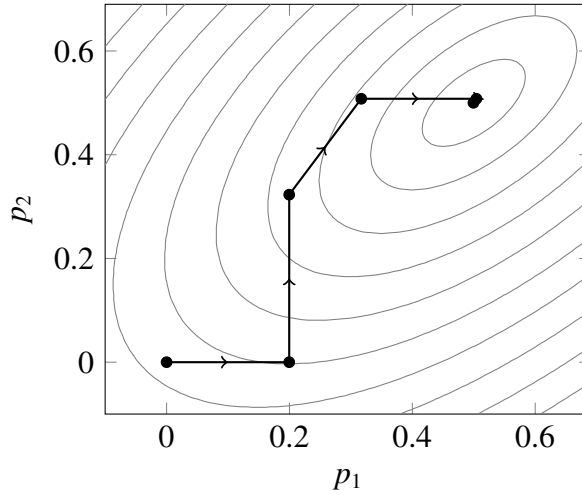


Figure 3.2: An example of the trajectory followed by the modified Powell's method for the simple function given in Equation 3.11

### 3.3.2 PSwarm

This is a derivative-free global optimisation method which combines a pattern search and a particle swarm. It attempts to find the minimum of functions subject to simple

bounds (i.e. each parameter can vary between an upper and a lower bound). The developers of the method compared its performance with other global optimisation methods using extensive numerical experiments. PSwarm was found to perform well, and to be more robust to different types of function than the others tested. Another advantage is that the method can be parallelised, however this has not been implemented here.

The particle swarm part of the method involves a swarm of a given number of particles, which was set in this work to the default value suggested by the software developers of 42 for all optimisations. Each particle is randomly assigned a starting position and starting velocity. The position of the  $i$ th particle at time step  $t$  is then updated according to

$$\mathbf{x}_i(t + 1) = \mathbf{x}_i(t) + \mathbf{v}_i(t + 1) \quad (3.12)$$

where  $\mathbf{v}_i$  is the velocity of the  $i$ th particle updated by

$$v_{i,j}(t + 1) = I(t)v_{i,j}(t) + \frac{\omega_{1,j}}{2} (y_{i,j}(t) - x_{i,j}(t)) + \frac{\omega_{2,j}}{2} (\hat{y}_j(t) - x_{i,j}(t)) \quad (3.13)$$

for each direction  $j = 1, \dots, n$  where  $n$  is the number of parameters. The values  $\omega_{1,j}$  and  $\omega_{2,j}$  are random numbers drawn from a uniform distribution between 0 and 1. The weighting  $I(t)$  is known as the inertial factor. It has a value of 0.9 at  $t = 0$  which is decreased linearly at each time step such that it would reach 0.4 when the maximum number of permitted time steps is reached. The positions  $\mathbf{y}_i(t)$  and  $\hat{\mathbf{y}}(t)$  are the best positions of the  $i$ th particle and of the whole swarm respectively, found up to time  $t$ . Equation 3.13 therefore represents reducing the magnitude of the previous velocity, and adding a random combination of the directions from the particle to its best position, and to the swarm's best position, for each parameter.

The PSwarm algorithm proceeds by implementing a particle swarm as above. An iteration is considered successful if the overall best position of the swarm  $\hat{\mathbf{y}}$  is improved upon by any of the particles at that time step. Following a successful iteration, another particle swarm step is carried out. However, if the iteration is unsuccessful, i.e. no improvement upon  $\hat{\mathbf{y}}$  is found, a poll step is executed. This is the pattern search part of the method, which is included to help achieve convergence.

In the poll step, the objective function is evaluated at points surrounding the overall best position  $\hat{\mathbf{y}}$ , generated by increasing and decreasing each parameter by a step length  $\alpha$ . Initially,  $\alpha$  is set to one fifth of the distance between the upper and lower bounds of the parameter for which this distance is a minimum. If an improvement is found in the poll step, the best particle is moved to this position, and the iteration is considered successful. If no improvement is found, the iteration is considered unsuccessful, and

the step length parameter  $\alpha$  is halved. Following the poll step, another swarm step is executed. If there are two successful poll steps at consecutive iterations in the same direction,  $\alpha$  is doubled.

The process continues until  $\alpha$  and all the particle velocities are smaller than their given tolerance values. Particles which are too close to the best particle are removed from the simulation to reduce the number of function evaluations required.

### **3.3.3 Bayesian methods**

Another way of inferring parameters is to use Bayesian methods. These aim to determine the posterior probability distribution for a set of parameters by multiplying a likelihood function by the prior probability distribution of the parameters. The likelihood can be thought of as the probability of the observed data given the model and the parameter values. The advantage of Bayesian methods is that they result in a probability distribution rather than a single point in parameter space. However, their main disadvantage is that they require a much greater number of function evaluations, and therefore often cannot be used due to constraints on time and computational power. For this reason, Bayesian methods have not been used in this work, but they are discussed further in Chapter 7.

## **3.4 Sensitivity analysis**

Techniques for sensitivity analysis can be thought of as either local or global. Local techniques usually involve calculating derivatives at a given point in parameter space. Global techniques aim to evaluate the effects of a parameter over the whole of parameter space, i.e. all parameters are varied simultaneously within their given ranges. This is important when the model is non-linear and involves significant interactions between parameters, which is usually the case for large complex models such as the ones used in this work. The difficulty with global methods, is that they require a large number of model evaluations, and are therefore computationally expensive compared with local methods. Techniques have been developed which aim to estimate global effects with a minimal number of function evaluations. One of these techniques is explained below.

## Morris' method

The method of Morris [206] is a widely used method in situations where there are a large number of parameters and the cost of model evaluation is high. It is a simple method, but effective as a tool for screening parameters. For a function of  $k$  parameters

$$f(\mathbf{p}), \quad \mathbf{p} = (p_1, p_2, \dots, p_k) \quad (3.14)$$

a maximum ( $p_{i,\max}$ ) and minimum ( $p_{i,\min}$ ) are defined for each parameter. The parameter space is divided into a grid such that each parameter can take  $n$  possible values given by

$$p_{i,\min} + m \frac{p_{i,\max} - p_{i,\min}}{n - 1} \quad (3.15)$$

where  $m$  is an integer between 0 and  $n - 1$ . The jump  $\Delta$  is defined as an integer number of steps on the parameter grid i.e.

$$\Delta_i = m_\Delta \frac{p_{i,\max} - p_{i,\min}}{n - 1} \quad (3.16)$$

where  $m_\Delta$  is a fixed integer between 0 and  $n - 1$ . An elementary effect is defined as

$$d_i(\mathbf{p}) = \frac{f(p_1, \dots, p_i + \Delta_i, \dots, p_k) - f(\mathbf{p})}{\Delta_i} \quad (3.17)$$

i.e. it is the overall gradient of  $f$  between  $p_i$  and  $p_i + \Delta_i$  with all the other parameters held constant. There are a total of  $n^{(k-1)}(n - m_\Delta)$  elementary effects. If  $n$  is chosen to be even, and  $m_\Delta$  to be  $n/2$  (as they are in the implementations in this thesis) the number of elementary effects becomes  $n^k/2$ .

The Morris method consists of sampling from these elementary effects, and calculating the sample mean  $\mu$  (or more commonly the mean of the absolutes  $\mu^*$ ) and the standard deviation  $\sigma$  for each parameter. To implement the method, a base point  $\mathbf{p}^0$  is chosen at random. From these base points, a sequence of  $k + 1$  values of  $\mathbf{p}$  are generated by incrementing each parameter  $p_i$  by  $\pm\Delta_i$  in turn. For the case of  $m_\Delta = n/2$  the step  $\Delta_i$  can only be taken in one direction from each point whilst still remaining in the allowed parameter range. Since each value of  $\mathbf{p}$  differs from the previous value in only one parameter, the method is known as the Morris one at a time (OAT) method. The  $k + 1$  values of  $\mathbf{p}$  define a trajectory in parameter space with  $k$  steps of length  $\Delta$ . The value of the function at these points is used to calculate the elementary effects. Each point (except the first and last) is involved in the calculation of two elementary effects. This is then repeated  $r$  times, requiring a total of  $r(k + 1)$  function evaluations. Although the points within the trajectory are dependent, each sample contains only one elementary

effect from each of the  $r$  trajectories, and is therefore made up of independent points.

The calculated values  $\mu$ ,  $\mu^*$  and  $\sigma$  can be used to assess the importance of the parameters on the output. The mean of the absolutes  $\mu^*$  is used to allow for parameters which have non-linear effects, or strong interactions with other parameters. To make it easier to compare these values, the parameters are scaled to lie between 0 and 1 before calculating the elementary effects. Parameters with a large  $\mu^*$  can be considered to have an important effect on the output, whilst those with a small  $\mu^*$  are unimportant. The standard deviation  $\sigma$  can be used to distinguish between parameters which have a linear independent effect (small  $\sigma$ ) and those which have a non-linear effect or interact with other parameters (large  $\sigma$ ). The main limitation of this method is that it only gives qualitative results.

### **Other methods**

Techniques for quantitative global sensitivity analysis are usually based on the variance of the model output. These requires a greater number of model evaluations. However, there are methods (for example the Sobol' method [207]) which can estimate quantitative sensitivity indices with fewer computations. These methods generally require that the input parameters are independent, and that the function is solvable over the whole of the parameter space defined by the inner product of the individual parameter intervals. This is not the case in the BrainPiglet model; at many points in this space, the model fails to give a solution. For the Morris method, undefined results are simply excluded from the calculations of  $\mu^*$  and  $\sigma$ .

### **Implementation**

Sensitivity analyses were carried out using the R sensitivity package [208]. Firstly, the R functions are used to generate the complete list of parameter values for which simulations should be run. These values are saved in a simple database. Multiple simulations are then run in parallel, until all the simulations are completed. Around 200 000 simulations are run for each of the sensitivity analyses in this work. The results of each simulation are saved to an HDF5 file, which can be used by the R algorithm to calculate the relevant sensitivity indices.

## 3.5 Summary

The BRAINCIRC modelling environment has been used to implement the model. This software was developed to simulate biological systems and it was previously used to develop the BrainSignals model. BRAINCIRC allows a model to be specified in an easy to read text format, and can simulate systems of DAEs. A new SBML exporter has been developed, which can be used to export the BrainPiglet model. This allowed the libSBML library to be used to check the consistency of the units.

Several improvements have been made to the BRAINCIRC environment to increase the speed of simulations, and extensions have been added using the Python programming language to perform parameter optimisation and sensitivity analysis. The SciPy Powell's method and the PSwarm method were used for parameter optimisations to attempt to minimise the mean square error or root mean square error between measured and (potentially scaled and/or offset) modelled data. Sensitivity analyses to determine the most influential parameters were carried out using the Morris method, implemented with the R sensitivity package.

# Chapter 4

## Hypercapnia in healthy adults

This chapter describes the application of the BrainSignals model to simulate a study involving healthy adults breathing increased levels of CO<sub>2</sub> gas. Much of this work has been published in Moroz *et al.* [209] which is reproduced at the end of this thesis. CO<sub>2</sub> is used clinically to treat increased intracranial pressure and cerebral ischaemia [210]. Changes in CO<sub>2</sub> levels are also used as a safe way to alter CBF in experiments. The BrainSignals model was used to investigate the changes in the NIRS signal TOI in response to a CO<sub>2</sub> challenge by considering some of the physiological effects of CO<sub>2</sub> which are described below.

### 4.1 CO<sub>2</sub> and brain physiology

Typical P<sub>a</sub>CO<sub>2</sub> is around 40 mmHg. A greater than average P<sub>a</sub>CO<sub>2</sub> is known as hypercapnia, and the opposite, hypocapnia. They are usually caused by hypo- or hyperventilation respectively. Most of the CO<sub>2</sub> in the blood is in the form of bicarbonate ions (HCO<sub>3</sub><sup>-</sup>). CO<sub>2</sub> levels therefore influence blood pH. Hypercapnia can lead to acidosis (pH lower than 7.35) whilst hypocapnia can cause alkalosis (pH greater than 7.45).

A well known effect of hypercapnia is an increase in CBF [25]. This is accompanied by an increase in CBV, although to a lesser extent. Ito *et al.* [211] used positron emission tomography (PET) to determine a CBF increase of 6 % mmHg<sup>-1</sup> and a CBV increase of 2 % mmHg<sup>-1</sup>. Hypocapnia has the opposite effect, and so decreases CBF and CBV. However, the changes measured are usually smaller: the same study found a CBF decrease of -3.5 % mmHg<sup>-1</sup> and CBV decrease of -1 % mmHg<sup>-1</sup>. These changes are due to dilation or constriction of the cerebral arteries, thought to be caused by extracellular

pH levels [212, 213]. Dilation occurs in vitro even after removal of extravascular cells and endothelium [214], suggesting the response originates in the vessel wall itself. The blood brain barrier allows free diffusion of CO<sub>2</sub> but is fairly impermeable to HCO<sub>3</sub><sup>-</sup>.

The effects of CO<sub>2</sub> on metabolism however are less well known. During hypercapnia, there is a decrease in pH. Most studies have also found a decrease in PCr and pyruvate, and an increase in P<sub>i</sub> [26]. Some studies also report changes in ATP [215]. A decrease in PCr concentration and an increase in the lactate/pyruvate ratio typically indicates that energy demand is exceeding supply. However, these equilibria are sensitive to pH, and it is possible that the changes seen during hypercapnia are caused solely by pH changes. The reduced pyruvate concentration is thought to be caused by a reduction in glucose metabolism as a result of a decrease in the rate of glycolysis [216]. It has been suggested that oxygen metabolism can be maintained by recruiting substrates, leading to a 'substrate depletion' [217]. In experiments carried out over longer periods in animals, recovery from some of the effects of CO<sub>2</sub> has been observed. For example, Arieff *et al.* [218] investigated pH in the brain of anaesthetised dogs and found that for moderate hypercapnia and hypocapnia, changes in intracellular pH were no longer present after three hours. The majority of studies on the metabolic effects of CO<sub>2</sub> have used anaesthetised animals. It is possible that different effects would be seen in conscious animals or in humans. Friedman *et al.* [99] studied hypocapnia in healthy adults with MRS, and found smaller changes in metabolites than those seen in similar animal studies.

There is disagreement over the effects of CO<sub>2</sub> on the rate of oxygen metabolism [219]. Examples can be found reporting an increase [220, 221], a decrease [222, 223], and no change [51] in cerebral oxygen metabolism during hypercapnia. It is generally accepted in the fMRI literature that CMRO<sub>2</sub> is unchanged. This allows CO<sub>2</sub> breathing protocols to separate flow and metabolic components of the BOLD signal [224]. Recently Zappe *et al.* [225] have studied anaesthetised macaque monkeys using EEG. They found that during inhalation of 6 % CO<sub>2</sub>, spontaneous neural activity was reduced by 15 %. Similar findings were reported in conscious humans by Xu *et al.* [226]. In addition, they used an MRI technique to measure CMRO<sub>2</sub> and found a decrease of 13 % during mild hypercapnia.

## 4.2 Previous NIRS studies

A number of studies have used NIRS to investigate the effects of altering CO<sub>2</sub> levels in humans. They are summarised in Table 4.1. All the studies except one (Cho *et al.* [227]) involved periods of both hypocapnia and hypercapnia and monitored either

$V_{mca}$  or CBF. The flow changes seen were in the expected direction and ranged from  $2.4\% \text{ mmHg}^{-1}$  to  $4.8\% \text{ mmHg}^{-1}$ , the largest changes being seen in the  $V_{mca}$  of the anaesthetised patients studied by Yoshitani *et al.* [87]. The study with by far the largest number of subjects (Smielewski *et al.* [228]) observed a  $V_{mca}$  change of  $3.2\% \text{ mmHg}^{-1}$ .

The NIRS measurements obtained depend on the instruments that were used. The  $rSO_2$  (INVOS 4100 and 3100A) and TOI (NIRO 300) are both estimates of the physiological quantity TOS (see 1.3.1). Both the mentioned INVOS spectrometers use two wavelengths of around 730 nm and 810 nm and detect light at two distances from the source, which allows a subtraction algorithm to be used to reduce extracranial contamination of the signal. The NIRO 300 uses four wavelengths (775 nm, 825 nm, 850 nm and 904 nm). Spatially resolved spectroscopy is used to calculate TOI from three differently spaced detectors. Two of the studies in Table 4.1 measured  $rSO_2$  [227, 87] and the latter also measured TOI. The first study recorded an increase in  $rSO_2$  of  $0.5\% \text{ mmHg}^{-1}$  during hyperoxic hypercapnia. The second recorded an increase in  $rSO_2$  of  $0.83\% \text{ mmHg}^{-1}$  during hypercapnia and a decrease of  $-0.75\% \text{ mmHg}^{-1}$  during hypocapnia in anaesthetised patients. The corresponding changes in TOI were  $0.42\% \text{ mmHg}^{-1}$  and  $-0.88\% \text{ mmHg}^{-1}$ . Although the  $rSO_2$  and TOI changes were of a similar size, Yoshitani *et al.* concluded there was unacceptable disagreement between the two measurements.

Absolute changes in  $HbO_2$  and  $HHb$  can be measured by the NIRO instruments. The earlier NIRO models, NIRO 500 and NIRO 1000, use four and six wavelengths respectively in the range 700–910 nm but do not use spatially resolved spectroscopy and therefore cannot calculate TOI. Changes in  $\Delta HbO_2$  and  $\Delta HHb$  were measured in four of the studies. Germon *et al.* [229] do not report absolute concentrations, but that the change seen in  $\Delta HHb$  was 34% larger for the farther spaced optodes (55 mm compared with 27 mm). Smielewski *et al.* observed changes of  $0.27 \mu\text{M mmHg}^{-1}$  in  $\Delta HbO_2$  and  $-0.08 \mu\text{M mmHg}^{-1}$  in  $\Delta HHb$  between hypocapnia and hypercapnia in 50 healthy volunteers using an optode spacing of 60 mm. Despite a smaller optode spacing averaging 41 mm, Rostrup *et al.* [230] found larger changes of  $0.47 \mu\text{M mmHg}^{-1}$  in  $\Delta HbO_2$  and  $-0.11 \mu\text{M mmHg}^{-1}$  in  $\Delta HHb$ . The changes observed by Cho *et al.* [227] were much larger,  $\Delta HbO_2$  increased by  $0.79 \mu\text{M mmHg}^{-1}$  and  $\Delta HHb$  decreased by  $-0.46 \mu\text{M mmHg}^{-1}$ . However in this study, hypercapnia was also accompanied by hyperoxia and an increase in blood pressure.

Overall, the studies show similar patterns in the changes of NIRS measurements during  $P_aCO_2$  changes. There is not good numerical agreement between the studies, but this would be expected considering the range of experimental protocols and measurement instruments, and the small number of subjects included in some of the studies.

Paper and year	Subjects	System used	Optode position and spacing (mm)	P <sub>a</sub> CO <sub>2</sub> (mmHg)	Conc. Change (μM mmHg <sup>-1</sup> )		TOI/rSO <sub>2</sub> (%)	V <sub>mca</sub> (cm s <sup>-1</sup> )
					ΔHbO <sub>2</sub>	ΔHHb		
Smielewski <i>et al.</i> [228] 1995	50 healthy volunteers	NIRO 1000	One side of forehead	baseline 35				58
		DPF - 5.93	60	change of 7.5–30	0.27 ± 0.01	-0.08 ± 0.01		3.2 % mmHg <sup>-1</sup>
Germon <i>et al.</i> [229] 1998	10 healthy males	prototype NIR spectrometer	Top left forehead	oligaemia				
			55	from 48.8 ± 3	34% greater change for 55 mm spacing		38.7 ± 7	
Cho <i>et al.</i> [227] 2000	5 healthy volunteers	Comparison	One on each side of forehead	baseline 42 ± 2				
		INVOS 3100A NIRO 500	30 and 40	to 56 ± 3	0.79 ± 0.2	-0.46 ± 0.3	+7.3 ± 0.2	
Rostrup <i>et al.</i> [230] 2002	5 healthy volunteers	NIRO 500	Left forehead	baseline 32–44 (mean 38)	hypocapnia - hypercapnia			CBF and CBV
		DPF - 5.98	mean 41 range 35-47	38–55 (mean 48) 23–36 (mean 29)	0.47	-0.11		measured by PET CBF – 1.9 ml 100 g <sub>brain</sub> <sup>-1</sup> min <sup>-1</sup> mmHg <sup>-1</sup> CBV – 0.08 ml 100 g <sub>brain</sub> <sup>-1</sup> mmHg <sup>-1</sup>

Table 4.1: A summary of NIRS studies of CO<sub>2</sub> challenges

Paper and year	Subjects	System used	Optode position and spacing (mm)	P <sub>a</sub> CO <sub>2</sub> (mmHg)	Conc. Change ( $\mu\text{M mmHg}^{-1}$ )		TOI/rSO <sub>2</sub> (%)	V <sub>mca</sub> (cm s <sup>-1</sup> )
					$\Delta\text{HbO}_2$	$\Delta\text{HHb}$		
Yoshitani <i>et al.</i> [87] 2002	19 anaesthetised patients	Comparison	Right forehead					
		INVOS 4100	30 and 40	baseline	$40 \pm 4$		$66 \pm 8$	$48 \pm 15$
					$32 \pm 4$		$60 \pm 8$	$34 \pm 11$ ( $-4.1\% \text{ mmHg}^{-1}$ )
					$52 \pm 5$		$75 \pm 8$	$80 \pm 25$ ( $4.8\% \text{ mmHg}^{-1}$ )
		NIRO 300	40 or 50	baseline	$40 \pm 4$		$66 \pm 7$	
					$32 \pm 4$		$59 \pm 7$	
	$52 \pm 5$				$71 \pm 6$			

Table 4.1: A summary of NIRS studies of CO<sub>2</sub> challenges

## 4.3 Method and results

### 4.3.1 Experimental protocol

Data were taken from a hypercapnia study carried out by Tachtsidis *et al.* [83]. The study was approved by the Joint Research Ethics Committee of the National Hospital for Neurology and Neurosurgery and the Institute of Neurology, University College London. The experiment involved 14 subjects breathing normal air for five minutes to establish a baseline. The inspired CO<sub>2</sub> was then increased to about 6% to increase EtCO<sub>2</sub> by 11 mmHg. This was maintained for ten minutes and followed by a further five minutes at baseline. Throughout the study, the subjects' heart rate, MABP and S<sub>a</sub>O<sub>2</sub> were monitored. The V<sub>mca</sub> was also monitored, using transcranial Doppler. The TOI was measured using the NIRO 300 (Hamamatsu Photonics KK), and ΔoxCCO was measured with a NIRS broadband system [77].

### 4.3.2 Data analysis and modelling

All signals were smoothed and filtered. In a few cases, breaks in the signal caused by instrumentation error were identified manually and replaced by a linear interpolation. This was necessary in six of the signals, all from different subjects: the S<sub>a</sub>O<sub>2</sub> signal from one subject (a total of 150 s replaced in 6 places); the MABP signal from another subject (a total of 27 s replaced in 7 places); and the EtCO<sub>2</sub> signal from four of the subjects (8–12 s removed from a single place in each subject). An example of one of these is shown in Figure 4.1.

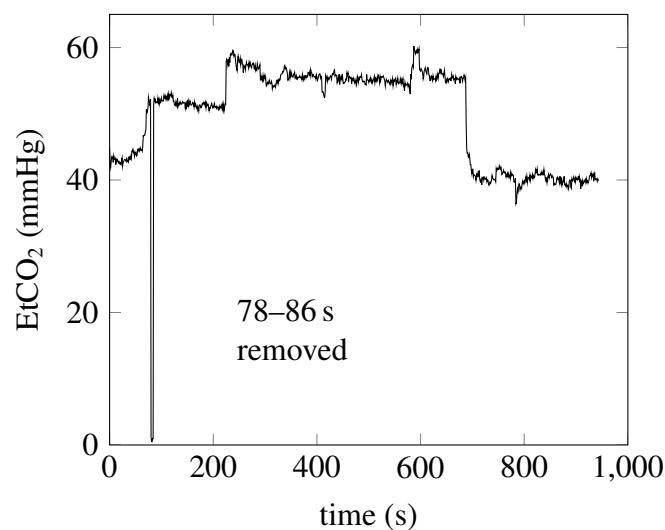


Figure 4.1: Example of instrumentation error in the EtCO<sub>2</sub> signal from one subject

$S_aO_2$ ,  $EtCO_2$  and MABP were input to the model, and its outputs of TOS ( $TOS_m$ ),  $V_{mca}$  ( $V_{mcam}$ ) and  $\Delta oxCCO$  ( $\Delta oxCCO_m$ ) were compared to their measured equivalents  $TOI_d$ ,  $V_{mcad}$  and  $\Delta oxCCO_d$ .

To calculate the response, a period of hypercapnia and a subsequent baseline period were identified by inspection of the  $EtCO_2$  trace for each subject. The baseline period was chosen at the end of the study because, for most subjects, there was a longer, more stable baseline here than at the beginning. The response  $\rho$  was calculated from the means during these periods, after resampling to 1 Hz, as follows

$$\rho_{TOS} = \overline{TOS}(\text{hypercapnia}) - \overline{TOS}(\text{baseline}) \quad (4.1)$$

$$\rho_{V_{mca}} = \frac{\overline{V_{mca}}(\text{hypercapnia}) - \overline{V_{mca}}(\text{baseline})}{\overline{V_{mca}}(\text{baseline})} \times 100 \% \quad (4.2)$$

$$\rho_{\Delta oxCCO} = \overline{CCO}(\text{hypercapnia}) - \overline{CCO}(\text{baseline}) \quad (4.3)$$

The  $V_{mca}$  response is given as a percentage because the absolute value of  $V_{mca}$  can vary but it is assumed to be proportional to CBF (see Section 1.3.3) so it is the relative change that is of interest.

The measured data are summarised in Table 4.2. There were significant differences between normocapnia and hypercapnia for both  $TOI$  and  $V_{mca}$  with mean responses of  $(1.1 \pm 0.8) \%$  and  $(26 \pm 11) \%$  respectively. There was no significant difference between the mean values of  $\Delta oxCCO_d$  during hypercapnia and baseline; the mean  $\Delta oxCCO_d$  response was  $(0.02 \pm 0.16) \mu M$ . Using 10 subjects from the same study, Tachtsidis *et al.* [83] found a significant difference of  $(0.25 \pm 0.17) \mu M$  between  $\Delta oxCCO$  during hypercapnia and at baseline. The analysis was different from the one used here, most importantly the baseline value was taken at a different time and some subjects with poor  $\Delta oxCCO$  data were excluded.

	Normocapnia	Hypercapnia
Duration (s)	$240 \pm 20$	$500 \pm 50$
$EtCO_2$ (mmHg)	$39 \pm 2$	$52 \pm 2$
$TOI_d$ (%)	$69 \pm 6$	$70 \pm 6$
$V_{mcad}$ ( $cm s^{-1}$ )	$42 \pm 11$	$52 \pm 13$
$\Delta oxCCO_d$ ( $\mu M$ )	$0.11 \pm 0.30$	$0.13 \pm 0.30$

Table 4.2: Summary of the measured hypercapnia data, mean  $\pm$  SD across the 14 subjects

### 4.3.3 Initial optimisations

#### Methods

Optimisations were carried out as described in Section 3.3 to minimise the mean square error (MSE) between the measured and simulated signals. Each optimisation was performed with both the SciPy Powell's method and the PSwarm method. An overview of the modelling and optimisation process is illustrated in Figure 4.2.

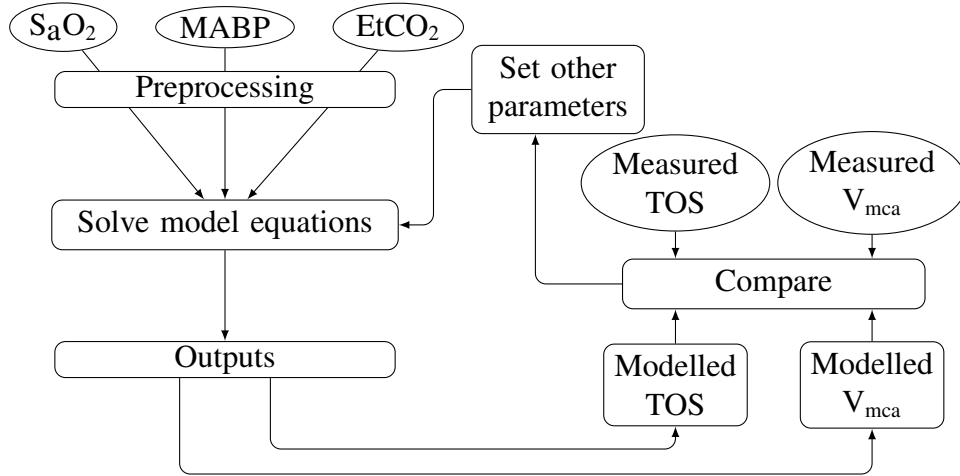


Figure 4.2: Modelling and optimisation process for TOS and  $V_{mca}$

For each simulation, the following errors were calculated:

- $E_{TOS}$  The MSE between  $TOS_m$  and  $TOI_d$  (see Equation 3.6),
- $E_{V_{mca}}$  The MSE between the scaled  $V_{mcam}$  and  $V_{mca d}$  (see Equation 3.8),
- $E_{CCO}$  The MSE between the offset  $\Delta xCCO_m$  and  $\Delta xCCO_d$  (see Equation 3.7).

Optimisations were performed per subject to minimise either  $E_{TOS}$ ,  $E_{V_{mca}}$  or a combination of the two.  $E_{CCO}$  was not minimised, but its values resulting from the TOS and  $V_{mca}$  optimisations were compared.

Six optimisations were performed in total, the first two being

1. Minimise  $E_{TOS}$  with respect to two parameters: concentration of blood haemoglobin oxygen binding sites (four times blood haemoglobin concentration) [Hbtot], chosen for its influence on the absolute TOS value, and  $R_C$  which represents the sensitivity of the flow response to  $P_aCO_2$  changes.
2. Minimise  $E_{V_{mca}}$  with respect to  $R_C$ . [Hbtot] was not included in this optimisation

since it was included in Optimisation 1 specifically for its effect on the TOS baseline value, and it does not have this effect on  $V_{mca}$ . There is no need to optimise a parameter to match the  $V_{mca}$  baseline, because the modelled signal is scaled to match the measured data. [Hbtot] was instead set to its value from optimisation 1 to allow a better comparison of  $E_{TOS}$  values between optimisations 1 and 2.

The results of these optimisations were used to define two further error functions.

$$\mathcal{E}_{TOS} = \frac{E_{TOS} - {}^1E_{TOS}}{{}^2E_{TOS} - {}^1E_{TOS}} \quad (4.4)$$

$$\mathcal{E}_{V_{mca}} = \frac{E_{V_{mca}} - {}^2E_{V_{mca}}}{{}^1E_{V_{mca}} - {}^2E_{V_{mca}}} \quad (4.5)$$

where  ${}^1E_{TOS}$  and  ${}^2E_{TOS}$  are the  $E_{TOS}$  values after optimisations 1 and 2 as listed above and similarly  ${}^1E_{V_{mca}}$  and  ${}^2E_{V_{mca}}$  are the values of  $E_{V_{mca}}$ . These expressions were used in order to assess the ability to fit TOS and  $V_{mca}$  simultaneously, compared with the ability to fit them alone. The third optimisation was

3. Minimise the sum of  $\mathcal{E}_{TOS}$  and  $\mathcal{E}_{V_{mca}}$  by varying parameters [Hbtot] and  $R_C$ . The resulting errors  ${}^3\mathcal{E}_{TOS}$  and  ${}^3\mathcal{E}_{V_{mca}}$  would be expected to lie between 0 and 1, with 0 meaning the fit is as good as for optimisation to that signal alone, and 1 meaning the fit is as poor as for optimisation to the other signal.

## Results

With no optimisation, mean  $\rho_{TOS_m}$  was  $(7.2 \pm 1.2)\%$ , much larger than the measured value of  $(1.1 \pm 0.8)\%$ .  $V_{mca}$  changes were better predicted, with a mean  $\rho_{V_{mca_m}}$  of  $(32 \pm 6)\%$ , closer to the measured response of  $(26 \pm 11)\%$ . The resulting errors from the three initial optimisations are shown in Table 4.3. The errors with no optimisation (Optimisation 0) are also shown. There were no difference between the two optimisation methods.

Optimisation	$\mathcal{E}_{TOS}$	$\mathcal{E}_{V_{mca}}$
0	$12 \pm 15$	$2 \pm 5$
1	0	1
2	1	0
3	$0.22 \pm 0.03$	$0.13 \pm 0.08$

Table 4.3: Initial optimisation results for  $CO_2$  studies

As expected, optimising to both the TOI and  $V_{mca}$  signals simultaneously produced er-

rors larger than when optimising to that signal alone. The differences between the measured and modelled responses in TOS and  $V_{mca}$  are shown in Figure 4.3. Comparing the responses of the individual subjects gives further information on how the optimisations differ, and why the simultaneous optimisation was less successful. The responses of both signals could be matched well when optimising to that signal alone. However, the value of  $R_C$  resulting from optimisation 2 was larger than that from optimisation 1 for every subject; i.e. a greater sensitivity of blood flow to  $CO_2$  was required to explain the changes in  $V_{mca}$ , than that required to explain the changes in  $TOI_d$ . Consequently, when optimising to both signals, in every case, the modelled TOS response was larger than measured, whilst the modelled  $V_{mca}$  response was smaller.

By considering the physiology and measurements, three possible reasons for this discrepancy were proposed and amendments were made to the model to investigate their consequences.

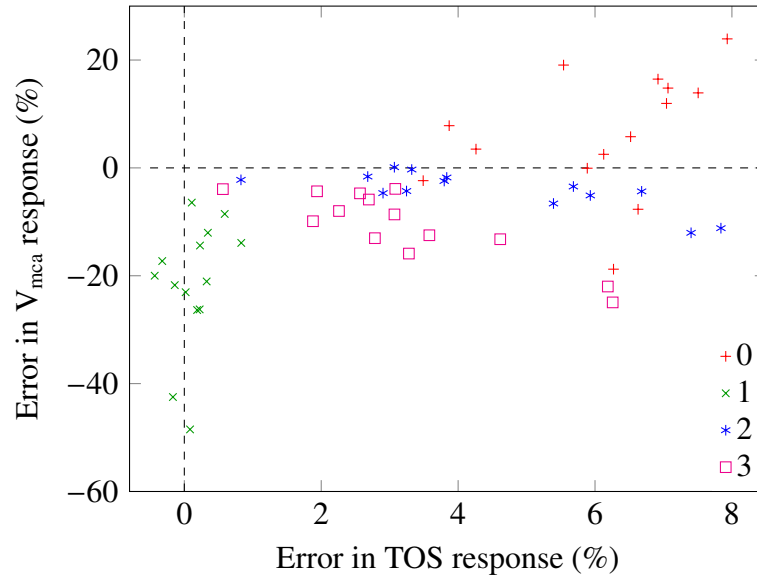


Figure 4.3: Error in response  $\rho_{TOS_m} - \rho_{TOI_d}$  vs  $\rho_{V_{mcam}} - \rho_{V_{mca}}$  for all fourteen subjects for no optimisation (0) and for optimisations 1–3 as described in the text.

#### 4.3.4 Model extensions

##### Methods

Three new mechanisms were added to the model in turn and three further optimisations were performed to minimise the sum of  $\mathcal{E}_{TOS}$  and  $\mathcal{E}_{V_{mca}}$ .

4. The TOI measurement may be contaminated by an extracranial component. If

it is assumed that the TOS value of this component does not change with  $\text{CO}_2$  levels, the measured change in TOI will be smaller than the TOS change occurring in the brain.

To simulate an extracerebral contribution to TOI,  $\text{TOS}(\text{corrected})$  was calculated as the weighted sum of intra and extracerebral compartments

$$\text{TOS}_m(\text{corrected}) = (1 - \alpha)\text{TOS}_m(\text{ic}) + \alpha\text{TOS}_m(\text{ec}) \quad (4.6)$$

where  $\alpha$  is the fractional contribution of the extracerebral compartment, and  $\text{TOS}_m(\text{ec})$  its fixed TOS value.  $\text{TOS}_m(\text{ic})$ , the intracerebral TOS, was calculated as before (see Equation C.68).  $\text{TOS}_m(\text{ec})$  and  $\alpha$  were optimised together with  $R_C$ .

5. Venous volume in the BrainSignals model is fixed at 0.75 (as a fraction of normal total blood volume  $V_{\text{blood,n}}$ ). If venous volume were to increase during hypercapnia, deoxyhaemoglobin concentration would be increased to a greater extent than oxyhaemoglobin, leading to a lower TOS during hypercapnia and thus a lower TOS response.

To simulate this possibility, venous volume ( $V_v$ ) was varied with  $\text{CO}_2$  levels. Previously, it was fixed at 0.75 (as a fraction of the normal total blood volume  $V_{\text{blood,n}}$ ). This was changed to

$$V_v = (0.75 + \nu(P_a\text{CO}_2 - P_a\text{CO}_{2,n})) \quad (4.7)$$

where  $P_a\text{CO}_{2,n}$  is the model's normal value of  $P_a\text{CO}_2$ . The constant  $\nu$  was included as an optimisation parameter. No limit was imposed on total blood volume, and the effect of volume changes on ICP was not taken into account. For many purposes this would be an oversimplification, but it is sufficient to determine whether a venous volume change could reconcile the discrepancy between TOS and  $V_{\text{mca}}$  response and estimate how large this change would need to be.

6. An increase in cerebral metabolic rate during hypercapnia would lead to a greater oxygen extraction fraction, and therefore to a reduced TOS and lower response.

To investigate this, a change linking metabolic rate to  $\text{CO}_2$  levels was introduced, via the parameter  $u$  representing the demand. This was varied in a similar

way to venous volume

$$u = 1 + d(P_a\text{CO}_2 - P_a\text{CO}_{2,n}) \quad (4.8)$$

and  $d$  was optimised. Demand affects metabolic rate by altering the rate of ADP phosphorylation (see Equation C.64) and it also effects the [NAD]/[NADH] ratio (see Equation C.120) Changes in demand also have a direct effect on the blood flow (see Equation C.33); but this was removed here by setting the relevant parameter  $R_u$  to zero.

In these optimisations, [Hbtot] was again set to its value from optimisation 1. This was done because inclusion of [Hbtot] led to problems in identifying the parameters. The additional mechanisms affected the baseline TOS value, however it was their effect on changes in TOS that was of interest.

## Results

The six differently optimised datasets are summarised in Table 4.4. Parameter values not given in the table were set at their defaults, except for [Hbtot] which was fixed at its value from optimisation 1 as explained previously. The two optimisation methods produced the same results to the accuracy given in the table for every simulation.

Optimisation		1	2	3	4	5	6
	$R_C$	$0.3 \pm 0.2$	$1.5 \pm 0.6$	$1.1 \pm 0.4$	$1.5 \pm 0.6$	$1.4 \pm 0.5$	$1.2 \pm 0.4$
Parameters Optimised	[Hbtot] (mM)	$8.5 \pm 3.0$		$7.8 \pm 2.7$			
	$\alpha$				$0.78 \pm 0.14$		
	TOS <sub>m</sub> (ec)(%)				$69 \pm 6$		
	$\nu$ (mmHg <sup>-1</sup> )					$0.06 \pm 0.05$	
	$d$ (mmHg <sup>-1</sup> )						$0.16 \pm 0.16$
Signals optimised to	TOI <sub>d</sub>	✓		✓	✓	✓	✓
	V <sub>mca</sub>		✓	✓	✓	✓	✓
Errors	$\mathcal{E}_{\text{TOS}}$	0	1	$0.22 \pm 0.03$	$-0.32 \pm 0.31$	$0.02 \pm 0.04$	$0.01 \pm 0.05$
	$\mathcal{E}_{\text{Vmca}}$	1	0	$0.13 \pm 0.08$	$0.001 \pm 0.003$	$0.01 \pm 0.01$	$0.00 \pm 0.06$

Table 4.4: Details of the optimisation methods and results. The first row contains the mean  $\pm$  SD of the optimised parameter values. No value given indicates that a parameter was fixed.

The errors in TOS and  $V_{mca}$  response for each subject in each of these optimisation sets, and for no optimisation, are shown in Figure 4.4.

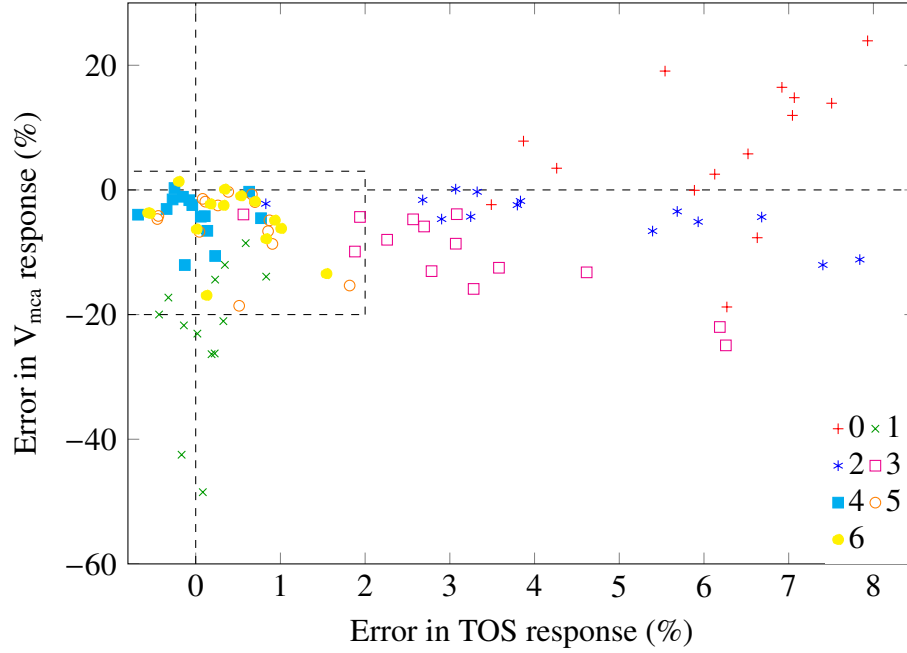


Figure 4.4: Error in response  $\rho_{TOS_m} - \rho_{TOI_d}$  vs  $\rho_{V_{mcam}} - \rho_{V_{mca d}}$  for all fourteen subjects in each optimisation method. The legend refers to the six optimisation methods described in Table 4.4. Series 0 represents no optimisation. The box at the origin surrounds all the points from optimisations 4–6, where new mechanisms were introduced.

All three new model mechanisms were capable of reducing the discrepancy between TOS and  $V_{mca}$  response:

1. The additional compartment for  $TOS_m$  was the most successful, leading to a mean  $\rho_{TOS_m}$  of  $(1.1 \pm 0.7) \%$  and a mean  $\rho_{V_{mcam}}$  of  $(22 \pm 9) \%$ . The mean optimum weight of the extracerebral compartment was 0.8 (range 0.45–0.95). The negative value of  $\mathcal{E}_{TOS}$  for this optimisation was a consequence of the reduction in the size of the modelled fluctuations in TOS.
2. With a varying venous volume, mean  $\rho_{TOS_m}$  was reduced to  $(1.6 \pm 1.0) \%$  and mean  $\rho_{V_{mcam}}$  to  $(20 \pm 7) \%$ , which therefore matched better the measured signals. However, this corresponded to a mean venous volume change of 100%, (range 20–230 %).
3. When optimising the change in oxygen metabolism, the mean resulting  $CMRO_2$  increase was  $(18.0 \pm 8.4) \%$ . The mean  $\rho_{TOS_m}$  and  $\rho_{V_{mcam}}$  were  $(1.5 \pm 1.0) \%$  and  $(21 \pm 8) \%$  respectively, which matched well with the measured signals.

An example of the  $CMRO_2$  change in one subject, along with  $TOS_m$ ,  $TOI_d$ ,  $V_{mcam}$  and

$V_{m_{cad}}$ , is shown in Figure 4.5. The plausibility of these changes and their consequences are considered in the discussion.

## $\Delta\text{oxCCO}$

A plot of the response of  $\Delta\text{oxCCO}_d$  vs the response of  $\Delta\text{oxCCO}_m$  for the seven differently optimised datasets is shown in Figure 4.6. It is clear from the graph, that there is a much greater variation in  $\rho_{\Delta\text{oxCCO}_d}$  than in  $\rho_{\Delta\text{oxCCO}_m}$ . The model shows an increase of  $\Delta\text{oxCCO}$  during hypercapnia for all subjects, whereas in the data, some subjects show a decrease. There is no clear correlation between  $\rho_{\Delta\text{oxCCO}_m}$  and  $\rho_{\Delta\text{oxCCO}_d}$  for any of the optimisation sets. From Figure 4.7 it can be seen that there is little difference between the mean  $E(\Delta\text{oxCCO})$  for any of the optimisations, except optimisation 6, where there was a change in demand. The model predicts an increase in demand during hypercapnia to cause an increased change in  $\Delta\text{oxCCO}_m$ . However, the difference in the mean error is small compared with the variation between subjects.

One of the difficulties with analysing  $\Delta\text{oxCCO}$  data, is that there is a lot of noise in the signal. A more thorough analysis would require looking at the data on an individual basis. Figure 4.8 shows  $\Delta\text{oxCCO}_m$  and  $\Delta\text{oxCCO}_d$  after optimisation 6 for two subjects: one where the models prediction compared well with the data, and one where it compared poorly. Optimisation of the model to the  $\Delta\text{oxCCO}$  signal would give further information. However it is unlikely that the model could fit closely the data from the second example subject shown, even with optimisation.

## 4.4 Discussion

As expected,  $V_{m_{cad}}$  and  $\text{TOI}_d$  increased during hypercapnia. The model behaviour was qualitatively correct, but there were several differences between the modelled and measured data. Also, the fluctuations seen in  $\text{TOS}_m$  were greater than the fluctuations in  $\text{TOI}_d$ . These fluctuations originate from blood pressure changes. Therefore, the model predicts  $\text{TOI}$  to be more sensitive to changes in blood pressure than what is seen. This will require more investigation but is not discussed further here.

The fact that both optimisation methods gave the same results increases confidence in the results of the optimisations, and the performance of the optimisation algorithms. It also suggests, since the SciPy Powell's method is a local method, that there were not multiple minima in the functions investigated. Fewer function evaluations were

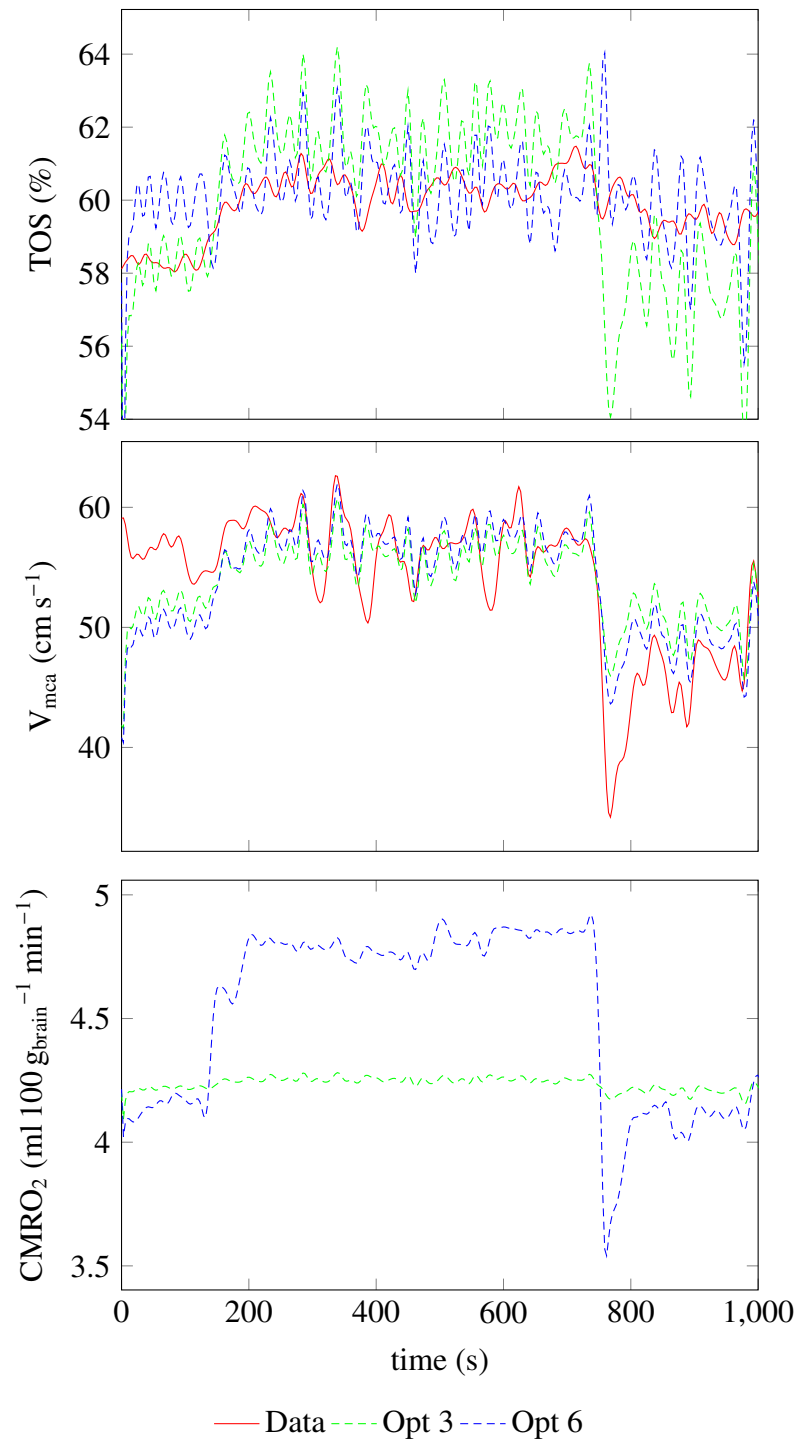


Figure 4.5: Examples of TOS,  $V_{mca}$  and  $CMRO_2$  from one volunteer. The graphs show the measured signal, the modelled signal after optimisation 3, and the modelled signal after optimisation 6 as described by Table 4.4.

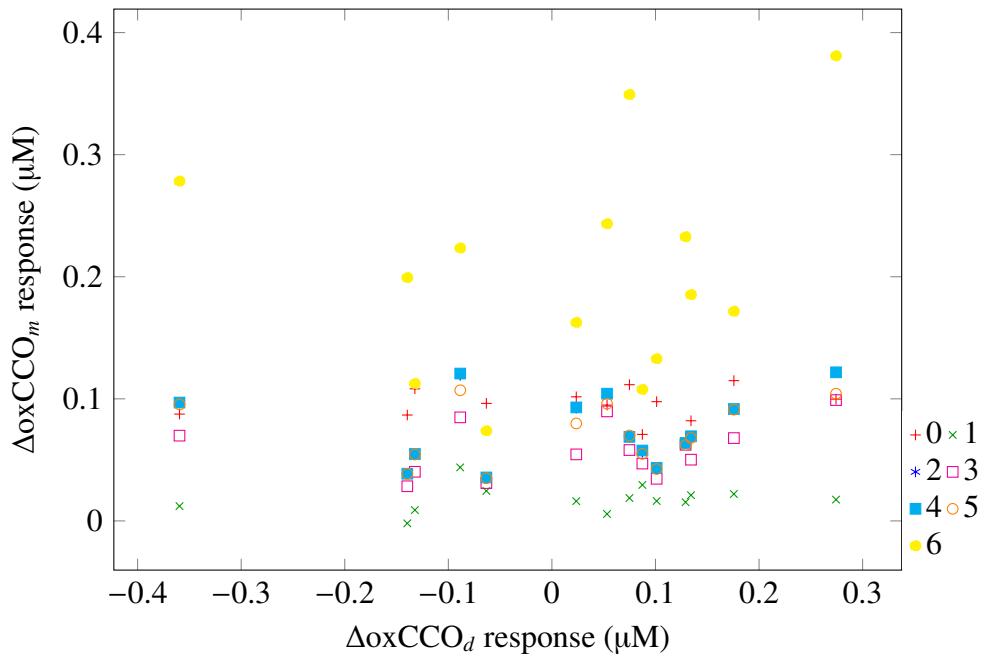


Figure 4.6: Response  $\rho_{\Delta\text{oxCCO}_m}$  vs  $\rho_{\Delta\text{oxCCO}_d}$  for all fourteen subjects in each optimisation method. The legend refers to the six optimisation methods described in Table 4.4. Series 0 represents no optimisation.

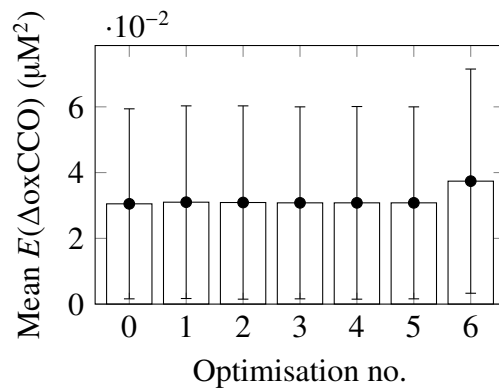


Figure 4.7: MSE for CCO across all subjects after optimising according to Table 4.4

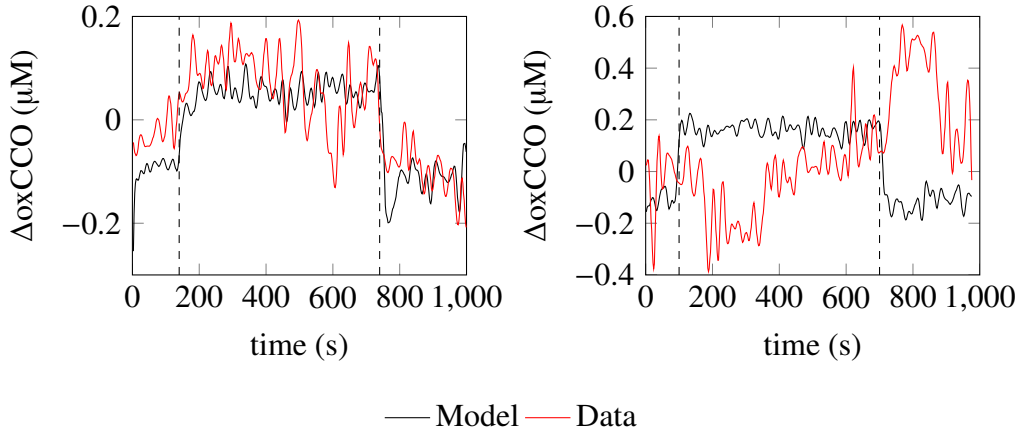


Figure 4.8: Comparison of modelled and measured  $\Delta\text{oxCCO}$  for two subjects. The period of hypercapnia is indicated by the dashed lines.

required for Powell’s method, on average 3 times fewer than for PSwarm (ranging from 1.5–6) However, using the global PSwarm method provides more confidence that the overall minimum has been found.

The particular aspect of the model investigated here was the ratio of  $\text{TOS}_m$  response to  $V_{mcam}$  response, which was consistently higher than that seen in the measured data. All three additional mechanisms improved the simulations; however the changes required for optimum fitting suggested that no single mechanism is likely to be successful in its own right.

The method used here of changing venous volume was very simplistic. A more realistic method could be incorporated, for example as in the model by Ursino and Lodi [142]. However, a large change in venous volume would still be required to model  $\text{TOI}_a$  response accurately. Since it is well known that hypercapnia increases CBV, it is reasonable to suppose there might be an increase in cerebral venous volume. However, when Ito *et al.* [231] attempted to measure this using PET they found no change in combined capillary and venous volume i.e. the CBV change was attributed solely to arterial volume changes. A study in anaesthetised rats did find a small increase in venous volume with increased  $\text{CO}_2$  levels [232]. A linear relationship was found between venous volume and CBF changes, such that a doubling of CBF caused a 15% increase in venous volume. Assuming a CBF change of  $2\% \text{ mmHg}^{-1}$  (as seen in  $V_{mca}$  in this study) this is equivalent to a  $\nu$  of 0.002 in Equation 4.7, which would therefore predict a venous volume increase of 3.5% in this study. The model optimisations suggest a  $\nu$  of 0.06 (corresponding to a doubling of the venous volume during the hypercapnia challenge) would be required to reconcile the observed TOS and  $V_{mca}$  responses. This is an extremely large change and therefore venous volume change is unlikely to be an

important factor.

Linking of  $\text{CMRO}_2$  to  $\text{CO}_2$  levels allowed improved fits to  $V_{\text{mca}d}$  and  $\text{TOI}_d$ . But as before, the 18 % increase in  $\text{CMRO}_2$  was unexpectedly large. The direction of the change also disagreed with some recent studies on hypercapnia using EEG and MRI [225, 226]. These studies suggest  $\text{CMRO}_2$  should decrease with increasing  $\text{CO}_2$ . If a mechanism to implement this were added to the model, it would increase the ratio of the  $\text{TOI}_m$  response to the  $V_{\text{mca}m}$  response, leading to a greater discrepancy with the measured responses.

The measured  $\Delta\text{oxCCO}$  signal could potentially be used with the model to further investigate  $\text{CMRO}_2$  changes. However, the relationship between  $\text{CMRO}_2$  and  $\Delta\text{oxCCO}$  is complex, and in addition, some of the  $\Delta\text{oxCCO}$  measurements from this study have high levels of noise. Although this analysis did not show a significant change in  $\Delta\text{oxCCO}$  during hypercapnia, Tachtsidis *et al.* [83] found a significant increase in  $\Delta\text{oxCCO}$  using a different analysis and a slightly smaller set of subjects from the same experiment. The authors found that this increase could not be attributed exclusively to the increase in oxygen delivery, which suggests an increase in  $\text{CMRO}_2$ . However, any changes in  $\text{CMRO}_2$  which may occur with changing  $\text{CO}_2$  levels must be small and will therefore only have a small effect on TOS.

Finally, this analysis suggested that an 80:20 extracerebral to intracerebral weighting was required to optimise the fit to the  $\text{TOI}_d$  datasets. Monte Carlo simulations of photons travelling through tissue have shown that the sensitivity of NIRS oxygenation measurements to changes in scalp and skin oxygenation is dependent on the distance between the source and detectors [233]. It is therefore likely that a different extracerebral to intracerebral weighting would have been required to optimise the fit if the measurement had originated from a different instrument or used a different algorithm (see Section 1.3.1).  $\text{TOI}$  has been shown to have a high sensitivity and specificity to intracerebral changes [92]. However, the consistency of NIRS measurements of the cerebral effects of  $\text{PaCO}_2$  changes has previously been questioned [234].

## 4.5 Conclusions

The use of a physiological model has shown that there is a discrepancy between the modelled and measured  $\text{TOI}$  and  $V_{\text{mca}}$  responses to hypercapnia i.e. the measurements obtained are not compatible with the assumptions about brain physiology incorporated in the model. This is not obvious from a more simple numerical analysis. The model has

also been used to show that changes in venous volume or in  $CMRO_2$  during hypercapnia would have to be implausibly large to account for this discrepancy, and it therefore suggests the origin of the TOI measurement should be questioned. The conclusions are dependent on the accuracy of the model. However, additional validation of the model is provided by its use to study data from hypoxia challenges [235]. Also, the magnitude of the changes required to correct the discrepancy here were large and they are therefore likely to remain despite small changes in model parameters or equations. In this analysis, the additional model mechanisms have been considered in turn, since the data is not sufficient to distinguish between them. Combining the mechanisms and considering more data could help to refine the model's predictions. Addition of the  $\Delta HbT$  signal to the analysis would give further information on volume changes, and consideration of the  $\Delta oxCCO$  signal may help with investigating  $CMRO_2$  changes.

# Chapter 5

## The BrainPiglet model and anoxia in piglets

This chapter describes the BrainPiglet model, and shows its behaviour during steady state simulations. The model is then applied to measurements from a study in which newborn piglets were subjected to brief anoxia. This work has been published using an earlier version of the model very similar to the one described here [236]. The anoxic insults are shorter and less severe than hypoxic-ischaemic insults, and are not expected to cause any cellular damage. The data can therefore be used as an initial test of the applicability of the model to neonatal piglets. The model is used to simulate both NIRS and MRS measurements, allowing evaluation of the model as a tool for multimodal data integration.

### 5.1 The BrainPiglet model

The BrainPiglet model was created by extending and adapting the BrainSignals model (see Section 2.3.7). The model was adapted by changing several parameters to values appropriate to newborn piglets. These parameters were chosen by considering which physiological quantities represented by the parameters were likely to differ between piglets and adult humans. These are shown in Table 5.1, and their use is described in the text below. The model was extended firstly in order to simulate variables measured by MRS in addition to NIRS, and secondly to allow simulation of HI induced by carotid artery occlusion, described in Chapter 6. The first of these involves extensive expansion of the metabolic part of the model, in particular the metabolic processes occurring in the cytoplasm. The BrainPiglet model has 24 variables and 114 parameters (see Appendix

Parameter	Description	Units	BrainSignals	Piglet	Source
$CBF_n$	Normal CBF	$\text{ml } 100 \text{ g}_{\text{brain}}^{-1} \text{ min}^{-1}$	61	46	[59]
$[CCO]_{\text{tis}}$	Total CCO concentration in tissue	$\mu\text{M}$	5.5	2.2	[75, 237]
$\text{Cu}_{\text{A,frac,n}}$	Normal fraction of CCO oxidised		0.8	0.67	[237]
$\text{CMRO}_{2,n}$	Normal $\text{CMRO}_2$	$\mu\text{M } 100 \text{ g}_{\text{brain}}^{-1} \text{ min}^{-1}$	194	114	[59, 238]
$P_a$ and $P_{a,n}$	Mean arterial blood pressure	mmHg	100	50	[59]
$[\text{Hbtot}]$ and $[\text{Hbtot}]_n$	Total blood haemoglobin $\text{O}_2$ binding site concentration	mM	9.1	5.4	[239]
$V_{\text{blood,n}}$	Normal brain blood fraction		0.04	0.0325	[238]
$P_{ic}$ and $P_{ic,n}$	Intracranial pressure	mmHg	9.5	4.5	[240]

Table 5.1: Parameters that were changed from their BrainSignals values in the BrainPiglet model

D), whereas BrainSignals has 12 variables and 80 parameters (see Appendix C). A schematic diagram of the BrainPiglet model is shown in Figure 5.1, and the aspects of the model which are additional to or changed from BrainSignals are described below.

### 5.1.1 Circulation

The circulatory part of the model was altered by introducing a changing venous volume, and adding a supplying arterial compartment to allow simulation of carotid artery occlusion. A diagram showing the circulation of the BrainPiglet model in electrical circuit form is shown in Figure 5.2.

The conductances  $G_0$ ,  $G$  and  $G_v$  are the conductances of the supplying arterial, cerebral arterial and venous compartments respectively.  $P_a$ ,  $P_{a2}$  and  $P_v$  are the pressures at the start of these compartments.  $P_1$  is the pressure at the midpoint of the arterial compartment,  $P_{vs}$  is the pressure at the venous sinuses,  $P_{ic}$  is the intracranial pressure and  $P_{v,n}$  is the normal venous pressure. The capacitors in the diagram are included to represent the volume changes of the arterial and venous compartments. However, the circulatory part of the model is considered to be always at steady state, and therefore no differential equations related to capacitance are included. The validity of this assumption is explored in the following section. The volume of the arterial compartment is represented by the charge on the variable capacitor labelled  $C_a$ . However, this is for illustrative purposes only, as arterial compliance is not included directly in the model and  $C_a$  is not a parameter or variable in the model. Arterial volume is calculated from

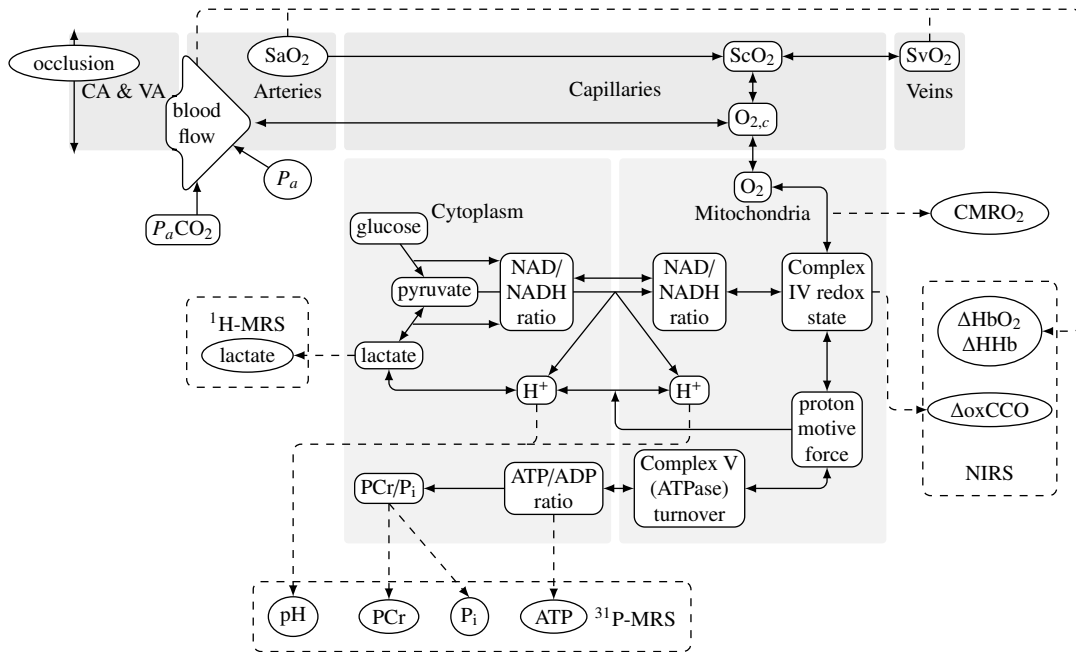


Figure 5.1: Schematic diagram of the BrainPiglet model. CA and VA represent the carotid and vertebral arteries

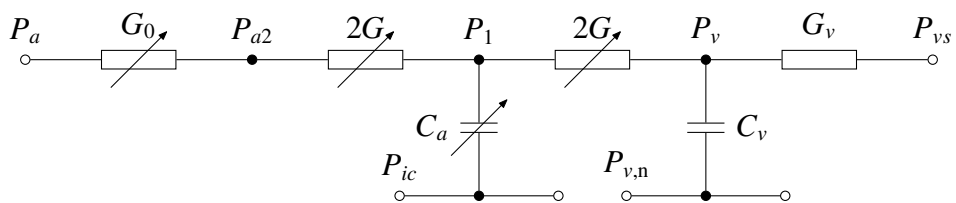


Figure 5.2: A diagram showing the circulation part of the BrainPiglet model in electrical circuit form

the arterial radius  $r$  by

$$V_a = V_{a,n} \left( \frac{r}{r_n} \right)^2 \quad (5.1)$$

where  $V_{a,n}$  is the arterial volume and  $r_n$  the arterial radius under normal conditions. The radius is determined by the algebraic equation

$$T_e + T_m - (P_1 - P_{ic})r = 0 \quad (5.2)$$

where the muscular and elastic tensions  $T_e$  and  $T_m$  vary as described in Section 2.3.7.

The difference in venous volume from its normal value ( $V_v - V_{v,n}$ ) is represented by the charge on the capacitor labelled  $C_v$ . The venous volume is therefore given by

$$V_v = V_{v,n} + C_v (P_v - P_{v,n}) \quad (5.3)$$

where  $C_v$  is the compliance of the venous compartment which is a constant. The conductance of the veins  $G_v$  is assumed to be constant, following Ursino and Lodi [142] who assign a constant conductance to the proximal venous compartment in their model.

To simulate carotid artery occlusion, an extra compartment representing the arteries supplying the brain was added to the model. Reducing the conductance  $G_0$  of the supplying artery compartment represents occluding the carotid arteries, and causes a decrease in pressure of the blood entering the brain. The pressure at the cerebral arteries  $P_{a2}$  is calculated by equating the blood flow through the two arterial compartments

$$P_{a2} = \frac{G_0 P_a + G P_v}{G + G_0} \quad (5.4)$$

The pressure at the veins is calculated from  $G_v$  as a fraction of the total conductance  $G_t$

$$P_v = \frac{G_t}{G_v} (P_a - P_{vs}) + P_{vs} \quad (5.5)$$

where  $P_{vs}$  is the constant pressure at the venous sinuses, and  $G_t$  is given by

$$G_t = \frac{G G_0 G_v}{G G_0 + G G_v + G_v G_0}. \quad (5.6)$$

### Steady state approximation

As in BrainSignals, the circulation part of the BrainPiglet model is assumed to be always at steady state. This was done for simplicity, since the model is not intended to study short time scale responses. The effect of changes in input parameters on the ar-

terial wall tension are subject to time delays and represented with differential equations (see Equations D.18 to D.21). However, no other differential equations are used in the circulation part of the model, and therefore a steady state is assumed.

In order to investigate this assumption, two submodels were created, comprising of just the circulatory part of the BrainPiglet model, with a fixed blood oxygen concentration. One of these submodels was altered so that a steady state was not assumed. To do this, two model equations were replaced with differential equations. First, to represent the time course of changes in arterial radius, Equation D.97 ( $P_1 = (P_{a2} + P_v)/2$ ) was replaced with

$$\frac{dr}{dt} = \frac{G(P_{a2} - 2P_1 + P_v)}{K_r r} \quad (5.7)$$

where  $K_r$  is a constant of proportionality between arterial volume and radius

$$K_r = \frac{V_{a,n} V_{\text{blood},n}}{r_n^2} \quad (5.8)$$

where  $V_{a,n}$  is the normal arterial volume as a fraction of total blood volume, and  $V_{\text{blood},n}$  is the fraction of brain volume which is blood. The second differential equation describes how venous pressure changes with time

$$\frac{dP_v}{dt} = \frac{2G(P_1 - P_v) - G_v(P_v - P_{vs})}{C_v V_{\text{blood},n}} \quad (5.9)$$

and replaces Equation D.103:

$$P_v = \frac{G_t}{G_v} (P_a - P_{vs}) + P_{vs}. \quad (5.10)$$

The change in arterial radius for both submodels in response to a step change in pressure is shown in Figure 5.3. There is a small difference between the two, however, since the changes in pressure and other inputs in the data occur over longer time periods, the assumption that the circulation is at steady state is reasonable. However, it should also be noted that the response of the model to changes in pressure also depends on how autoregulation is modelled.

## 5.1.2 Metabolism

In order to simulate measurements from MRS, several metabolic processes were added to the model. The processes that relate to glycolysis, lactate and the TCA cycle are summarized in Figure 5.4. Glycolysis is modelled as a single stage Michaelis-Menten

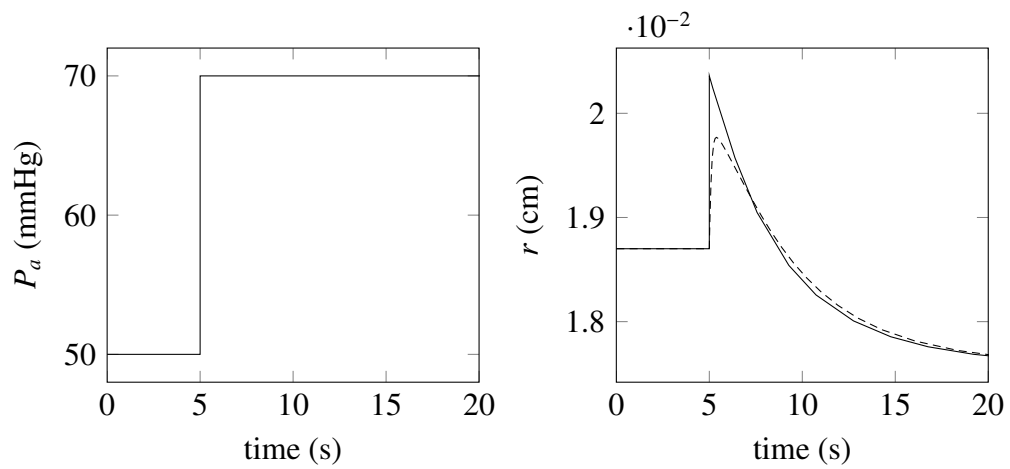


Figure 5.3: Difference in the change in arterial radius between submodels using differential equations (dashed) and the steady state assumption (solid) caused by the step change in arterial pressure shown on the left.

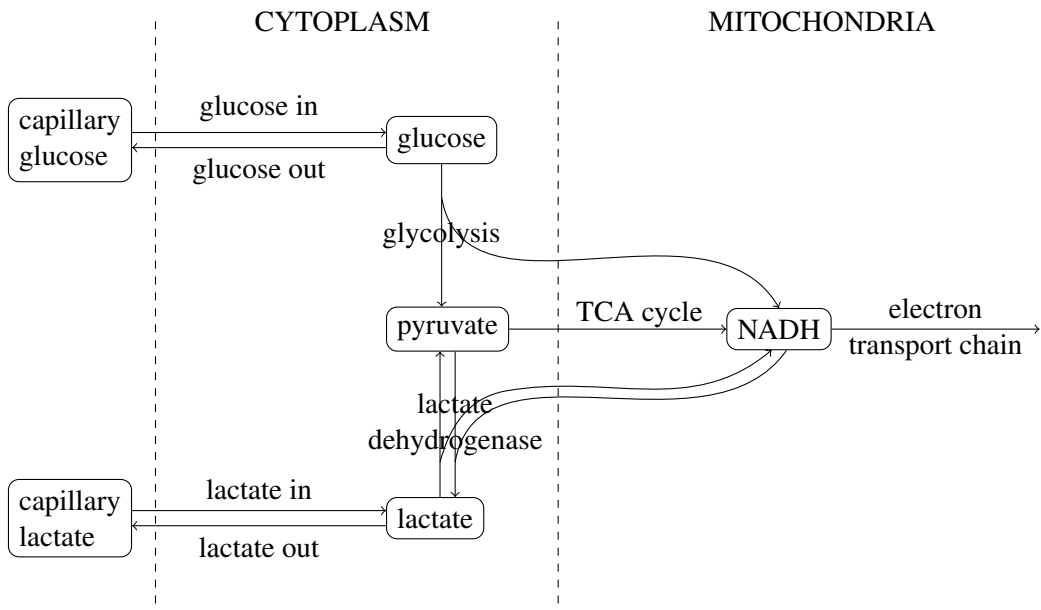


Figure 5.4: Metabolic processes relating to glycolysis, lactate and the TCA cycle

process with a maximum rate  $v_{\text{glyc}}$  which depends on the energy state of the cell and varies as

$$v_{\text{glyc}} = \frac{v_{\text{glyc},n} (I + 1)}{1 + I \frac{[\text{ATP}] [\text{AMP}]_n}{[\text{ATP}]_n [\text{AMP}]}} \quad (5.11)$$

where  $v_{\text{glyc},n}$  is the normal maximum rate, and  $I$  is a parameter which determines how much the rate of glycolysis can change depending on the ATP and AMP concentrations. The normal rate of glycolysis is set to match the normal rate of glucose consumption  $\text{CMR}_{\text{gluc},n}$ . The net rate of glucose transport between the cell and capillaries is given by

$$T_{\text{Gluc}_{\text{in}}} - T_{\text{Gluc}_{\text{out}}} = v_{\text{glut}} \left( \frac{[\text{gluc}_c]}{[\text{gluc}_c] + k_{\text{glut}}} - \frac{[\text{gluc}]}{[\text{gluc}] + k_{\text{glut}}} \right) \quad (5.12)$$

where  $[\text{gluc}]$  is the cytoplasm glucose concentration and  $[\text{gluc}_c]$  is the capillary glucose concentration which is assumed to be constant. The maximum rate  $v_{\text{glut}}$  is set such that the net rate of glucose transport into the cell is equal to  $\text{CMR}_{\text{gluc},n}$  when the glucose concentration is at its normal value. The parameter  $k_{\text{glut}}$  is an average of the different GLUT transporters found in the brain and is set from [241].

Lactate transport into and out of the cell is modelled in the same way, but also involves the transport of a proton, so that the net rate is

$$T_{\text{Lac}_{\text{in}}} - T_{\text{Lac}_{\text{out}}} = v_{\text{MCT}} \left( \frac{[\text{lac}_c][\text{H}^+]_n}{(k_{\text{MCT}} + [\text{lac}_c])([\text{H}^+]_n + k_{\text{MCT},\text{H}^+})} - \frac{[\text{lac}][\text{H}^+]_{\text{cyt}}}{([\text{lac}] + k_{\text{MCT}})([\text{H}^+]_{\text{cyt}} + k_{\text{MCT},\text{H}^+})} \right) \quad (5.13)$$

where the lactate concentration in the capillaries  $[\text{lac}_c]$  is also assumed to be constant. Transport of lactate between brain cells has been the subject of much recent modelling, owing to the interest in the ANLS [147, 154, 152]. Neurons and astrocytes have different expression of the MCT family members, leading to different  $k_{\text{MCT}}$  [36]. In the BrainPiglet model however, there is no distinction between the two cell types and an intermediate value for  $k_{\text{MCT}}$  is used. The maximum rate of lactate transport  $v_{\text{MCT}}$  is calculated from the normal cerebral rate of lactate consumption  $\text{CMR}_{\text{lac}}$ . For the model to be at a steady state under normal conditions, the stoichiometry of the reactions requires that

$$\frac{1}{6} \text{CMRO}_{2,n} - \text{CMR}_{\text{gluc},n} = \frac{1}{2} \text{CMR}_{\text{lac},n} \quad (5.14)$$

Satisfying this equation with the chosen values for  $\text{CMR}_{\text{gluc},n}$  and  $\text{CMRO}_{2,n}$  results in a negative value of  $\text{CMR}_{\text{lac},n}$  i.e. lactate is produced in the cytoplasm at baseline conditions and transported into the blood.

The interconversion between pyruvate and lactate is modelled as a mass action reaction, which is fast, and therefore effectively always at equilibrium and has a rate given by

$$T_{\text{PytoLac}} = k_{\text{pl}}[\text{Py}][\text{H}_{\text{cyt}}^+] - k_{\text{pl}}^-[\text{lac}][\text{NAD}_{\text{cyt}}] \quad (5.15)$$

where  $k_{\text{pl}}^-$  is a constant and  $k_{\text{pl}}$  depends on  $[\text{NADH}_{\text{cyt}}]$ . The ratio of the rate constants is set so that under normal conditions the net rate of the reaction is equal to  $\text{CMR}_{\text{lac,n}}$ .

The processes relating to ADP and ATP occurring in the cytoplasm (and mitochondria) are shown in Figure 5.5. The ATP hydrolysis rate has a Michaelis Menten form de-

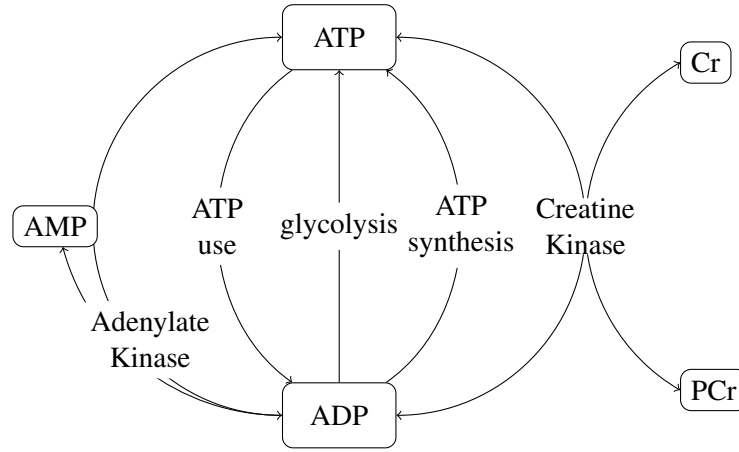


Figure 5.5: Metabolic processes in the cytoplasm and mitochondria relating to ATP use, synthesis and buffering

pending only on ATP concentration. It has a small  $k_M$  so that the rate of hydrolysis does not decrease significantly until ATP levels are low. The maximum rate of ATP use is proportional to the demand  $u$ . ATP is buffered by the creatine kinase reaction and the adenylate kinase reaction which are both modelled as mass action reactions and have rates

$$T_{\text{CK}} = k_{\text{PCr}}[\text{PCr}][\text{ADP}][\text{H}_{\text{cyt}}^+] - k_{\text{PCr}}^-[\text{ATP}][\text{Cr}] \quad (5.16)$$

and

$$T_{\text{AK}} = k_{\text{AK}}[\text{ADP}]^2 - k_{\text{AK}}^-[\text{ATP}][\text{AMP}] \quad (5.17)$$

respectively. Both of these reactions are assumed to be fast compared to other processes and therefore to be effectively at equilibrium at all times.

The malate aspartate shuttle is modelled as a mass action process with a rate given by

$$T_{\text{MAshuttle}} = k_{\text{MAshut}}[\text{H}_{\text{cyt}}^+][\text{NAD}] - k_{\text{MAshut}}^-[\text{NAD}_{\text{cyt}}][\text{H}_{\text{m}}^+] \quad (5.18)$$

where, again, the concentrations of cytoplasmic and mitochondrial NADH are included within the rate parameters.

Unlike the BrainSignals model, the BrainPiglet model simulates cytoplasmic pH. Buffering of  $H^+$  ions in the cytoplasm is modelled in an analogous way to that of the mitochondria (see Equation 2.32) with the same value for  $dpH$  and a slightly higher value for  $C_{\text{buff},c}$  following Korzeniewski and Zoladz [144].

The mitochondrial part of the model has been expanded to include the TCA cycle. The transformation of pyruvate to acetyl-CoA and the whole TCA cycle are combined into a single reaction that consumes one molecule of pyruvate and produces five reducing equivalents which are all assumed to be NADH for simplicity. The rate is given by

$$T_{\text{TCA}} = \frac{v_{\text{TCA}}[\text{Py}][\text{NAD}]}{(k_{m,\text{tcaN}} + [\text{NAD}])(k_{m,\text{tcaP}} + [\text{Py}])}. \quad (5.19)$$

The  $k_m$  values were estimated from the detailed model of the TCA cycle by Wu *et al.* [170]. The  $k_m$  for pyruvate is small, since this model suggests that the TCA cycle rate is not sensitive to pyruvate concentration unless it falls very low. The rate of the TCA cycle is also influenced by ATP and ADP concentrations. However, the main controlling factor is thought to be the NAD/NADH ratio [242].

ATP synthesis takes place in the mitochondria. The transport of ATP and ADP into and out of the mitochondria is not explicitly modelled. The rate of return of protons through Complex V is adjusted from BrainSignals (Equation 2.46) so that

$$\theta = k_{CV} \left( \Delta p + \frac{Z}{n_a} \log \left( \frac{g_p}{g_{p,n}} \right) - \Delta p_{CV0} \right) \quad (5.20)$$

where  $n_a$  is the number of protons required to phosphorylate one ATP, including the proton used in the exchange of ADP and ATP across the mitochondrial membrane, and  $g_p$  is the phosphorylation potential

$$g_p = \frac{([\text{ADP}]/c^\ominus)([\text{P}_i]/c^\ominus)}{([\text{ATP}]/c^\ominus)}. \quad (5.21)$$

This is the equilibrium constant for the hydrolysis of ATP. Equilibrium constants are calculated from thermodynamic activities, which are considered to be dimensionless. If the concentration of a solute is low (as they are in this case) the activity is given by the solute concentration divided by a standard concentration  $c^\ominus$  (1 M). Therefore,  $g_p$  is a dimensionless quantity, and is calculated in the BrainPiglet model by

$$g_p = \frac{[\text{ADP}][\text{P}_i]}{(1000 \text{ mM}) [\text{ATP}]}. \quad (5.22)$$

where the factor of 1000 arises because the concentrations are given in units of mM rather than M. The Gibbs free energy of ATP hydrolysis  $\Delta G$  is calculated by

$$\Delta G = \Delta G^\circ + ZF \log(g_p) \quad (5.23)$$

where  $\Delta G^\circ$  is the standard Gibbs free energy of ATP hydrolysis and  $F$  is the Faraday constant. The protonmotive force at which there would be no net flow of protons is given by

$$\Delta p_{CV0} = \frac{-\Delta G_n}{n_a F} \quad (5.24)$$

where  $\Delta G_n$  is the normal value of  $\Delta G$ . Finally, ATP is synthesised in the mitochondria by Complex V at a rate of

$$T_{ADPtoATP} = \frac{L_{CV} V_{mit}}{n_a}. \quad (5.25)$$

## 5.2 Steady state simulations

Figure 5.6 shows the results of steady state simulations for a varying oxygen saturation in the model, with all other parameters at their default values. As expected, as  $SaO_2$  decreases, both CBF and CBV (shown as total blood volume as a fraction of its normal value  $V_t/V_{t,n}$ ) increase. There is a slight decrease in  $CMRO_2$  and a drop in  $\Delta oxCCO$ . The concentration of PCr decreases whilst the concentration of ATP remains constant, showing the expected buffering relationship. Lactate concentration increases as  $SaO_2$  decreases.  $SaO_2$  is not reduced below 50% because at lower  $SaO_2$  lactate continues to build up in the cells and no steady state is reached. This is because the rate of lactate production exceeds the maximum rate at which it can be transported out of the cells.

The points on the plots are experimental values taken from Tsuji *et al.* [125] showing how CCO oxidation and PCr and ATP concentrations change with  $SaO_2$ . These should be compared with the model predictions with caution since the piglets were one month old, and the periods of hypoxia used were only brief. Also  $P_aCO_2$  and MABP were not held constant. Each of the eight piglets were subjected to brief hypoxic periods with increasing severity. The PCr and ATP concentrations (measured by MRS) are given as percentage decreases, and here are multiplied by the normal model concentrations for comparison. The  $\Delta oxCCO$  changes were given in  $\mu M$  multiplied by the differential path length factor (DPF). Here they have been converted to  $\mu M$  by using the DPF for human infant brains of 4.39 quoted in the paper. The experimental values show a different shape than the model prediction, with CCO not becoming reduced until  $SaO_2$  is around 60%. This difference is discussed further in the following section.

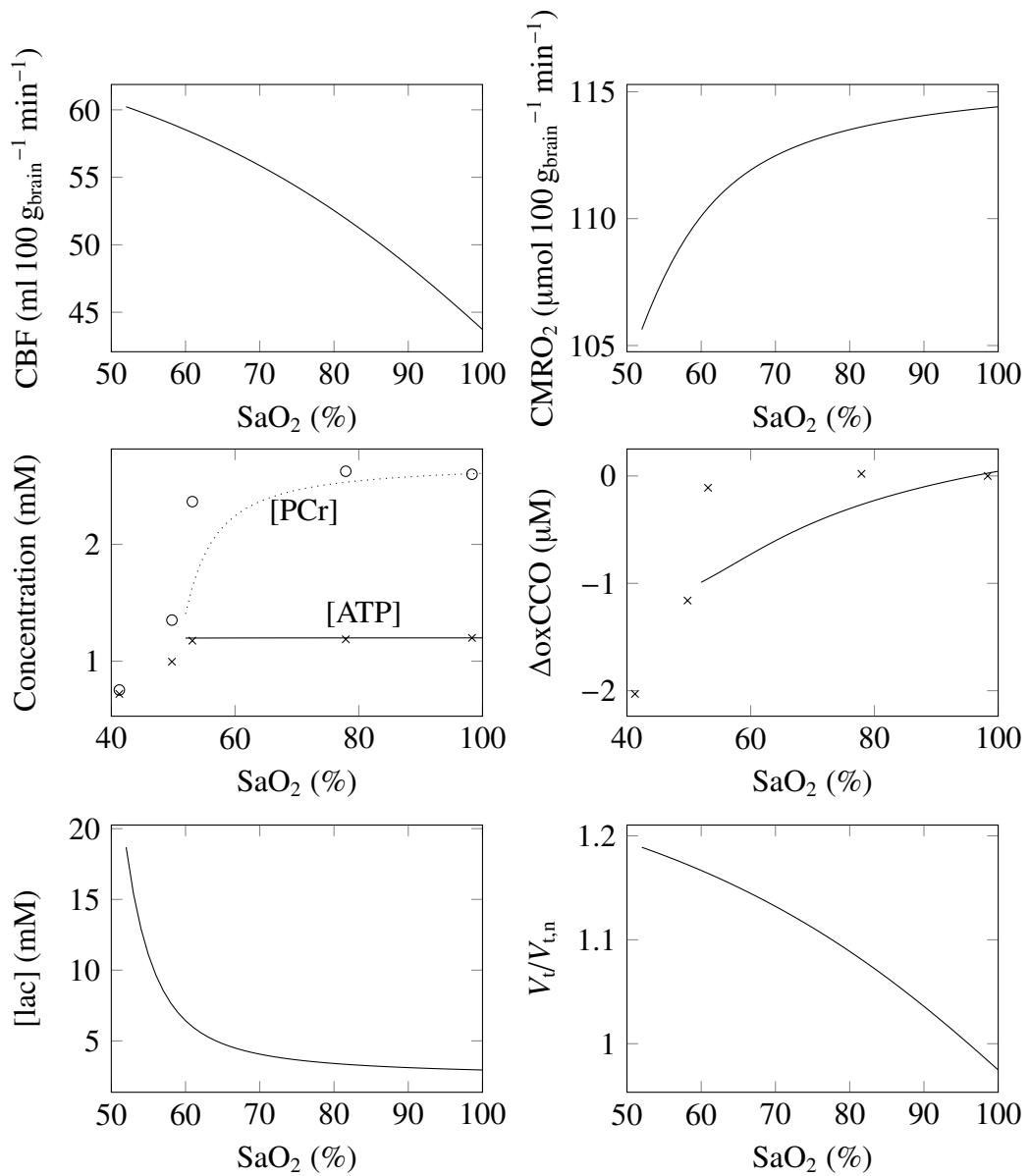


Figure 5.6: Steady state plots vs arterial oxygen saturation for the BrainPiglet model. The points show experimental values taken from Tsuji *et al.* [125].

Modelled CBF and CBV as a function of  $P_a$  are shown in Figure 5.7. The shape of the autoregulation curve is not significantly changed from the BrainSignals model, but the position of the plateau is shifted to the normal blood pressure of the piglet. Experiments investigating autoregulation in piglets have found CBF remains constant in the range 50–80 mmHg [243, 244, 245]. The model shows a smaller range of blood pressure over which constant CBF is maintained.

The points in Figure 5.7 are experimental data taken from Chemtob *et al.* [244] showing the variation of CBF with MABP. Eight newborn piglets were subjected to one episode of hypertension and one of hypotension. CBF was measured using microspheres. The results show a similar pattern to that predicted by the model, but the position and value of the plateau are different. The piglets in this experiment had significantly higher baseline MABP (73 mmHg) and CBF ( $92 \text{ ml } 100 \text{ g}_{\text{brain}}^{-1} \text{ min}^{-1}$ ) than the model values (see Table 5.1) making it hard to compare with the model. Differences may be caused by differences in experimental protocol and anaesthesia.

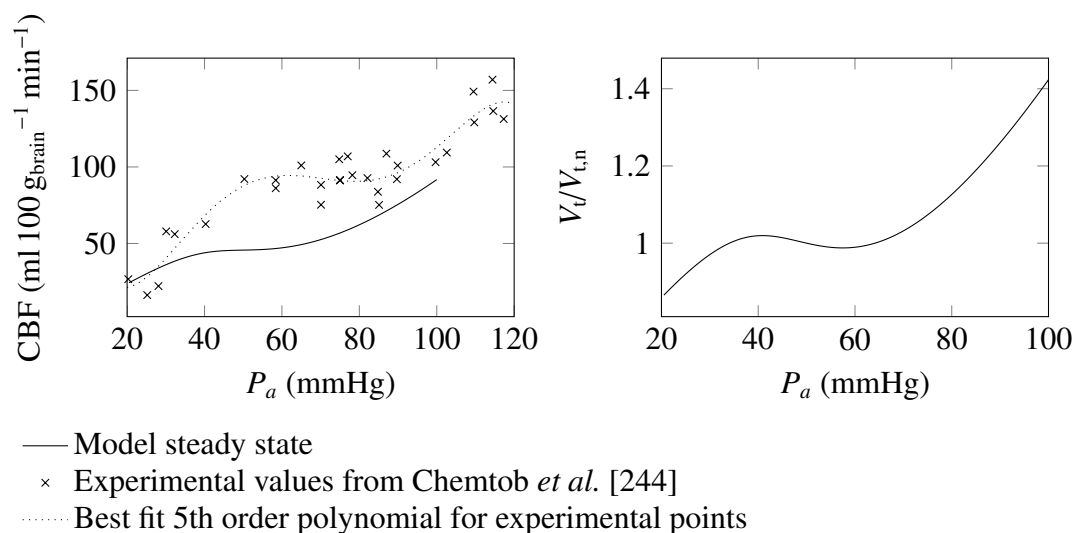


Figure 5.7: CBF and  $V_t/V_{t,n}$  vs  $P_a$  for steady state simulations. It should be noted that the piglets in the experiment from which the data in the left plot were taken had a higher baseline blood pressure than the model and in the experimental data with which it is later compared in detail.

Figure 5.8 shows modelled CBF and CBV as a function of  $P_a\text{CO}_2$ . The points show experimental values taken from Brown *et al.* [246]. Six newborn piglets were subjected to either one period of hypercapnia, one of hypocapnia, or one of each. CBF was measured using NIRS methods. A mean reactivity of  $1.4 \text{ ml } 100 \text{ g}_{\text{brain}}^{-1} \text{ min}^{-1} \text{ mmHg}^{-1}$  was found. This is higher than the  $0.75 \text{ ml } 100 \text{ g}_{\text{brain}}^{-1} \text{ min}^{-1} \text{ mmHg}^{-1}$  predicted by the model. The baseline CBF of the piglets in this experiment was lower than the value chosen for the model. The experimental datasets compared with the model in detail in

the next two chapters do not include  $P_a\text{CO}_2$  changes, and therefore  $\text{CO}_2$  reactivity is not considered further.

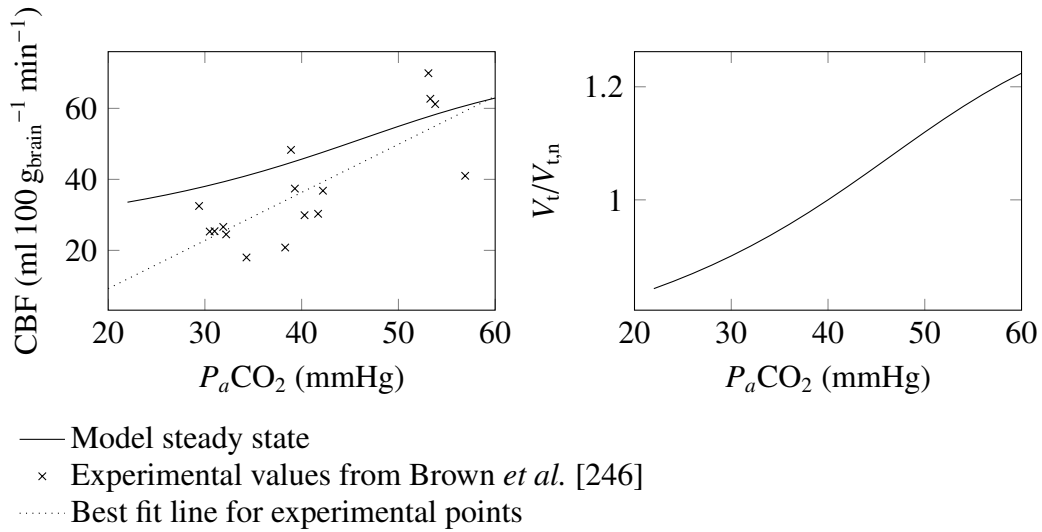


Figure 5.8: CBF and  $V_t/V_{t,n}$  vs  $P_a\text{CO}_2$  for steady state simulations.

In general, comparison of steady state simulations with experimental data is difficult, since there are limited data available for newborn piglets. Also, it is difficult to keep other systemic values constant when performing this type of experiment, and anaesthesia may affect the results.

## 5.3 Modelling anoxia

The application of the model to data from an anoxia study in newborn piglets is now described.

### 5.3.1 Methods

The experimental data were taken from a publication in 2000 by Springett *et al.* [247]. The experiment involved subjecting six newborn piglets to brief periods of anoxia. The piglets were anaesthetised with isoflurane and artificially ventilated. Their  $\text{FiO}_2$  was reduced from 40% to 0% for 105 s. After returning  $\text{FiO}_2$  to 40% for 10 min, the anoxia was repeated six times for each piglet. MABP was monitored throughout, and continuous NIRS and  $^{31}\text{P}$ -MRS measurements were recorded.

The data were presented in the publication [247] as plots which are shown in Figure

5.9. The left figure (Figure 1 in the paper) shows the results from one piglet, described by the authors as typical, averaged over all anoxias. The right figure (Figure 2 in the paper) shows the results averaged over all anoxias for all piglets. The average MABP was extracted from the left figure, since the MABP averaged over all piglets was not available, and this was used as an input to the model.  $S_aO_2$  was also used as an input. This was estimated from the experimental protocol as no measurements were available.  $CO_2$  levels were not reported during the challenge, and were assumed to remain constant. The model inputs are shown in Figure 5.10. The NIRS and MRS measurements were extracted from the plots on the right of Figure 5.9 and compared with the model outputs.

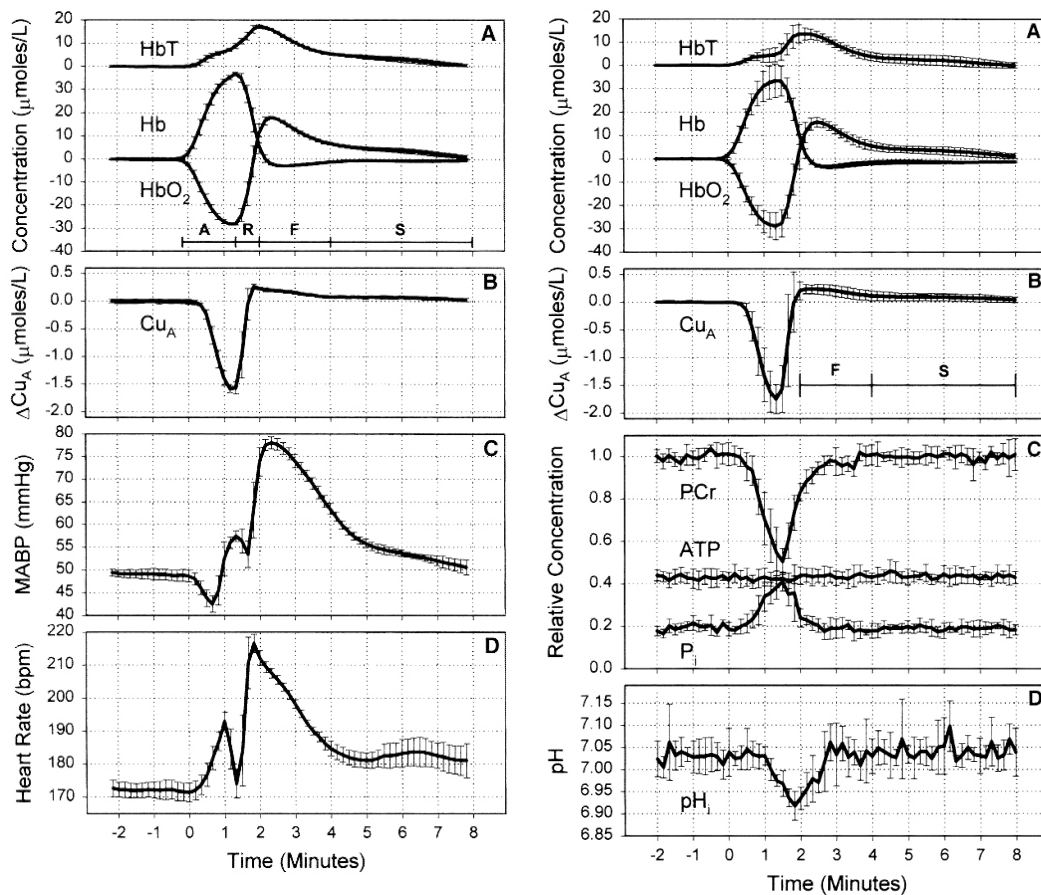


Figure 5.9: Plots from Springett *et al.* [247] showing results averaged over six anoxias from left: one piglet and right: six piglets. The periods marked are defined by the authors as A) anoxia R) reoxygenation F) fast recovery phase and S) slow recovery phase. In the top graphs HbT is offset for clarity.

The experimental results showed a decrease in  $\Delta HbO_2$  and an increase in  $\Delta HbT$  during anoxia. Immediately after anoxia, there was an increase in  $\Delta HbT$  indicating an increase in CBF. There was a reduction of  $Cu_A$  (a drop in  $\Delta oxCCO$ ) during anoxia and a small hyperoxidation upon reoxygenation. The MRS results showed a decrease in PCr con-

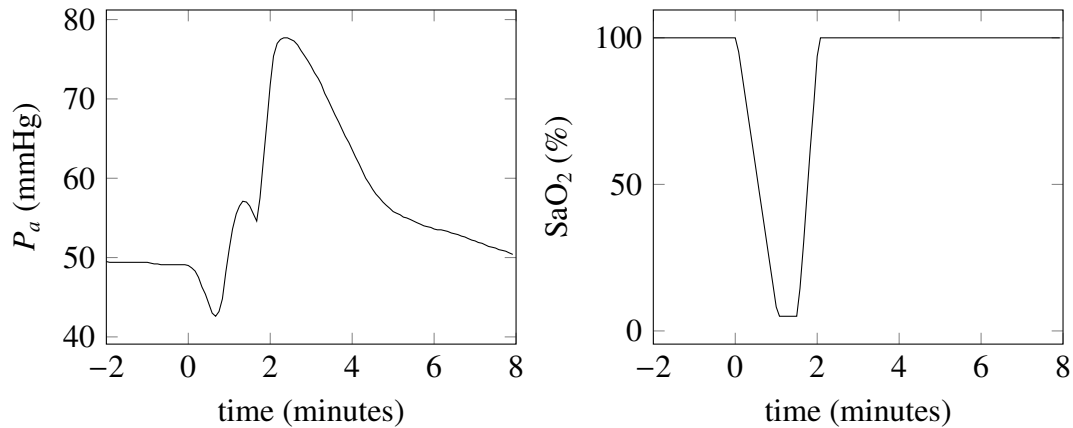


Figure 5.10: Arterial blood pressure and arterial oxygen saturation used as model inputs to simulate anoxia [247]. Blood pressure was taken from the measurements from one typical piglet (see Figure 5.9).  $S_aO_2$  was estimated from the experimental protocol.

centration and an increase in  $P_i$  concentration, but no changes in ATP concentration were seen.

### 5.3.2 Results

The results of the simulations, with all the parameters set to their default values, are compared with the measured results in Figure 5.11. The model matches the direction of change for all the measurements, however there are some differences between the magnitudes of the changes, particularly for PCr and  $P_i$ . From a knowledge of the model, and the relevant physiology, four model parameters were changed to improve the simulations: these are listed in Table 5.2. Each was chosen to improve a specific aspect of the simulations.

Parameter	Default Value	Changed Value
$[PCr]_n/[P_i]_n$	1.5	2.7
$I$	3	50
$k_{aut}$	1.0	0.5
$[NAD]_n/[NADH]_n$	9.0	1.5

Table 5.2: Parameters that were changed to improve the simulations of anoxia.

- To improve the simulation of the overshoot of  $\Delta HbO_2$  following anoxia, the autoregulation capacity in the model was decreased by reducing the parameter  $k_{aut}$  from 1.0 to 0.5. After this change, the maximum venous volume increase was approximately 45%. The improvement in the simulation of  $\Delta HbT$  is shown in

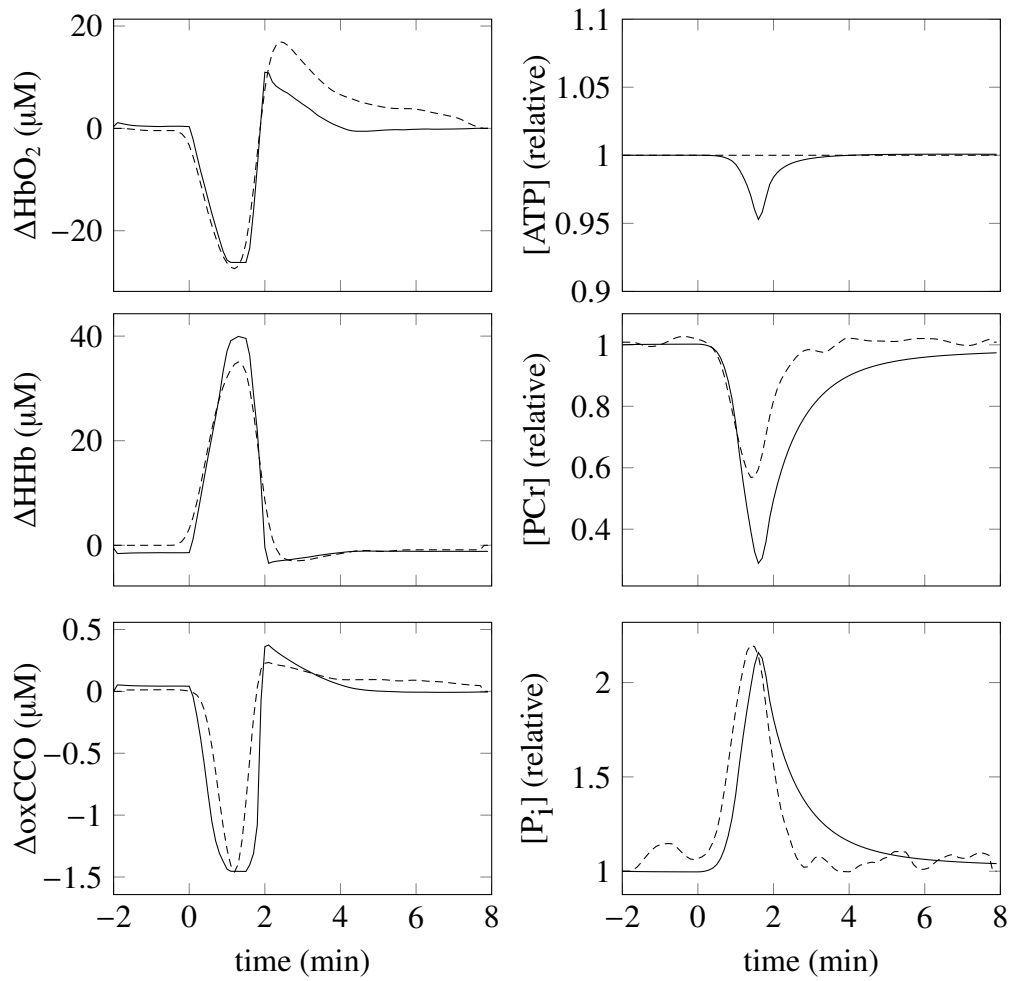


Figure 5.11: Model simulations (solid line) compared with measurements (dashed line) from (left) NIRS and (right) <sup>31</sup>P-MRS during anoxia in piglets. The measured results are taken from Springett *et al.* [247] and the simulations were carried out with all model parameters set to their default values

Figure 5.12. The effect of changing  $k_{\text{aut}}$  on autoregulation in the model is also shown.

- To reduce the magnitude of the drop in simulated [PCr], the glycolysis rate was made more sensitive to changes in AMP and ATP concentration by increasing the parameter  $I$  from 3 to 50. This resulted in an approximately sevenfold increase in glycolysis rate during anoxia which reduced the drop in [PCr] during anoxia from 75 % to 45 %
- To correctly simulate the magnitude of the change in  $[P_i]$ , the ratio of normal concentrations  $[PCr]_n/[P_i]_n$  was increased from 1.5 to 2.7. In the model, if [ATP] is constant, changes in [PCr] and  $[P_i]$  are equal and opposite (ignoring AMP which is present only at small concentrations). The experimental results therefore require the ratio  $[PCr]_n/[P_i]_n$  to be 2.7. With this ratio, the model will accurately simulate the  $P_i$  measurement, providing PCr is accurately simulated.
- To decrease the rate of reduction of CCO, the normal ratio  $[NAD]_n/[NADH]_n$  was decreased from 9 to 1.5. This resulted in a slower drop of simulated  $\Delta\text{oxCCO}$ .

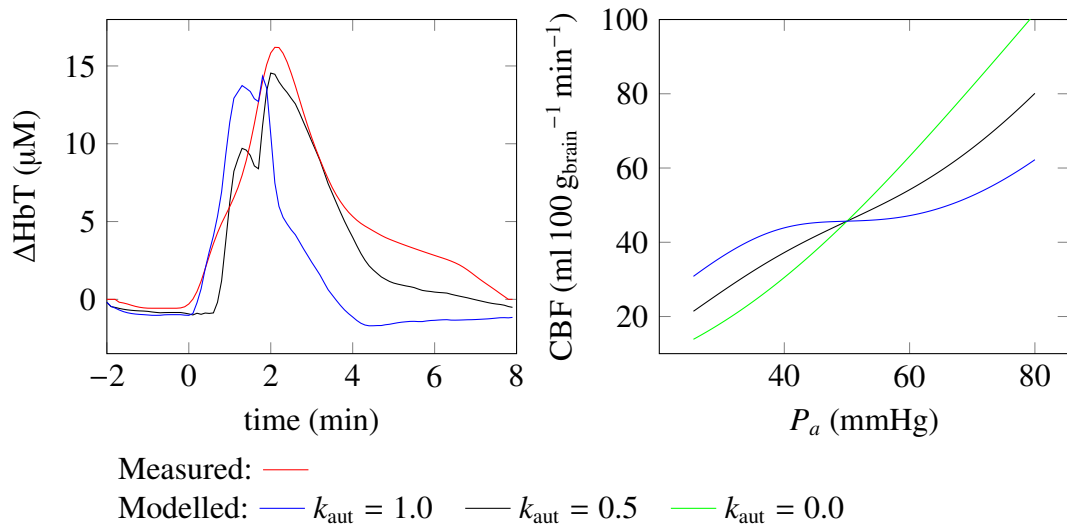


Figure 5.12: Effect of varying  $k_{\text{aut}}$  with other parameters set to the values show in Table 5.2. Left: Modelled and measured  $\Delta\text{HbT}$  vs time and right: Modelled steady state CBF vs arterial blood pressure.

The comparison between modelled and measured results after these parameter changes is shown in Figure 5.13. It can be seen that the modelled results matched the measured results more closely, and there are improvements in the aspects listed above. The plausibility of these parameter changes based on evidence from the literature is considered in the discussion. The modelled lactate concentration is shown in Figure 5.14 and shows a rise in lactate during anoxia as expected.

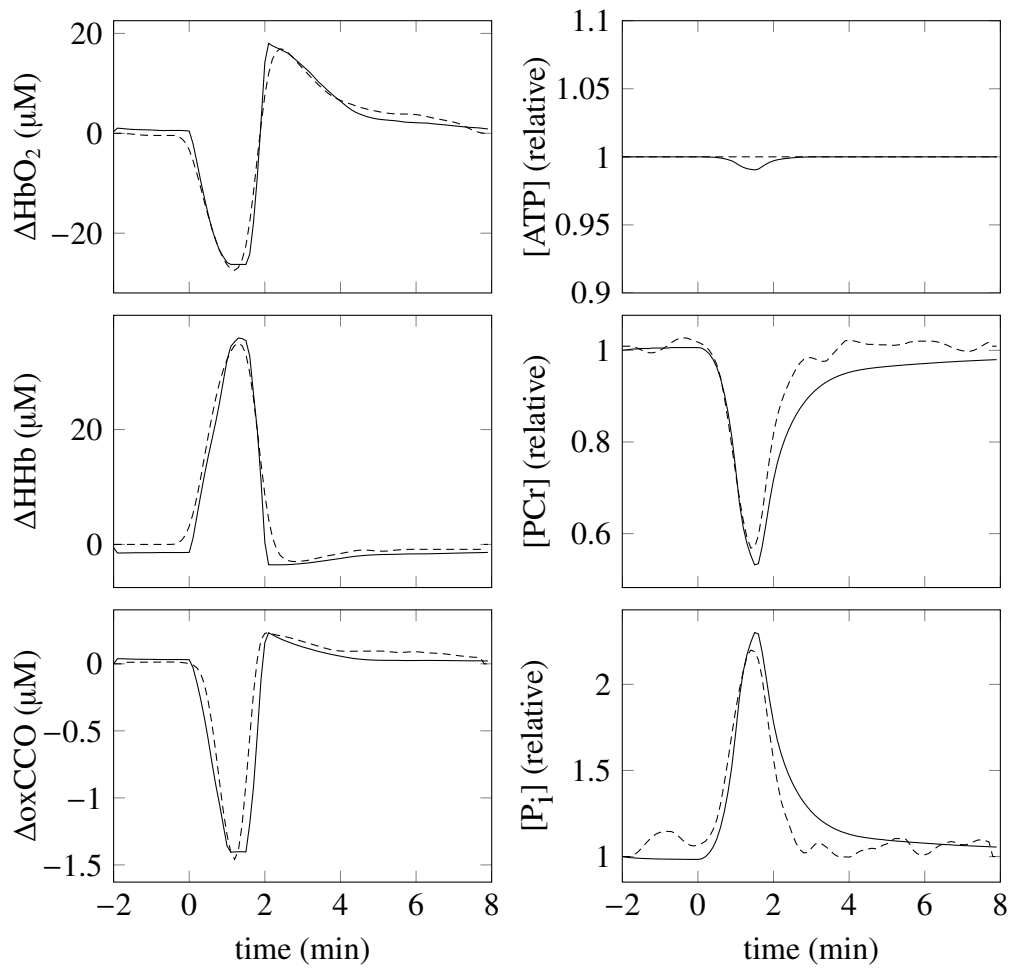


Figure 5.13: Model simulations (solid line) compared with measurements (dashed line) from (left) NIRS and (right)  $^{31}\text{P}$ -MRS during anoxia in piglets. The measured results are taken from Springett *et al.* [247] and the simulations were carried out with the parameter changes shown in Table 5.2

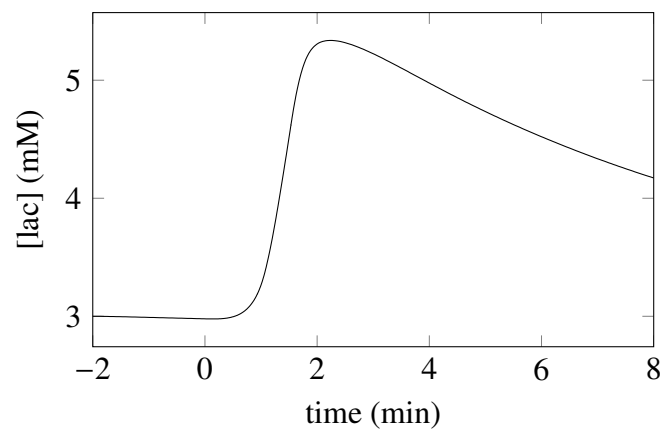


Figure 5.14: Modelled lactate concentration during anoxia with parameter values shown in Table 5.2

The effect of the parameter changes on the steady state behaviour of the model is shown in Figures 5.15, 5.16 and 5.17. The reduction in autoregulation causes a reduced increase in CBF and CBV as SaO<sub>2</sub> drops. It also leads to smaller changes in CBF and CBV with changing CO<sub>2</sub>, but larger changes with changing arterial pressure. A reduction in SaO<sub>2</sub> causes CMRO<sub>2</sub> to fall. This fall is greater for the changed parameter values. This is partly caused by the reduced oxygen delivery from the lower autoregulation and consequently smaller CBF. However, there is a greater effect from the reduction in [NAD]<sub>n</sub>/[NADH]<sub>n</sub>. As SaO<sub>2</sub> falls, the reduced oxygen concentration at the mitochondria causes CMRO<sub>2</sub> to fall. This is somewhat counteracted by the build-up of electrons in the transport chain and build-up of NADH giving an increased concentration of cyt a<sub>3,r</sub>. The effect is smaller when [NAD]<sub>n</sub>/[NADH]<sub>n</sub> is lower because the increase in NADH has a smaller effect on the first reaction in the electron transport chain (Equation D.28) and therefore, the drop in CMRO<sub>2</sub> is greater. For the same reason, CCO becomes less reduced when [NAD]<sub>n</sub>/[NADH]<sub>n</sub> is lower. A larger drop in CMRO<sub>2</sub> also causes a larger drop in PCr concentration and a larger increase in lactate concentration. Increasing the parameter *I* leads to a smaller drop in PCr concentration in the dynamic simulation by increasing the rate of glycolysis. However, this only has an effect once PCr is depleted enough for the ATP concentration to begin to fall, at arterial saturations lower than 50 %.

Following these parameter changes, the model's simulations of changes in ΔoxCCO were further investigated. The model did not replicate the delay between the onset of anoxia and the reduction of Cu<sub>A</sub> which was seen in the measurements. In order to investigate this, and also to explore the hyperoxidation seen following anoxia, which is seen in the measurements but is not well understood, the model was further altered. Initially, the equation representing the transfer of electrons to oxygen was changed from its original form (Equation 2.43) to

$$f_3 = k_3 \text{cyt a}_{3,r} \frac{[\text{O}_2]}{[\text{O}_2] + k} (k + [\text{O}_2]_n) \left( \frac{e^{-c3(\Delta p - \Delta p_{30})}}{1 + e^{-c3(\Delta p - \Delta p_{30})}} \right). \quad (5.26)$$

This form was chosen to create a Michaelis-Menten relationship between oxygen and CMRO<sub>2</sub>. This is a simplification because the reaction is not a single enzyme-catalysed reaction. The effective *k<sub>M</sub>* for oxygen *k* was set to 5 μM. By choosing this value for *k*, which is much lower than the normal value for [O<sub>2</sub>] of 0.0240 mM, the rate of the reaction remains high until [O<sub>2</sub>] is low. This would therefore be predicted to delay the drop in ΔoxCCO. The model was then further changed such that there was no dependence of ATP synthesis rate on the phosphorylation potential by replacing *g<sub>p</sub>* with its normal

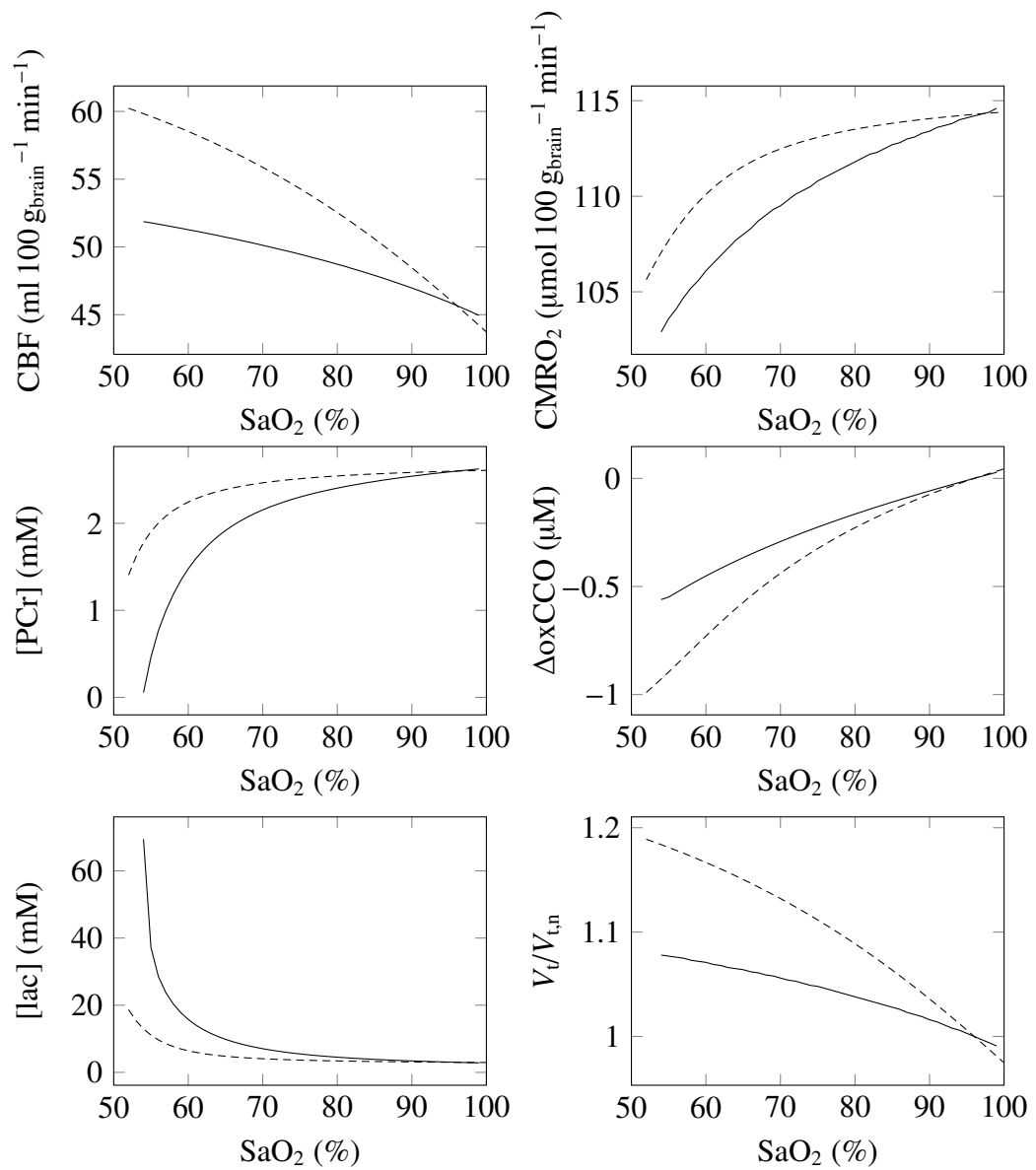


Figure 5.15: Steady state plots vs arterial oxygen saturation for the BrainPiglet model with default parameter values as in Figure 5.6 (dashed) and parameter changes as in Table 5.2 (solid).

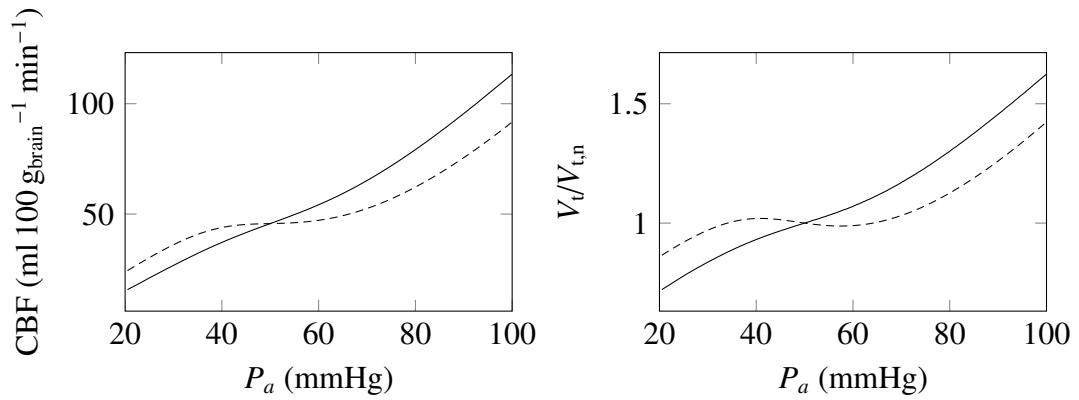


Figure 5.16: CBF and  $V_t/V_{t,n}$  vs  $P_a$  for steady state simulations with the BrainPiglet model using default parameter values as in Figure 5.7 (dashed) and parameter changes as in Table 5.2 (solid).

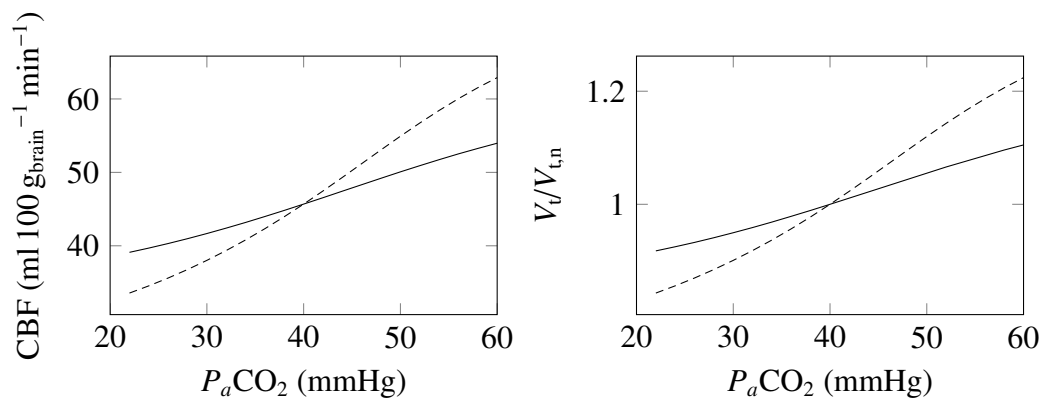


Figure 5.17: CBF and  $V_t/V_{t,n}$  vs  $P_a\text{CO}_2$  for steady state simulations with the BrainPiglet model using default parameter values as in Figure 5.8 (dashed) and parameter changes as in Table 5.2 (solid).

value in Equation 5.20 such that

$$\theta = k_{CV} (\Delta p - \Delta p_{CV0}). \quad (5.27)$$

The results of these changes are shown in Figure 5.18. When Equation 5.26 is used, the simulation of  $Cu_A$  is significantly improved as  $S_aO_2$  begins to drop (although the simulation is slightly worse at lower  $S_aO_2$ ). Also, the magnitude of hyperoxidation of  $Cu_A$  during recovery is decreased. When, in addition, the dependence of ATP synthesis rate on phosphorylation potential is removed, no hyperoxidation is seen.

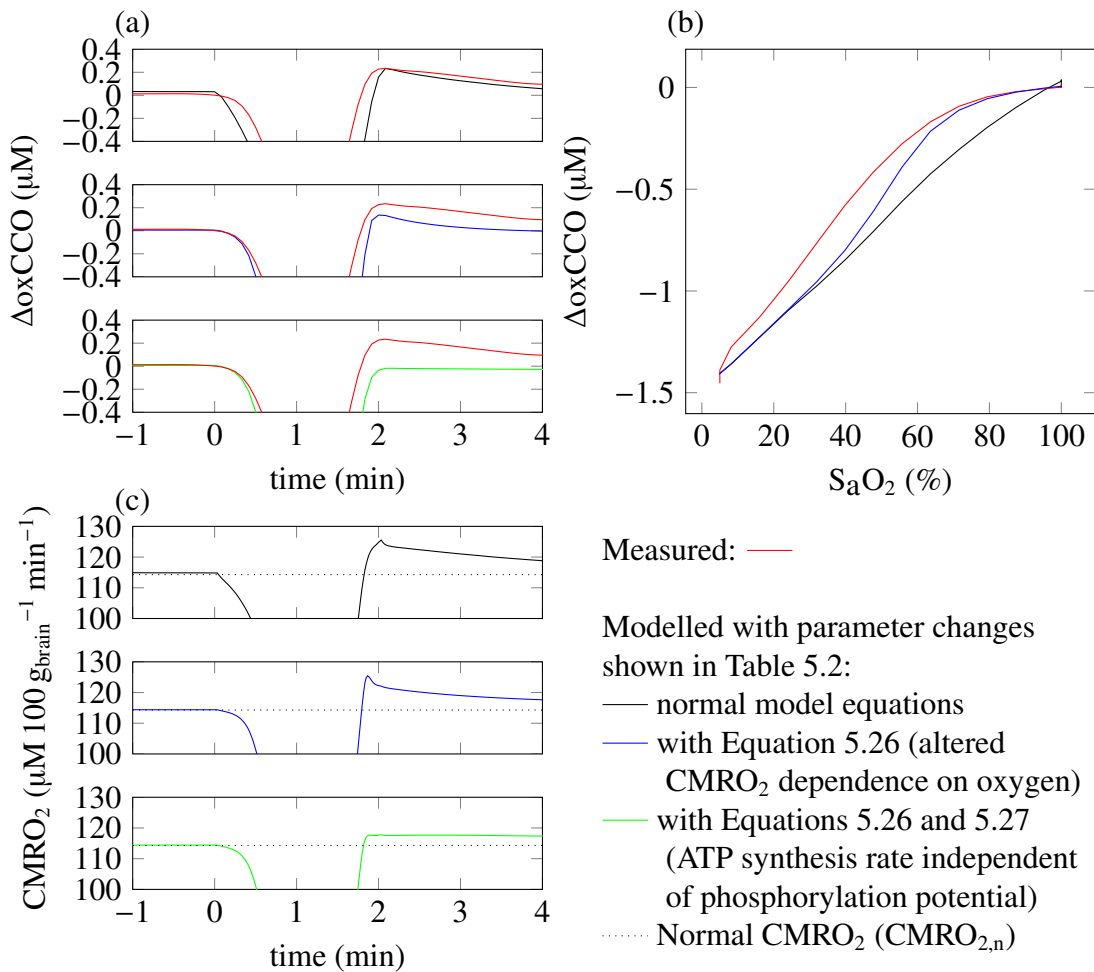


Figure 5.18: (a) Comparison of measured  $\Delta oxCCO$  and modelled  $\Delta oxCCO$  vs time. (b) Comparison of measured and modelled  $\Delta oxCCO$  vs oxygen saturation at the onset of anoxia. (c) Modelled  $CMRO_2$

### 5.3.3 Discussion

The model was applied successfully to simulate oxygenation and metabolic changes in the brains of newborn piglets during anoxia. It correctly predicted no significant changes in ATP concentration throughout the experiments. To simulate the other measured signals, changes to the original model were required. These changes offer an insight into the physiological interpretation of the experimental results as discussed below. In addition, the model allows predictions of variables that are more difficult to measure, including  $CMRO_2$  and lactate concentration.

During recovery from anoxia, a large increase in MABP accompanied by an increase in  $\Delta HbO_2$  was measured. As there was not a corresponding reduction in  $\Delta HHb$ , this implies an increase in CBV. The model suggests that this hyperaemia cannot be attributed to changes in the arterial volume alone. A dilation of the cerebral arteries to this extent would be predicted to cause a several-fold increase in CBF, which, unless accompanied by a corresponding increase in  $CMRO_2$ , would lead to a decrease in  $\Delta HHb$  via a washout effect. It is more likely, therefore, that the increased blood volume following anoxia has a significant venous contribution, which is driven by the increase in blood pressure. However, the autoregulation behaviour of the model causes changes in arterial pressure of this magnitude to be damped by changes in arterial resistance before they are felt at the veins. A reduction of the parameter  $k_{aut}$  from 1.0 to 0.5 reduces this cancelling effect, and so led to a better replication of the observed hyperaemia. Previous studies in piglets have found that CBF does not change in the range of 50–80 mmHg [243, 244, 245]. However, these studies used piglets older than 24 h. In one study involving piglets of different ages, it was found that for piglets less than 4 days old, the average change in CBF as blood pressure was varied was  $1.0\% \text{ mmHg}^{-1}$ , whereas for piglets older than 4 d it was  $0\% \text{ mmHg}^{-1}$  [248]. The interpretation of the anoxia measurements using our model suggests that cerebral autoregulation was impaired or not fully developed in these newborn piglets.

The relationship between PCr and ATP concentrations in the model as oxygen saturation falls shows the expected buffering of ATP by PCr, with ATP not decreasing until PCr is low. The model predicts that ATP concentration will begin to decrease when  $S_aO_2$  falls below 40%. However, the model predicted a drop in PCr concentration during anoxia larger than that observed. Increasing the parameter  $I$  allowed a greater increase in glycolysis rate, and therefore a greater rate of ATP synthesis during anoxia. This glycolysis rate could not be sustained for longer anoxias, because the model predicts that glucose is used faster than its maximum rate of transport into the cell. The value of  $I$  was increased from 3 to 50. Above this value, there is almost no further change

in glycolysis rate, because changes in ATP and AMP concentrations become limiting. For large  $I$ , the glycolysis rate in the model increased approximately sevenfold. This is greater than the fivefold increase calculated to occur in foetal rats during ischaemia [249]. It should be noted that the extent of PCr concentration decrease in the model is also sensitive to the normal PCr concentration ( $[PCr]_n$ ).

There are two features of particular interest in the  $\Delta\text{oxCCO}$  experimental results: (i) the delay between the drop in  $\Delta\text{HbO}_2$ , and the reduction of  $\text{Cu}_A$ , and (ii) the hyperoxidation of  $\text{Cu}_A$  during recovery. The former was not reproduced by the model in its original form, but the latter was. It has been observed previously in piglets that  $\text{Cu}_A$  redox state is not affected by mild hypoxia [125]. A similar effect has also been observed in adult rats [67, 250], but not in adult humans [95, 83]. The mechanisms for this effect are unknown, and it does not emerge from the alteration of the BrainSignals model to simulate the neonatal piglet brain. But, when it was introduced directly through the use of Equation 5.26, it improved the simulation of  $\text{Cu}_A$  reduction at the onset of anoxia. As expected, it also decreased the magnitude of  $\text{Cu}_A$  hyperoxidation following anoxia, since this is partly caused by the increased oxygen tension at the mitochondria as a consequence of the increased oxygen delivery. An oxidation is still seen however, because the increased concentrations of ADP and  $P_i$  during and following anoxia increase the rate of ATP synthesis via Equations 2.46 and 5.22. The proton motive force across the mitochondrial membrane is decreased which increases  $\text{CMRO}_2$  and, with the parameter values used, results in an oxidation of  $\text{Cu}_A$ . If this dependency on phosphorylation potential is removed, no oxidation is seen. This supports the suggestion of Springett *et al.* [247] when reporting the experimental results, that the hyperoxidation following anoxia was a result of increased  $\text{CMRO}_2$ . A  $\text{Cu}_A$  hyperoxidation following anoxia was also observed in an earlier study [251]. The authors suggest that a pH drop could be partly responsible for the oxidation via a direct effect of pH on  $\text{Cu}_A$ . There is no mechanism for this effect in the BrainPiglet model, although a small change in pH was observed following anoxia, as measured by MRS.

Another possible explanation for the oxidation is a decrease in the substrate supply to the TCA cycle. Our model suggests the opposite is true for pyruvate, whose concentration increased during anoxia, and takes several minutes to return to normal (see Figure 5.19). However, there is an decrease in NAD/NADH ratio (also shown in Figure 5.19) which will tend to decrease the rate of the TCA cycle; but this appears to have only a small effect on the oxidation of  $\text{Cu}_A$ . The normal NAD/NADH ratio does however have a significant effect on the rate of reduction of  $\text{Cu}_A$  as illustrated in Figure 5.20. Although changes in mitochondrial NADH concentration can be measured by fluorescence, the NAD/NADH ratio is difficult to measure *in vivo* [252]. Estimates of this ratio differ, for

example in rat liver cells a ratio of 5–10 was measured [253], but in myocytes isolated from newborn piglets a ratio of 1.2 was found [254]. A decrease in the model's normal NAD/NADH ratio from 9 to 1.5 led to the simulated rate of  $\Delta\text{oxCCO}$  fall matching the experimental rate. However, there are other factors that affect this rate, including the form of the TCA cycle rate dependence on NAD/NADH ratio, and the sensitivity of the reactions of the electron transport chain to changes in the proton gradient.

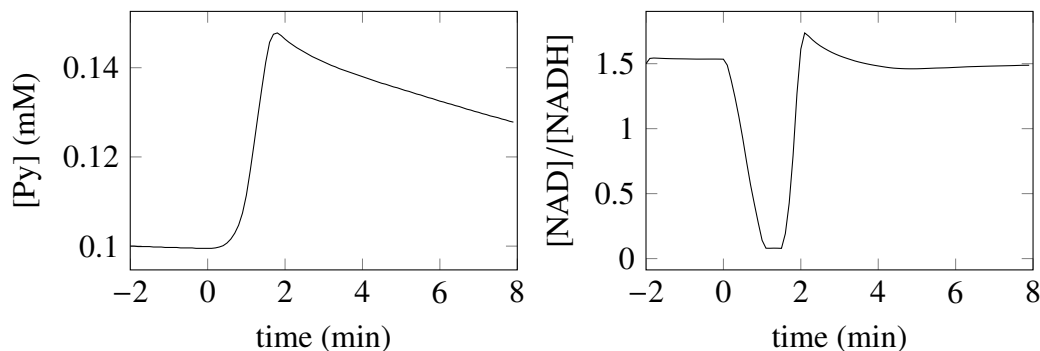


Figure 5.19: Modelled pyruvate concentration and  $[\text{NAD}]/[\text{NADH}]$  during anoxia.

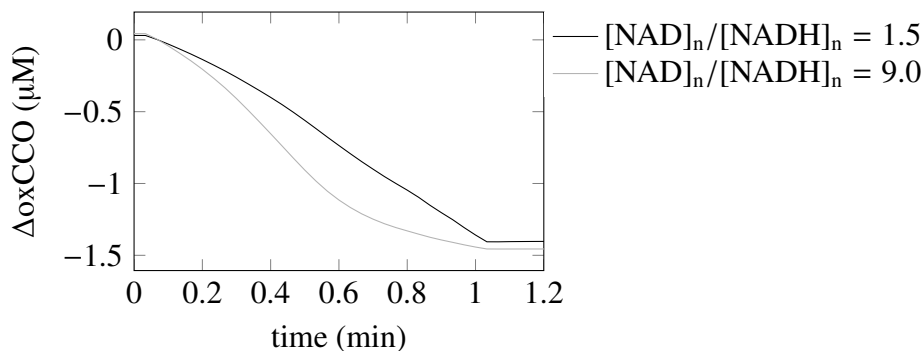


Figure 5.20: Reduction of modelled  $\Delta\text{oxCCO}$  during anoxia with parameter values as in Table 5.2 (except  $[\text{NAD}]_n/[\text{NADH}]_n$  with values as shown).

## 5.4 Conclusions

This work was the first step towards modelling oxygen deprivation in the neonatal piglet brain, and has been published [236]. The model was able to reproduce the experimental data well. This required assuming a reduced autoregulation capacity, a hypothesis which could be tested experimentally. The model was also used to confirm that an increased ADP concentration could lead to hyperoxidation of CCO following anoxia. In this chapter, model parameters were chosen and altered based on consideration of the model structure and the physiological quantities represented by the parameters. Numerical parameter optimisation was not used because only one averaged dataset was

available, and the  $S_aO_2$  measurement used as an input was only an estimate. In the following chapter, datasets from individual piglets subjected to HI are modelled, and sensitivity analysis and parameter optimisation are carried out. This is the next step in validating the model for simulating oxygenation and blood flow changes in newborn piglets.

# Chapter 6

## Hypoxia-ischaemia in piglets

This chapter concentrates on the modelling of HI. Some of this work has been published [255]. First, the results of a Morris sensitivity analysis on the BrainPiglet model are presented. Then the steady-state behaviour of the model when simulating carotid artery occlusion is reported. The model is then applied to data from individual piglets subjected to HI. The model is compared to data from NIRS and both H-MRS and  $^{31}\text{P}$ -MRS. The fit of the model to the data is investigated and improved by using sensitivity analysis and parameter optimisation tools. Finally, failure of some of the piglets to recover is investigated by simulating cell death.

### 6.1 Sensitivity analysis

Sensitivity analysis was used to identify the settable parameters that have the most important effect on the model outputs. A Morris sensitivity analysis was carried out using an 8 level grid with an  $m_{\Delta}$  of 4 (see Section 3.4). The parameter ranges were set at  $\pm 20\%$  of the model value for all parameters. This range was then increased as appropriate in cases where the parameter had been set heuristically, or was known to have a large uncertainty. The ranges of some parameters were also adjusted because they were intended to fall within a specific range e.g. 0–1. Several parameters were excluded, either because they are accurately known physical constants such as the Faraday constant  $F$ , or because their sensitivity index was not of interest, such as the offset of the NIRS signals. In total, 99 parameters were included in the sensitivity analysis. The ranges used for each parameter are given in Section D.6. The number of repeats used was 2000 which gave a total of 200 000 simulations.

Simulations were run using the BrainPiglet model as described in the previous chapter. The parameters were set to their chosen values, and the model run for 1000 s. The outputs were taken at the final point of the simulation and used to calculate the  $\mu^*$  values. This gives a measure of the sensitivity of the steady state of the model to the parameter values. It should be noted that there are several parameters which do not affect the steady state of the model, for example the rates of the mass action reactions which are at equilibrium (e.g.  $t_{1/2,PCr}$ ) and the time constants controlling the delay between changes in input parameters and their effect on circulation (e.g.  $\tau_{O_2}$ ). The sensitivity of the dynamics of the model to parameter values can be investigated in many different ways, and the results will depend on the particular aspect being investigated. Some aspects will affect the fit of the model to HI data, and will therefore influence the sensitivity analysis in Section 6.4.2. But in this section, the steady states of the model are investigated. This is of interest since most aspects of the model reach steady state fairly quickly relative to the time scales of interest in the simulations, although lactate dynamics is a notable exception to this.

Figure 6.1 shows the results of this sensitivity analysis for the model output of [ATP]. It can be seen that many of the parameters have small  $\mu^*$  values. The normal ATP concentration  $[ATP]_n$  has a much larger  $\mu^*$  value than the other parameters. Around 70 % of the parameters have a  $\mu^*$  of less than 1 % and 97 % have  $\mu^*$  less than 10 % of that of  $[ATP]_n$ . This parameter also has a smaller  $\sigma$  value relative to its  $\mu^*$  compared with the other parameters, and therefore has a more linear effect on the value of ATP.

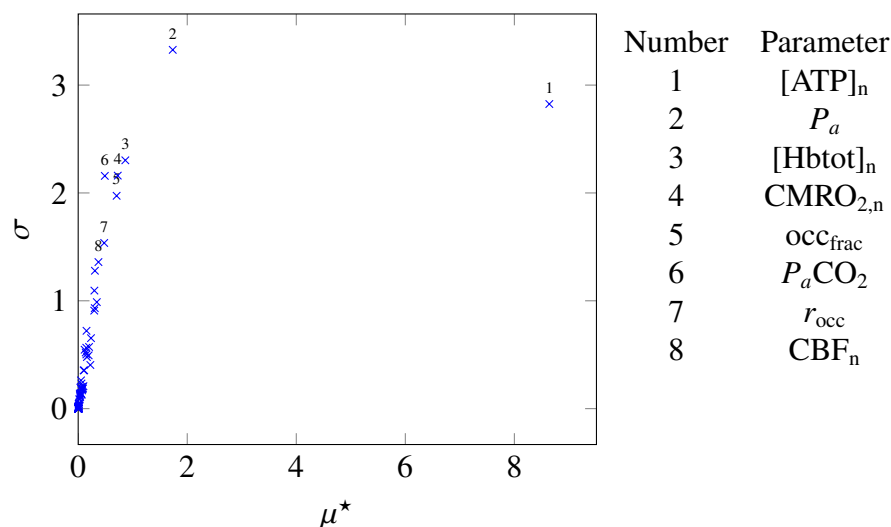


Figure 6.1:  $\mu^*$  vs  $\sigma$  for [ATP] in steady state simulations.

The  $\mu^*$  values were normalised for each variable, and those parameters with normalised  $\mu^*$  greater than 0.2 are shown in Table 6.1. It can be seen that the parameters which are generally used as inputs have the largest effects on the outputs. The two parameters

	$\Delta\text{HbO}_2$	$\Delta\text{HHb}$	$\Delta\text{oxCCO}$	[lac]	[ATP]	[PCr]	[P <sub>i</sub> ]
SaO <sub>2</sub>	1.00	1.00	1.00	0.55		0.34	
P <sub>a</sub>	0.96	0.46	0.29	0.49	0.20	0.38	
[Hbtot] <sub>n</sub>	0.60	0.60	0.29	0.24			
k <sub>aut</sub>	0.72	0.23					
r <sub>occ</sub>	0.59						
r <sub>n</sub>	0.48						
P <sub>a,n</sub>	0.31						
V <sub>blood,n</sub>	0.28	0.25					
r <sub>m</sub>	0.28						
r <sub>0</sub>	0.22						
occ <sub>frac</sub>	0.21						
Cu <sub>A,frac,n</sub>			0.86				
[CCO] <sub>tis</sub>			0.62				
SaO <sub>2,n</sub>			0.23				
[lac] <sub>n</sub>				1.00			
[ATP] <sub>n</sub>					1.00		
[PCr] <sub>n</sub>						1.00	0.78
[PCr] <sub>n</sub> /[P <sub>i</sub> ] <sub>n</sub>							1.00

Table 6.1: Grid showing the normalised  $\mu^*$  values of most influential parameters in the BrainPiglet model at steady state for each output that can be compared with a measured signal.

most commonly used as inputs, SaO<sub>2</sub> and P<sub>a</sub>, have a strong influence on many of the variables, and are most influential overall. The normal concentration of haemoglobin O<sub>2</sub> binding sites in the blood [Hbtot]<sub>n</sub> also has a strong influence on several of the parameters. Besides these parameters, there is not much overlap between the parameters which have the largest effect on the different variables. The  $\Delta\text{HbO}_2$  variable has the largest number of parameters (11) with a normalised  $\mu^*$  greater than 0.2. For this variable, 20% of parameters have a normalised  $\mu^*$  of greater than 0.1, but still only 37% of parameters have a normalised  $\mu^*$  of greater than 0.01. Overall, about one third of the parameters have a normalised  $\mu^*$  of less than 0.01 and two thirds have a normalised  $\mu^*$  of less than 0.1 for all 7 variables. As expected, the parameters which affect only the dynamic behaviour of the model (such as the time constants for the input parameters  $\tau_{\text{O}_2}$ ,  $\tau_{P_a}$ ,  $\tau_{\text{CO}_2}$  and  $\tau_u$ ) have very small  $\mu^*$  values.

## 6.2 Modelling carotid artery occlusion

Figure 6.2 shows the relationship between the steady state CBF as a fraction of its normal value, and the conductance of the supplying arterial compartment. The parameter determining the shape of this curve is the normal conductance of the supplying artery

compartment  $G_{0,n}$ . This is set as a fraction ( $G_{0,frac}$ ) of the normal conductance of the cerebral arterial compartment. If  $G_{0,frac}$  is large, CBF remains high until  $G_0$  is low. If  $G_{0,frac}$  is small the relationship becomes more linear, however this situation is unlikely since the large supplying vessels offer less resistance to blood flow than the smaller cerebral vessels.  $G_0$  is modified by changing the (normalised) radius of the supplying artery compartment

$$G_0 = G_{0,n} (1 - r_{frac} r_{occ})^4 \quad (6.1)$$

The control parameter  $r_{occ}$  represents the extent to which the carotid arteries are occluded, and  $r_{frac}$  is the fraction by which the radius would be reduced if the carotid arteries were completely occluded.

$$r_{frac} = 1 - \left( \frac{(G_0)_{occluded}}{G_{0,n}} \right)^{1/4} = 1 - (1 - occ_{frac})^{1/4} \quad (6.2)$$

where  $occ_{frac}$  is the fraction of total CBF which normally passes through the carotid arteries.

In man, approximately 40% of blood supplying the brain flows through each carotid artery [13]. This is assumed to apply to the piglet also ( $occ_{frac} = 0.8$ ). A few studies have reported CBF measurements in piglets when one or both of the carotid arteries were occluded, and oxygen levels were normal. The occlusion of just one carotid artery did not significantly reduce CBF. With both carotid arteries occluded, Kurth *et al.* [256] found that CBF fell to  $(74 \pm 22)$  % of its baseline value, whereas Oriot *et al.* [257] reported  $(46 \pm 20)$  %. However, in both experiments there were changes in the systemic arterial pressure, and in the latter case, the baseline CBF was about twice the normal reported value for piglets. A value for  $G_{0,frac}$  of 5 was chosen so that the curve lay between these two values at a  $G_0$  of 20 % its baseline value.

The pressure drop through the model compartments is illustrated in Figure 6.3 for different levels of occlusion.

### 6.3 Experimental protocol

The data were provided by collaborators carrying out experiments at UCL Institute of Neurology. Some data from these experiments have been published [258] and a full description of the experimental protocol can be found there. This thesis uses data from 14 male piglets aged less than 24 h. All experiments were performed under UK Home Office Guidelines. The piglets were sedated with intramuscular midazo-

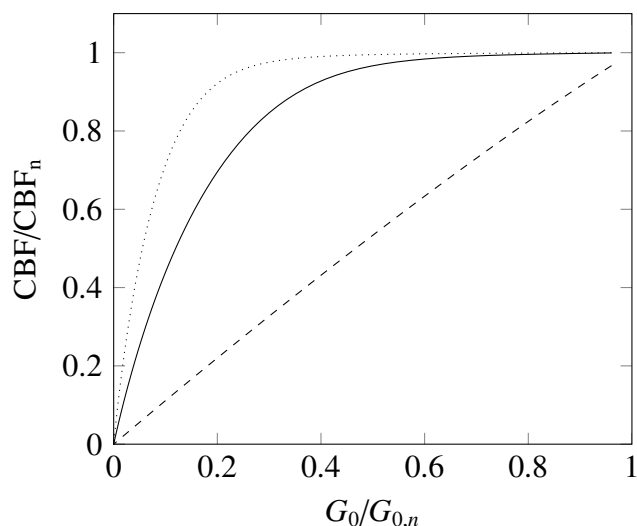


Figure 6.2: CBF vs  $G_0$  in the BrainPiglet model with  $G_{0,\text{frac}} = 10.0$  (dotted)  $G_{0,\text{frac}} = 5.0$  (solid) and  $G_{0,\text{frac}} = 0.1$  (dashed). Complete occlusion of the carotid arteries is equivalent to reducing  $G_0$  to 0.2 of its normal value.

lam ( $0.2 \text{ mg kg}^{-1}$ ) and isoflurane anaesthesia (3% during surgery, otherwise 2%) was maintained. The piglets were mechanically ventilated with settings adjusted to maintain  $P_{\text{aO}_2}$  and  $P_{\text{aCO}_2}$  in the ranges 8–13 kPa and 4.5–6.5 kPa.  $S_{\text{aO}_2}$  was monitored continuously. Both common carotid arteries were surgically isolated at the level of the fourth cervical vertebra and encircled by remotely controlled vascular occluders. An umbilical arterial catheter was inserted to monitor heart rate and blood pressure, and to take blood samples to measure  $P_{\text{aO}_2}$ ,  $P_{\text{aCO}_2}$ , pH, electrolytes, glucose, and lactate. An umbilical venous catheter was inserted for infusion of maintenance fluids (10% dextrose,  $60 \text{ ml kg}^{-1} \text{ d}^{-1}$ ), fentanyl ( $3\text{--}6 \mu\text{g kg}^{-1} \text{ h}^{-1}$ ), and antibiotics. Bolus infusions of colloid and inotropes maintained the mean arterial blood pressure above 40 mmHg. After surgery, the piglets were positioned prone in a plastic pod and the head immobilised in a stereotactic frame.

For all 14 piglets, NIRS data was acquired using an in house developed broadband spectrometer. Optodes were placed on either side of the piglet head, and secured using the stereotactic frame. NIR spectra in the range 650–980 nm were collected at 1 min intervals throughout the experiment. The NIRS measurements  $\Delta\text{HbO}_2$ ,  $\Delta\text{HHb}$  and  $\Delta\text{oxCCO}$  were determined from the attenuation spectra between 780 and 900 nm using the UCLn algorithm [259] after correction for wavelength dependence of path-length [260].

For 5 of the piglets, whole brain  $^1\text{H}$ -MRS was acquired using a 9.4 T spectrometer and a 60 mm diameter MRS surface coil. The acquired voxel was a cube of side length 19 mm contained entirely within the brain. The repetition time was 5 s, with an echo time of 288 ms; data from 12 averages was used resulting in an acquisition time of 1 min per

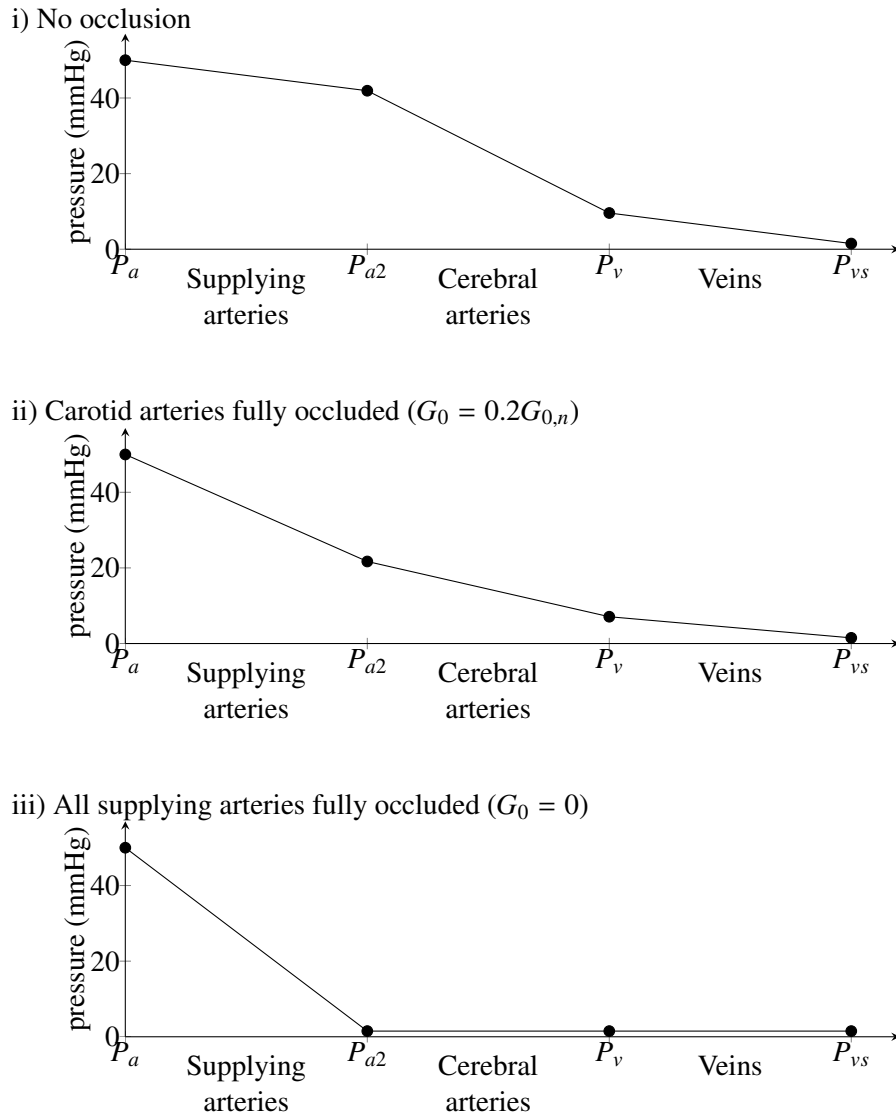


Figure 6.3: Diagram illustrating the drop in pressure through the compartments at different levels of occlusion

spectrum. The spectra were acquired continuously and analysed using the AMARES algorithm [261] to calculate the Lac/Naa peak area ratio (along with other ratios that are not used in this thesis).

In these piglet, after 10 min of baseline measurements, HI was induced by occluding the common carotid arteries and reducing the  $\text{FiO}_2$  in steps to 8 %.  $\text{FiO}_2$  was then increased again after around 12 min in steps to its baseline value, after which the occluders were deflated. A further 60 min of measurements were collected.

For another 8 of the piglets, whole brain  $^{31}\text{P}$ -MRS was acquired every minute using a 9.4 T spectrometer and a 70 mm  $\times$  50 mm surface coil. The data were analysed with the AMARES algorithm to calculate the NTP/EPP, PCr/EPP, and  $\text{P}_i$ /EPP peak area ratios.

Baseline data were recorded for 10 min, followed by inflation of the occluders and reduction of  $\text{FiO}_2$  to 12 %. This was maintained until the height of the  $\beta$ -NTP peak had fallen to 50 % of its baseline value.  $\text{FiO}_2$  was then adjusted to maintain this peak between 30 % and 50 % of its baseline height for 12.5 min. The occluders were then deflated and  $\text{FiO}_2$  returned to normal.

## 6.4 Methods and results

### 6.4.1 Experimental results

Examples of results from two piglets, one measured with H-MRS and one with  $^{31}\text{P}$ -MRS, are shown in Figures 6.4 and 6.5. The results from all the piglets are shown in Appendix A. All piglets show a drop in  $\Delta\text{HbO}_2$  and a rise in  $\Delta\text{HHb}$  which both return close to their baseline values after the insult. Piglet LWP168 (monitored with H-MRS) shows an overshoot of  $\Delta\text{HbO}_2$  lasting approximately 10 min. This pattern is seen clearly in 4 of the 6 piglets monitored with H-MRS (see also Figures A.1, A.2 and A.6), but none of those monitored with  $^{31}\text{P}$ -MRS. For the 4 piglets with an overshoot, the maximum  $\Delta\text{HbO}_2$  within the 10 min following the insult is  $(21 \pm 4) \mu\text{M}$  (averaged across the 4 piglets). For the other 10 piglets the maximum is  $(-1 \pm 3) \mu\text{M}$ . All piglets show a reduction of CCO as expected. There is an increase in Lac/NAA ratio which recovers slowly after the insult. There is also a decrease in NTP/EPP and PCr/EPP and an increase in  $\text{P}_i$ /EPP.

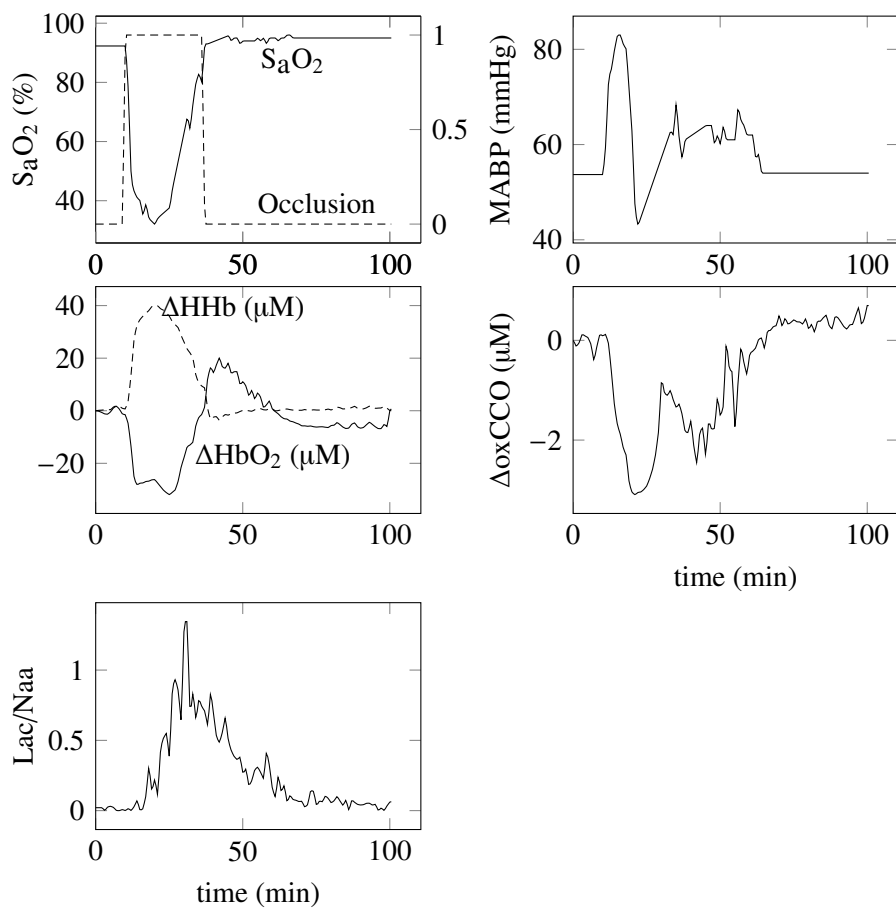


Figure 6.4: Measured results from one piglet (LWP168) with H-MRS

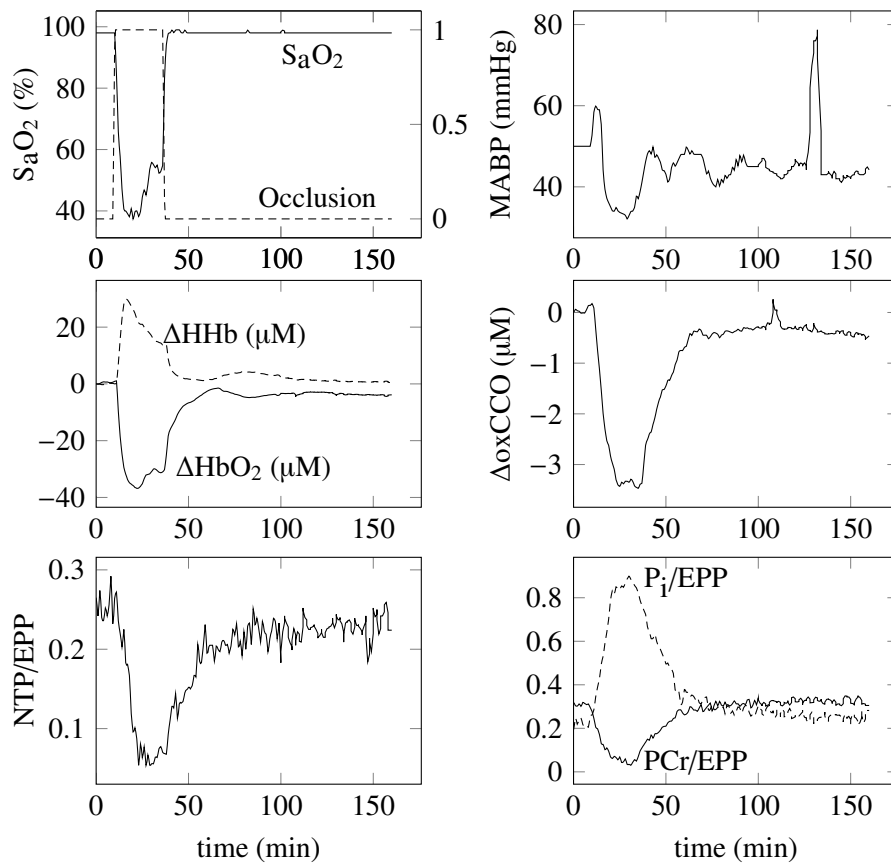


Figure 6.5: Measured results from one piglet (LWP180) with  $^{31}P$ -MRS

## 6.4.2 Data analysis

Each dataset was resampled to 1 point every six seconds. The beginning and end of the carotid artery occlusion were identified by examining the  $\Delta\text{Hb}_{\text{diff}}$  signal. The  $\text{S}_a\text{O}_2$  and mean arterial blood pressure measurements were used as inputs. An input for the carotid artery occlusion was created by varying the control parameter  $r_{\text{occ}}$  (see Equation 6.1) between 0 and 1 over a minute period at the onset of occlusion, and then back to 0 again at the end of the occlusion. Ideally this would happen instantaneously, but this caused the model to be unstable.

Before optimisation was performed, Morris sensitivity analysis was carried out for each piglet on the rms error between the modelled and measured signals. This was done to see which parameters had the most important effects on the fitting of the model to the data and so help decide which parameters should be optimised to improve the fit. The NIRS variables ( $\Delta\text{HbO}_2$ ,  $\Delta\text{HHb}$  and  $\Delta\text{oxCCO}$ ) were offset before comparing them with their measured equivalents. The  $^{31}\text{P}$ -MRS measured variables (NTP/EPP, PCr/EPP and  $\text{P}_i/\text{EPP}$ ) were compared with no scaling or offsets, and [lac] was both scaled and offset before being compared with the Lac/Naa ratio measured by proton MRS.

For each parameter and variable, the mean of the  $\mu^*$  and  $\sigma$  values was calculated across all the piglets for which the relevant signal was measured. These values are shown in Figure 6.6. These mean  $\mu^*$  values were then normalised for each variable. Parameters with a normalised  $\mu^* \geq 0.2$  are shown in Table 6.2.

The parameters representing the normal concentrations of the variables were found to be the most influential. Overall, 28 % of the parameters had normalised  $\mu^*$  values less than 0.01 and 57 % of the parameters had normalised  $\mu^*$  values less than 0.1 for all signals. The most influential parameters were different for all the signals, except for the related signals  $\Delta\text{HbO}_2$  and  $\Delta\text{HHb}$ , and [ATP], [PCr] and  $[\text{PCr}]_n/[\text{P}_i]_n$ . This was used to help to carry out parameter optimisation.

## 6.4.3 Parameter optimisation

Parameters identified by the sensitivity analysis were optimised for each of the piglets. Only those parameters with a normalised  $\mu^* \geq 0.5$  were included, to limit the number of parameters and therefore help prevent overfitting and increase parameter identifiability. The parameters were split into four groups based on the variables for which they were influential.

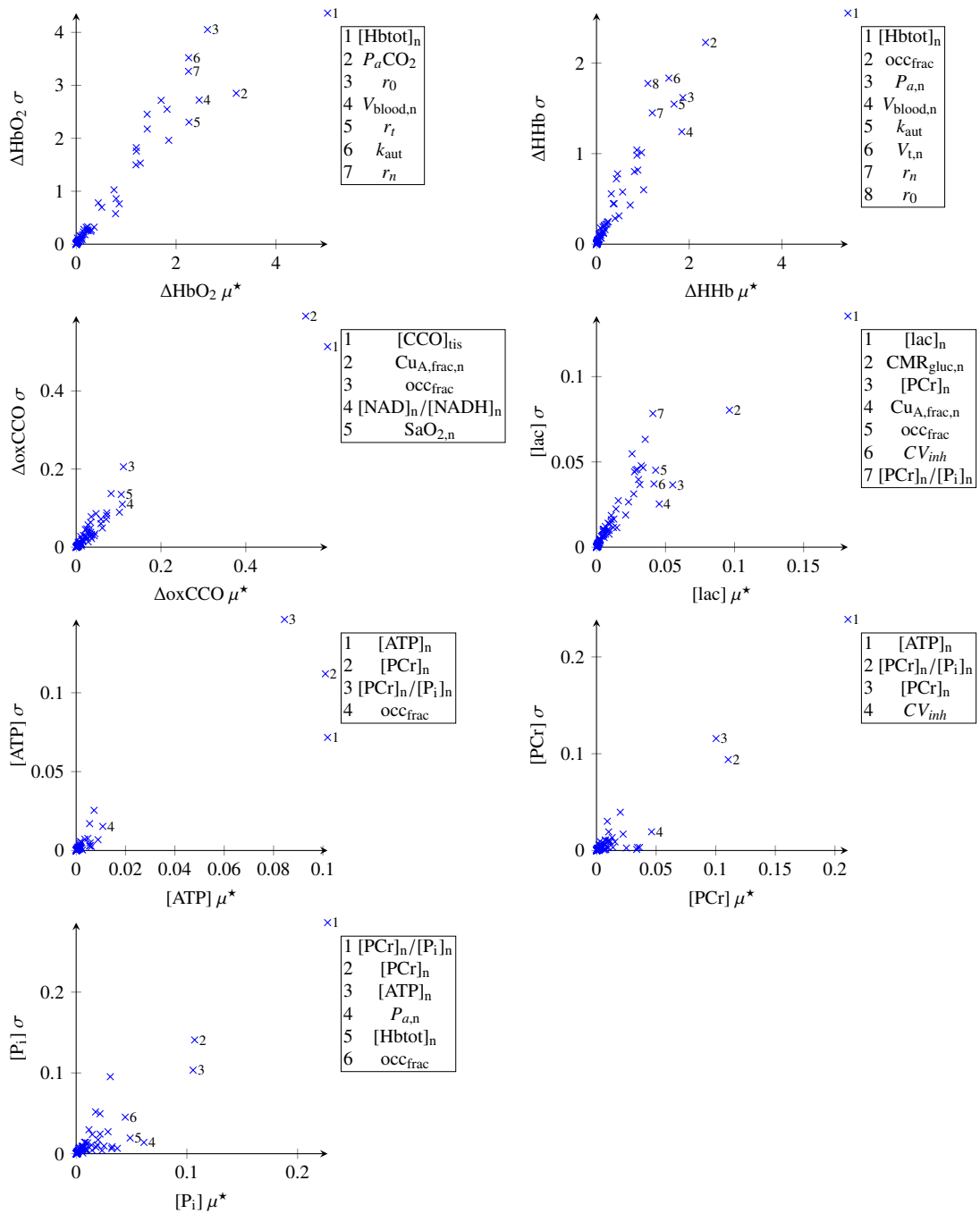


Figure 6.6: Mean  $\sigma$  vs mean  $\mu^*$  across all piglets from a Morris sensitivity analysis of the rms error between measured and modelled variables.

	$\Delta\text{HbO}_2$	$\Delta\text{HHb}$	$\Delta\text{oxCCO}$	[lac]	[ATP]	[PCr]	[P <sub>i</sub> ]
[Hbtot] <sub>n</sub>	1.00	1.00					0.21
$r_0$	0.52	0.20					
$V_{\text{blood},n}$	0.49	0.34					
$k_{\text{aut}}$	0.45	0.31					
$r_n$	0.45	0.22					
$r_t$	0.45						
$R_O$	0.36						
$r_m$	0.34						
$\text{occ}_{\text{frac}}$	0.28	0.43		0.24			
$K_\sigma$	0.28						
$\text{SaO}_{2,n}$	0.26						
$P_{a,n}$	0.24	0.34					0.27
$R_C$	0.24						
$R_P$	0.24						
[CCO] <sub>tis</sub>			1.00				
$\text{Cu}_{\text{A,frac},n}$			0.91	0.25			
[lac] <sub>n</sub>				1.00			
$\text{CMR}_{\text{gluc},n}$				0.53			
[ATP] <sub>n</sub>					1.00	1.00	0.46
[PCr] <sub>n</sub>				0.30	0.99	0.48	0.47
[PCr] <sub>n</sub> /[P <sub>i</sub> ] <sub>n</sub>				0.22	0.83	0.52	1.00
$CV_{\text{inh}}$				0.23		0.22	

Table 6.2: Normalised  $\mu^*$  values from a sensitivity analysis for the rms error between modelled and measured signals. Only parameters with a normalised  $\mu^* \geq 0.2$  are shown.

**Group 1** The parameters  $[\text{Hbtot}]_n$ ,  $P_a\text{CO}_2$  and  $r_0$  were optimised to minimise the sum of the rms error between the measured and modelled  $\Delta\text{HbO}_2$  and  $\Delta\text{HHb}$  signals.

**Group 2** The parameters  $[\text{CCO}]_{\text{tis}}$  and  $\text{Cu}_{\text{A,frac,n}}$  were optimised to minimise the rms difference between the measured and offset modelled  $\Delta\text{oxCCO}$ .  $\Delta\text{oxCCO}$  was only compared up to the nadir of the insult (the point where  $\text{SaO}_2$  began to increase), since some piglets did not show recovery of the CCO redox state and the model was not able to replicate this.

**Group 3** For those piglets which were monitored with H-MRS the parameters  $[\text{lac}]_n$  and  $\text{CMR}_{\text{gluc,n}}$  were optimised to minimise the sum of the rms difference between the measured and modelled  $\text{Lac/NAA}$ . Simulated  $\text{Lac/NAA}$  was estimated by both scaling and offsetting the modelled lactate concentration.

**Group 4** For the piglets which were monitored with  $^{31}\text{P}$ -MRS the parameters  $[\text{ATP}]_n$ ,  $[\text{PCr}]_n$  and  $[\text{PCr}]_n/[\text{P}_i]_n$  were optimised to minimise the rms difference between the modelled and measured  $\text{NTP/EPP}$ ,  $\text{PCr/EPP}$  and  $\text{P}_i/\text{EPP}$  signals. The signals were also only optimised to the nadir of the insult.

The optimisations were carried out with both the PSwarm and Powell methods. The resulting optimised parameter values are summarised in Table 6.3. Examples of modelled and measured signals before and after optimisation are shown in Figures 6.7 and 6.8.

In the majority of cases, the parameters found by the two optimisation methods were the same. In most cases, when they differed it was the point found by the PSwarm method that gave the lower error, however the difference was small. For the parameters used to optimise the MRS signals ( $[\text{ATP}]_n$ ,  $[\text{PCr}]_n$ ,  $[\text{PCr}]_n/[\text{P}_i]_n$ ,  $\text{CMR}_{\text{gluc,n}}$  and  $[\text{lac}]_n$ ) the values were the same for all piglets to the accuracy given. For the parameters used to optimise the NIRS haemoglobin signals ( $[\text{Hbtot}]_n$ ,  $P_a\text{CO}_2$  and  $r_0$ ) there were differences in 4 of the piglets of between 1 and 3 in the least significant figure to the accuracy given in the table. Finally, for the parameters used to optimise the  $\Delta\text{oxCCO}$  signal, 3 piglets had small differences between the optimised parameter values, and 1 piglet (LWP158) had a large difference (1.0  $\mu\text{M}$  for  $[\text{CCO}]_{\text{tis}}$  and 0.22 for  $\text{Cu}_{\text{A,frac,n}}$ ). However, the product of the two parameters ( $\text{Cu}_{\text{A,frac,n}}[\text{CCO}]_{\text{tis}}$ ) was the same for both methods in all cases. In 11 of the 14 piglets, the optimised value of  $[\text{CCO}]_{\text{tis}}$  reached the maximum allowed value (7  $\mu\text{M}$ ). The variation of the rms error between the modelled and measured  $\Delta\text{oxCCO}$  signals up to the nadir of the insult with the two parameters in one piglet (LWP180) is shown in Figure 6.9. This shows that the product of the two parameters, which is what determines the magnitude of the fall in  $\Delta\text{oxCCO}$ , is much better defined by the data than the individual parameter values.

Although the same values of  $[ATP]_n$  and  $[PCr]_n$  were found by both optimisation methods, there is a similar relationship between these parameters and the sum of the errors between the measured and modelled  $^{31}P$ -MRS signals up to the nadir of the insult. This time it is the ratio between the parameters ( $[ATP]_n/[PCr]_n$ ) which is more clearly defined than the parameters themselves as shown in Figure 6.10. This relationship is not surprising, since the variables are expressed as fractions of the total exchangeable phosphate pool ( $2[ATP]_n + [PCr]_n + [P_i]$ ), and therefore the baseline values of the three variables depend only on the ratios of  $[ATP]_n$ ,  $[PCr]$  and  $[P]_n$ .

Parameter	Units	Default Value	Optimised Value(SD)	
			PSwarm	Powell
$[Hbtot]_n$	mM	5.4	6.3(1.5)	6.2(1.5)
$P_aCO_2$	mmHg	40	39(12)	40(12)
$r_0$	cm	$1.26 \times 10^{-2}$	$1.22(0.08) \times 10^{-2}$	$1.23(0.08) \times 10^{-2}$
$[CCO]_{tis}$	mM	$2.2 \times 10^{-2}$	$6.3(1.5) \times 10^{-3}$	$6.2(1.7) \times 10^{-3}$
$Cu_{A,frac,n}$	(dimensionless)	0.67	0.50(0.16)	0.52(0.17)
$[lac]_n$	mM	3.0	3.3(1.6)	3.3(1.6)
$CMR_{gluc,n}$	$mM s^{-1}$	$4.4 \times 10^{-3}$	$4.2(1.0) \times 10^{-3}$	$4.2(1.0) \times 10^{-3}$
$[ATP]_n$	mM	1.2	3.5(1.7)	3.5(1.7)
$[PCr]_n$	mM	2.6	4.4(1.8)	4.4(1.8)
$[PCr]_n/[P_i]_n$	(dimensionless)	2.73	1.1(0.3)	1.1(0.3)

Table 6.3: Mean(SD) parameter values across all piglets after individual optimisations

#### 6.4.4 Effect of total haemoglobin concentration

It is clear from the previous results that the total blood haemoglobin concentration (proportional to  $[Hbtot]$ ) has an important effect on the modelled NIRS outputs. This parameter is assumed to remain constant throughout the experiment. However, this concentration was measured several times throughout the experiment. In each piglet, haemoglobin concentration ( $[Hb]$ ) was measured at least twice, and up to 13 times over a period ranging from 2–48 h. These measurements are shown for each piglet in Figure 6.11. There were large variations in  $[Hb]$ , with a range across all 14 piglets of 3.4–20.4  $g dl^{-1}$ . The range in an individual piglet varied from 1.7  $g dl^{-1}$  to 10.5  $g dl^{-1}$  and on average was 4.9  $g dl^{-1}$ . These changes arose from the taking of blood and giving of fluid to the piglets throughout the experiment for various reasons. The fluctuation may have caused significant changes in the NIRS signal; the direction of which depends on the arterial oxygen saturation, as illustrated by the simulations shown in Figure 6.12. The haemoglobin concentration was not measured frequently enough during the modelled period to investigate whether changes in the haematocrit were responsible for changes

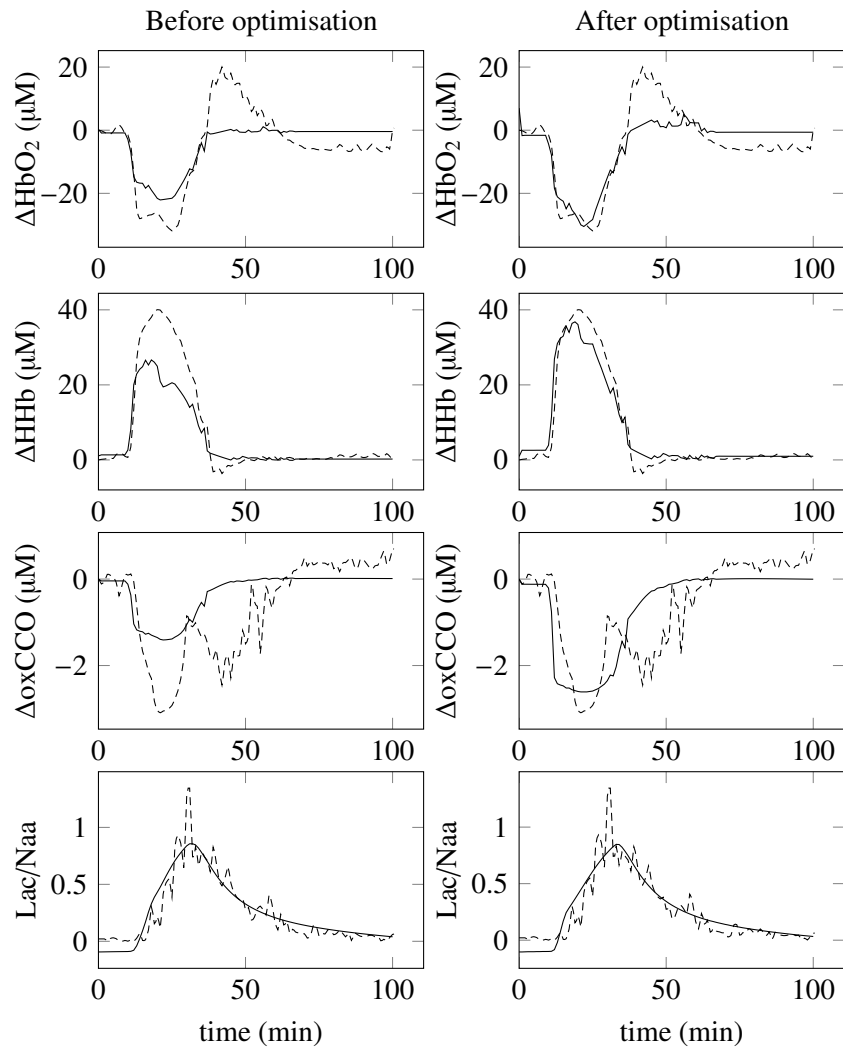


Figure 6.7: Plots comparing the modelled and measured NIRS and MRS signals before and after optimisation for a piglet monitored with H-MRS (piglet LWP168)

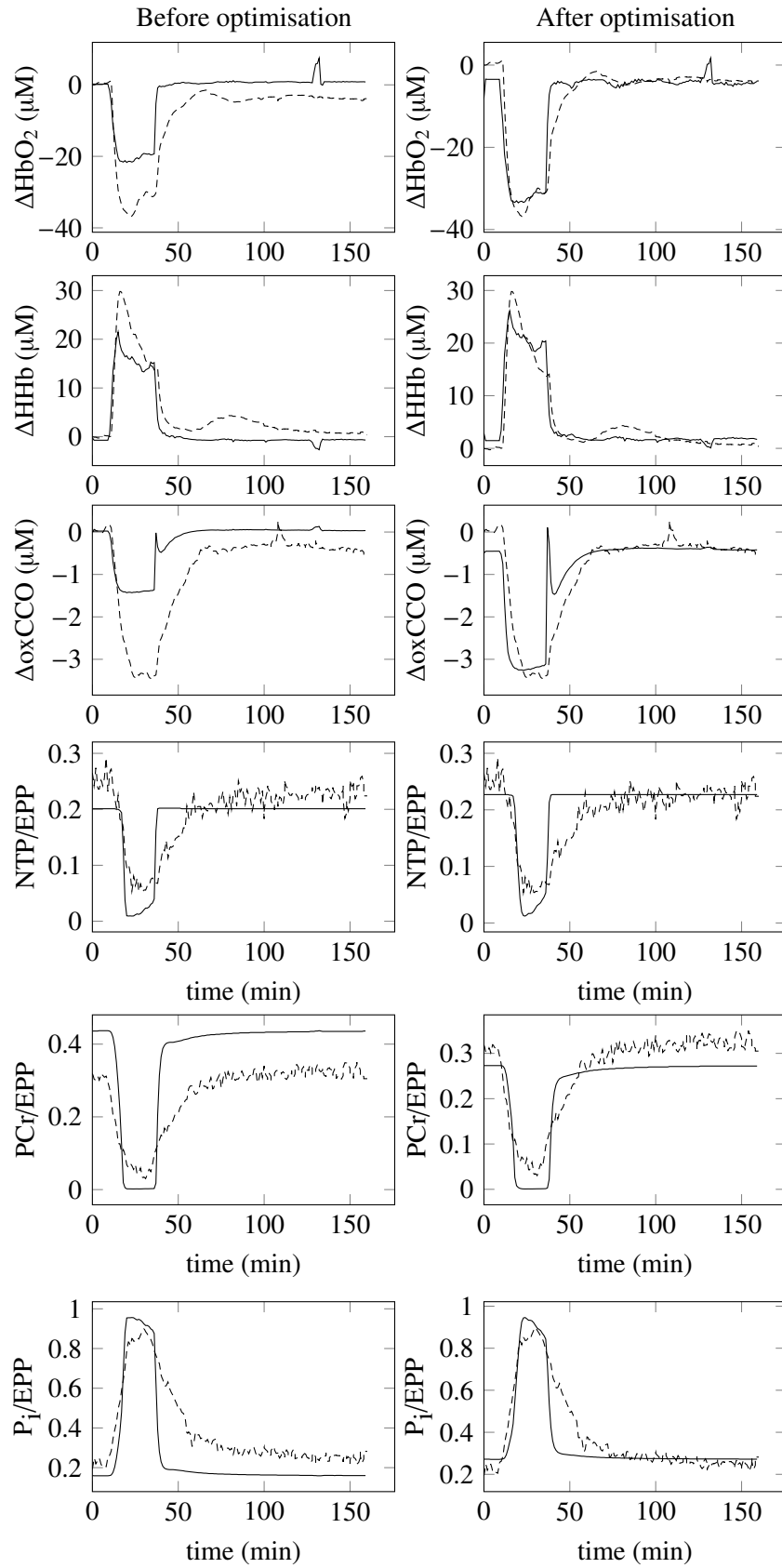


Figure 6.8: Plots comparing the modelled and measured NIRS and MRS signals before and after optimisation for a piglet monitored with  $^{31}\text{P}$ -MRS (piglet LWP180)

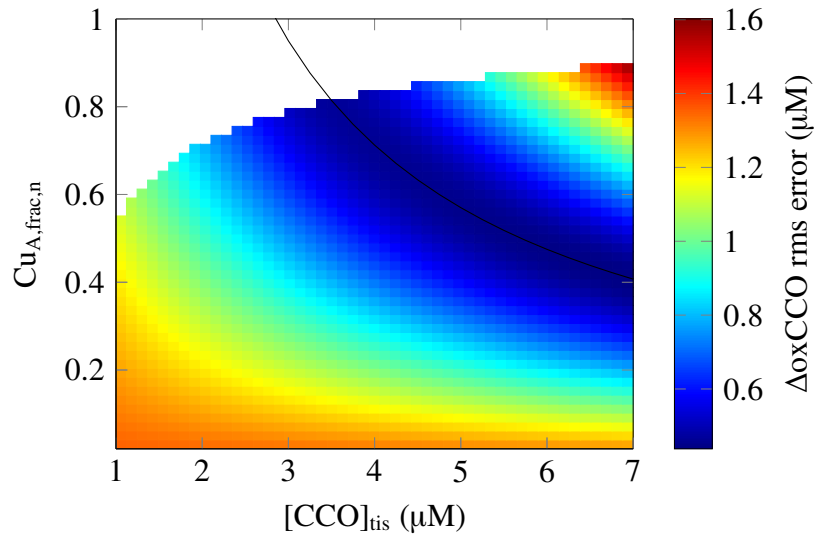


Figure 6.9: rms error between modelled and measured  $\Delta\text{oxCCO}$  as a function of  $[\text{CCO}]_{\text{tis}}$  and  $\text{Cu}_{\text{A,frac},n}$  for piglet LWP180. The line shows  $\text{Cu}_{\text{A,frac},n}[\text{CCO}]_{\text{tis}} = 2.85 \mu\text{M}$  (the value for the optimised parameter). The uncoloured area indicates unsuccessful simulations.

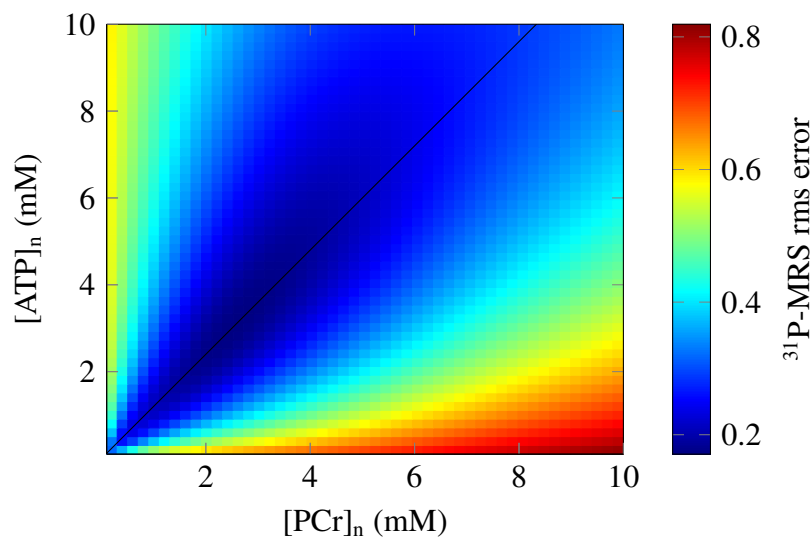


Figure 6.10: Sum of the rms errors between modelled and measured  $^{31}\text{P}$ -MRS variables as a function of  $[\text{ATP}]_n$  and  $[\text{PCr}]_n$  for piglet LWP180. The line shows  $[\text{PCr}]_n = 2.1[\text{ATP}]_n$  (the value for the optimised parameters)

in the NIRS signals, although such an analysis may be possible over longer timescales. It is therefore important to consider possible haematocrit changes when interpreting the results.

## 6.4.5 Cell death

### Relationship between signals following HI

Several of the piglets showed incomplete recovery of  $\Delta\text{oxCCO}$  and the  $^{31}\text{P}$ -MRS signals following HI i.e. these signals did not return to close to their baseline values after the insult and for the duration of the experiment. This was investigated by calculating a recovery fraction for each signal. Three periods during the signal were identified, and means were calculated as follows:

**baseline** Mean of the first 500 s of data

**nadir** Mean of the 200 s before the nadir of the insult, taken as the point at which the  $\text{S}_a\text{O}_2$  began to be increased.

**recovery** Mean of the last 500 s of data ((100  $\pm$  20) min after nadir)

These periods are illustrated for the  $\Delta\text{oxCCO}$  signal of a piglet which did not fully recover in Figure 6.13

The recovery fractions for CCO, NTP and PCr were then calculated as follows

$$\text{CCO recovery fraction} = \frac{\text{recovery} - \text{nadir}}{\text{baseline} - \text{nadir}} \quad (6.3)$$

$$\text{NTP and PCr recovery fraction} = \frac{\text{recovery}}{\text{baseline}} \quad (6.4)$$

Figure 6.14 shows the relationship between the CCO recovery fraction and the NTP and PCr recovery fractions for each piglet. The graphs show a clear relationship between these fractions. However, with only three piglets having a low recovery fraction, there is not enough data for a quantitative statistical analysis.

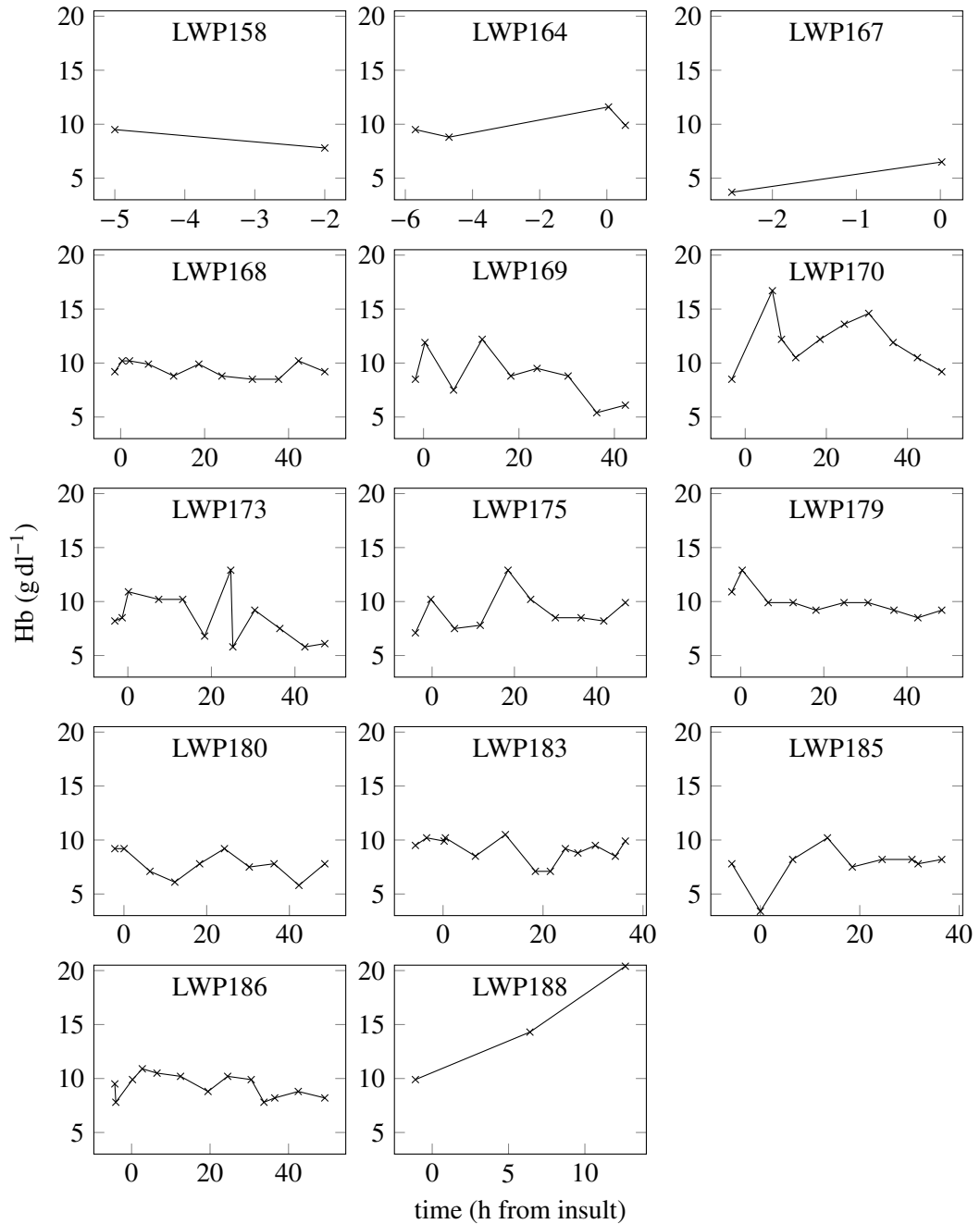


Figure 6.11: Measured blood haemoglobin concentration for each piglet over the full experiment for up to 48 h

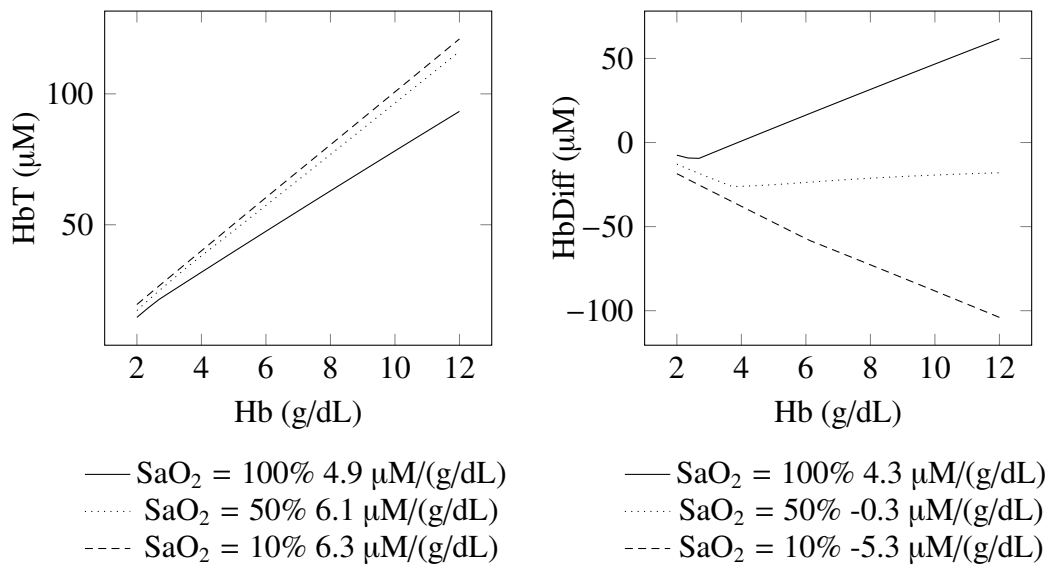


Figure 6.12: Simulated  $\Delta\text{HbT}$  and  $\Delta\text{Hb}_{\text{diff}}$  vs  $[\text{Hbtot}]$  at different  $\text{SaO}_2$

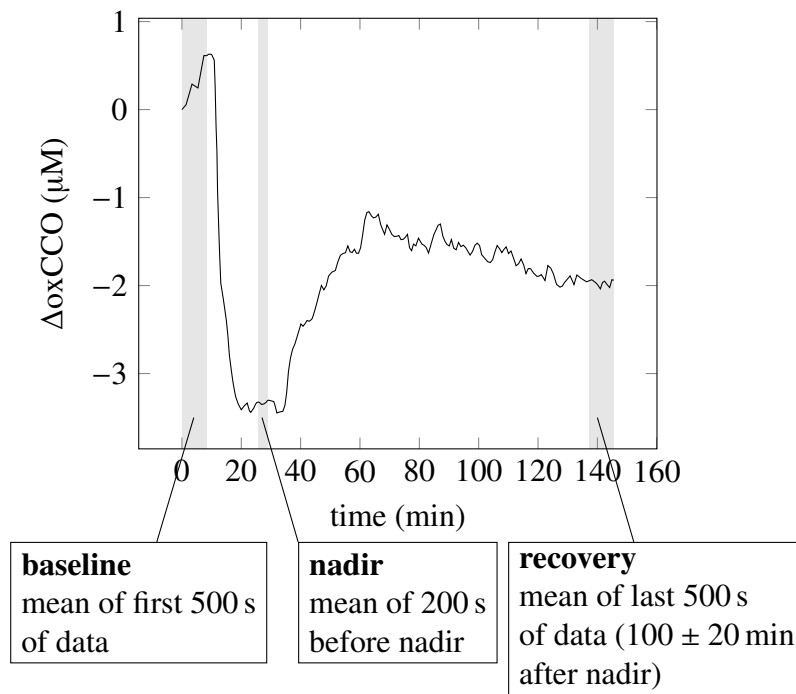


Figure 6.13: An example of the  $\Delta\text{oxCCO}$  signal from a piglet which did not recover following HI showing the periods used for calculating the recovery fraction

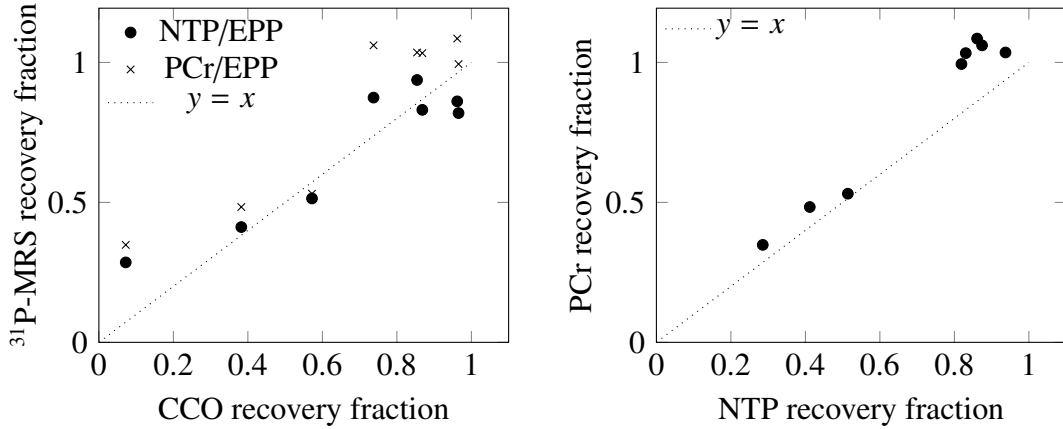


Figure 6.14: Relationship between recovery of CCO and NTP and PCr following HI

### Modelling cell death

One hypothesis for explaining these results is that a fraction of the cells in the brain have died during HI. This was modelled by assuming that during HI, CCO becomes fully reduced, and remains so in the dead cells. It was also assumed that in the dead cells, all the exchangeable phosphate was in the form of  $P_i$ . A parameter  $d_f$  was introduced to represent the fraction of cells which were considered to be dead. This parameter was set to 0 until the nadir of HI and to the value of parameter  $d$  following the nadir, using an input parameter  $\Delta_{\text{nadir}}$  functioning as a switch.

It was assumed that no oxygen consumption was taking place in the dead cells, and that their oxygen concentration would quickly equilibrate with that of the capillaries. The modelled rate of oxygen transfer from the capillaries to the mitochondria was therefore reduced to  $(1 - d_f)$  of its normal rate. This was the only change to the model, other than an alteration of some output variables (i.e. variables which have no effect on any other part of the model). The following model outputs were changed:

$$\text{output NTP/EPP} = \frac{(1 - d_f)[\text{ATP}]}{\text{EPP}} \quad (6.5)$$

$$\text{output PCr/EPP} = \frac{(1 - d_f)[\text{PCr}]}{\text{EPP}} \quad (6.6)$$

$$\text{output } P_i/\text{EPP} = \frac{(1 - d_f)[P_i]}{\text{EPP}} + d_f \quad (6.7)$$

$$\text{output } \Delta\text{oxCCO} = (1 - d_f)\Delta\text{oxCCO} - d_f\text{oxCCO}_n \quad (6.8)$$

$$\text{output CMRO}_2 = (1 - d_f)\text{CMRO}_2. \quad (6.9)$$

Parameter	Units	Default Value	Optimised Value(SD)	
			PSwarm	Powell
$[\text{CCO}]_{\text{tis}}$	mM	$2.2 \times 10^{-2}$	$5.8(1.0) \times 10^{-3}$	$5.1(1.2) \times 10^{-3}$
$\text{Cu}_{\text{A,frac,n}}$	(dimensionless)	0.67	0.69(0.10)	0.78(0.09)
$[\text{ATP}]_{\text{n}}$	mM	1.2	3.1(1.0)	2.3(1.2)
$[\text{PCr}]_{\text{n}}$	mM	2.6	4.4(1.6)	3.4(1.9)
$[\text{PCr}]_{\text{n}}/[\text{P}_i]_{\text{n}}$	(dimensionless)	2.73	1.7(0.9)	1.7(0.9)
$d$	(dimensionless)	0.0	0.31(0.29)	0.31(0.29)

Table 6.4: Results of optimisations of  $\Delta\text{oxCCO}$  and  $^{31}\text{P}$ -MRS variables including a fraction of dead cells

In order to investigate the effect of simulated cell death, the 6 parameters  $d_f$ ,  $[\text{CCO}]_{\text{tis}}$ ,  $\text{Cu}_{\text{A,frac,n}}$ ,  $[\text{ATP}]_{\text{n}}$ ,  $[\text{PCr}]_{\text{n}}$  and  $[\text{PCr}]_{\text{n}}/[\text{P}_i]_{\text{n}}$  were optimised to minimise the rms difference between the measured and modelled  $\Delta\text{oxCCO}$ , NTP/EPP, PCr/EPP and  $\text{P}_i$ /EPP signals during the baseline, nadir and recovery periods as defined in Figure 6.13. The signals were fitted during only these periods, rather than over the whole signal, to prevent inaccuracies in modelling the time course of the changes from affecting the results. The parameters  $[\text{Hbtot}]_{\text{n}}$ ,  $P_a\text{CO}_2$  and  $r_0$  were set to the values previously optimised to the NIRS haemoglobin signals.

The results of these optimisations are shown in Table 6.4. The mean optimised value of  $d$  across the 8 piglets was  $0.31 \pm 0.29$  with a range of 0.01 to 0.87. Figure 6.15 shows the results from one piglet comparing  $d = 0$  and the optimised value of  $d = 0.37$ . With  $d = 0.37$  the means of the simulated  $\Delta\text{HbO}_2$  and  $\Delta\text{HHb}$  during recovery were  $-1.0 \mu\text{M}$  and  $-2.2 \mu\text{M}$  compared with  $-6.3 \mu\text{M}$  and  $8.5 \mu\text{M}$  for  $d = 0$ . The corresponding measured values were  $-7.0 \mu\text{M}$  and  $10.6 \mu\text{M}$ . Therefore, whilst adding a dead compartment to the model improved the simulation of  $\Delta\text{oxCCO}$  and the  $^{31}\text{P}$ -MRS variables, the haemoglobin simulations were further from the measured data.

Again, the optimisations were carried out with both the PSwarm and modified Powell methods. There were no differences between the two methods in the optimised values of the parameters  $d$  and  $[\text{PCr}]_{\text{n}}/[\text{P}_i]_{\text{n}}$ . However, the values of  $[\text{CCO}]_{\text{tis}}$ ,  $\text{Cu}_{\text{A,frac,n}}$ ,  $[\text{ATP}]_{\text{n}}$  and  $[\text{PCr}]_{\text{n}}$  found were different. But the values of  $\text{Cu}_{\text{A,frac,n}}[\text{CCO}]_{\text{tis}}$  and  $[\text{ATP}]_{\text{n}}/[\text{PCr}]_{\text{n}}$  were again the same for all piglets. This can be explained by the landscapes of the rms errors illustrated in Figures 6.9 and 6.10. The PSwarm method found a point with a lower error for four of the piglets, whilst for the other four piglets the Powell method found a better point.

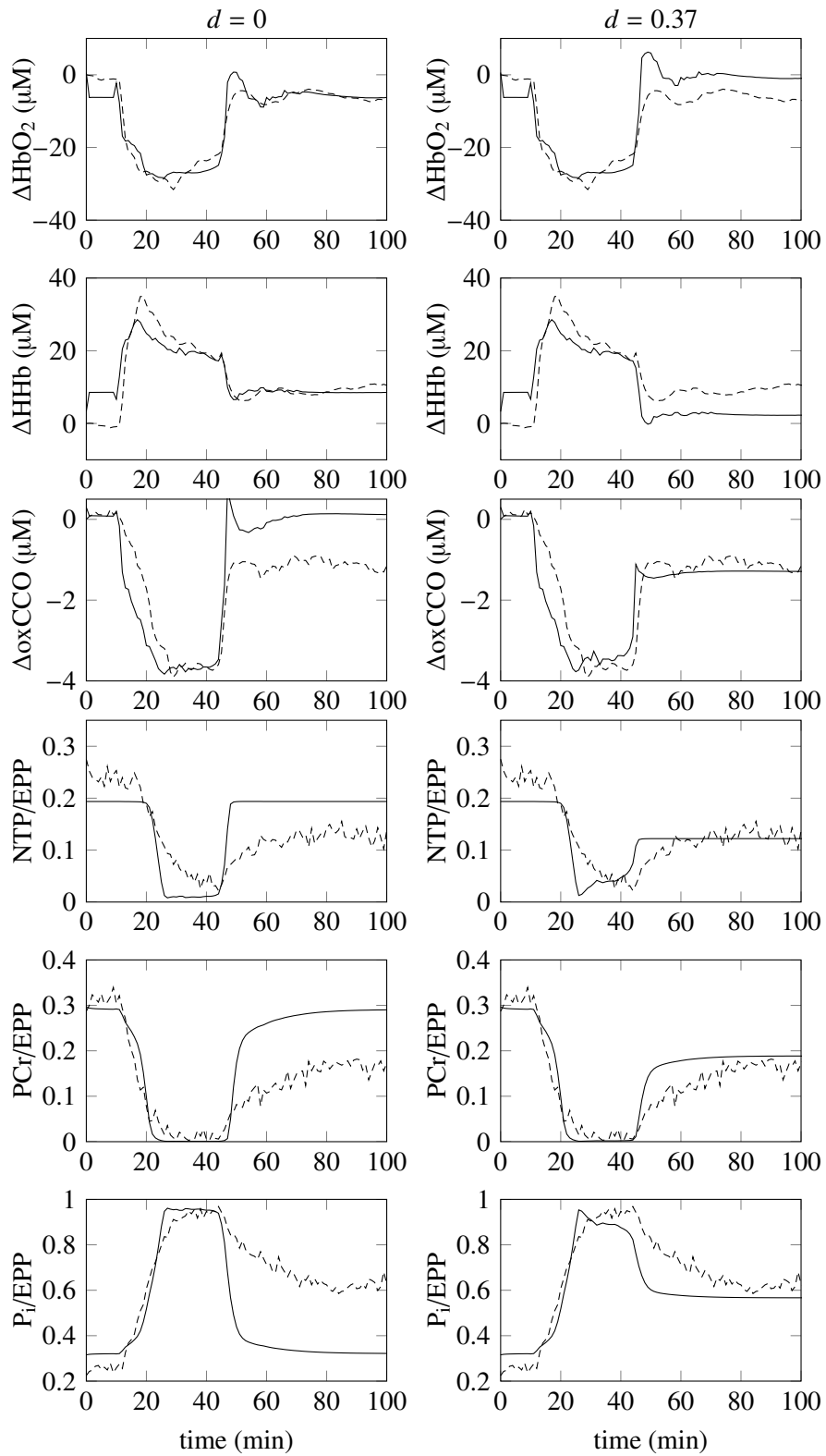


Figure 6.15: Comparison between measured (dashed) and modelled (solid) results from a piglet which did not recover using (left)  $d = 0$  and (right)  $d = 0.37$

## 6.5 Discussion

The model has been used to simulate data from individual piglets subjected to HI. NIRS and MRS measurements have been simulated, and sensitivity analysis and optimisation techniques have been used to investigate and improve the results.

### 6.5.1 Sensitivity analysis

A systematic method of sensitivity analysis is important for a model as large and as complex as the BrainPiglet model. The Morris method is a useful way of exploring the whole of the given parameter space and screening for influential parameters. However, the results of the method are heavily dependent on the input parameter distributions. It is therefore important that these distributions are set with sufficient consideration. For the results presented here, the majority of the parameters had their ranges set to  $\pm 20\%$  of their default value, and all parameters were given uniform distributions. In the future this could be improved by, as far as possible, deriving parameter distributions from the available experimental data and allowing other types of distribution, such as normal distributions.

Despite this reservation, the results of this sensitivity analysis are still valuable. They show that the most influential parameters are the ones which are generally used as inputs. They also show that the normal concentrations of the variables representing the measured signals are important, which is to be expected. It is also encouraging, since these parameters are most likely to vary between individuals and could potentially be optimised for each individual.

Two sensitivity analyses were carried out: one investigating the steady state of the model, and the other investigating the rms error between the modelled and measured signals during HI. There was a lot of similarity between the results of these two. The parameters with very small  $\mu^*$  values for all signals were the same for both the sensitivity analyses. Parameters which only effect the dynamic behaviour of the model therefore did not have a strong influence on the rms error between the measured and modelled data. The fairly large proportion of parameters with small  $\mu^*$  values across all signals and both sensitivity analyses confirms the Morris method is a good screening tool to distinguish between influential and non-influential parameters. The parameters found to be most influential were also the same between the two analyses (aside from the input parameters which were fixed at their measured values in the second analysis).

However, there were differences between the two analyses. For example,  $P_a\text{CO}_2$  had the second highest normalised  $\mu^*$  of 0.64 for  $\Delta\text{HbO}_2$  in the data sensitivity analysis, but a normalised  $\mu^*$  of only 0.15 in the steady state analysis. Similarly,  $\text{CMR}_{\text{gluc,n}}$  had the second highest normalised  $\mu^*$  of 0.53 for lactate in the data analysis, but a normalised  $\mu^*$  of only 0.06 in the steady state analysis. These differences may be caused by the differences in the simulations. These parameters may be much more influential when the oxygen supply is low.

Ideally, the robustness of the method would be checked by repeating the analyses and using different numbers of simulations. However this was not possible due to the time taken to carry out each sensitivity analysis. On the machine available (with an Intel Core 2 Duo processor) one sensitivity analysis as described takes 20–30 h.

The Morris method was used here because it is less computationally intensive than other methods. Other sensitivity analysis methods are based on decomposition of the variance of the model output, and therefore provide more quantitative information [262]. However these methods require more simulations, and some methods such as the Sobol' method cannot be used, as the model does not have a solution at all points in the parameter space as described in Section 3.4.

## 6.5.2 Parameter optimisation

Without parameter optimisation, the model was able to correctly predict the direction of change for all the signals, however it did not correctly predict the magnitude of these changes. Sensitivity analysis showed that different groups of parameters were the most influential for different signals. This allowed simpler parameter optimisation by treating the groups separately. Following optimisation, the simulations were improved, but there were still significant differences between the modelled and measured signals. In general, the haemoglobin signals were fitted well. However, the overshoot of  $\Delta\text{HbO}_2$  following the insult seen in some of the piglets was not reproduced by the model. The cause of this overshoot is not known but it may be a consequence of the carotid artery occlusion itself, for example, blood may build up behind the occluders. The fact that was seen only in piglets monitored with H-MRS suggests it is related to the details of the experimental protocol.

The other signals were less well simulated, in particular the time course of the changes were not matched well. The model changes occurred more quickly than those that were measured, in particular in the recovery of the  $^{31}\text{P}$ -MRS and CCO signals. This may be because there are physiological changes occurring, or processes taking place, which are

not included in the model and this will require further investigation.

The optimisation may have been improved if different parameters or more parameters were included. Although sensitivity analysis is helpful in identifying parameters that influence the fit, this method did not distinguish parameters that improved the fit from those that worsened it. A different metric could be used in the sensitivity analysis to identify parameters that are able to improve the fit, and optimising these may result in a more successful fit.

In most cases, there was good agreement between the parameter values found by the two optimisation methods. However there were some differences, particularly when the dead compartment was included, when more parameters were optimised simultaneously. The modified Powell method tended to find points closer to the starting parameter values, as would be expected. Although, in some cases, these points had a slightly lower error than the points found by the global PSwarm method. It is possible the performance of the PSwarm method would be improved if its settings were altered, in particular, if the number of particles in the swarm was increased. This will require further investigation.

## **Lactate**

In all of the piglets where Lac/NAA ratio was measured except for one, the lactate measured signal showed a delay before beginning to increase relative to the other signals and relative to the model. Although a delay was also seen in the model, it was less than that in the measured data.

The comparison of the modelled lactate with the experimental measurement is complicated by two facts. Firstly, it is the lactate to NAA ratio that was measured rather than absolute lactate concentration. NAA concentration is an important marker of cell death and also of cell function, and it has been shown to decrease following HI [124]. However this is likely to occur on a longer time scale than changes in lactate concentration and so here is assumed to remain constant throughout. It will be necessary to include NAA in future versions of the model, if it is to be used for longer-term applications such as investigating secondary energy failure and treatments of HI. This will require a distinction between astrocytes and neurons which may also benefit the modelling of lactate. The second difficulty in comparing lactate with measured Lac/NAA ratio comes from the inability to determine the lactate concentration at baseline conditions. It is not known at exactly what concentration the lactate can be detected. The choice to both scale and offset the modelled lactate signal is based on these considerations. The scaling

factor represents an unknown (but constant) concentration of NAA. The offset allows for low concentrations of lactate not being measurable. An alternative to an offset is a cutoff i.e. a concentration of lactate below which the lactate measured was considered to be 0. This was attempted, but gave poor results. This is because a step would be seen as the Lac/NAA concentration returned to baseline following the insult. This was not seen in the experimental results: instead a gradual return to baseline was seen.

A difficulty in modelling cell lactate concentration is caused by the unknown concentration of lactate in the blood. Lactate from the blood is metabolised mainly by the liver. Modelling this is beyond the scope of the model, since it is a model of the brain. Although blood lactate levels were measured during the experiment, this occurred infrequently. The blood lactate concentration was therefore assumed to remain constant throughout the experiment. Further investigation into how large an effect this plays upon the rate of recovery of lactate would be helpful. Alternative solutions to this problem, such as setting blood lactate concentration based on cell lactate concentration and blood lactate measurements, could also be investigated.

### 6.5.3 Cell death

Modelling a fraction of the cells as dead was able to account for the incomplete recovery of NTP and  $\Delta\text{oxCCO}$  following HI. However, it was not able to account for the  $\Delta\text{HbO}_2$  and  $\Delta\text{HHb}$  measurements that were observed. The model predicted that a reduced number of cells metabolising oxygen would lead to an overall reduction in  $\text{CMRO}_2$  and therefore a drop in oxygen extraction fraction. This would mean that more oxygen remained in the blood and so  $\Delta\text{HbO}_2$  would rise and  $\Delta\text{HHb}$  would fall. However this was not seen in the measurements. In some of the piglets which did not recover, the opposite was seen i.e.  $\Delta\text{HbO}_2$  was significantly decreased relative to baseline and  $\Delta\text{HHb}$  was increased. Assuming the hypothesis of dead cells is correct, the two possible explanations which appear most likely are: firstly, that blood is no longer flowing to all parts of the brain. This would cause a decrease in CBF and therefore a decrease in oxygen delivery, despite normal  $\text{S}_a\text{O}_2$  levels. The second explanation is that  $\text{CMRO}_2$  in the functioning cells is greatly increased. This may occur as a result of uncoupling in the mitochondria between the reduction of oxygen and the synthesis of ATP. Uncoupling is known to occur after hypoxic or ischaemic injury [263]. It would generally be expected to cause an oxidation of CCO; but if uncoupling occurred alongside cell death, this oxidation may be masked by the larger reduction effect. Another possibility is that oxygen consumption is taking place in the dead cells but by NADPH oxidase rather than via CCO which can occur following phagocytosis [264].

If the assumption of cell death is incorrect, it is more difficult to explain the relationships between the  $\Delta\text{oxCCO}$  and MRS measurements. Uncoupling in the mitochondria could lead to a reduced NTP concentration. The model includes a simple way of representing uncoupling (see Equation 2.47). Figure 6.16 shows the effects of increasing the uncoupling parameter  $k_{\text{unc}}$  from its default value of 1.0 to 5 after the nadir of the insult. With the other parameters at their normal values, the model predicts an oxidation of  $\text{Cu}_A$ . A small oxidation of  $\text{Cu}_A$  has also been observed experimentally after the administration of an uncoupler (dinitrophenol) to newborn piglets [265]. However, the effect of uncouplers on  $\text{Cu}_A$  redox state is not straightforward [266] and altering the model parameter  $c_{k2}$  from 0.02 to  $-0.02$  causes  $\text{Cu}_A$  to instead become more reduced. This change has only a small effect on the NTP concentration and the  $\text{CMRO}_2$ , which the model predicts to be increased slightly from baseline. The parameter  $c_{k2}$  controls how the rate of the second reaction, of the three that represent the electron transport chain, depends on the protonmotive force. It is one of several parameters which could change the way that the oxidation state of  $\text{Cu}_A$  responds to uncoupling, and this is an area of the model which requires further investigation. However, the relationship seen in the model between NTP and PCr concentrations does not match that seen in the measurements. The model predicts that the typical buffering relationship between NTP and PCr will still be present despite mitochondrial dysfunction, and therefore PCr concentration is predicted to be low after HI. This is observed in secondary energy failure in piglets subjected to HI i.e. the relationship between NTP and  $\text{PCr}/\text{P}_i$  is the same in the primary insult and in the delayed secondary energy failure, suggesting mitochondrial dysfunction [267]. However, these measurements show a similar drop in PCr and NTP concentrations which is more consistent with cell death.

Other possible explanations for the results include an impairment in glycolysis or the TCA cycle, but this would lead to an oxidation in CCO. A large decrease in oxygen delivery relative to baseline may also explain the results. This is unlikely since  $\text{S}_a\text{O}_2$  levels returned to normal, however measurements of CBF would give further confirmation of this.

Several factors need to be kept in mind when analysing this data. Firstly, the NIRS and MRS measurements do not come from exactly the same area of the brain and it is known that HI damages different parts of the brain to different extents. Secondly, there are other changes to the brain following HI. In particular, cerebral oedema is likely to occur [268] which could have an effect on the measurements. Finally, the haemoglobin measurements may also be influenced by changes in haematocrit that have taken place during or after the insult.

In order to further investigate these changes, it will be helpful to simulate two or more

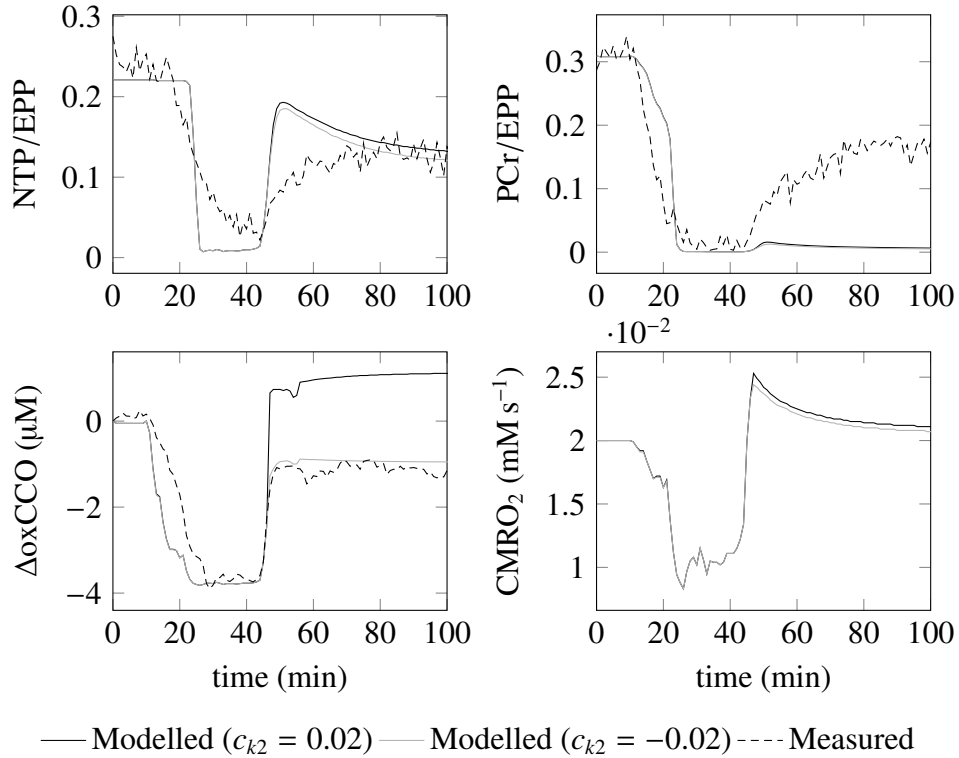


Figure 6.16: Comparison of measured (dashed) results from piglet LWP188 and modelled results with uncoupling parameter  $k_{unc}$  increased from 1.0 to 5.0 at the nadir of HI. Modelled results are shown for  $c_{k2} = 0.02$  (black) and  $c_{k2} = -0.02$  (grey)

cell populations which may have been damaged in different ways or to different extents. This is currently not easy to do using the BRAINCIRC environment, but it is important since brain metabolism is likely to become more heterogeneous after damage is incurred during HI. It will also be necessary to look more closely at mitochondrial uncoupling in the model. Although it is currently possible to simulate uncoupling, even severe uncoupling does not lead to the large increase in  $CMRO_2$  that might be expected. Measurements from a greater number of piglets and measurements of CBF will also allow these effects to be investigated further.

## 6.6 Conclusions

The BrainPiglet model was applied to data from 14 piglets subjected to HI. The model was found to reproduce the patterns seen in the data well, but there were differences, particularly in the speed at which the changes occurred. Morris sensitivity analysis was used to determine which parameters had a significant influence on the fit of the model to the data. The parameters identified were optimised, leading to a significant improvement in the fit of the model to the data, confirming that the Morris method is useful

for screening parameters. However, parameter optimisation led to some physiologically unrealistic parameter values, suggesting the parameters could not all be uniquely identified.

Introducing a dead compartment to the model improved the simulation of data from piglets which did not recover. Simulation of mitochondrial uncoupling by the model suggests that dead cells (possibly in combination with mitochondrial uncoupling) is a more likely explanation for the non-recovery of the piglets than mitochondrial uncoupling alone. More investigation will be required to understand why the measured haemoglobin signals are not consistent with the predictions of the model when a dead compartment is included.

# Chapter 7

## Discussion

### 7.1 Summary

This thesis described the use and development of novel physiological models of cerebral circulation and metabolism. The models were developed with the aim of simulating the non-invasive measurements made by near-infrared spectroscopy (NIRS) and magnetic resonance spectroscopy (MRS). As far as possible, the models aim to represent the underlying physiological processes occurring, whilst also simplifying where possible to reduce complexity. Where appropriate, parts of other relevant models have been modified and incorporated, and standard biological modelling techniques have been used. The models were developed, and simulations were carried out using the BRAINCIRC modelling environment.

Firstly, in Chapter 4, the BrainSignals model [12] was used to simulate cerebral responses to a hypercapnia challenge in healthy adult humans. The model correctly predicted that during hypercapnia, tissue oxygenation index (TOI) and velocity of blood in the middle cerebral artery ( $V_{mca}$ ) would both increase as a consequence of the well known vasodilation effect of  $CO_2$ . In order for the model to correctly reproduce the magnitudes of the changes in TOI and  $V_{mca}$ , the parameter  $R_C$ , representing the sensitivity of blood flow to carbon dioxide levels, was optimised for each of the fourteen subjects. For TOI, the haemoglobin concentration [Hbtot] was also optimised to allow matching of the baseline TOI value. After optimising these parameters using both the modified Powell's method and the PSwarm method to minimise the mean square error between modelled and measured signals, the model was able to reproduce the changes in TOI and  $V_{mca}$  when optimising to each signal individually. However, the model was not able to reproduce both measured signals simultaneously. Matching the

measured TOI signal required a smaller sensitivity to  $\text{CO}_2$  (i.e. a smaller value for  $R_C$ ) than matching the measured  $V_{\text{mca}}$ .

Three possible reasons for this discrepancy were investigated using the model. Firstly, that changes in venous volume (held fixed in the BrainSignals model) could be important; secondly, that changes in oxygen metabolism caused by  $\text{CO}_2$  may not be accounted for in the model and finally, that the TOI signal may not originate entirely from within the brain. The model was used to show that the first two of these effects would have to be large in order to account for the discrepancy, much larger than suggested by relevant previously reported experiments in humans and animals. Therefore, the model suggests that TOI measurements should be interpreted with caution, and may not accurately reflect the tissue oxygen saturation of the brain tissue. More information could be gained by investigating other signals such as changes in the total haemoglobin concentration, which is related to cerebral blood volume, or oxidation changes of CCO which can reflect changes in oxidative metabolism. The work from this chapter has been published in *Advances in Experimental Medicine and Biology* [209].

Chapter 5 described the modification and extension of the BrainSignals model to create the BrainPiglet model and apply this type of modelling to neonatal piglets for the first time. Several of the model parameters were altered to values appropriate for newborn piglets. The metabolic part of the model was expanded to allow simulation of metabolite concentrations measurable by MRS. This included the addition of ATP production and use to simulate the concentrations of ATP, phosphocreatine and inorganic phosphate which can be measured by  $^{31}\text{P}$ -MRS. It also included the addition of lactate dynamics for comparison of lactate concentration changes with measurements from H-MRS. The circulation part of the model was also altered to include a varying venous volume, and a supplying arterial compartment was added for simulating carotid artery occlusion.

The BrainPiglet model was first applied to data from a study in which newborn piglets were subjected to brief periods of anoxia [247]. Blood pressure data, presented in the paper, and oxygen saturation estimated from the protocol were used as inputs to the model, and its outputs were compared with averaged data measured by NIRS and  $^{31}\text{P}$ -MRS. Initial comparisons between the simulations and measured data showed four key differences which were improved by changing the values of particular model parameters. In order to simulate the hyperaemia observed following the resumption of the oxygen supply, the autoregulation parameter was reduced from 1 to 0.5. This supports the hypothesis that autoregulation may be impaired or not fully developed in these piglets. However, this would need further investigation to confirm, since the autoregulation curve of piglets is not well known and may depend on a number of factors including the anaesthesia used and the age of the piglets. It is also possible a temporary impair-

ment in autoregulation may have occurred following the anoxia. The ratio between the changes in PCr and  $P_i$  measured in the experiment required that, given the normal concentration of PCr assumed in the model, the normal ratio of PCr to  $P_i$  be increased to 2.7. The normal NAD to NADH ratio was decreased in order to reduce the rate of CCO reduction, and the sensitivity of glycolysis rate to changes in ATP concentration was increased to decrease the simulated drop in PCr.

With these parameters, the model was able to reproduce the measured data well. However, it is possible that changes to other parameter values could also produce these results, particularly in the case of the last two parameters mentioned. It is therefore important that physiological knowledge is combined with a systematic, mathematical analysis of the effects of changing parameter values, which was consequently included when using the model to simulate hypoxia ischaemia (HI) which was the subject of the following chapter.

The final aspect of the results from the anoxia study investigated using the model was two previously observed, but not well understood features of the  $\Delta_{ox}CCO$  signal. The model was used to demonstrate that a low affinity of CCO for oxygen could explain the delay in reduction of CCO, although the mechanism for this effect, and the reasons why it is observed in piglets but not in adult humans remain unknown. The model also demonstrated that this low affinity of CCO for oxygen is consistent with the hyperoxidation of CCO seen following anoxia; and although the effect is reduced when the affinity for oxygen is reduced in the model, it is still present. The hyperoxidation is not seen in the model, however, when the dependence of metabolic rate on phosphorylation potential is removed. Therefore, the model supports the suggestion that increased metabolism following anoxia is a likely cause of the observed hyperoxidation of CCO. The work from this chapter has been published in the Journal of Royal Society Interface [236].

The BrainPiglet model was then used to simulate data from individual piglets subjected to HI and monitored by NIRS and MRS which was the subject of Chapter 6. Before applying the model to the data, a Morris sensitivity analysis was used to investigate which of the parameters were most influential on the steady state of the model. Around one third of the parameters were found to have very little, or no influence on the steady state values of any of the model variables that are compared with measured data in this thesis. For most of these variables, there were one or two parameters with a much greater influence than the others. In most cases, the parameters with the largest influence were those that represent the normal concentration of the variable. The results of a Morris sensitivity analysis depend on the ranges that are used for the parameters. Here the range was set to  $\pm 20\%$  for most parameters, and the analysis could be improved by considering

the ranges more carefully and incorporating existing physiological knowledge into their ranges.

The oxygen saturation, blood pressure measurements and occlusion times from fourteen piglets in which HI had been induced by carotid artery occlusion and reduced oxygen inspiration fraction were used as inputs to the model. Its outputs were compared with NIRS measurements for all piglets and H-MRS measurements for some piglets and <sup>31</sup>P-MRS measurements for others. The model predicted the direction of change, but did not replicate the magnitude and time course of the changes. For some piglets, the CCO and <sup>31</sup>P-MRS measurements did not return to baseline following the insult. The model was not able to replicate this. Further Morris sensitivity analysis was performed to assess which parameters influenced the fit of the model to the data. The results identified several parameters which were then optimised to the signals for each individual piglet. In order to simplify the optimisations, the parameters were only optimised to the signals for which they were found to be influential. After optimising these parameters, the fit of the model to the data was improved, however not all of the parameter values were well identified by the data.

In the piglets which did not recover following HI, the data showed a relationship between the extent of CCO, ATP and PCr recovery. To investigate this, a fraction of the brain was modelled as dead following the insult. This was done in a simple way, by assuming no oxygen consumption in the dead cells, with CCO fully reduced and all exchangeable phosphate in the form of P<sub>i</sub>. The fraction of cells considered as dead was optimised, and the optimised values ranged from almost 0 to 0.8. This greatly improved simulation of CCO and MRS signals in the piglets that did not recover. However, there was a worsening of the fit of the simulated haemoglobin signals to the data following HI. The reasons for this will require further investigation. Different mechanisms of cell death will also need to be investigated. Mitochondrial uncoupling was also considered as a cause of the non-recovery of the CCO and MRS signals. Although mitochondrial uncoupling would generally be expected to cause an oxidation of CCO, the model suggested it could also be associated with a reduction depending on the properties of the electron transport chain. However, the model also demonstrated that the relationship between the ATP and PCr signals was not consistent with mitochondrial uncoupling being the sole cause of the failure of the <sup>31</sup>P-MRS signals to fully recover. Part of the work from this chapter has been published in *Advances in Experimental Medicine and Biology* [255] and part of this work has also been submitted to *PLOS Computational Biology*.

The BrainPiglet model has been shown to aid data interpretation from experiments on newborn piglets, and help to generate and assess hypotheses relating to the underlying

physiology. To our knowledge, this is the first time that this type of model has been applied to HI in piglets. There are many ways in which the model and the modelling process can be improved, both to widen the measurements and situations to which the model can be applied, and to increase accuracy and confidence in its predictions. These are discussed below.

## **7.2 Future work**

This section discusses research which is beyond the scope of the work in this thesis. Possible areas of future improvement and expansion are outlined. I have carried out some preliminary work related to improvements in parameter estimation which is described here. This, and other areas of research are currently being pursued by other members of the group.

### **7.2.1 Mathematical and computational techniques**

#### **Sensitivity analysis**

Improved methods of sensitivity analysis will allow a more rigorous and in-depth analysis of the model. Morris sensitivity analysis could be improved by choosing the parameter distributions more carefully, choosing different functions as the output of interest, and investigating the effect of using different numbers of repeats. Other methods of sensitivity analysis could also be investigated, such as a variance based approach using Monte Carlo methods [262].

#### **Parameter estimation**

Parameter estimation could be improved by using different frameworks, such as Bayesian methods. This has already begun to be carried out, and will therefore be described briefly here.

For a set of model parameters  $\theta$  and measured data  $D$ , Bayes theorem states that

$$P(\theta|D) = \frac{P(D|\theta)P(\theta)}{P(D)} \quad (7.1)$$

where  $P(\theta)$  is the prior probability distribution of the parameters,  $P(\theta|D)$  is the likelihood of the measured data given the parameters and  $P(D)$  is known as the marginal likelihood. Bayesian inference aims to determine the posterior distribution  $P(\theta|D)$ . Usually, the relative probabilities are compared and  $P(D)$  is not calculated.

For a deterministic model  $M$  and a set of measurements at different times  $D$  with independent identically, normally distributed errors with precision  $\tau = 1/\sigma^2$ , the likelihood at each time point is given by

$$\sqrt{\frac{\tau}{2\pi}} \left( \frac{-\tau (M(t) - D(t))^2}{2} \right) \quad (7.2)$$

and the log of the overall likelihood for  $N$  time points is

$$\log P(\theta|D) = \frac{-\tau}{2} \sum_{t=1}^N (M(t) - D(t))^2 + \frac{N}{2} \log \frac{\tau}{2\pi}. \quad (7.3)$$

Therefore, maximising the likelihood is equivalent to minimising the mean square error between modelled and measured data, as is typical in traditional parameter optimisation. Bayesian methods are superior to these methods in two ways: i) they incorporate prior information about the distribution of the parameters and ii) instead of finding a single point in the parameter space, they generate a posterior parameter distribution, usually by the use of a Markov chain Monte Carlo (MCMC) sampling method. However, the disadvantages of these methods are that they require many more model evaluations, and the assumption of independent, identically distributed errors may not be appropriate, or the precision of the errors may not be known. Bayesian methods have recently begun to be used for parameter estimation in models of dynamic biological systems [269].

If a model is not deterministic, calculating the likelihood is usually not possible within a reasonable time frame. Likelihood-free Bayesian inference methods provide an estimate of the posterior distribution without requiring calculation of the likelihood. One of these methods is approximate Bayesian computation (ABC). In its simplest form, ABC can be implemented with a rejection sampler. A trial point is chosen by sampling from the prior distribution. A distance between the simulated data at this trial point and the measured data is then calculated. A typical choice for this distance is the sum of the squared errors at each of the time points. If the distance is less than a chosen tolerance, the trial point is accepted, otherwise it is rejected. This is then continued until the chosen number of points have been accepted, and these points make up the estimate of the posterior distribution. This method can be very inefficient (i.e. have a very low acceptance rate) and it is has therefore been combined with MCMC methods [270]. A high tolerance value is used initially, which is then gradually reduced over a series of

sample populations until a final small tolerance is reached. ABC methods have been used in systems biology for both parameter estimation and model selection [270, 271].

ABC-SysBio [272] is a software package that performs parameter estimation and model selection using ABC. It is now being used for parameter estimation with the Brain-Signals model. This involved writing extensions to the package to enable the simulations to be carried out using the BRAINCIRC environment. An example of applying this method to hypercapnia data from one of the 14 subjects described in Chapter 4 is described here. To take into account the uncertainty in the measurements used as inputs, normally distributed random errors with fixed variance were added to the input data at each time point for each simulation. As in Chapter 4, the  $P_a\text{CO}_2$ ,  $\text{SaO}_2$  and  $P_a$  measurements were used as inputs, but this time with added random errors of standard deviation 1 mmHg, 1 % and 0.5 mmHg respectively. An example is shown in Figure 7.1.

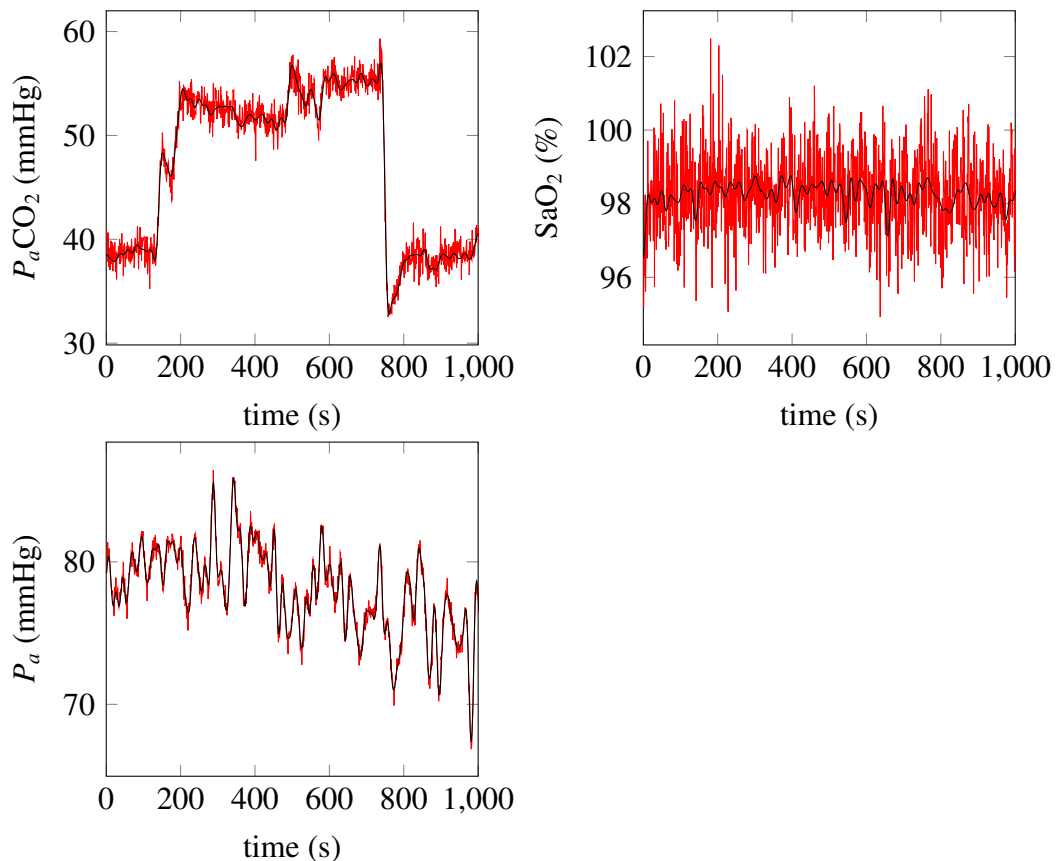


Figure 7.1: Measured  $P_a\text{CO}_2$ ,  $\text{SaO}_2$  and  $P_a$  during a hypercapnia challenge in one subject (black), and model inputs generated by adding normally distributed noise to the measurements (red).

Two parameters were used (the same as those optimised in Chapter 4):  $[\text{Hbtot}]$  with a normal prior of mean 9.1 mM and standard deviation of 5.0 mM and  $R_C$  with a uniform

prior from -1 to 10. The modelled and measured TOI and  $V_{mca}$  were compared. The details of the ABC MCMC method can be found in Toni *et al.* [270].

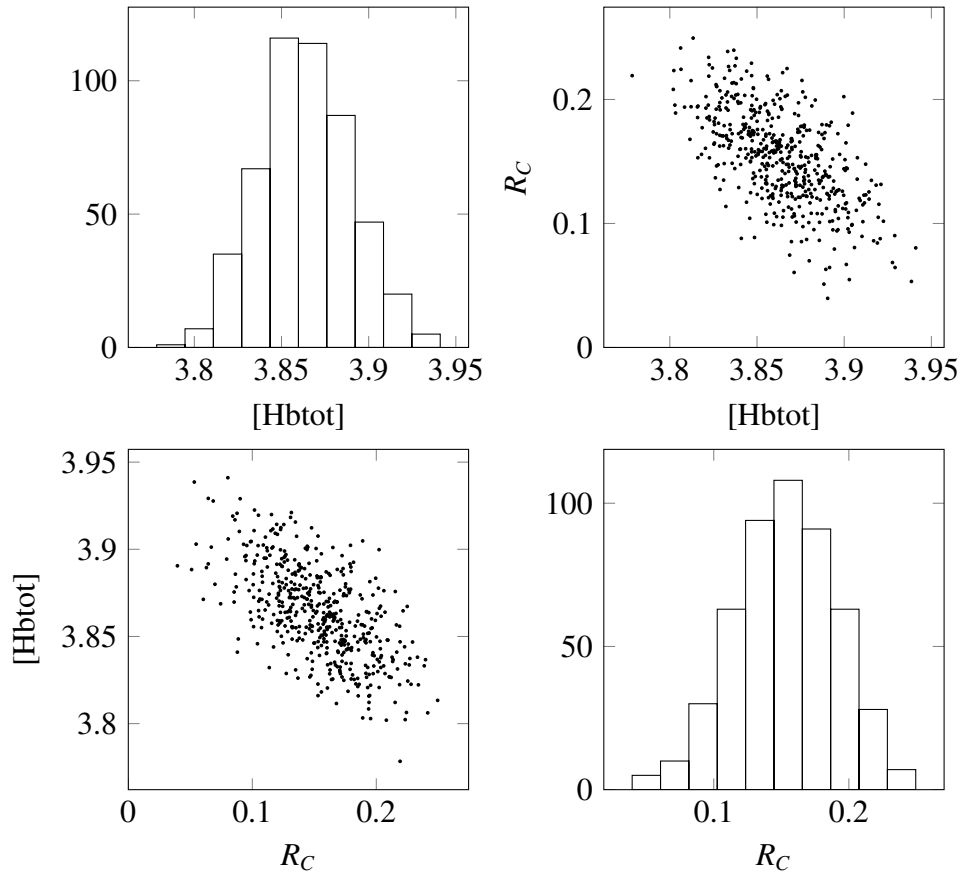


Figure 7.2: Example of ABC parameter estimation. Estimated posterior distribution for model parameters  $[Hbtot]$  and  $R_C$  generated by comparing measured and simulated TOI and  $V_{mca}$  signals.

A population size of 500 was used, and an automated tolerance schedule was run, with the final tolerance set to a small value which was not reached. The process was stopped after 120 populations by which time the acceptance rate had fallen to 0.004 indicating that the tolerance was very close to its minimum possible value. The resulting sample of 500 points, which serve as an estimate of the posterior distribution, is shown in Figure 7.2. There is a slight relationship between the two parameters, but both have been identified to within a fairly narrow range. It is difficult to compare this with the optimisation from Chapter 4 since the weightings used in that optimisation affect the results.

This is ongoing work. In particular, the effect of using different distributions to represent uncertainty in the input will be investigated. Also, different numbers and groups of parameters will be used, since a major advantage of this method is that it can show relationships between parameters and help to assess whether their values have been

successfully identified.

### **Modelling language**

Improvements can be made by extending and enhancing the BRAINCIRC modelling environment. Improving the compatibility with SBML and CellML would make experimentation with other models simpler, and could also enable inclusion of other models in a modular way. It would also improve the ability to make use of SBML software tools developed by other groups, of which there are many [187]. In particular, the Systems Biology Workbench is an opensource project that provides a framework for different simulation software to communicate in order to encourage code reuse and tool sharing [273]. Making BRAINCIRC compatible with this framework would help to integrate its use with other tools.

### **7.2.2 Representation of physiology**

Future improvements to the model itself will include a more detailed analysis of several of the simulated processes, including the TCA cycle and glycolysis, in order to further validate the simplified equations that are used. In addition, the model would benefit from separating the cellular compartments to differentiate between astrocytes and neurons. This feature is present in many models, and other models have also been altered in this way. For example, the model by Aubert and Costalat of brain metabolism and haemodynamics [174] was later modified to distinguish between the two cell types [147]. The metabolic differences between astrocytes and neurons include their glucose and lactate transport properties, a consequence of the different type and distribution of their transport proteins as discussed in Section 1.2.3. The aim of this modification for our model would be to better simulate the changes in lactate concentration which are an important feature of HI. It would also allow the simulation of NAA which is visible on the H-MRS spectrum. NAA is found only in neurons, but it undergoes a metabolic cycle in the brain involving astrocytes and oligodendrocytes [274]. NAA concentration has been observed to decrease following HI [124], and H-MRS measurements are often expressed as Lac/NAA ratios, so its simulation is important.

### 7.2.3 Spatial resolution

The model could also be improved by adding spatial resolution. This is a significant change which would make the model more complex and therefore increase the time taken to solve it. At its simplest, this would involve creating multiple copies of the model with different input parameters. For example, regional measurements of CBF could be used as an input. CBF varies throughout the brain, and its pattern is likely to be altered during ischaemia. This is particularly the case for piglets subjected to carotid artery occlusion whose remaining cerebral circulation is provided via the vertebral arteries and the circle of Willis [122]. Furthermore, it is known that different regions of the brain are affected differently by HI, for example the cerebellum and hippocampus are particularly vulnerable to HI [275]. Other than varying CBF, the possible causes of this regional variation of HI damage include differing metabolic rates. By altering parameter values across the model to reflect regional differences, these hypotheses could be investigated. It would also be interesting to add an extracellular space compartment to the model so that the diffusion of metabolites including glucose and lactate could be modelled. This approach has recently been used to investigate brain damage caused by stroke [276].

Similar to, but simpler than adding spatial resolution to the model, would be simulating distinct (but spatially unrelated) populations of cells, representing, for example, damaged and healthy cells following HI. This is an extension to the simplified method of modelling cell death used in Chapter 6. It will also be necessary to investigate and simulate mechanisms of cell death, rather than using a switch parameter. Modelling of uncoupling will also be investigated further, which may help improve the simulation of the recovery period following HI.

### 7.2.4 Comparison with new measurements

The model has been developed to simulate measured signals, and its development will continue to be driven by this aim. Additional available measurements will allow further validation and testing of the model. Measurements of CBF from arterial spin labelling should become available, and will help to improve and validate the modelling of carotid artery occlusion and other aspects of blood flow. It is already possible to simulate pH changes with the model, and its simulations are currently being compared with measurements from  $^{31}\text{P}$ -MRS [277]. Further in the future, it is planned to collect EEG measurements during the insult, and the model could be extended to simulate these. More details on pH and EEG measurements are discussed below. Finally, simulation of

cell death may be improved by information from histological analysis of brain samples from the piglets which is currently in progress.

In this thesis, averaged datasets for HI in piglets were not used. This is because the number of piglets included was fairly small, and differences in the experimental protocol and the timings of the insult between piglets make these difficult to create. Measurements from a greater number of piglets will allow averaged datasets to be generated. In particular, datasets from groups of piglets classified as having good and poor outcomes could be compared. Modelling of averaged data will complement modelling of data from individual piglets, which allows differences between piglets to be investigated. Simultaneous data from  $^1\text{H}$ -MRS and  $^{31}\text{P}$ -MRS may also become available, which would help with understanding the relationships between the signals.

## **pH**

Measurements of pH from  $^{31}\text{P}$ -MRS are currently being compared with simulated pH. Acidosis is an important feature of HI, and a shift in brain pH is known to occur following HI [278]. Changes in pH can alter protein structure and consequently affect cell function. It is therefore important that pH is properly taken into account in the BrainPiglet model. Some measurements of pH calculated from the chemical shifts of the  $\text{P}_i$  and phosphoethanolamine (PEt) peaks of the  $^{31}\text{P}$ -MRS spectra by the method described by Cady *et al.* [279] are available. A preliminary comparison of this measurement with simulated cytoplasmic pH for one piglet is shown in Figure 7.3. The simulated mitochondrial pH is also shown. There is promising agreement between the measured pH and simulated cytoplasmic pH. More work in this area has been published by Hapuarachchi *et al.* [277].

One difficulty in interpreting these measurements is that they originate from different compartments. The model shows an increase in mitochondrial pH during the insult and a fall following it. It is very difficult to measure mitochondrial pH, so it will be interesting to look further into the model's predictions.

## **EEG**

Another measurement that may become available is EEG. Mathematical modelling of electrical activity in neurons has a long history. One of the most well-known mathematical models in biology is the Hodgkin-Huxley model which describes the action potential of a neuron [280]. Neuronal activity in the brain has also been extensively

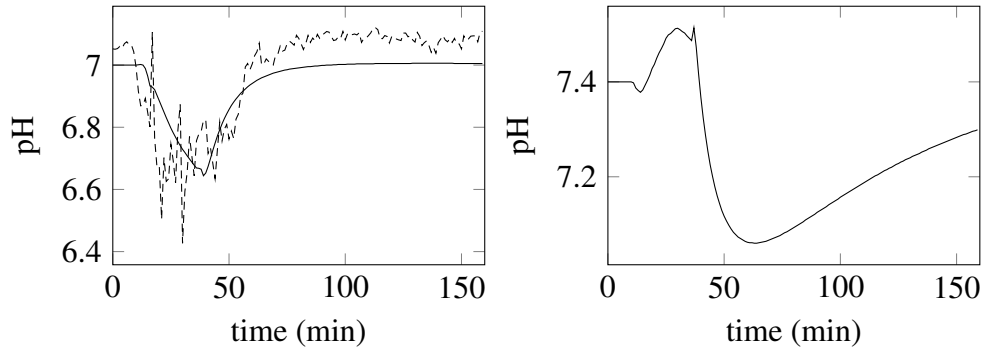


Figure 7.3: Left: Modelled cytoplasmic pH (solid) and pH calculated from <sup>31</sup>P-MRS spectra (dashed) for piglet LWP180 Right: Modelled mitochondrial pH

studied and modelled using networks and graph theory [281]. Several models exist which link neuronal activity throughout the brain to EEG signals [282, 283]. Sotero *et al.* [284] have linked a model of this type to a simple model of metabolism and blood flow which aims to explain the BOLD response seen in fMRI. The EEG part of the model involves spatial interactions between voxels, whereas the metabolic and blood flow part of the model is solved separately for each voxel i.e. no spatial interactions between metabolites are considered. A similar integration with a model of electrical activity and EEG measurements may be possible with the BrainPiglet model. Solving the model equations for many different voxels would be more computationally expensive than for a single voxel as is currently the case. However, since the NIRS and MRS measurements collected during the HI experiments do not have spatial resolution, it may be possible to reduce the resolution required for the model.

### 7.2.5 Adaptation to humans

Long-term, the aim is to use the model in a clinical setting to help inform and monitor the treatment of birth-asphyxiated infants. Adaptation of the model to human infants will require taking into account the physiological differences between human babies and piglets. For example, the CBF in a newborn human is 10–20 ml 100 g<sub>brain</sub><sup>-1</sup> min<sup>-1</sup> which is approximately one third of the adult value [285]. In piglets, the CBF is higher at around 50 ml 100 g<sub>brain</sub><sup>-1</sup> min<sup>-1</sup> [59] and much closer to the value in the adult pig [286]. The CMRO<sub>2</sub> in newborn humans is around 0.5–1.5 ml 100 g<sub>brain</sub><sup>-1</sup> min<sup>-1</sup> [287] whereas the value in an adult is approximately 3 ml 100 g<sub>brain</sub><sup>-1</sup> min<sup>-1</sup> [288]. Again, the pig has a higher CMRO<sub>2</sub> at birth of 2.5 ml 100 g<sub>brain</sub><sup>-1</sup> min<sup>-1</sup> [238] but the adult value of 2.5–3.5 ml 100 g<sub>brain</sub><sup>-1</sup> [286, 289] is not much greater.

The effects of anaesthesia must also be considered. In general, piglets are anaesthetised

throughout experiments involving HI, whereas human infants will not usually be anaesthetised. Isoflurane anaesthesia, which has been used in the experiments analysed in this thesis, is generally reported to either have no effect on CBF or to slightly increase it, but to significantly decrease CMRO<sub>2</sub> [290, 291, 292]. The values used in the BrainPiglet model are appropriate to anaesthetised piglets. However, the fact that these values are different from the ‘normal’ awake values has not been taken into account and this may have consequences when adapting the animal model to the human.

### **7.2.6 Secondary energy failure and treatment**

Before adapting the model to humans, the modelled period must be extended to include secondary energy failure. This is essential, since data from the period of asphyxia will not be available for human infants. To do this, it will be necessary to simulate additional biochemical processes. This will include modelling additional metabolites such as glutamate and nitric oxide (NO) so that the processes involved in secondary energy failure as discussed in Section 1.2.4 can be simulated. Addition of NO to the BrainPiglet model would be aided by previous work involving the addition of NO to the BrainSignals model to investigate hypoxic vasodilation [293]. It is hoped the model will help to suggest hypotheses and experiments that will improve understanding of secondary energy failure. Modelling the mechanisms that lead to damage will also allow the possibility of modelling therapies which target these mechanisms, for example xenon, which is an antagonist of the NMDA glutamate receptor. Simulation of the effects of hypothermia, one of the most commonly used treatments, will help to bring the model closer to a tool which can be used in the clinic.

## **7.3 Summary**

As part of this PhD a new physiological model (BrainPiglet) has been developed to simulate circulation and metabolism in the brain of neonatal piglets. This model can integrate multimodal data and has been used to simulate NIRS and MRS measured signals during both anoxia and HI in piglets. The piglet HI experiments are used to mimic birth asphyxia in human infants, and it is of great clinical importance to be able to understand the circulatory and metabolic changes that happen during and after these episodes. The modelling approach developed as part of this PhD has demonstrated the potential of the use of computational modelling to aid in the interpretation and integration of these multimodal non-invasive measurements, with the aim of enhancing our understanding

of HI. In particular, the use of the model suggested that autoregulation was impaired in the piglets subjected to anoxia, and that the failure to recover following HI seen in some piglets was caused by cell death. In addition, this thesis demonstrated and applied mathematical techniques for sensitivity analysis and parameter optimisation to physiological models. These techniques can enhance the interpretation of these models by suggesting important physiological connections between measured data and model parameters. Further work is concentrated on extending the model to simulate the human neonatal brain, and improving optimisation and parameter fitting methods such as the Bayesian method described in this chapter.

# Appendix A

## Piglet data

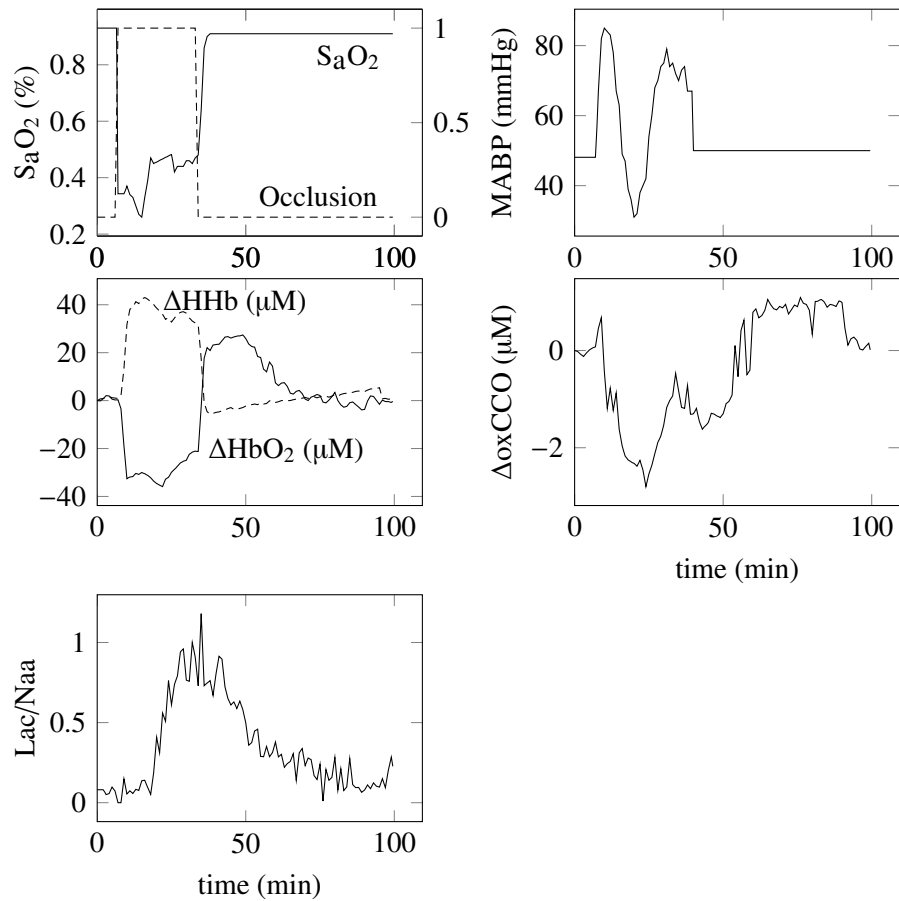


Figure A.1: Measured data for Piglet LWP158

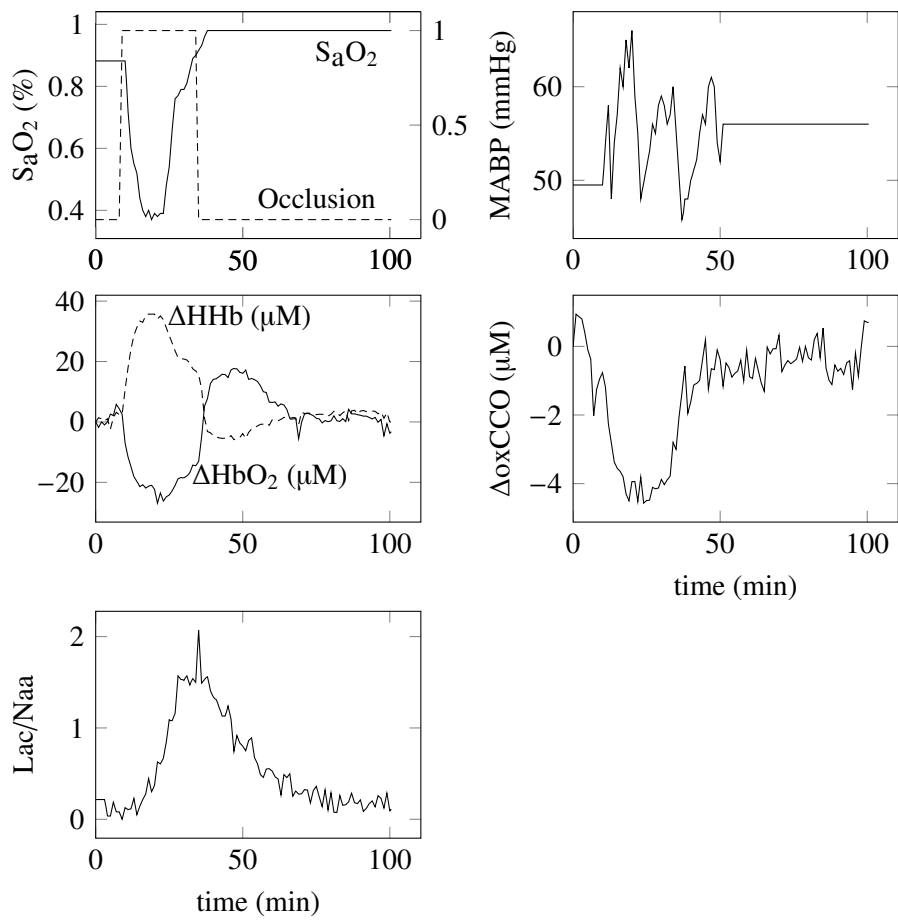


Figure A.2: Measured data for Piglet LWP164

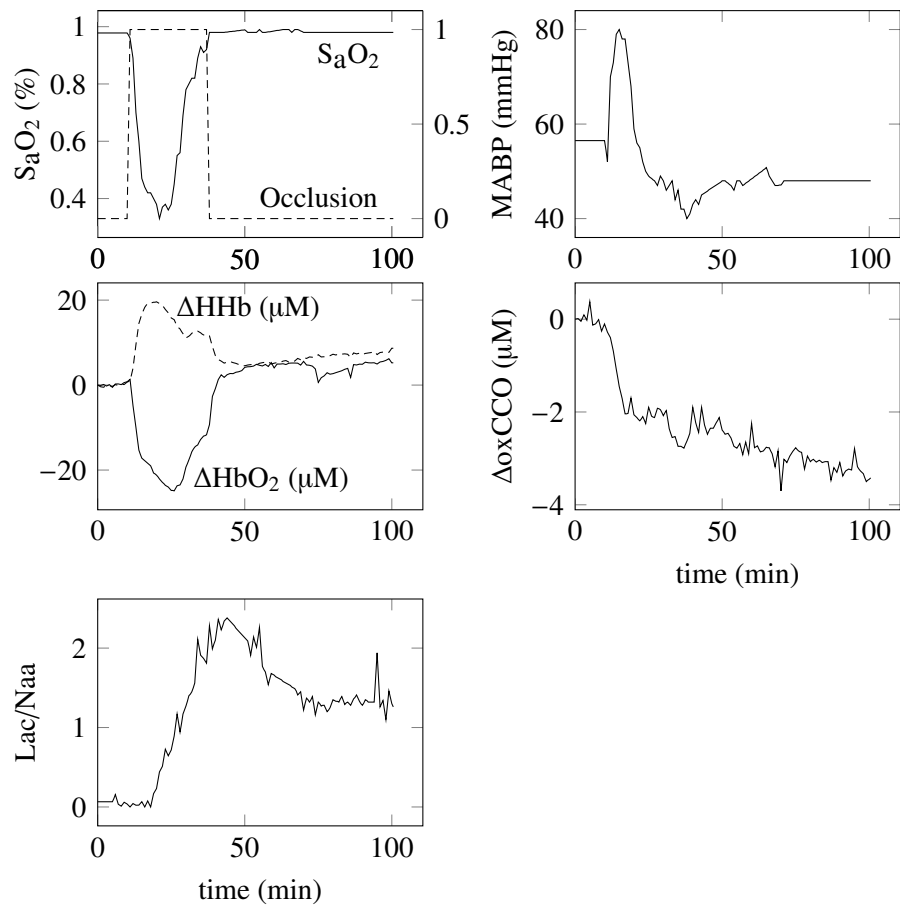


Figure A.3: Measured data for Piglet LWP167

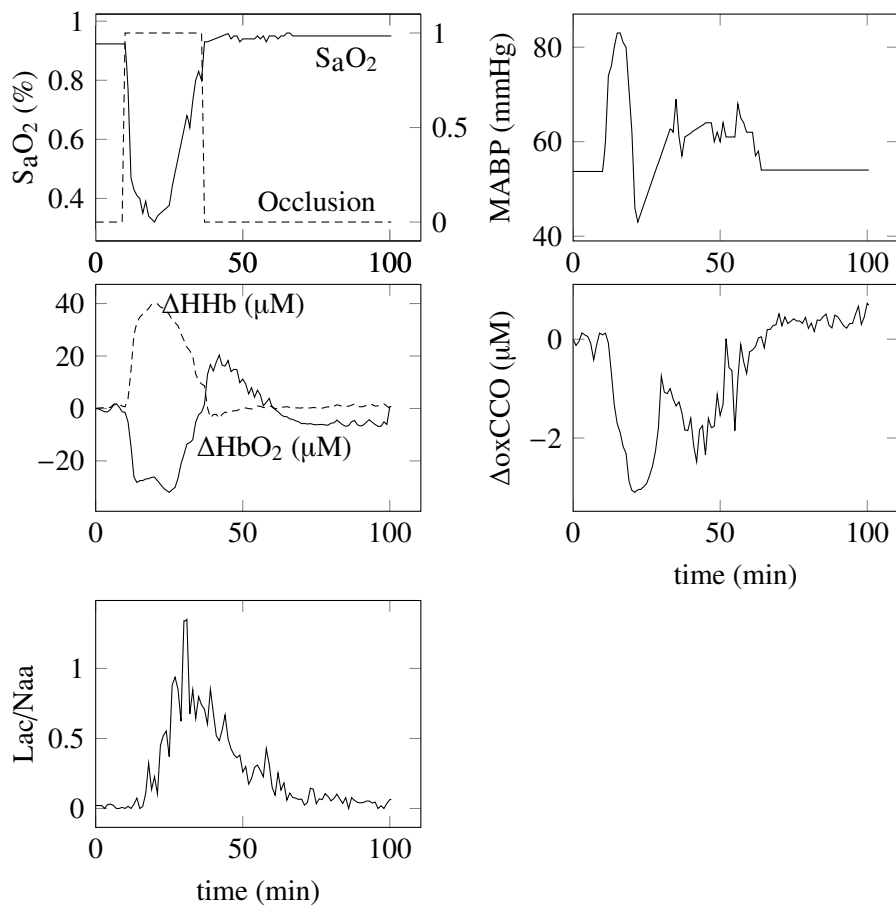


Figure A.4: Measured data for Piglet LWP168

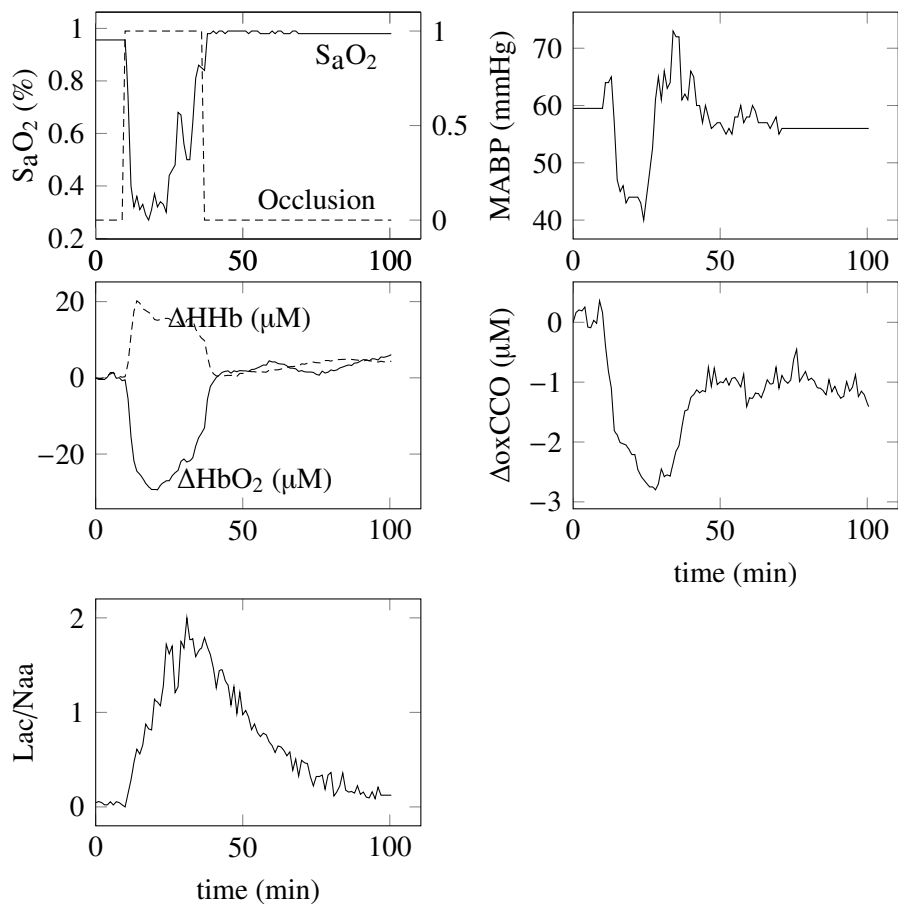


Figure A.5: Measured data for Piglet LWP169

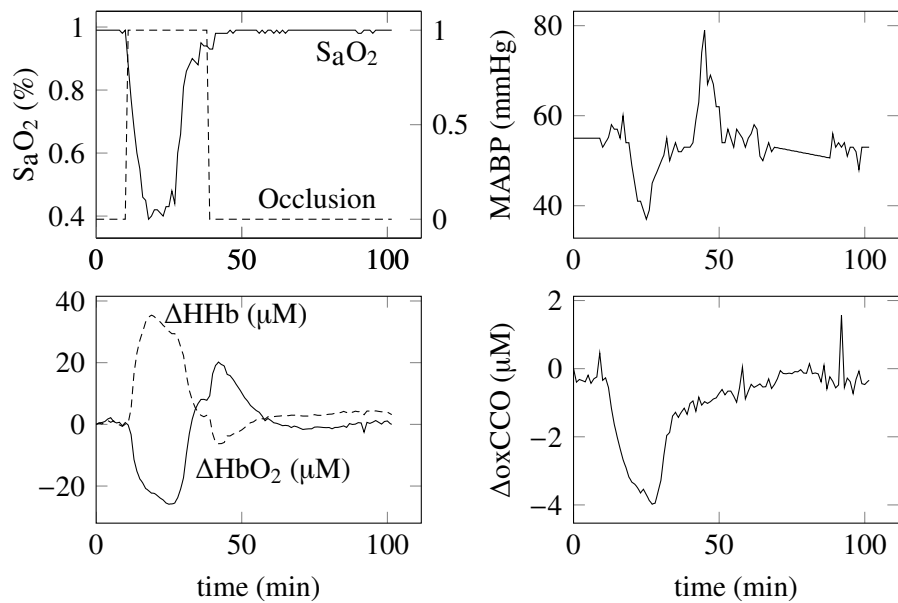


Figure A.6: Measured data for Piglet LWP170

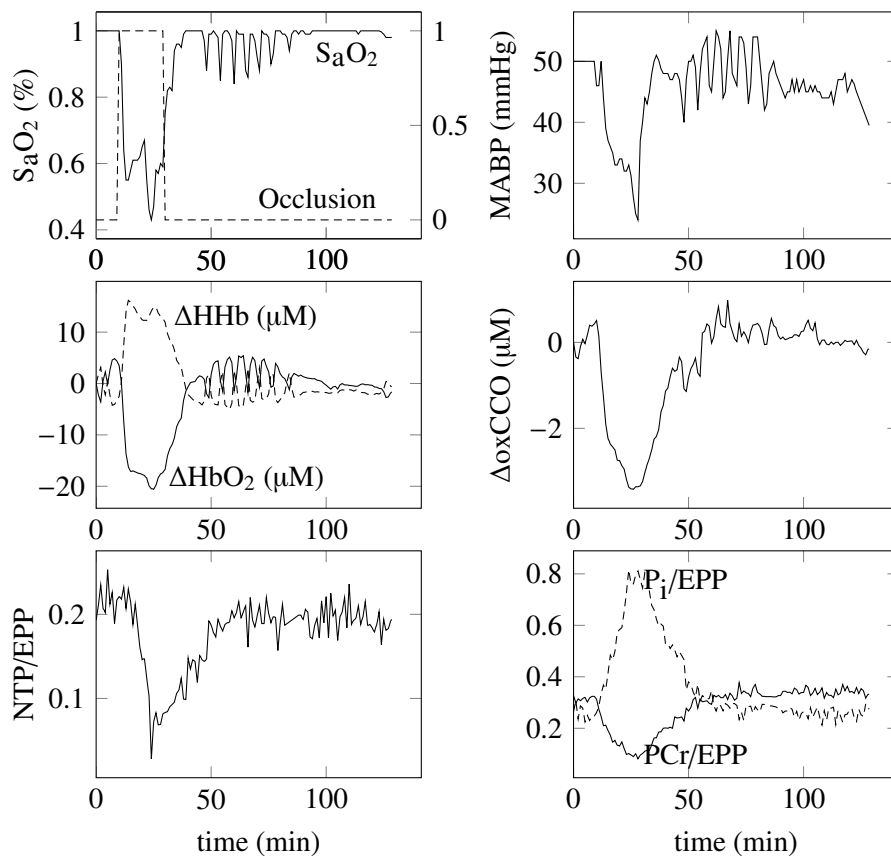


Figure A.7: Measured data for Piglet LWP173

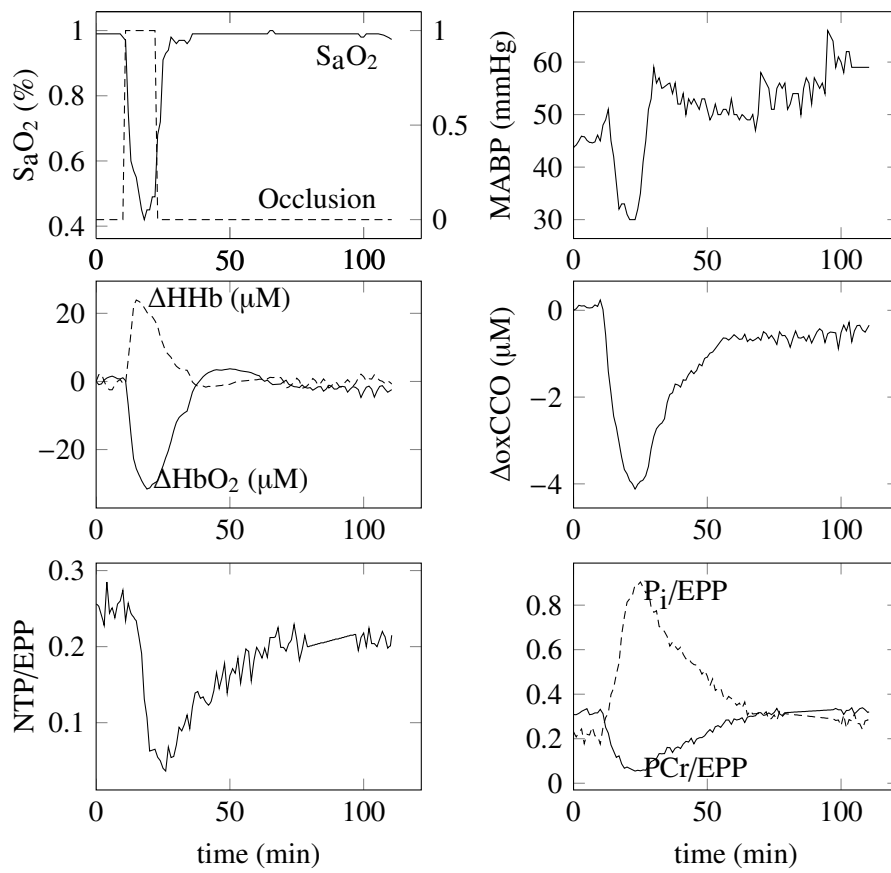


Figure A.8: Measured data for Piglet LWP175

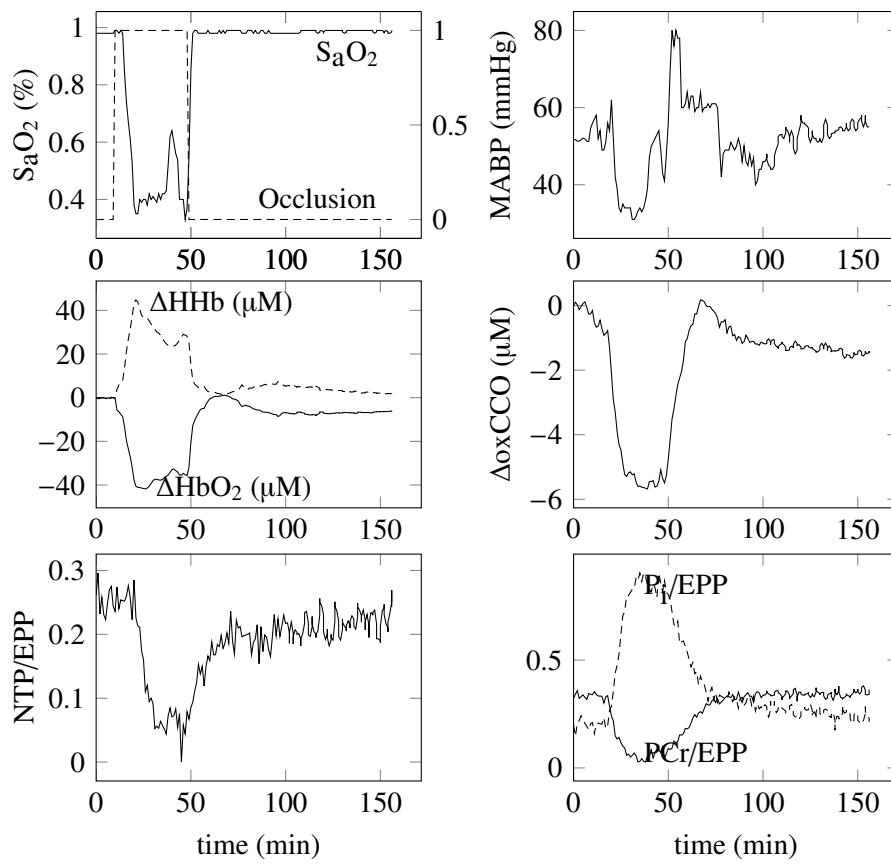


Figure A.9: Measured data for Piglet LWP179

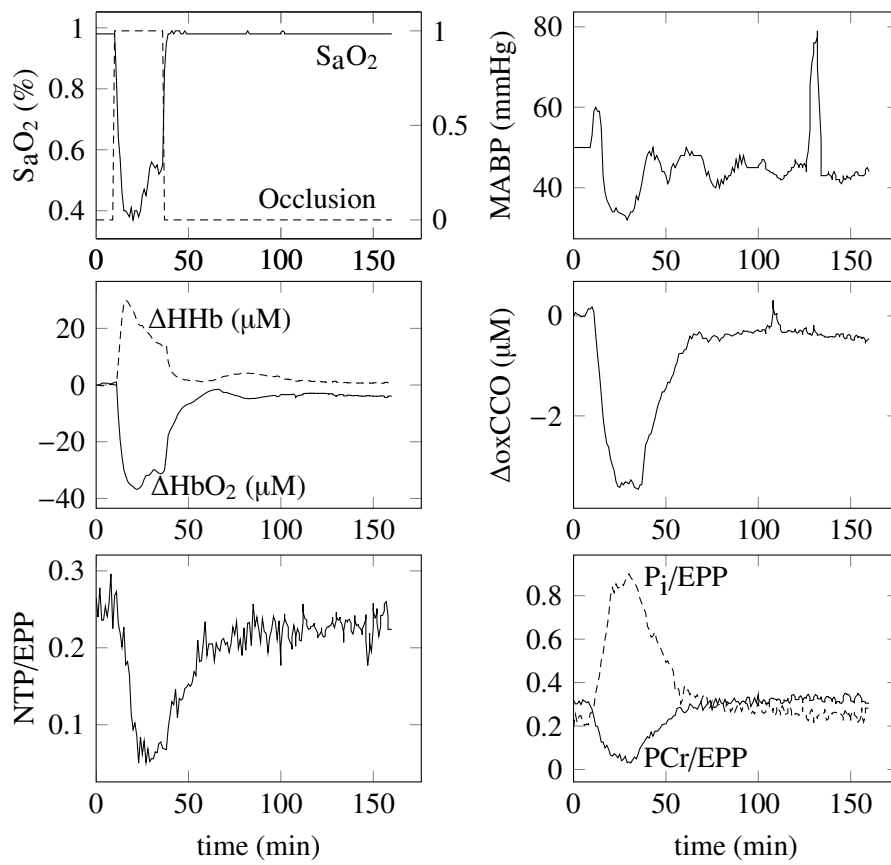


Figure A.10: Measured data for Piglet LWP180

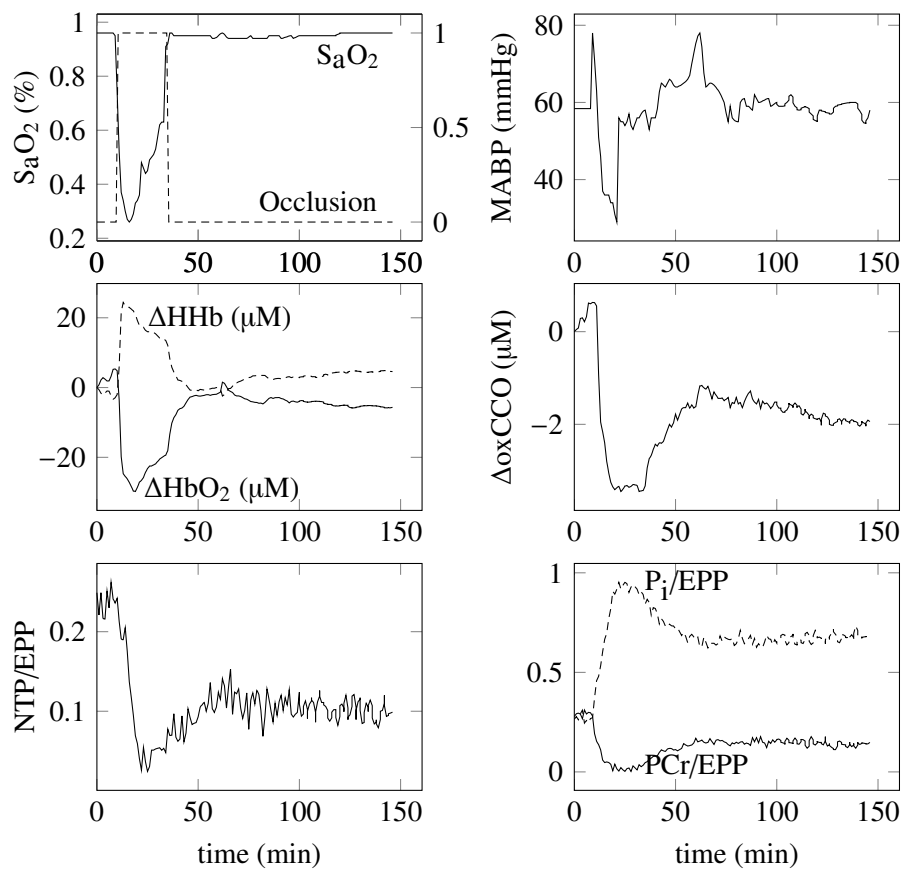


Figure A.11: Measured data for Piglet LWP183

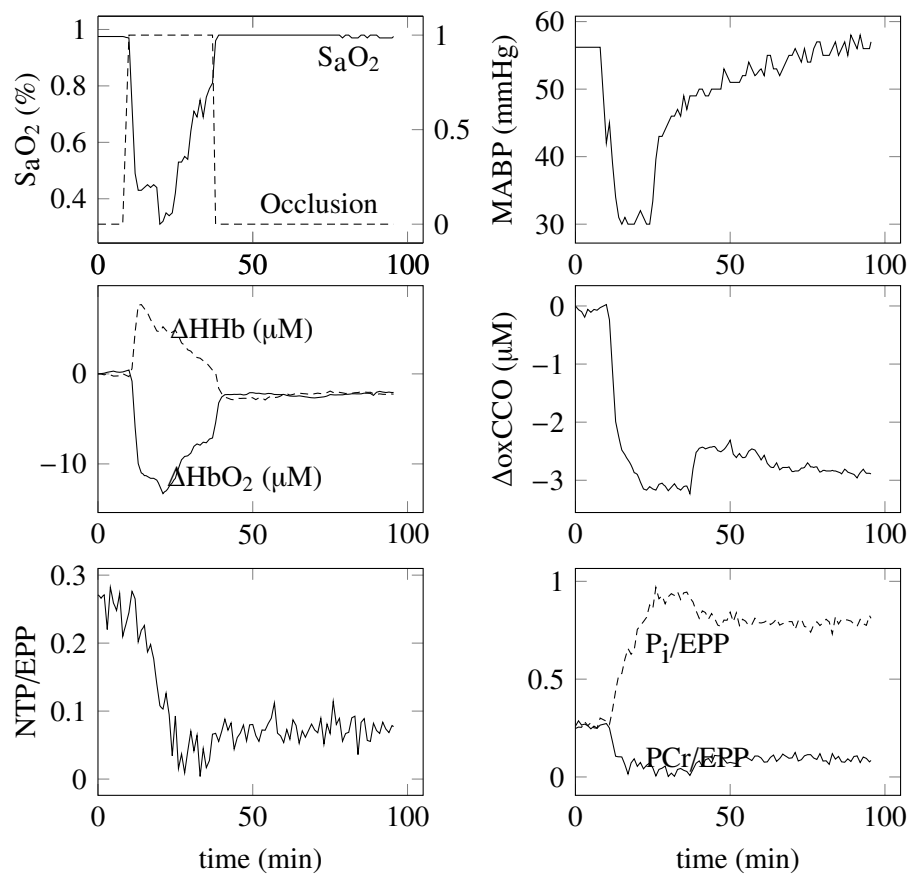


Figure A.12: Measured data for Piglet LWP185

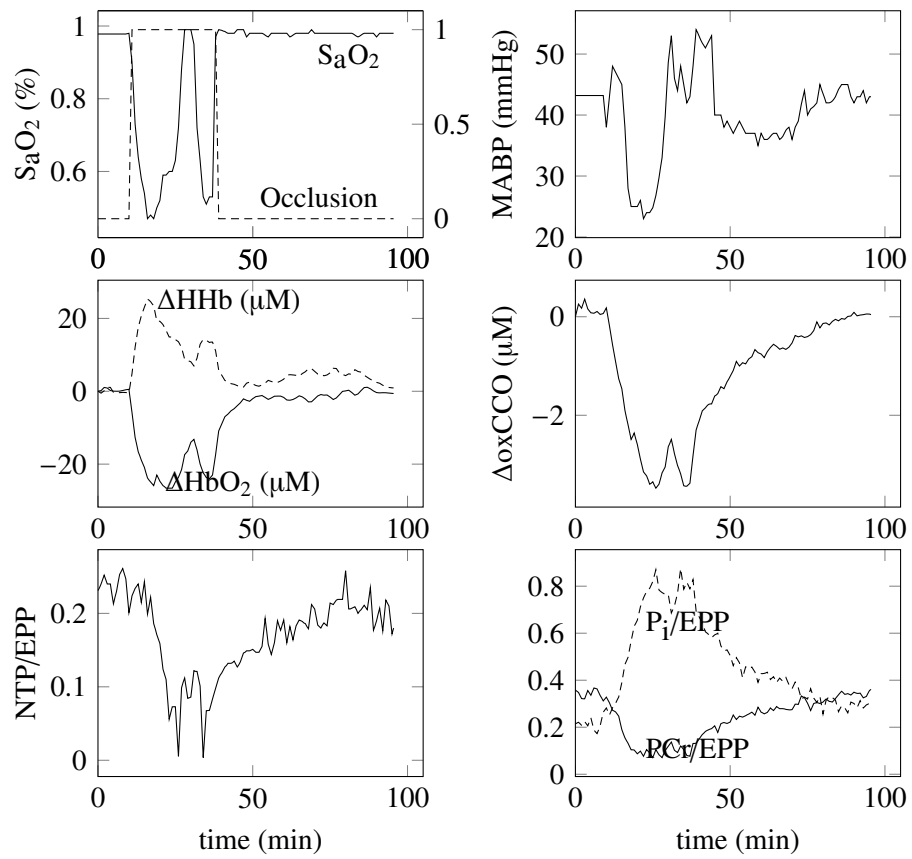


Figure A.13: Measured data for Piglet LWP186

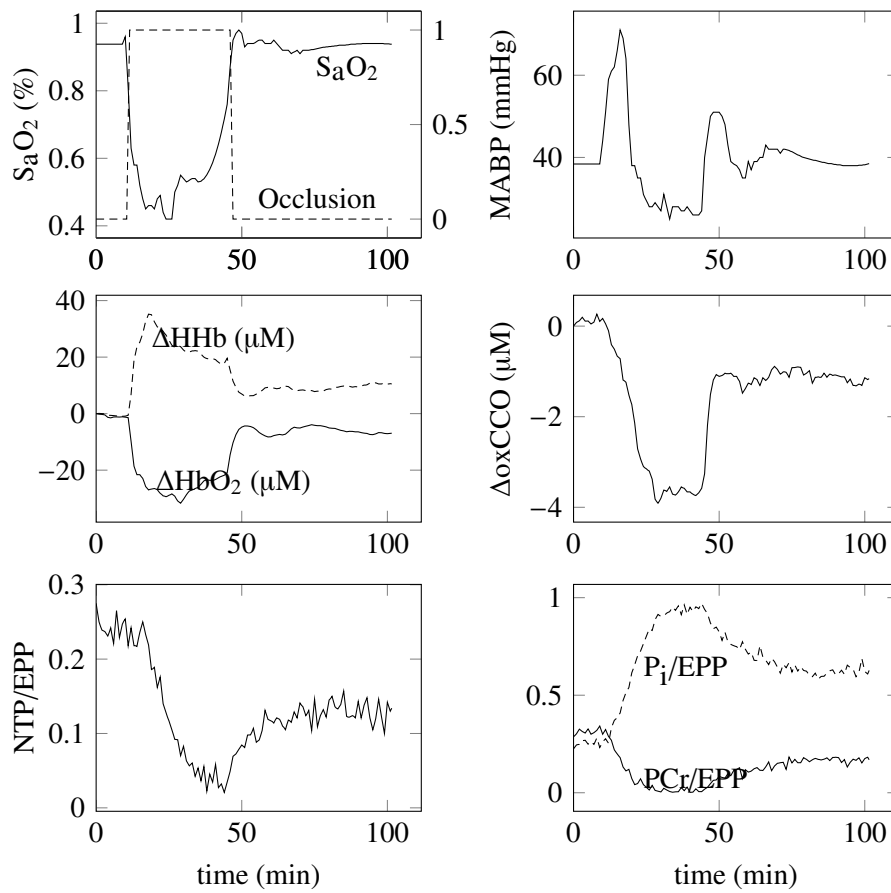


Figure A.14: Measured data for Piglet LWP188

# Appendix B

## Error Calculations

The aim is to find the values of  $f_1$  and  $f_2$  which minimise the mean square error (MSE) between a modelled signal  $X$  and a measured signal  $Y$ , where  $X$  has been scaled by a factor  $f_1$  and offset by a factor  $f_2$ . If there are  $N$  measurements then

$$\text{MSE} = \frac{1}{N} \sum_i (f_1 X_i + f_2 - Y_i)^2. \quad (\text{B.1})$$

The partial derivatives are given by

$$\frac{\partial \text{MSE}}{\partial f_1} = \frac{1}{N} \sum_i 2X_i (f_1 X_i + f_2 - Y_i) = 2 \left( f_1 \overline{X^2} + f_2 \bar{X} - \overline{XY} \right) \quad (\text{B.2})$$

$$\frac{\partial \text{MSE}}{\partial f_2} = \frac{1}{N} \sum_i 2(f_1 X_i + f_2 - Y_i) = 2(f_1 \bar{X} + f_2 - \bar{Y}) \quad (\text{B.3})$$

using the notation  $\bar{A} = \sum_i A_i / N$ . When there is only scaling and no offset ( $f_2 = 0$ ) then B.2 must be zero, and so

$$f_1 = \frac{\overline{XY}}{\overline{X^2}}. \quad (\text{B.4})$$

When there is only offset and no scaling ( $f_1 = 1$ ) then B.3 must be zero, and so

$$f_2 = \bar{Y} - \bar{X}. \quad (\text{B.5})$$

When there is both scaling and offset, both B.2 and B.3 must be zero, and so

$$f_2 = \bar{Y} - f_1 \bar{X} \quad (\text{B.6})$$

$$f_1 = \frac{\overline{XY} - \bar{Y} \cdot \bar{X}}{\overline{X^2} - \bar{X}^2}. \quad (\text{B.7})$$

Therefore for the four cases

1. No scale or offset (unmodified)
2. Only offset
3. Only scale
4. Both scale and offset

the minimum MSEs between the measured signal and the modified modelled signals are

$$\text{MSE}_u = \frac{1}{N} \sum_i (X_i - Y_i)^2 \quad (\text{B.8})$$

$$\text{MSE}_o = \frac{1}{N} \sum_i \left( X_i - (\bar{X} + \bar{Y}) - Y_i \right)^2 \quad (\text{B.9})$$

$$\text{MSE}_s = \frac{1}{N} \sum_i \left( \frac{\overline{XY}}{\overline{X^2}} X_i - Y_i \right)^2 \quad (\text{B.10})$$

$$\text{MSE}_{so} = \frac{1}{N} \sum_i \left( aX_i - (a\bar{X} - \bar{Y}) - Y_i \right) \quad a = \frac{\overline{XY} - \bar{Y} \cdot \bar{X}}{\overline{X^2} - \bar{X}^2}. \quad (\text{B.11})$$

# Appendix C

## BrainSignals model equations, variables and parameters

### C.1 Differential Equations

$$\frac{dCu_{A,o}}{dt} = 4T_{\text{aox}} - 4T_{\text{ared}} \quad (\text{C.1})$$

$$\frac{d\text{cyt } a_{3,r}}{dt} = 4T_{\text{aox}} - 4T_{\text{box}} \quad (\text{C.2})$$

$$\frac{d\Delta\Psi}{dt} = \frac{p_2 f_2 + p_1 f_1 + p_3 f_3 - L}{C_{im}} \quad (\text{C.3})$$

$$\frac{d[H_m^+]}{dt} = \frac{-p_2 T_{\text{aox}}}{R_{Hi}} - \frac{p_1 T_{\text{ared}}}{R_{Hi}} - \frac{p_3 T_{\text{box}}}{R_{Hi}} + \frac{T_{\text{psiout}}}{R_{Hi}} \quad (\text{C.4})$$

$$\frac{d[O_2]}{dt} = -T_{\text{box}} + \frac{T_{O_2\text{in}}}{V_{\text{mit}}} \quad (\text{C.5})$$

$$\frac{dv_{CO_2}}{dt} = \frac{1}{\tau_{CO_2}} (P_a CO_2 - v_{CO_2}) \quad (\text{C.6})$$

$$\frac{dv_{O_2}}{dt} = \frac{1}{\tau_{O_2}} ([O_{2,c}] - v_{O_2}) \quad (\text{C.7})$$

$$\frac{dv_{P_a}}{dt} = \frac{1}{\tau_{P_a}} (P_a - v_{P_a}) \quad (\text{C.8})$$

$$\frac{dv_u}{dt} = \frac{1}{\tau_u} (u - v_u) \quad (\text{C.9})$$

## C.2 Algebraic Equations

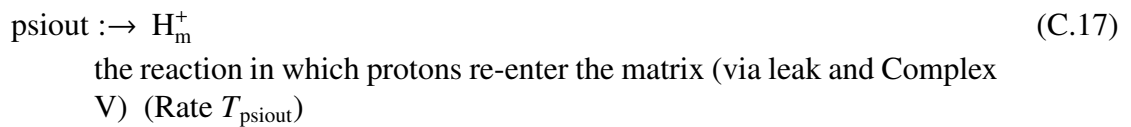
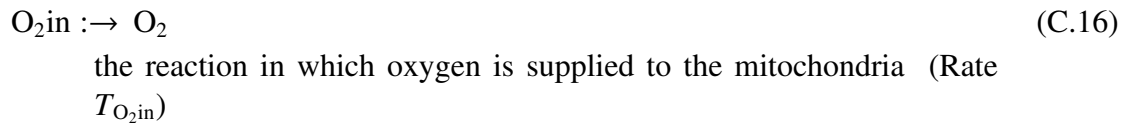
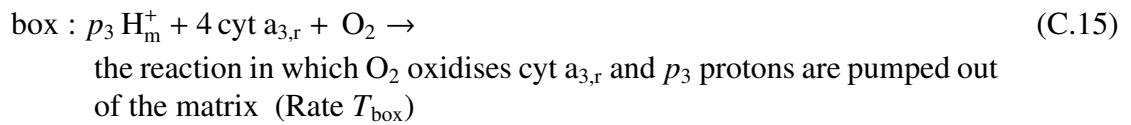
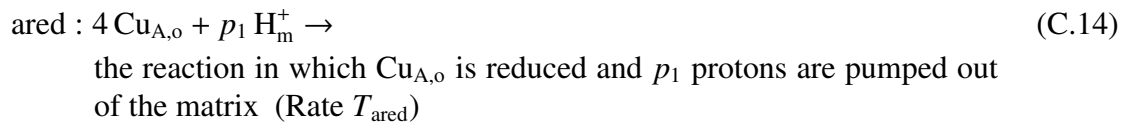
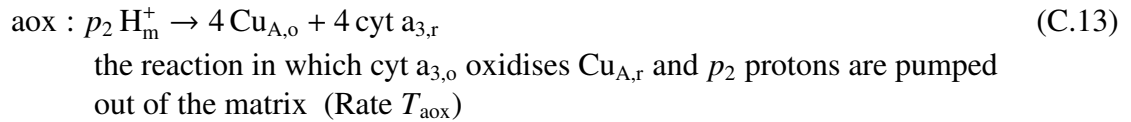
$$\phi \left( \frac{ScO_2}{1 - ScO_2} \right)^{1/n_h} - [O_{2,c}] = 0 \quad (C.10)$$

$$T_e + T_m - (P_1 - P_{ic}) r = 0 \quad (C.11)$$

$$CBF([HbO_{2,a}] - [HbO_{2,v}]) - J_{O_2} = 0 \quad (C.12)$$

## C.3 Chemical Reactions

Reactions are represented as terms in differential equations (see section C.1).



## C.4 Variables

$Cu_{A,o}$  (mM) Inital Value =  $Cu_{A,o,init} = 0.06567$  mM  
the concentration of oxidised cytochrome-c-oxidase

$\text{cyt } a_{3,r}$  (mM) Inital Value =  $\text{cyt } a_{3,r,init} = 0.001408$  mM  
concentration of reduced cytochrome  $a_3$  in mitochondria

$\Delta\Psi$  (mV) Inital Value =  $\Delta\Psi_{init} = 145$  mV  
mitochondrial inner membrane potential

$[H_m^+]$  (mM) Inital Value =  $H_{m,init}^+ = 3.981e - 05$  mM  
 concentration of hydrogen ions in mitochondria  
 $[O_2]$  (mM) Inital Value =  $[O_2]_{init} = 0.024$  mM  
 the concentration of oxygen in the mitochondria  
 $[O_{2,c}]$  (mM) Inital Value =  $[O_{2,c}]_{init} = 0.06061$  mM  
 the concentration of oxygen in the capillary  
 $r$  (cm) Inital Value =  $r_{init} = 0.0187$  cm  
 typical radius of cerebral vessels  
 $\nu_{CO_2}$  (mmHg) Inital Value =  $\nu_{CO_2,n} = 40$  mmHg  
 $P_aCO_2$  passed through a first order filter  
 $\nu_{O_2}$  (mM) Inital Value =  $\nu_{O_2,n} = 0.06061$  mM  
 $[O_{2,c}]$  passed through a first order filter  
 $\nu_{P_a}$  (mmHg) Inital Value =  $\nu_{P_a,n} = 100$  mmHg  
 ABP passed through a first order filter  
 $\nu_u$  (dimensionless) Inital Value =  $\nu_{u,n} = 1$  (dimensionless)  
 the demand parameter  $u$  passed through a first order filter  
 $[HbO_{2,v}]$  (mM) Inital Value =  $[HbO_{2,v}]_{init} = 5.573$  mM  
 the concentration of bound oxygen in the veins

## C.5 Temporary Variables

$$Cu_{A,r} = [CCO]_{mit} - Cu_{A,o}, \quad (\text{mM}) \quad (\text{C.18})$$

the concentration of reduced cytochrome-c-oxidase in the mitochondria

$$AVR = \frac{V_a}{V_v}, \quad (\text{dimensionless}) \quad (\text{C.19})$$

arterio-venous volume ratio

$$cyt a_{3,o} = [CCO]_{mit} - cyt a_{3,r}, \quad (\text{mM}) \quad (\text{C.20})$$

concentration of oxidised cytochrome  $a_3$  in mitochondria

$$C_{0i} = \frac{10^{-pH_m} - 10^{-pH_m - dpH}}{dpH}, \quad (\text{dimensionless}) \quad (\text{C.21})$$

natural buffering capacity for protons in mitochondria

$$CBF = G(P_a - P_v), \quad (\text{ml}_{\text{blood}} \text{ml}_{\text{brain}}^{-1} \text{s}^{-1}) \quad (\text{C.22})$$

cerebral blood flow

$$\Delta \text{oxCCO} = \Delta \text{oxCCO}_{\text{offset}} + 1000V_{mit} (Cu_{A,o} - Cu_{A,o,n}), \quad (\mu\text{M}) \quad (\text{C.23})$$

the expected CCO signal (as measured by NIRS)

$$CMRO_2 = f_3 V_{mit}, \quad (\text{mM s}^{-1}) \quad (\text{C.24})$$

cerebral metabolic rate of oxygen consumption

$$C_{\text{NADH}} = \frac{Z}{2} \log \left( \frac{1}{[\text{NAD}]/[\text{NADH}]} \right), \quad (\text{mV}) \quad (\text{C.25})$$

redox potential minus standard redox potential for NADH at normal demand

$$\Delta G_1 = -4 \left( E_1 + Z \log \left( \frac{\text{Cu}_{\text{A},\text{o}}}{\text{Cu}_{\text{A},\text{r}}} \right) \right) + p_1 \Delta p, \quad (\text{mV}) \quad (\text{C.26})$$

free energy associated with reaction ared

$$\Delta G_2 = -4 \left( E_2 + Z \left( \log \left( \frac{\text{Cu}_{\text{A},\text{r}}}{\text{Cu}_{\text{A},\text{o}}} \right) - \log \left( \frac{\text{cyt } a_{3,\text{r}}}{\text{cyt } a_{3,\text{o}}} \right) \right) \right) + p_2 \Delta p, \quad (\text{mV}) \quad (\text{C.27})$$

free energy associated with reaction aox

$$\Delta \text{Hbdiff} = \Delta \text{Hbdiff}_{\text{offset}} + \Delta \text{HbO}_2 - \Delta \text{HHb}, \quad (\mu\text{M}) \quad (\text{C.28})$$

change in (HbO<sub>2</sub> – HHb) (NIRS)

$$\Delta \text{HbO}_2 = \Delta \text{HbO}_{2,\text{offset}} + \text{HbO}_2 - \text{HbO}_{2,\text{n}}, \quad (\mu\text{M}) \quad (\text{C.29})$$

change in total oxygenated haemoglobin (NIRS)

$$\Delta \text{Hbt} = \Delta \text{HbT}_{\text{offset}} + \text{Hbt} - \text{Hbt}_{\text{n}}, \quad (\mu\text{M}) \quad (\text{C.30})$$

change in total haemoglobin (NIRS)

$$\Delta \text{HHb} = \Delta \text{HHb}_{\text{offset}} + \text{HHb} - \text{HHb}_{\text{n}}, \quad (\mu\text{M}) \quad (\text{C.31})$$

change in total deoxygenated haemoglobin (NIRS)

$$\Delta p = \Delta \Psi + Z (\text{pH}_{\text{m}} - \text{pH}_{\text{o}}), \quad (\text{mV}) \quad (\text{C.32})$$

the proton motive force across the mitochondrial inner membrane

$$\eta = R_P \left( \frac{v_{P_a}}{v_{P_a,\text{n}}} - 1 \right) + R_O \left( \frac{v_{\text{O}_2}}{v_{\text{O}_2,\text{n}}} - 1 \right) + R_u \left( 1 - \frac{v_u}{v_{u,\text{n}}} \right) + R_C \left( 1 - \frac{v_{\text{CO}_2}}{v_{\text{CO}_2,\text{n}}} \right), \quad (\text{dimensionless}) \quad (\text{C.33})$$

total autoregulatory stimuli

$$f_1 = k_1 \text{Cu}_{\text{A},\text{o}} - k_{-1} \text{Cu}_{\text{A},\text{r}}, \quad (\text{mM s}^{-1}) \quad (\text{C.34})$$

the rate at which Cu<sub>A,o</sub> is reduced

$$f_2 = k_2 \text{Cu}_{\text{A},\text{r}} \text{cyt } a_{3,\text{o}} - k_{-2} \text{Cu}_{\text{A},\text{o}} \text{cyt } a_{3,\text{r}}, \quad (\text{mM s}^{-1}) \quad (\text{C.35})$$

the rate at which Cu<sub>A,r</sub> is oxidised and cyt a<sub>3,o</sub> reduced

$$f_3 = \frac{k_3 [\text{O}_2] \text{cyt } a_{3,\text{r}} \exp \left( -c_3 (\Delta p - \Delta p_{30}) \right)}{1 + \exp \left( -c_3 (\Delta p - \Delta p_{30}) \right)}, \quad (\text{mM s}^{-1}) \quad (\text{C.36})$$

the rate at which cyt a<sub>3,r</sub> is oxidised

$$G = K_G r^4, \quad (\text{ml}_{\text{blood}} \text{ml}_{\text{brain}}^{-1} \text{mmHg}^{-1} \text{s}^{-1}) \quad (\text{C.37})$$

resistance of cerebral circulation

$$h = -r + \sqrt{r^2 + 2r_0 h_0 + h_0^2}, \quad (\text{cm}) \quad (\text{C.38})$$

wall thickness of cerebral vessels

$$\text{HbO}_2 = 1000 \frac{V_a[\text{HbO}_{2,a}] + V_v[\text{HbO}_{2,v}]}{4} V_{\text{blood},n}, \quad (\mu\text{M}) \quad (\text{C.39})$$

total oxygenated haemoglobin (NIRS)

$$\text{Hbt} = 1000 \frac{(V_a + V_v) [\text{Hbtot}]}{4} V_{\text{blood},n}, \quad (\mu\text{M}) \quad (\text{C.40})$$

total haemoglobin (NIRS)

$$\text{HHb} = 1000 \frac{V_a[\text{HHb}_a] + V_v[\text{HHb}_v]}{4} V_{\text{blood},n}, \quad (\mu\text{M}) \quad (\text{C.41})$$

total deoxygenated haemoglobin (NIRS)

$$J_{\text{O}_2,\text{min}} = \min \left( D_{\text{O}_2} \left( [\text{O}_{2,c}] - [\text{O}_2] \right) \text{CBF}[\text{HbO}_{2,a}] \right), \quad (\text{mM s}^{-1}) \quad (\text{C.42})$$

rate at which oxygen is supplied to the mitochondria, minimum of diffusion rate and delivery rate

$$J_{\text{O}_2} = J_{\text{O}_2,\text{min}}, \quad (\text{mM s}^{-1}) \quad (\text{C.43})$$

the rate at which oxygen is supplied to the mitochondria

$$k_1 = k_{1,0} \exp \left( -c_{k1} (\Delta p - \Delta p_n) \right), \quad (\text{s}^{-1}) \quad (\text{C.44})$$

forward rate constant for reaction ared

$$k_2 = k_{2,n} \exp \left( -c_{k2} (\Delta p - \Delta p_n) \right), \quad (\text{mM}^{-1} \text{s}^{-1}) \quad (\text{C.45})$$

forward rate constant for reaction aox

$$\text{Keq}_1 = 10^{(-1/Z)(p_1 \Delta p / 4 - E_1)}, \quad (\text{dimensionless}) \quad (\text{C.46})$$

equilibrium constant for reaction ared

$$\text{Keq}_2 = 10^{(-1/Z)(p_2 \Delta p / 4 - E_2)}, \quad (\text{dimensionless}) \quad (\text{C.47})$$

equilibrium constant for reaction aox

$$k_{-1} = \frac{k_1}{\text{Keq}_1}, \quad (\text{s}^{-1}) \quad (\text{C.48})$$

backward rate constant for reaction ared

$$k_{-2} = \frac{k_2}{\text{Keq}_2}, \quad (\text{mM}^{-1} \text{s}^{-1}) \quad (\text{C.49})$$

backward rate constant for reaction aox

$$L = L_{\text{CV}} + L_{lk}, \quad (\text{mM s}^{-1}) \quad (\text{C.50})$$

the rate at which protons reenter the mitochondrial matrix

$$L_{\text{CV}} = \frac{CV_{inh} L_{\text{CV},\text{max}} (1 - e^{-\theta})}{1 + r_{\text{CV}} e^{-\theta}}, \quad (\text{mM s}^{-1}) \quad (\text{C.51})$$

the rate at which protons reenter the mitochondrial matrix associated with ADP phosphorylation

$$L_{lk} = k_{\text{unc}} L_{lk0} \left( \exp(\Delta p k_{lk2}) - 1 \right), \quad (\text{mM s}^{-1}) \quad (\text{C.52})$$

the rate at which protons reenter the mitochondrial matrix through leak channels

$$\mu = \frac{\mu_{\min} + \mu_{\max} e^{\eta}}{1 + e^{\eta}}, \quad (\text{dimensionless}) \quad (\text{C.53})$$

total autoregulatory stimuli filtered through sigmoidal function

$$\text{pH}_m = -\log\left(\frac{[\text{H}_m^+]}{1000}\right), \quad (\text{dimensionless}) \quad (\text{C.54})$$

mitochondrial pH

$$r_{\text{buffi}} = \frac{C_{\text{buffi}}}{C_{\text{O}_i}}, \quad (\text{dimensionless}) \quad (\text{C.55})$$

buffering capacity for protons in mitochondria

$$R_{\text{Hi}} = r_{\text{buffi}}, \quad (\text{dimensionless}) \quad (\text{C.56})$$

relative mitochondrial volume for protons

$$\text{ScO}_2 = \frac{\text{SaO}_2 + \text{SvO}_2}{2}, \quad (\text{dimensionless}) \quad (\text{C.57})$$

capillary oxygen saturation

$$\sigma_e = \sigma_{e0} \left( \exp\left(\frac{K_{\sigma}(r - r_0)}{r_0}\right) - 1 \right) - \sigma_{\text{coll}}, \quad (\text{mmHg}) \quad (\text{C.58})$$

elastic stress in vessel walls

$$\text{SvO}_2 = \frac{[\text{HbO}_{2,v}]}{[\text{Hbtot}]}, \quad (\text{dimensionless}) \quad (\text{C.59})$$

venous oxygen saturation

$$T_{\text{aox}} = f_2, \quad (\text{mM s}^{-1}) \quad (\text{C.60})$$

Rate of reaction aox

$$T_{\text{ared}} = f_1, \quad (\text{mM s}^{-1}) \quad (\text{C.61})$$

Rate of reaction ared

$$T_{\text{box}} = f_3, \quad (\text{mM s}^{-1}) \quad (\text{C.62})$$

Rate of reaction box

$$T_e = \sigma_e h, \quad (\text{mmHg cm}) \quad (\text{C.63})$$

elastic tension in vessel walls

$$\theta = k_{CV} (\Delta p + Z \log(u) - \Delta p_{CV0}), \quad (\text{dimensionless}) \quad (\text{C.64})$$

driving force for Complex V

$$T_m = T_{\max} \exp\left(-\left(\frac{r - r_m}{r_t - r_m}\right)^{n_m}\right), \quad (\text{mmHg cm}) \quad (\text{C.65})$$

muscular tension in vessel walls

$$T_{\max} = T_{\max0} (1 + k_{\text{aut}} \mu), \quad (\text{mmHg cm}) \quad (\text{C.66})$$

maximum muscular tension developed by circulation

$$T_{\text{O}_2\text{in}} = J_{\text{O}_2}, \quad (\text{mM s}^{-1}) \quad (\text{C.67})$$

Rate of reaction O<sub>2</sub>in

$$TOS = \frac{100}{[Hbtot]} \left( \frac{\left(\frac{r}{r_n}\right)^2 [HbO_{2,a}]}{\left(\frac{r}{r_n}\right)^2 + VArat_n} + \frac{VArat_n [HbO_{2,v}]}{\left(\frac{r}{r_n}\right)^2 + VArat_n} \right), \quad (\text{dimensionless}) \quad (C.68)$$

tissue oxygenation index

$$T_{psiout} = L, \quad (\text{mM s}^{-1}) \quad (C.69)$$

Rate of reaction psiout

$$V_{mca} = CBF_{CBFscale}, \quad (\text{cm s}^{-1}) \quad (C.70)$$

the velocity of blood in the middle cerebral artery

$$V_a = V_{a,n} \left(\frac{r}{r_n}\right)^2, \quad (\text{dimensionless}) \quad (C.71)$$

arterial blood volume as a fraction of normal total blood volume

$$V_t = V_a + V_v, \quad (\text{dimensionless}) \quad (C.72)$$

normalised total blood volume

$$[HHb_v] = [Hbtot] - [HbO_{2,v}], \quad (\text{mM}) \quad (C.73)$$

concentration of haemoglobin O<sub>2</sub> binding sites not occupied by O<sub>2</sub> (four times deoxyhaemoglobin concentration) in the veins

## C.6 Parameters

$$Cu_{A,frac,n} = 0.8 \quad (\text{dimensionless})$$

normal oxidised fraction of Cu<sub>A</sub>

$$V_{blood,n} = 0.04 \quad (\text{dimensionless})$$

normal blood volume as a fraction of brain tissue volume

$$c3 = 0.11 \text{ mV}^{-1}$$

parameter controlling the sensitivity of reaction box to Δp

$$CBF_n = 0.01075 \text{ ml}_{\text{blood}} \text{ ml}_{\text{brain}}^{-1} \text{ s}^{-1}$$

normal cerebral blood flow

$$CBFscale = 5000 \text{ cm}$$

ratio between V<sub>mca</sub> and CBF

$$C_{buffi} = 0.022 \quad (\text{dimensionless})$$

buffering capacity for protons in mitochondria

$$\Delta oxCCO_{offset} = 0 \text{ } \mu\text{M}$$

an arbitrary baseline offset to the ΔoxCCO signal (NIRS)

$$C_{im} = 0.00675 \text{ mM mV}^{-1}$$

capacitance of mitochondrial inner membrane

$$c_{k1} = 0.01 \text{ mV}^{-1}$$

parameter controlling sensitivity of k<sub>1</sub> to Δp

$$c_{k2} = 0.02 \text{ mV}^{-1}$$

parameter controlling sensitivity of  $k_2$  to  $\Delta p$

$CMRO_{2,n} = 0.034 \text{ mM s}^{-1}$   
The resting  $CMRO_2$

$CV_{inh} = 1$  (dimensionless)  
a control parameter representing the action of Complex V inhibitors

$[CCO]_{tis} = 0.0055 \text{ mM}$   
concentration of cytochrome c oxidase in tissue

$\Delta Hbdiff_{offset} = 0 \text{ }\mu\text{M}$   
an arbitrary baseline offset to the  $\Delta Hbdiff$  signal (NIRS)

$\Delta HbO_{2,offset} = 0 \text{ }\mu\text{M}$   
an arbitrary baseline offset to the  $\Delta HbO_2$  signal (NIRS)

$\Delta HbT_{offset} = 0 \text{ }\mu\text{M}$   
an arbitrary baseline offset to the  $\Delta Hbt$  signal (NIRS)

$\Delta HHb_{offset} = 0 \text{ }\mu\text{M}$   
an arbitrary baseline offset to the  $\Delta HHb$  signal (NIRS)

$D_{NADH} = 0.01$  (dimensionless)  
 $D_{NADH} \times Z$  is the change in NADH redox potential for a ten-fold increase in  $u$

$\Delta p_{3,corr} = -25 \text{ mV}$   
 $\Delta p_{30}$  minus normal  $\Delta p$

$\Delta p_{CV0} = 90 \text{ mV}$   
a constant in the rate of Complex V

$dpH = 0.001$  (dimensionless)  
a constant in the buffering relationship

$\Delta \Psi_n = 145 \text{ mV}$   
normal mitochondrial inner membrane potential

$\mathcal{E}_0(\text{cyt } a_3) = 350 \text{ mV}$   
cytochrome  $a_3$  standard redox potential

$\mathcal{E}_0(\text{Cu}_A) = 247 \text{ mV}$   
 $\text{Cu}_A$  standard redox potential

$\mathcal{E}_0(\text{NADH}) = -320 \text{ mV}$   
NADH standard redox potential

$h_0 = 0.003 \text{ cm}$   
vascular wall thickness when radius is  $r_0$

$k_{H,O_2} = 0.0014 \text{ mM mmHg}^{-1}$   
constant setting relationship between oxygen saturation and oxygen concentration in artery

$k_{3,0} = 2.5e + 05 \text{ mM}^{-1} \text{ s}^{-1}$   
an apparent second-order rate constant for reaction box at zero  $\Delta p$

$k_{aut} = 1$  (dimensionless)  
control parameter allowing destruction of autoregulation

$k_{lk2} = 0.038 \text{ mV}^{-1}$   
second constant controlling rate of  $L_{lk}$  of  $\Delta p$

$K_\sigma = 10$  (dimensionless)

$k_{\text{unc}} = 1$  (dimensionless)  
 parameter controlling sensitivity of  $\sigma_e$  to radius  
 a parameter representing the action of uncouplers  
 $L_{\text{CV},0} = 0.4$  (dimensionless)  
 normal Complex V flux as a fraction of maximum possible flux  
 $L_{\text{lk,frac}} = 0.25$  (dimensionless)  
 normal fraction of proton entry into mitochondria which is via leak channels  
 $\mu_{\text{max}} = 1$  (dimensionless)  
 maximum value of  $\mu$   
 $\mu_{\text{min}} = -1$  (dimensionless)  
 minimum value of  $\mu$   
 $\mu_n = 0$  (dimensionless)  
 normal value of  $\mu$   
 $[\text{NAD}]_n / [\text{NADH}]_n = 9$  (dimensionless)  
 normal NAD/NADH ratio  
 $N_t = 3$  mM  
 total mitochondrial NAD and NADH concentration  
 $n_h = 2.5$  (dimensionless)  
 Hill coefficient for haemoglobin saturation  
 $n_m = 1.83$  (dimensionless)  
 exponent in the muscular tension relationship  
 $[\text{O}_2]_n = 0.024$  mM  
 normal oxygen concentration in mitochondria  
 $P_a = 100$  mmHg  
 arterial blood pressure  
 $P_a\text{CO}_2 = 40$  mmHg  
 arterial partial pressure of  $\text{CO}_2$   
 $P_a\text{CO}_{2,n} = 40$  mmHg  
 normal arterial partial pressure of  $\text{CO}_2$   
 $P_{a,n} = 100$  mmHg  
 normal value of ABP  
 $\phi = 0.036$  mM  
 value of  $\text{O}_2$  concentration at half maximal saturation  
 $\text{pH}_{\text{m},n} = 7.4$  (dimensionless)  
 normal mitochondrial pH  
 $\text{pH}_o = 7$  (dimensionless)  
 extra-mitochondrial pH  
 $\text{pH}_{o,n} = 7$  (dimensionless)  
 normal extra-mitochondrial pH  
 $P_{ic} = 9.5$  mmHg  
 intracranial blood pressure  
 $P_{ic,n} = 9.5$  mmHg  
 normal intracranial blood pressure

$p_{tot} = 20$  (dimensionless)  
 total protons pumped by reactions aed, aox and box  
 $P_v = 4$  mmHg  
 venous blood pressure  
 $P_{v,n} = 4$  mmHg  
 normal venous blood pressure  
 $r_0 = 0.0126$  cm  
 a special radius in the elastic tension relationship  
 $R_C = 2.2$  (dimensionless)  
 parameter controlling sensitivity of  $\eta$  to  $P_a\text{CO}_2$   
 $R_O = 1.5$  (dimensionless)  
 parameter controlling sensitivity of  $\eta$  to  $[\text{O}_{2,c}]$   
 $R_P = 4$  (dimensionless)  
 parameter controlling sensitivity of  $\eta$  to  $P_a$   
 $R_u = 0.5$  (dimensionless)  
 parameter controlling sensitivity of  $\eta$  to  $u$   
 $r_{CV} = 5$  (dimensionless)  
 a parameter controlling the ratio of maximal to minimal rates of oxidative phosphorylation  
 $r_m = 0.027$  cm  
 value of vessel radius giving maximum muscular tension  
 $r_n = 0.0187$  cm  
 normal radius of blood vessels  
 $r_t = 0.018$  cm  
 parameter in the muscular tension relationship  
 $\text{SaO}_{2,n} = 0.96$  (dimensionless)  
 normal saturation of the arterial haemoglobin  
 $\text{SaO}_2 = 0.96$  (dimensionless)  
 saturation of the arterial haemoglobin  
 $\sigma_{\text{coll}} = 62.79$  mmHg  
 value of pressure at which vessels collapse  
 $\sigma_{e0} = 0.1425$  mmHg  
 parameter in relationship determining  $\sigma_e$   
 $\tau_{\text{CO}_2} = 5$  s  
 the time constant associated with  $v_{\text{CO}_2}$   
 $\tau_{\text{O}_2} = 20$  s  
 the time constant associated with  $v_{\text{O}_2}$   
 $\tau_{P_a} = 5$  s  
 the time constant associated with  $v_{P_a}$   
 $\tau_u = 0.5$  s  
 the time constant associated with  $v_u$   
 $u = 1$  (dimensionless)  
 the representation of “demand” in the model  
 $u_n = 1$  (dimensionless)

resting “demand”  
 $V_{\text{Arat}_n} = 3$  (dimensionless)  
the normal ratio of the volume of the veins to the volume of the arteries  
 $V_{\text{mit}} = 0.067$  (dimensionless)  
fraction of brain water which is mitochondria  
 $V_{t,n} = 1$  (dimensionless)  
normal total blood volume  
 $[\text{Hbtot}] = 9.1$  mM  
total concentration of haemoglobin  $\text{O}_2$  binding sites in the arteries and veins (four times haemoglobin concentration)  
 $[\text{Hbtot}]_n = 9.1$  mM  
normal total concentration of haemoglobin  $\text{O}_2$  binding sites in the arteries and veins (four times haemoglobin concentration)  
 $Z = 59.03$  mV  
 $2.303 \times RT/F$  where  $R$  is the ideal gas constant ( $8300 \text{ mJ K}^{-1} \text{ mol}^{-1}$ ),  $T$  is the temperature (298 K),  $F$  is the Faraday constant ( $9.65 \times 10^4 \text{ C mol}^{-1}$ ) and 2.303 arises from  $1/\log_{10} e$ .

## C.7 Derived Parameters

$$\text{Cu}_{\text{A},\text{o},\text{init}} = \text{Cu}_{\text{A},\text{o},\text{n}} = 0.06567 \text{ mM} \quad (\text{C.74})$$

initial oxidized  $\text{Cu}_A$

$$\text{Cu}_{\text{A},\text{o},\text{n}} = [\text{CCO}]_{\text{mit}} \text{Cu}_{\text{A},\text{frac},\text{n}} = 0.06567 \text{ mM} \quad (\text{C.75})$$

normal oxidized  $\text{Cu}_A$

$$\text{Cu}_{\text{A},\text{r},\text{n}} = [\text{CCO}]_{\text{mit}} - \text{Cu}_{\text{A},\text{o},\text{n}} = 0.01642 \text{ mM} \quad (\text{C.76})$$

the resting amount of reduced cytochrome-c-oxidase

$$a_{3,\text{frac},\text{n}} = 1 - \frac{\text{cyt } a_{3,\text{r},\text{n}}}{[\text{CCO}]_{\text{mit}}} = 0.9829 \text{ (dimensionless)} \quad (\text{C.77})$$

normal oxidised fraction of cytochrome  $a_3$

$$\text{cyt } a_{3,\text{o},\text{n}} = [\text{CCO}]_{\text{mit}} - \text{cyt } a_{3,\text{r},\text{n}} = 0.08068 \text{ mM} \quad (\text{C.78})$$

normal oxidised cytochrome  $a_3$

$$\text{cyt } a_{3,\text{r},\text{init}} = \text{cyt } a_{3,\text{r},\text{n}} = 0.001408 \text{ mM} \quad (\text{C.79})$$

initial reduced cytochrome  $a_3$

$$\text{cyt } a_{3,\text{r},\text{n}} = \frac{f_n \left( 1 + \exp \left( -c_3 \left( \Delta p_n - \Delta p_{30} \right) \right) \right)}{k_3 [\text{O}_2]_n \exp \left( -c_3 \left( \Delta p_n - \Delta p_{30} \right) \right)} = 0.001408 \text{ mM} \quad (\text{C.80})$$

normal reduced cytochrome  $a_3$

$$C_{\text{NADH},n} = \frac{Z}{2} \log \left( \frac{1}{[\text{NAD}]_n / [\text{NADH}]_n} \right) = -28.16 \text{ mV} \quad (\text{C.81})$$

normal value of  $C_{\text{NADH}}$

$$[\text{CCO}]_{\text{mit}} = \frac{[\text{CCO}]_{\text{tis}}}{V_{\text{mit}}} = 0.08209 \text{ mM} \quad (\text{C.82})$$

concentration of cytochrome c oxidase in mitochondria

$$\Delta G_{1,n} = -4 \left( E_{1,n} + Z \log \left( \frac{\text{Cu}_{\text{A},\text{o},n}}{\text{Cu}_{\text{A},\text{r},n}} \right) \right) + p_1 \Delta p_n = -274.2 \text{ mV} \quad (\text{C.83})$$

normal free energy associated with reaction ared

$$\Delta G_{2,n} = -4 \left( E_2 + Z \left( \log \left( \frac{\text{Cu}_{\text{A},\text{r},n}}{\text{Cu}_{\text{A},\text{o},n}} \right) - \log \left( \frac{\text{cyt } a_{3,\text{r},n}}{\text{cyt } a_{3,\text{o},n}} \right) \right) \right) + p_2 \Delta p_n = -10.56 \text{ mV} \quad (\text{C.84})$$

normal free energy associated with reaction aox

$$D_{\text{O}_2} = \frac{J_{\text{O}_2,n}}{[\text{O}_{2,\text{c}}]_n - [\text{O}_2]_n} = 0.9287 \text{ s}^{-1} \quad (\text{C.85})$$

diffusion rate between capillaries and mitochondria

$$\Delta p_{30} = \Delta p_n + \Delta p_{3,\text{corr}} = 143.6 \text{ mV} \quad (\text{C.86})$$

value of PMF at which reaction box is maximally sensitive to  $\Delta p$

$$\Delta \text{pH}_n = \text{pH}_{\text{m},n} - \text{pH}_{\text{o},n} = 0.4 \text{ (dimensionless)} \quad (\text{C.87})$$

the resting value of pH difference across mitochondrial inner membrane

$$\Delta p_n = \Delta \Psi_n + Z \Delta \text{pH}_n = 168.6 \text{ mV} \quad (\text{C.88})$$

the resting value of the proton motive force

$$\Delta \Psi_{\text{init}} = \Delta \Psi_n = 145 \text{ mV} \quad (\text{C.89})$$

initial value of mitochondrial inner membrane potential

$$E_1 = E_{1,\text{NADH}} = 538.8 \text{ mV} \quad (\text{C.90})$$

the energy provided by electron transfer to  $\text{Cu}_{\text{A},\text{o}}$

$$E_{1,n} = E_{1,\text{NADH},n} = 538.8 \text{ mV} \quad (\text{C.91})$$

the normal value of  $E_1$

$$E_{1,\text{NADH}} = \mathcal{E}_0(\text{Cu}_\text{A}) - \mathcal{E}_0(\text{NADH}) + C_{\text{NADH}} = 538.8 \text{ mV} \quad (\text{C.92})$$

$E_1$  when the reducing substrate is NADH

$$E_{1,\text{NADH},n} = \mathcal{E}_0(\text{Cu}_\text{A}) - \mathcal{E}_0(\text{NADH}) + C_{\text{NADH},n} = 538.8 \text{ mV} \quad (\text{C.93})$$

normal value of  $E_{1,\text{NADH}}$

$$E_2 = \mathcal{E}_0(\text{cyt } a_3) - \mathcal{E}_0(\text{Cu}_\text{A}) = 103 \text{ mV} \quad (\text{C.94})$$

the energy provided by transfer of four electrons from  $\text{Cu}_{\text{A},\text{r}}$  to  $\text{cyt } a_{3,\text{o}}$

$$f_n = \frac{\text{CMRO}_{2,n}}{V_{\text{mit}}} = 0.5075 \text{ mM s}^{-1} \quad (\text{C.95})$$

normal resting rate of  $f_1$  and  $f_2$

$$G_n = \frac{CBF_n}{P_{a,n} - P_{v,n}} = 0.000112 \text{ ml}_{\text{blood}} \text{ ml}_{\text{brain}}^{-1} \text{ mmHg}^{-1} \text{ s}^{-1} \quad (\text{C.96})$$

normal resistance of cerebral circulation

$$\text{HbO}_{2,n} = 1000 \frac{V_{a,n}[\text{HbO}_{2,a}]_n + V_v[\text{HbO}_{2,v}]_n}{4} V_{\text{blood},n} = 63.64 \mu\text{M} \quad (\text{C.97})$$

normal total oxygenated haemoglobin (NIRS)

$$\text{Hbt}_n = 1000 \frac{(V_{a,n} + V_v)[\text{Hbtot}]_n}{4} V_{\text{blood},n} = 91 \mu\text{M} \quad (\text{C.98})$$

normal total haemoglobin (NIRS)

$$\text{HHb}_n = 1000 \frac{V_{a,n}[\text{HHb}_a]_n + V_v[\text{HHb}_v]_n}{4} V_{\text{blood},n} = 27.36 \mu\text{M} \quad (\text{C.99})$$

normal total deoxygenated haemoglobin (NIRS)

$$\text{H}_{\text{m,init}}^+ = \text{H}_{\text{m,n}}^+ = 3.981e - 05 \text{ mM} \quad (\text{C.100})$$

initial hydrogen ion concentration in mitochondria

$$\text{H}_{\text{m,n}}^+ = 10^{3-\text{pH}_{\text{m,n}}} = 3.981e - 05 \text{ mM} \quad (\text{C.101})$$

normal hydrogen ion concentration in mitochondria

$$h_n = -r_n + \sqrt{r_n^2 + 2r_0h_0 + h_0h_0} = 0.00214 \text{ cm} \quad (\text{C.102})$$

normal wall thickness of cerebral vessels

$$J_{\text{O}_2,n} = \text{CMRO}_{2,n} = 0.034 \text{ mM s}^{-1} \quad (\text{C.103})$$

the resting rate of supply of oxygen to the mitochondria

$$k_{1,0} = \frac{k_{1,n}\text{NADH}}{\text{NADH}_n} = 8.3 \text{ s}^{-1} \quad (\text{C.104})$$

forward rate constant for reaction ared at normal  $\Delta p$

$$k_{1,n} = \frac{f_n}{\text{Cu}_{\text{A,o,n}} - \frac{1}{\text{Keq}_{1,n}}\text{Cu}_{\text{A,r,n}}} = 8.3 \text{ s}^{-1} \quad (\text{C.105})$$

the value of  $k_1$  at normal  $\Delta p$  and NADH

$$k_{2,n} = \frac{f_n}{\text{Cu}_{\text{A,r,n}}\text{cyt a}_{3,\text{o,n}} - \frac{1}{\text{Keq}_{2,n}}\text{Cu}_{\text{A,o,n}}\text{cyt a}_{3,\text{r,n}}} = 3916 \text{ mM}^{-1} \text{ s}^{-1} \quad (\text{C.106})$$

normal forward rate constant for reaction aox

$$k_3 = \frac{k_{3,0} \left( 1 + \exp(-c3(0 - \Delta p_{30})) \right)}{\exp(-c3(0 - \Delta p_{30}))} = 2.5e + 05 \text{ mM}^{-1} \text{ s}^{-1} \quad (\text{C.107})$$

rate constant for reaction box

$$k_{\text{CV}} = \frac{-1}{\Delta p_n - \Delta p_{\text{CV}0}} \ln \left( \frac{1 - L_{\text{CV}0}}{1 + r_{\text{CV}}L_{\text{CV}0}} \right) = 0.02047 \text{ mV}^{-1} \quad (\text{C.108})$$

a parameter controlling the sensitivity of Complex V flux to driving

force

$$K_{eq1,n} = 10^{(-1/Z)(p_1 \Delta p_n / 4 - E_{1,n})} = 3.623 \text{ (dimensionless)} \quad (C.109)$$

normal equilibrium constant for reaction ared

$$K_{eq2,n} = 10^{(-1/Z)(p_2 \Delta p_n / 4 - E_{2,n})} = 0.07735 \text{ (dimensionless)} \quad (C.110)$$

normal equilibrium constant for reaction aox

$$K_G = \frac{G_n}{r_n^4} = 915.7 \text{ ml}_{\text{blood}} \text{ ml}_{\text{brain}}^{-1} \text{ mmHg}^{-1} \text{ s}^{-1} \text{ cm}^{-4} \quad (C.111)$$

constant of proportionality relating pressure drop to flow

$$L_{CV, \text{frac}} = 1 - L_{lk, \text{frac}} = 0.75 \text{ (dimensionless)} \quad (C.112)$$

normal fraction of proton entry into mitochondria associated with ADP phosphorylation

$$L_{CV, \text{max}} = \frac{L_{CV, n}}{L_{CV, 0}} = 19.03 \text{ mM s}^{-1} \quad (C.113)$$

the maximum rate of proton flow through Complex V

$$L_{CV, n} = L_n L_{CV, \text{frac}} = 7.612 \text{ mM s}^{-1} \quad (C.114)$$

the resting flow of protons into the matrix through Complex V

$$L_{lk0} = \frac{L_{lk, n}}{\exp(\Delta p_n k_{lk2}) - 1} = 0.004193 \text{ mM s}^{-1} \quad (C.115)$$

first constant controlling rate of  $L_{lk}$  of  $\Delta p$

$$L_{lk, n} = L_n L_{lk, \text{frac}} = 2.537 \text{ mM s}^{-1} \quad (C.116)$$

the resting flow of protons into the matrix via leak channels

$$L_n = p_{tot} f_n = 10.15 \text{ mM s}^{-1} \quad (C.117)$$

the total flow of protons back into mitochondria

$$\text{NADH} = \frac{N_t}{1 + [\text{NAD}]/[\text{NADH}]} = 0.3 \text{ mM} \quad (C.118)$$

concentration of NADH in the mitochondria

$$\text{NADH}_n = \frac{N_t}{1 + [\text{NAD}]_n/[\text{NADH}]_n} = 0.3 \text{ mM} \quad (C.119)$$

normal concentration of NADH in the mitochondria

$$[\text{NAD}]/[\text{NADH}] = \frac{[\text{NAD}]_n/[\text{NADH}]_n}{u^{2D_{\text{NADH}}}} = 9 \text{ (dimensionless)} \quad (C.120)$$

NAD/NADH ratio

$$[\text{O}_{2, a}] = \phi \left( \frac{\text{SaO}_2}{1 - \text{SaO}_2} \right)^{1/n_h} = 0.1283 \text{ mM} \quad (C.121)$$

arterial dissolved oxygen concentration

$$[\text{O}_{2, c}]_{\text{init}} = [\text{O}_{2, c}]_n = 0.06061 \text{ mM} \quad (C.122)$$

initial concentration of dissolved oxygen in the capillary

$$[\text{O}_{2,c}]_n = \phi \left( \frac{\text{ScO}_{2,n}}{1 - \text{ScO}_{2,n}} \right)^{1/n_h} = 0.06061 \text{ mM} \quad (\text{C.123})$$

normal concentration of dissolved oxygen in the capillary

$$[\text{O}_2]_{\text{init}} = [\text{O}_2]_n = 0.024 \text{ mM} \quad (\text{C.124})$$

initial oxygen concentration in mitochondria

$$P_1 = \frac{P_a + P_v}{2} = 52 \text{ mmHg} \quad (\text{C.125})$$

average blood pressure in vessels

$$p_1 = p_{\text{tot}} - p_{23} = 12 \text{ (dimensionless)} \quad (\text{C.126})$$

the number of protons pumped by reaction aed

$$P_{1,n} = \frac{P_{a,n} + P_{v,n}}{2} = 52 \text{ mmHg} \quad (\text{C.127})$$

normal average blood pressure in vessels

$$p_2 = 4 \times 1 = 4 \text{ (dimensionless)} \quad (\text{C.128})$$

total protons pumped by reaction aox

$$p_{23} = 4 \times 2 = 8 \text{ (dimensionless)} \quad (\text{C.129})$$

total protons pumped by reactions aox and box

$$p_3 = p_{23} - p_2 = 4 \text{ (dimensionless)} \quad (\text{C.130})$$

total protons pumped by reaction box

$$\text{PaO}_2 = \frac{[\text{O}_{2,a}]}{k_{\text{H},\text{O}_2}} = 91.68 \text{ mmHg} \quad (\text{C.131})$$

partial pressure of oxygen in the arteries

$$r_{\text{init}} = r_n = 0.0187 \text{ cm} \quad (\text{C.132})$$

initial radius of blood vessels

$$\text{ScO}_{2,n} = \frac{\text{SaO}_{2,n} + \text{SvO}_{2,n}}{2} = 0.7862 \text{ (dimensionless)} \quad (\text{C.133})$$

normal capillary oxygen saturation

$$\sigma_{e,n} = \sigma_{e0} \left( \exp \left( \frac{K_\sigma (r_n - r_0)}{r_0} \right) - 1 \right) - \sigma_{\text{coll}} = -44.89 \text{ mmHg} \quad (\text{C.134})$$

normal elastic stress in vessel walls

$$\text{SvO}_{2,n} = \frac{[\text{HbO}_{2,v}]_n}{[\text{Hbtot}]_n} = 0.6124 \text{ (dimensionless)} \quad (\text{C.135})$$

normal venous oxygen saturation

$$T_{e,n} = \sigma_{e,n} h_n = -0.09604 \text{ mmHg cm} \quad (\text{C.136})$$

normal elastic tension in vessel walls

$$T_{\text{max}0} = \frac{T_{\text{max},n}}{1 + k_{\text{aut}} \mu_n} = 2.11 \text{ mmHg cm} \quad (\text{C.137})$$

$T_{\text{max}}$  at normal  $\mu$

$$T_{\max,n} = \frac{T_{m,n}}{\exp\left(-\left(\frac{r_n - r_m}{r_t - r_m}\right)^{n_m}\right)} = 2.11 \text{ mmHg cm} \quad (\text{C.138})$$

normal maximum muscular tension developed by circulation

$$T_{m,n} = (P_{1,n} - P_{ic,n})r_n - T_{e,n} = 0.8908 \text{ mmHg cm} \quad (\text{C.139})$$

normal muscular tension in vessel walls

$$v_{\text{CO}_2,n} = P_a \text{CO}_{2,n} = 40 \text{ mmHg} \quad (\text{C.140})$$

normal value of  $v_{\text{CO}_2}$  ( $P_a \text{CO}_2$  passed through a first order filter)

$$V_{a,n} = \frac{V_{t,n}}{1 + \text{VArat}_n} = 0.25 \text{ (dimensionless)} \quad (\text{C.141})$$

normal arterial blood volume as a fraction of total blood volume

$$V_v = V_{t,n} \frac{\text{VArat}_n}{1 + \text{VArat}_n} = 0.75 \text{ (dimensionless)} \quad (\text{C.142})$$

venous blood volume as a fraction of total blood volume

$$v_{\text{O}_2,n} = [\text{O}_{2,c}]_n = 0.06061 \text{ mM} \quad (\text{C.143})$$

normal value of  $v_{\text{O}_2}$  ( $[\text{O}_{2,c}]$  passed through a first order filter)

$$v_{P_a,n} = P_{a,n} = 100 \text{ mmHg} \quad (\text{C.144})$$

normal value of  $v_{P_a}$  ( $P_a$  passed through a first order filter)

$$v_{u,n} = u_n = 1 \text{ (dimensionless)} \quad (\text{C.145})$$

normal value of  $v_u$  ( $u$  passed through a first order filter)

$$[\text{HHb}_a] = [\text{Hbtot}] (1 - \text{SaO}_2) = 0.364 \text{ mM} \quad (\text{C.146})$$

concentration of haemoglobin  $\text{O}_2$  binding sites not occupied by  $\text{O}_2$  (four times deoxyhaemoglobin concentration) in the arteries

$$[\text{HHb}_a]_n = [\text{Hbtot}]_n (1 - \text{SaO}_{2,n}) = 0.364 \text{ mM} \quad (\text{C.147})$$

normal concentration of haemoglobin  $\text{O}_2$  binding sites not occupied by  $\text{O}_2$  (four times deoxyhaemoglobin concentration) in the arteries

$$[\text{HbO}_{2,a}] = [\text{Hbtot}]\text{SaO}_2 = 8.736 \text{ mM} \quad (\text{C.148})$$

concentration of  $\text{O}_2$  bound to arterial haemoglobin (four times oxyhaemoglobin concentration)

$$[\text{HbO}_{2,a}]_n = [\text{Hbtot}]_n \text{SaO}_{2,n} = 8.736 \text{ mM} \quad (\text{C.149})$$

normal concentration of  $\text{O}_2$  bound to arterial haemoglobin (four times oxyhaemoglobin concentration)

$$[\text{HbO}_{2,v}]_{\text{init}} = [\text{HbO}_{2,v}]_n = 5.573 \text{ mM} \quad (\text{C.150})$$

initial concentration of  $\text{O}_2$  bound to venous haemoglobin (four times oxyhaemoglobin concentration)

$$[\text{HbO}_{2,v}]_n = \frac{\text{CBF}_n [\text{HbO}_{2,a}]_n - J_{\text{O}_2,n}}{\text{CBF}_n} = 5.573 \text{ mM} \quad (\text{C.151})$$

normal concentration of  $\text{O}_2$  bound to venous haemoglobin (four times

oxyhaemoglobin concentration)

$$[\text{HHb}_v]_n = [\text{Hbtot}]_n - [\text{HbO}_{2,v}]_n = 3.527 \text{ mM} \quad (\text{C.152})$$

normal concentration of haemoglobin O<sub>2</sub> binding sites not occupied by O<sub>2</sub> (four times deoxyhaemoglobin concentration) in the veins

# Appendix D

## BrainPiglet model equations, variables and parameters

### D.1 Differential Equations

$$\frac{d\text{Cu}_{A,o}}{dt} = 4T_{\text{aox}} - 4T_{\text{ared}} \quad (\text{D.1})$$

$$\frac{d[\text{ADP}]}{dt} = -T_{\text{CK}} - T_{\text{ADPtoATP}} + T_{\text{ATPtoADP}} - 2T_{\text{AK}} - 2T_{\text{Glycolysis}} \quad (\text{D.2})$$

$$\frac{d[\text{AMP}]}{dt} = T_{\text{AK}} \quad (\text{D.3})$$

$$\frac{d[\text{ATP}]}{dt} = T_{\text{CK}} + T_{\text{ADPtoATP}} - T_{\text{ATPtoADP}} + T_{\text{AK}} + 2T_{\text{Glycolysis}} \quad (\text{D.4})$$

$$\frac{d\text{cyt } a_{3,r}}{dt} = 4T_{\text{aox}} - 4T_{\text{box}} \quad (\text{D.5})$$

$$\frac{d[\text{Cr}]}{dt} = T_{\text{CK}} \quad (\text{D.6})$$

$$\frac{d\Delta\Psi}{dt} = \frac{p_2 f_2 + p_1 f_1 + p_3 f_3 - L}{C_{im}} \quad (\text{D.7})$$

$$\frac{d[\text{gluc}]}{dt} = -T_{\text{Glycolysis}} + T_{\text{Gluc}_{in}} - T_{\text{Gluc}_{out}} \quad (\text{D.8})$$

$$\frac{d[\text{H}_m^+]}{dt} = \frac{-p_2 T_{\text{aox}}}{R_{\text{Hi}}} - \frac{\left(p_1 + \frac{10}{6}\right) T_{\text{ared}}}{R_{\text{Hi}}} - \frac{p_3 T_{\text{box}}}{R_{\text{Hi}}} + \frac{T_{\text{psiout}}}{R_{\text{Hi}}} + \frac{4T_{\text{TCA}}}{R_{\text{Hi}}} + \frac{T_{\text{MAshuttle}}}{R_{\text{Hi}} V_{\text{mit}}} \quad (\text{D.9})$$

$$\frac{d[\text{H}_{\text{cyt}}^+]}{dt} = \frac{p_2 T_{\text{aox}} V_{\text{mit}}}{R_{\text{Hi,c}}} + \frac{(p_1 + 4) T_{\text{ared}} V_{\text{mit}}}{R_{\text{Hi,c}}} - \frac{T_{\text{psiout}} V_{\text{mit}}}{R_{\text{Hi,c}}} - \frac{T_{\text{CK}}}{R_{\text{Hi,c}}} + \frac{4T_{\text{Glycolysis}}}{R_{\text{Hi,c}}} - \frac{T_{\text{PytoLac}}}{R_{\text{Hi,c}}} - \frac{T_{\text{TCA}} V_{\text{mit}}}{R_{\text{Hi,c}}} + \frac{T_{\text{Lac,in}}}{R_{\text{Hi,c}}} - \frac{T_{\text{Lac,out}}}{R_{\text{Hi,c}}} - \frac{T_{\text{MAshuttle}}}{R_{\text{Hi,c}}} \quad (\text{D.10})$$

$$\frac{d[\text{lac}]}{dt} = T_{\text{PytoLac}} + T_{\text{Lac,in}} - T_{\text{Lac,out}} \quad (\text{D.11})$$

$$\frac{d[\text{NAD}]}{dt} = 2T_{\text{ared}} - 5T_{\text{TCA}} - \frac{T_{\text{MAshuttle}}}{V_{\text{mit}}} \quad (\text{D.12})$$

$$\frac{d[\text{NAD}_{\text{cyt}}]}{dt} = -2T_{\text{Glycolysis}} + T_{\text{PytoLac}} + T_{\text{MAshuttle}} \quad (\text{D.13})$$

$$\frac{d[\text{O}_2]}{dt} = -T_{\text{box}} + \frac{T_{\text{O}_2\text{in}}}{V_{\text{mit}}(1 - d_f)} \quad (\text{D.14})$$

$$\frac{d[\text{P}_i]}{dt} = -T_{\text{ADPtoATP}} + T_{\text{ATPtoADP}} - 2T_{\text{Glycolysis}} \quad (\text{D.15})$$

$$\frac{d[\text{PCr}]}{dt} = -T_{\text{CK}} \quad (\text{D.16})$$

$$\frac{d[\text{Py}]}{dt} = 2T_{\text{Glycolysis}} - T_{\text{PytoLac}} - \frac{T_{\text{TCA}} V_{\text{mit}}}{1} \quad (\text{D.17})$$

$$\frac{dv_{\text{CO}_2}}{dt} = \frac{1}{\tau_{\text{CO}_2}} (P_a \text{CO}_2 - v_{\text{CO}_2}) \quad (\text{D.18})$$

$$\frac{dv_{\text{O}_2}}{dt} = \frac{1}{\tau_{\text{O}_2}} ([\text{O}_{2,c}] - v_{\text{O}_2}) \quad (\text{D.19})$$

$$\frac{dv_{P_a}}{dt} = \frac{1}{\tau_{P_a}} (P_{a2} - v_{P_a}) \quad (\text{D.20})$$

$$\frac{dv_u}{dt} = \frac{1}{\tau_u} (u - v_u) \quad (\text{D.21})$$

## D.2 Algebraic Equations

$$\phi \left( \frac{\text{ScO}_2}{1 - \text{ScO}_2} \right)^{1/n_h} - [\text{O}_{2,c}] = 0 \quad (\text{D.22})$$

$$T_e + T_m - (P_1 - P_{ic}) r = 0 \quad (\text{D.23})$$

$$\text{CBF}([\text{HbO}_{2,a}] - [\text{HbO}_{2,v}]) - J_{\text{O}_2} = 0 \quad (\text{D.24})$$

### D.3 Chemical Reactions

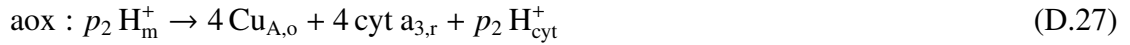
Reactions are represented as terms in differential equations (see section D.1).



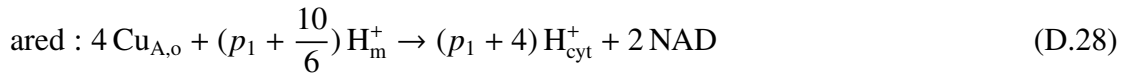
a two way reaction in which two molecules of ADP are converted into one of ATP and one of AMP catalysed by adenylate kinase (Rate  $T_{\text{AK}}$ )



phosphorylation of ADP by Complex V (Rate  $T_{\text{ADPtoATP}}$ )



the reaction in which  $\text{cyt } a_{3,o}$  oxidises  $\text{Cu}_{\text{A},r}$  and  $p_2$  protons are pumped out of the matrix (Rate  $T_{\text{aox}}$ )



the reaction in which  $\text{Cu}_{\text{A},o}$  is reduced and  $p_1$  protons are pumped out of the matrix (Rate  $T_{\text{ared}}$ )



hydrolysis of ATP (Rate  $T_{\text{ATPtoADP}}$ )



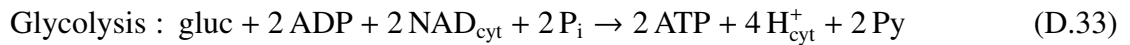
the reaction in which  $\text{O}_2$  oxidises  $\text{cyt } a_{3,r}$  and  $p_3$  protons are pumped out of the matrix (Rate  $T_{\text{box}}$ )



transport of glucose from the blood to the cytoplasm (fixed rate) (Rate  $T_{\text{Gluc}_{\text{in}}}$ )



transport of glucose from the cytoplasm to the blood (Rate  $T_{\text{Gluc}_{\text{out}}}$ )



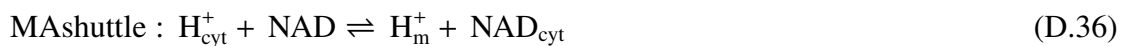
a one way Michaelis Menten reaction which is assumed to capture the process of glycolysis (Rate  $T_{\text{Glycolysis}}$ )



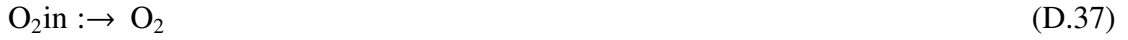
transport of lactate from the blood to the cytoplasm (fixed rate) (Rate  $T_{\text{Lac}_{\text{in}}}$ )



transport of lactate from the cytoplasm to the blood (Rate  $T_{\text{Lac}_{\text{out}}}$ )



malate aspartate shuttle: transfer between NAD/NADH in the cytoplasm and the mitochondria (Rate  $T_{MAshuttle}$ )



the reaction in which oxygen is supplied to the mitochondria (Rate  $T_{O_{2in}}$ )



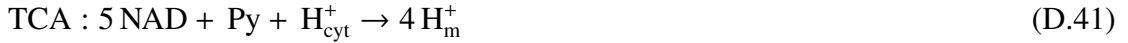
a two way mass action reaction representing the interconversion of PCr and ADP to Cr and ATP (Rate  $T_{CK}$ )



the reaction in which protons re-enter the matrix (via leak and Complex V) (Rate  $T_{psiout}$ )



interconversion between pyruvate and lactate (Rate  $T_{PytoLac}$ )



one step simple representation of pyruvate dehydrogenase and the TCA cycle (Rate  $T_{TCA}$ )

## D.4 Variables

$Cu_{A,o}$  (mM) Inital Value =  $Cu_{A,o,init} = 0.022$  mM

the concentration of oxidised cytochrome-c-oxidase

$[ADP]$  (mM) Inital Value =  $[ADP]_n = 0.012$  mM

ADP concentration in cytoplasm

$[AMP]$  (mM) Inital Value =  $[AMP]_n = 0.000334$  mM

AMP concentration in cytoplasm

$[ATP]$  (mM) Inital Value =  $[ATP]_n = 1.2$  mM

ATP concentration in cytoplasm

$cyt a_{3,r}$  (mM) Inital Value =  $cyt a_{3,r,init} = 0.000828$  mM

concentration of reduced cytochrome  $a_3$  in mitochondria

$[Cr]$  (mM) Inital Value =  $[Cr]_n = 4.316$  mM

creatine concentration in cytoplasm

$\Delta\Psi$  (mV) Inital Value =  $\Delta\Psi_{init} = 145$  mV

mitochondrial inner membrane potential

$[gluc]$  (mM) Inital Value =  $[gluc]_n = 1.2$  mM

concentration of glucose in the cytoplasm

$[H_m^+]$  (mM) Inital Value =  $H_{m,init}^+ = 3.981e - 05$  mM

concentration of hydrogen ions in mitochondria

$[H_{cyt}^+]$  (mM) Inital Value =  $[H^+]_n = 0.0001$  mM

concentration of hydrogen ions in the cytoplasm

[lac] (mM) Inital Value = [lac]<sub>n</sub> = 3 mM  
concentration of lactate in the cytoplasm

[NAD] (mM) Inital Value = [NAD]<sub>n</sub> = 2.7 mM  
concentration of NAD in the mitochondria

[NAD<sub>cyt</sub>] (mM) Inital Value = [NAD<sub>cyt</sub>]<sub>n</sub> = 359 mM  
concentration of NAD in the cytoplasm

[O<sub>2</sub>] (mM) Inital Value = [O<sub>2</sub>]<sub>init</sub> = 0.024 mM  
the concentration of oxygen in the mitochondria

[O<sub>2,c</sub>] (mM) Inital Value = [O<sub>2,c</sub>]<sub>init</sub> = 0.05343 mM  
the concentration of oxygen in the capillary

[P<sub>i</sub>] (mM) Inital Value = [P]<sub>n</sub> = 0.9524 mM  
inorganic phosphate concentration in cytoplasm

[PCr] (mM) Inital Value = [PCr]<sub>n</sub> = 2.6 mM  
phosphocreatine concentration in cytoplasm

[Py] (mM) Inital Value = [Py]<sub>n</sub> = 0.1 mM  
concentration of pyruvate in the cytoplasm

*r* (cm) Inital Value = *r*<sub>n</sub> = 0.0187 cm  
typical radius of cerebral vessels

*v*<sub>CO<sub>2</sub></sub> (mmHg) Inital Value = *v*<sub>CO<sub>2,n</sub></sub> = 40 mmHg  
*P<sub>a</sub>*CO<sub>2</sub> passed through a first order filter

*v*<sub>O<sub>2</sub></sub> (mM) Inital Value = *v*<sub>O<sub>2,n</sub></sub> = 0.05343 mM  
[O<sub>2,c</sub>] passed through a first order filter

*v*<sub>*P<sub>a</sub>*</sub> (mmHg) Inital Value = *v*<sub>*P<sub>a,n</sub>*</sub> = 43.31 mmHg  
ABP passed through a first order filter

*v<sub>u</sub>* (dimensionless) Inital Value = *v<sub>u,n</sub>* = 1 (dimensionless)  
the demand parameter *u* passed through a first order filter

[HbO<sub>2,v</sub>] (mM) Inital Value = [HbO<sub>2,v</sub>]<sub>init</sub> = 2.684 mM  
the concentration of bound oxygen in the veins

## D.5 Temporary Variables

$$Cu_{A,r} = [CCO]_{mit} - Cu_{A,o}, \quad (\text{mM}) \quad (\text{D.42})$$

the concentration of reduced cytochrome-c-oxidase in the mitochondria

$$AVR = \frac{V_a}{V_v}, \quad (\text{dimensionless}) \quad (\text{D.43})$$

arterio-venous volume ratio

$$cyt a_{3,o} = [CCO]_{mit} - cyt a_{3,r}, \quad (\text{mM}) \quad (\text{D.44})$$

concentration of oxidised cytochrome a<sub>3</sub> in mitochondria

$$C_{0i,m} = \frac{10^{-pH_m} - 10^{-pH_m - dpH}}{dpH}, \quad (\text{dimensionless}) \quad (\text{D.45})$$

natural buffering capacity for protons in mitochondria

$$C_{0i,c} = \frac{10^{-\text{pH}_o} - 10^{-\text{pH}_o - \text{dpH}}}{\text{dpH}}, \quad (\text{dimensionless}) \quad (\text{D.46})$$

natural buffering capacity for protons in the cytoplasm

$$\text{CBF} = G(P_{a2} - P_v), \quad (\text{ml}_{\text{blood}} \text{ ml}_{\text{brain}}^{-1} \text{ s}^{-1}) \quad (\text{D.47})$$

cerebral blood flow

$$\Delta\text{oxCCO} = \Delta\text{oxCCO}_{\text{offset}} + 1000V_{\text{mit}} \left( (1 - d_f) \text{Cu}_{\text{A,o}} - \text{Cu}_{\text{A,o,n}} \right), \quad (\mu\text{M}) \quad (\text{D.48})$$

the expected CCO signal (as measured by NIRS)

$$\text{CMR}_{\text{gluc}} = T_{\text{Gluc}_{\text{in}}} - T_{\text{Gluc}_{\text{out}}}, \quad (\text{mM s}^{-1}) \quad (\text{D.49})$$

rate of glucose metabolism

$$\text{CMR}_{\text{lac}} = T_{\text{Lac}_{\text{in}}} - T_{\text{Lac}_{\text{out}}}, \quad (\text{mM s}^{-1}) \quad (\text{D.50})$$

rate of lactate metabolism

$$\text{CMRO}_2 = (1 - d_f) f_3 V_{\text{mit}}, \quad (\text{mM s}^{-1}) \quad (\text{D.51})$$

cerebral metabolic rate of oxygen consumption

$$C_{\text{NADH}} = \frac{Z}{2} \log \left( \frac{1}{[\text{NAD}]/[\text{NADH}]} \right), \quad (\text{mV}) \quad (\text{D.52})$$

redox potential minus standard redox potential for NADH at normal demand

$$\Delta G_1 = -4 \left( E_1 + Z \log \left( \frac{\text{Cu}_{\text{A,o}}}{\text{Cu}_{\text{A,r}}} \right) \right) + p_1 \Delta p, \quad (\text{mV}) \quad (\text{D.53})$$

free energy associated with reaction ared

$$\Delta G_2 = -4 \left( E_2 + Z \left( \log \left( \frac{\text{Cu}_{\text{A,r}}}{\text{Cu}_{\text{A,o}}} \right) - \log \left( \frac{\text{cyt } a_{3,r}}{\text{cyt } a_{3,o}} \right) \right) \right) + p_2 \Delta p, \quad (\text{mV}) \quad (\text{D.54})$$

free energy associated with reaction aox

$$\Delta G = \Delta G^\circ + ZF \log(g_p), \quad (\text{J mol}^{-1}) \quad (\text{D.55})$$

Gibbs free energy of ATP hydrolysis

$$\Delta\text{Hbdiff} = \Delta\text{Hbdiff}_{\text{offset}} + \Delta\text{HbO}_2 - \Delta\text{HHb}, \quad (\mu\text{M}) \quad (\text{D.56})$$

change in (HbO<sub>2</sub> – HHb) (NIRS)

$$\Delta\text{HbO}_2 = \Delta\text{HbO}_{2,\text{offset}} + \text{HbO}_2 - \text{HbO}_{2,n}, \quad (\mu\text{M}) \quad (\text{D.57})$$

change in total oxygenated haemoglobin (NIRS)

$$\Delta\text{Hbt} = \Delta\text{HbT}_{\text{offset}} + \text{Hbt} - \text{Hbt}_n, \quad (\mu\text{M}) \quad (\text{D.58})$$

change in total haemoglobin (NIRS)

$$\Delta\text{HHb} = \Delta\text{HHb}_{\text{offset}} + \text{HHb} - \text{HHb}_n, \quad (\mu\text{M}) \quad (\text{D.59})$$

change in total deoxygenated haemoglobin (NIRS)

$$\Delta p = \Delta\Psi + Z\Delta\text{pH}, \quad (\text{mV}) \quad (\text{D.60})$$

the proton motive force across the mitochondrial inner membrane

$$\Delta p\text{H} = \text{pH}_m - \text{pH}_o, \quad (\text{dimensionless}) \quad (\text{D.61})$$

the pH difference across mitochondrial inner membrane

$$E_1 = E_{1,NADH}, \quad (\text{mV}) \quad (\text{D.62})$$

the energy provided by electron transfer to  $\text{Cu}_{A,o}$

$$E_{1,NADH} = \mathcal{E}_0(\text{Cu}_A) - \mathcal{E}_0(\text{NADH}) + C_{NADH}, \quad (\text{mV}) \quad (\text{D.63})$$

$E_1$  when the reducing substrate is NADH

$$\eta = R_P \left( \frac{v_{P_a}}{v_{P_a,n}} - 1 \right) + R_O \left( \frac{v_{O_2}}{v_{O_2,n}} - 1 \right) + R_u \left( 1 - \frac{v_u}{v_{u,n}} \right) + R_C \left( 1 - \frac{v_{CO_2}}{v_{CO_2,n}} \right), \quad (\text{dimensionless}) \quad (\text{D.64})$$

total autoregulatory stimuli

$$f_1 = k_1 \text{Cu}_{A,o} - k_{-1} \text{Cu}_{A,r}, \quad (\text{mM s}^{-1}) \quad (\text{D.65})$$

the rate at which  $\text{Cu}_{A,o}$  is reduced

$$f_2 = k_2 \text{Cu}_{A,r} \text{cyt } a_{3,o} - k_{-2} \text{Cu}_{A,o} \text{cyt } a_{3,r}, \quad (\text{mM s}^{-1}) \quad (\text{D.66})$$

the rate at which  $\text{Cu}_{A,r}$  is oxidised and  $\text{cyt } a_{3,o}$  reduced

$$f_3 = \frac{k_3 [\text{O}_2] \text{cyt } a_{3,r} \exp(-c_3 (\Delta p - \Delta p_{30}))}{1 + \exp(-c_3 (\Delta p - \Delta p_{30}))}, \quad (\text{mM s}^{-1}) \quad (\text{D.67})$$

the rate at which  $\text{cyt } a_{3,r}$  is oxidised

$$G = K_G r^4, \quad (\text{ml}_{\text{blood}} \text{ml}_{\text{brain}}^{-1} \text{mmHg}^{-1} \text{s}^{-1}) \quad (\text{D.68})$$

resistance of cerebral circulation

$$g_p = \frac{[\text{ADP}][\text{P}_i]}{1000[\text{ATP}]}, \quad (\text{dimensionless}) \quad (\text{D.69})$$

(normalised) phosphorylation potential (or ADP/ATP ratio)

$$G_t = \frac{GG_0 G_v}{GG_0 + GG_v + G_v G_0}, \quad (\text{ml}_{\text{blood}} \text{ml}_{\text{brain}}^{-1} \text{mmHg}^{-1} \text{s}^{-1}) \quad (\text{D.70})$$

the total conductance of the cerebral blood vessels

$$h = -r + \sqrt{r^2 + 2r_0 h_0 + h_0^2}, \quad (\text{cm}) \quad (\text{D.71})$$

wall thickness of cerebral vessels

$$\text{HbO}_2 = 1000 \frac{V_a [\text{HbO}_{2,a}] + V_v [\text{HbO}_{2,v}]}{4} V_{\text{blood},n}, \quad (\mu\text{M}) \quad (\text{D.72})$$

total oxygenated haemoglobin (NIRS)

$$\text{Hbt} = 1000 \frac{(V_a + V_v) [\text{Hbtot}]}{4} V_{\text{blood},n}, \quad (\mu\text{M}) \quad (\text{D.73})$$

total haemoglobin (NIRS)

$$\text{HHb} = 1000 \frac{V_a [\text{HHb}_a] + V_v [\text{HHb}_v]}{4} V_{\text{blood},n}, \quad (\mu\text{M}) \quad (\text{D.74})$$

total deoxygenated haemoglobin (NIRS)

$$J_{O_2, \min} = \min \left( D_{O_2} ([O_{2,c}] - [O_2]) \text{CBF}[\text{HbO}_{2,a}] \right), \quad (\text{mM s}^{-1}) \quad (\text{D.75})$$

rate at which oxygen is supplied to the mitochondria, minimum of diffusion rate and delivery rate

$$J_{O_2} = J_{O_2, \min}, \quad (\text{mM s}^{-1}) \quad (\text{D.76})$$

the rate at which oxygen is supplied to the mitochondria

$$k_1 = k_{1,0} \exp(-c_{k1} (\Delta p - \Delta p_n)), \quad (\text{s}^{-1}) \quad (\text{D.77})$$

forward rate constant for reaction ared

$$k_{1,0} = \frac{k_{1,n} \frac{N_t}{1 + [\text{NAD}]/[\text{NADH}]}}{\text{NADH}_n}, \quad (\text{s}^{-1}) \quad (\text{D.78})$$

forward rate constant for reaction ared at normal  $\Delta p$

$$k_2 = k_{2,n} \exp(-c_{k2} (\Delta p - \Delta p_n)), \quad (\text{mM}^{-1} \text{s}^{-1}) \quad (\text{D.79})$$

forward rate constant for reaction aox

$$k_{\text{ATP,CV}} = \frac{L_{\text{CV}} V_{\text{mit}}}{n_a}, \quad (\text{mM s}^{-1}) \quad (\text{D.80})$$

rate of ATP synthesis by Complex V

$$\text{Keq}_1 = 10^{(-1/Z)(p_1 \Delta p / 4 - E_1)}, \quad (\text{dimensionless}) \quad (\text{D.81})$$

equilibrium constant for reaction ared

$$\text{Keq}_2 = 10^{(-1/Z)(p_2 \Delta p / 4 - E_2)}, \quad (\text{dimensionless}) \quad (\text{D.82})$$

equilibrium constant for reaction aox

$$k_{\text{MAshut}} = \frac{\text{CMRO}_{2,n} [\text{NADH}_{\text{cyt}}]}{3 \left( [\text{NADH}_{\text{cyt}}]_n [\text{NAD}]_n [\text{H}^+]_n - \frac{1}{\text{Keq}_{\text{MAshut}}} [\text{NAD}_{\text{cyt}}]_n \text{NADH}_n \text{H}_{\text{m,n}}^+ \right)}, \quad (\text{mM}^{-1} \text{s}^{-1}) \quad (\text{D.83})$$

rate of forward reaction in the malate-aspartate shuttle

$$k_{-1} = \frac{k_1}{\text{Keq}_1}, \quad (\text{s}^{-1}) \quad (\text{D.84})$$

backward rate constant for reaction ared

$$k_{-2} = \frac{k_2}{\text{Keq}_2}, \quad (\text{mM}^{-1} \text{s}^{-1}) \quad (\text{D.85})$$

backward rate constant for reaction aox

$$k_{\text{MAshut}}^- = \frac{k_{\text{MAshut}} [\text{NADH}]}{[\text{NADH}_{\text{cyt}}] \text{Keq}_{\text{MAshut}}}, \quad (\text{mM}^{-1} \text{s}^{-1}) \quad (\text{D.86})$$

rate of backward reaction in the malate-aspartate shuttle

$$k_{pl} = \frac{2\text{CMR}_{\text{gluc},n} - \frac{\text{CMRO}_{2,n}}{3} + k_{pl}^{-}[\text{lac}]_n[\text{NAD}_{\text{cyt}]_n} \frac{[\text{NADH}_{\text{cyt}]_n}}{[\text{NADH}_{\text{cyt}]_n}}}{[\text{Py}]_n[\text{H}^+]_n} \frac{[\text{NADH}_{\text{cyt}]_n}}{[\text{NADH}_{\text{cyt}]_n}}, \quad (\text{mM}^{-1} \text{s}^{-1}) \quad (\text{D.87})$$

rate of forward reaction in the pyruvate lactate equilibrium

$$k_{\text{TCA}} = \frac{v_{\text{TCA}}[\text{Py}][\text{NAD}]}{(k_{m,\text{tcaN}} + [\text{NAD}])(k_{m,\text{tcaP}} + [\text{Py}]}, \quad (\text{mM s}^{-1}) \quad (\text{D.88})$$

rate of the TCA cycle

$$L = L_{CV} + L_{lk}, \quad (\text{mM s}^{-1}) \quad (\text{D.89})$$

the rate at which protons reenter the mitochondrial matrix

$$L_{CV} = \frac{CV_{inh}L_{CV,\max}(1 - e^{-\theta})}{1 + r_{CV}e^{-\theta}}, \quad (\text{mM s}^{-1}) \quad (\text{D.90})$$

the rate at which protons reenter the mitochondrial matrix associated with ADP phosphorylation

$$L_{lk} = k_{unc}L_{lk0}(\exp(\Delta p k_{lk2}) - 1), \quad (\text{mM s}^{-1}) \quad (\text{D.91})$$

the rate at which protons reenter the mitochondrial matrix through leak channels

$$\mu = \frac{\mu_{\min} + \mu_{\max}e^{\eta}}{1 + e^{\eta}}, \quad (\text{dimensionless}) \quad (\text{D.92})$$

total autoregulatory stimuli filtered through sigmoidal function

$$[\text{NADH}] = N_t - [\text{NAD}], \quad (\text{mM}) \quad (\text{D.93})$$

concentration of NADH in the mitochondria

$$[\text{NADH}_{\text{cyt}}] = [\text{NAD}_{\text{cyt}]_n + [\text{NADH}_{\text{cyt}]_n} - [\text{NAD}_{\text{cyt}}], \quad (\text{mM}) \quad (\text{D.94})$$

concentration of NADH in the cytoplasm

$$[\text{NAD}]/[\text{NADH}] = \frac{[\text{NAD}]}{[\text{NADH}]}, \quad (\text{dimensionless}) \quad (\text{D.95})$$

NAD/NADH ratio

$$\text{NTP/EPP} = \frac{(1 - d_f)[\text{ATP}]}{\text{EPP}}, \quad (\text{dimensionless}) \quad (\text{D.96})$$

the ratio [ATP]/EPP

$$P_1 = \frac{P_{a2} + P_v}{2}, \quad (\text{mmHg}) \quad (\text{D.97})$$

average blood pressure in vessels

$$P_{a2} = \frac{G_0P_a + GP_v}{G + G_0}, \quad (\text{mmHg}) \quad (\text{D.98})$$

the pressure at the start of the cerebral artery compartment

$$\text{PCr/EPP} = \frac{(1 - d_f)[\text{PCr}]}{\text{EPP}}, \quad (\text{dimensionless}) \quad (\text{D.99})$$

the ratio [PCr]/EPP

$$pH_m = -\log\left(\frac{[H_m^+]}{1000}\right), \quad (\text{dimensionless}) \quad (\text{D.100})$$

mitochondrial pH

$$pH_o = -\log\left(\frac{[H_{\text{cyt}}^+]}{1000}\right), \quad (\text{dimensionless}) \quad (\text{D.101})$$

extra-mitochondrial pH

$$P_i/\text{EPP} = \frac{(1 - d_f)[P_i]}{\text{EPP}} + d_f, \quad (\text{dimensionless}) \quad (\text{D.102})$$

the ratio  $[P_i]/\text{EPP}$

$$P_v = \frac{G_t}{G_v}(P_a - P_{vs}) + P_{vs}, \quad (\text{mmHg}) \quad (\text{D.103})$$

venous blood pressure

$$R_{\text{ATPtoADP}} = \frac{[\text{ATP}]}{k_m + [\text{ATP}]}, \quad (\text{dimensionless}) \quad (\text{D.104})$$

Relative rate of reaction ATPtoADP

$$r_{\text{buffi,m}} = \frac{C_{\text{buffi,m}}}{C_{O_i,m}}, \quad (\text{dimensionless}) \quad (\text{D.105})$$

buffering capacity for protons in mitochondria

$$r_{\text{buffi,c}} = \frac{C_{\text{buffi,c}}}{C_{O_i,c}}, \quad (\text{dimensionless}) \quad (\text{D.106})$$

buffering capacity for protons in the cytoplasm

$$R_{\text{Gluc}_{\text{in}}} = V_{\text{glucosein}}, \quad (\text{dimensionless}) \quad (\text{D.107})$$

Relative rate of reaction  $\text{Gluc}_{\text{in}}$

$$R_{\text{Gluc}_{\text{out}}} = \frac{[\text{gluc}]}{k_{\text{glut}} + [\text{gluc}]}, \quad (\text{dimensionless}) \quad (\text{D.108})$$

Relative rate of reaction  $\text{Gluc}_{\text{out}}$

$$R_{\text{Glycolysis}} = \frac{[\text{ADP}]^2[\text{P}_i]^2[\text{gluc}][\text{NAD}_{\text{cyt}}]^2}{(k_{m,\text{glycA}} + [\text{ADP}])^2(k_{m,\text{glycP}} + [\text{P}_i])^2(k_{m,\text{glycG}} + [\text{gluc}])(k_{m,\text{glycN}} + [\text{NAD}_{\text{cyt}}])^2}, \quad (\text{dimensionless}) \quad (\text{D.109})$$

Relative rate of reaction Glycolysis

$$R_{\text{Hi}} = r_{\text{buffi,m}}, \quad (\text{dimensionless}) \quad (\text{D.110})$$

relative mitochondrial volume for protons

$$R_{\text{Hi,c}} = r_{\text{buffi,c}}, \quad (\text{dimensionless}) \quad (\text{D.111})$$

relative cytoplasmic volume for protons

$$R_{\text{Lac}_{\text{in}}} = V_{\text{lacin}}, \quad (\text{dimensionless}) \quad (\text{D.112})$$

Relative rate of reaction  $\text{Lac}_{\text{in}}$

$$R_{\text{Lac}_{\text{out}}} = \frac{[\text{lac}][\text{H}_{\text{cyt}}^+]}{(k_{\text{MCT}} + [\text{lac}])(k_{\text{MCT,H}^+} + [\text{H}_{\text{cyt}}^+])}, \quad (\text{dimensionless}) \quad (\text{D.113})$$

Relative rate of reaction Lac<sub>out</sub>

$$\text{ScO}_2 = \frac{\text{SaO}_2 + \text{SvO}_2}{2}, \quad (\text{dimensionless}) \quad (\text{D.114})$$

capillary oxygen saturation

$$\sigma_e = \sigma_{e0} \left( \exp \left( \frac{K_\sigma (r - r_0)}{r_0} \right) - 1 \right) - \sigma_{\text{coll}}, \quad (\text{mmHg}) \quad (\text{D.115})$$

elastic stress in vessel walls

$$\text{SvO}_2 = \frac{[\text{HbO}_{2,\text{v}}]}{[\text{Hbtot}]}, \quad (\text{dimensionless}) \quad (\text{D.116})$$

venous oxygen saturation

$$T_{\text{AK}} = k_{\text{AK}}[\text{ADP}]^2 - k_{\text{AK}}^-[\text{ATP}][\text{AMP}], \quad (\text{mM s}^{-1}) \quad (\text{D.117})$$

Rate of reaction AK

$$T_{\text{ADPtoATP}} = k_{\text{ATP,Cv}}, \quad (\text{mM s}^{-1}) \quad (\text{D.118})$$

Rate of reaction ADPtoATP

$$T_{\text{aox}} = f_2, \quad (\text{mM s}^{-1}) \quad (\text{D.119})$$

Rate of reaction aox

$$T_{\text{ared}} = f_1, \quad (\text{mM s}^{-1}) \quad (\text{D.120})$$

Rate of reaction ared

$$T_{\text{ATPtoADP}} = \frac{V_{\text{max,ATP}}[\text{ATP}]}{k_m + [\text{ATP}]}, \quad (\text{mM s}^{-1}) \quad (\text{D.121})$$

Rate of reaction ATPtoADP

$$T_{\text{box}} = f_3, \quad (\text{mM s}^{-1}) \quad (\text{D.122})$$

Rate of reaction box

$$T_e = \sigma_e h, \quad (\text{mmHg cm}) \quad (\text{D.123})$$

elastic tension in vessel walls

$$T_{\text{Gluc}_{\text{in}}} = v_{\text{glut}} V_{\text{glucosein}}, \quad (\text{mM s}^{-1}) \quad (\text{D.124})$$

Rate of reaction Gluc<sub>in</sub>

$$T_{\text{Gluc}_{\text{out}}} = \frac{v_{\text{glut}}[\text{gluc}]}{k_{\text{glut}} + [\text{gluc}]}, \quad (\text{mM s}^{-1}) \quad (\text{D.125})$$

Rate of reaction Gluc<sub>out</sub>

$$T_{\text{Glycolysis}} = \frac{v_{\text{glyc}}[\text{ADP}]^2[\text{P}_i]^2[\text{gluc}][\text{NAD}_{\text{cyt}}]^2}{(k_{m,\text{glycA}} + [\text{ADP}]^2)(k_{m,\text{glycP}} + [\text{P}_i]^2)(k_{m,\text{glycG}} + [\text{gluc}])(k_{m,\text{glycN}} + [\text{NAD}_{\text{cyt}}]^2)}, \quad (\text{mM s}^{-1}) \quad (\text{D.126})$$

Rate of reaction Glycolysis

$$\theta = k_{CV} \left( \Delta p + \frac{Z}{n_a} \log \left( \frac{g_p}{g_{p,n}} \right) - \Delta p_{CV0} \right), \quad (\text{dimensionless}) \quad (\text{D.127})$$

driving force for Complex V

$$T_{\text{Lac}_{\text{in}}} = v_{\text{MCT}} V_{\text{lac}_{\text{in}}}, \quad (\text{mM s}^{-1}) \quad (\text{D.128})$$

Rate of reaction Lac<sub>in</sub>

$$T_{\text{Lac}_{\text{out}}} = \frac{v_{\text{MCT}} [\text{lac}] [\text{H}_{\text{cyt}}^+]}{(k_{\text{MCT}} + [\text{lac}]) (k_{\text{MCT}, \text{H}^+} + [\text{H}_{\text{cyt}}^+])}, \quad (\text{mM s}^{-1}) \quad (\text{D.129})$$

Rate of reaction Lac<sub>out</sub>

$$T_m = T_{\text{max}} \exp \left( - \left( \frac{r - r_m}{r_t - r_m} \right)^{n_m} \right), \quad (\text{mmHg cm}) \quad (\text{D.130})$$

muscular tension in vessel walls

$$T_{\text{MAshuttle}} = k_{\text{MAshut}} [\text{H}_{\text{cyt}}^+] [\text{NAD}] - k_{\text{MAshut}}^- [\text{NAD}_{\text{cyt}}] [\text{H}_m^+], \quad (\text{mM s}^{-1}) \quad (\text{D.131})$$

Rate of reaction MAshuttle

$$T_{\text{max}} = T_{\text{max}0} (1 + k_{\text{aut}} \mu), \quad (\text{mmHg cm}) \quad (\text{D.132})$$

maximum muscular tension developed by circulation

$$T_{\text{O}_{2\text{in}}} = J_{\text{O}_2}, \quad (\text{mM s}^{-1}) \quad (\text{D.133})$$

Rate of reaction O<sub>2</sub>in

$$\text{TOS} = \frac{100}{[\text{Hbtot}]} \left[ \frac{\left( \frac{r}{r_n} \right)^2 [\text{HbO}_{2,a}] + \frac{V_v}{V_{a,n}} [\text{HbO}_{2,v}]}{\left( \frac{r}{r_n} \right)^2 + \frac{V_v}{V_{a,n}}} + \frac{\left( \frac{r}{r_n} \right)^2 + \frac{V_v}{V_{a,n}}}{\left( \frac{r}{r_n} \right)^2 + \frac{V_v}{V_{a,n}}} \right], \quad (\text{dimensionless}) \quad (\text{D.134})$$

tissue oxygenation index

$$T_{\text{CK}} = k_{\text{PCr}} [\text{PCr}] [\text{ADP}] [\text{H}_{\text{cyt}}^+] - k_{\text{PCr}}^- [\text{ATP}] [\text{Cr}], \quad (\text{mM s}^{-1}) \quad (\text{D.135})$$

Rate of reaction CK

$$T_{\text{psiout}} = L, \quad (\text{mM s}^{-1}) \quad (\text{D.136})$$

Rate of reaction psiout

$$T_{\text{PytoLac}} = k_{\text{pl}} [\text{Py}] [\text{H}_{\text{cyt}}^+] - k_{\text{pl}}^- [\text{lac}] [\text{NAD}_{\text{cyt}}], \quad (\text{mM s}^{-1}) \quad (\text{D.137})$$

Rate of reaction PytoLac

$$T_{\text{TCA}} = k_{\text{TCA}}, \quad (\text{mM s}^{-1}) \quad (\text{D.138})$$

Rate of reaction TCA

$$V_{\text{max,ATP}} = \left( \frac{L_{CV,n} V_{\text{mit}}}{n_a} + 2\text{CMR}_{\text{gluc},n} \right) (1 + k_{m,\text{ATP}}) u, \quad (\text{mM s}^{-1}) \quad (\text{D.139})$$

Vmax of ATP use

$$v_{\text{glyc}} = \frac{v_{\text{glyc},n} (I + 1)}{1 + I \frac{[\text{ATP}] [\text{AMP}]_n}{[\text{ATP}]_n [\text{AMP}]}}, \quad (\text{mM s}^{-1}) \quad (\text{D.140})$$

Vmax for glycolysis

$$V_{mca} = \text{CBFCBFscale}, \quad (\text{cm s}^{-1}) \quad (\text{D.141})$$

the velocity of blood in the middle cerebral artery

$$V_a = V_{a,n} \left( \frac{r}{r_n} \right)^2, \quad (\text{dimensionless}) \quad (\text{D.142})$$

arterial blood volume as a fraction of normal total blood volume

$$V_t = V_a + V_v, \quad (\text{dimensionless}) \quad (\text{D.143})$$

normalised total blood volume

$$V_v = V_{v,n} + C_v (P_v - P_{v,n}), \quad (\text{dimensionless}) \quad (\text{D.144})$$

venous blood volume as a fraction of total blood volume

$$[\text{HHb}_v] = [\text{Hbtot}] - [\text{HbO}_{2,v}], \quad (\text{mM}) \quad (\text{D.145})$$

concentration of haemoglobin O<sub>2</sub> binding sites not occupied by O<sub>2</sub> (four times deoxyhaemoglobin concentration) in the veins

## D.6 Parameters

$$[\text{ADP}]_n = 0.0120 \text{ mM} \quad \text{Range: } 0.0096 \text{ to } 0.0144$$

the normal concentration of ADP in the cytoplasm [294]

$$\text{Cu}_{A,\text{frac},n} = 0.67 \text{ (dimensionless)} \quad \text{Range: } 0.00 \text{ to } 1.00$$

normal oxidised fraction of Cu<sub>A</sub>

$$[\text{ATP}]_n = 1.2 \text{ mM} \quad \text{Range: } 0.1 \text{ to } 10.0$$

the normal concentration of ATP in the cytoplasm [295]

$$V_{\text{blood},n} = 0.0325 \text{ (dimensionless)} \quad \text{Range: } 0.0260 \text{ to } 0.0390$$

normal blood volume as a fraction of brain tissue volume

$$c3 = 0.110 \text{ mV}^{-1} \quad \text{Range: } 0.088 \text{ to } 0.120$$

parameter controlling the sensitivity of reaction box to  $\Delta p$

$$\text{CBF}_n = 0.0080 \text{ ml}_{\text{blood}} \text{ ml}_{\text{brain}}^{-1} \text{ s}^{-1} \quad \text{Range: } 0.0064 \text{ to } 0.0096$$

normal cerebral blood flow

$$\text{CBFscale} = 5000 \text{ cm} \quad \text{Not included in sensitivity analysis}$$

ratio between  $V_{mca}$  and CBF

$$C_{\text{buf},m} = 0.0220 \text{ (dimensionless)} \quad \text{Range: } 0.0176 \text{ to } 0.0264$$

buffering capacity for protons in mitochondria

$$C_{\text{buf},c} = 0.025 \text{ (dimensionless)} \quad \text{Range: } 0.020 \text{ to } 0.030$$

buffering capacity for protons in the cytoplasm

$$\Delta \text{oxCCO}_{\text{offset}} = 0 \text{ } \mu\text{M} \quad \text{Not included in sensitivity analysis}$$

an arbitrary baseline offset to the  $\Delta \text{oxCCO}$  signal (NIRS)

$$\text{occ}_{\text{frac}} = 0.80 \text{ (dimensionless)} \quad \text{Range: } 0.64 \text{ to } 0.96$$

fraction of arterial blood which flows through the carotid arteries under normal conditions

$C_{im} = 0.00675 \text{ mM mV}^{-1}$  Range: 0.00540 to 0.00810  
 capacitance of mitochondrial inner membrane  
 $c_{k1} = 0.010 \text{ mV}^{-1}$  Range: 0.008 to 0.012  
 parameter controlling sensitivity of  $k_1$  to  $\Delta p$   
 $c_{k2} = 0.020 \text{ mV}^{-1}$  Range: 0.016 to 0.024  
 parameter controlling sensitivity of  $k_2$  to  $\Delta p$   
 $\text{CMR}_{\text{gluc},n} = 0.00440 \text{ mM s}^{-1}$  Range: 0.00352 to 0.00528  
 normal rate of glucose metabolism for the brain [296]  
 $\text{CMRO}_{2,n} = 0.020 \text{ mM s}^{-1}$  Range: 0.016 to 0.024  
 The resting  $\text{CMRO}_2$   
 $C_v = 0.0470 \text{ mmHg}^{-1}$  Range: 0.0376 to 0.0564  
 compliance of the veins (normalised)  
 $CV_{inh} = 1.0$  (dimensionless) Range: 0.8 to 1.2  
 a control parameter representing the action of Complex V inhibitors  
 $[\text{CCO}]_{\text{tis}} = 0.0022 \text{ mM}$  Range: 0.0010 to 0.0070  
 concentration of cytochrome c oxidase in tissue  
 $d = 0$  (dimensionless) Not included in sensitivity analysis  
 a parameter controlling the fraction of cells considered as dead  
 $\Delta\text{Hbdiff}_{\text{offset}} = 0 \text{ }\mu\text{M}$  Not included in sensitivity analysis  
 an arbitrary baseline offset to the  $\Delta\text{Hbdiff}$  signal (NIRS)  
 $\Delta\text{HbO}_{2,\text{offset}} = 0 \text{ }\mu\text{M}$  Not included in sensitivity analysis  
 an arbitrary baseline offset to the  $\Delta\text{HbO}_2$  signal (NIRS)  
 $\Delta\text{HbT}_{\text{offset}} = 0 \text{ }\mu\text{M}$  Not included in sensitivity analysis  
 an arbitrary baseline offset to the  $\Delta\text{Hbt}$  signal (NIRS)  
 $\Delta\text{HHb}_{\text{offset}} = 0 \text{ }\mu\text{M}$  Not included in sensitivity analysis  
 an arbitrary baseline offset to the  $\Delta\text{HHb}$  signal (NIRS)  
 $\Delta p_{3,\text{corr}} = -25 \text{ mV}$  Range: -28 to -20  
 $\Delta p_{30}$  minus normal  $\Delta p$   
 $\text{dpH} = 0.0010$  (dimensionless) Range: 0.0008 to 0.0012  
 a constant in the buffering relationship  
 $\Delta\Psi_n = 145 \text{ mV}$  Range: 125 to 150  
 normal mitochondrial inner membrane potential  
 $\mathcal{E}_0(\text{cyt } a_3) = 350 \text{ mV}$  Range: 280 to 420  
 cytochrome  $a_3$  standard redox potential  
 $\mathcal{E}_0(\text{Cu}_A) = 247.0 \text{ mV}$  Range: 197.6 to 250.0  
 $\text{Cu}_A$  standard redox potential  
 $\mathcal{E}_0(\text{NADH}) = -320 \text{ mV}$  Range: -384 to -256  
 NADH standard redox potential  
 $F = 96.48 \text{ C mmol}^{-1}$  Not included in sensitivity analysis  
 Faraday constant  
 $G_{0,\text{frac}} = 5$  (dimensionless) Range: 4 to 6  
 ratio between the conductance of the cerebral arteries and the supplying  
 artery compartment  
 $[\text{gluc}_c] = 5.30 \text{ mM}$  Range: 4.24 to 6.36

concentration of glucose in the blood [237]  
 $[\text{gluc}]_n = 1.20 \text{ mM}$  Range: 0.96 to 1.44  
 normal cellular concentration of glucose [143]  
 $\Delta G^\circ = -3.05e + 04 \text{ J mol}^{-1}$  Range: -3.07e+04 to -3.03e+04  
 standard Gibbs free energy of ATP hydrolysis  
 $G_{\text{VArat},n} = 4.0$  (dimensionless) Range: 3.2 to 4.8  
 normal ratio of conductances between arteries and veins  $G_v/G_n$  (determines venous pressure) [142]  
 $h_0 = 0.0030 \text{ cm}$  Range: 0.0024 to 0.0036  
 vascular wall thickness when radius is  $r_0$   
 $k_{\text{H},\text{O}_2} = 0.0014 \text{ mM mmHg}^{-1}$  Not included in sensitivity analysis  
 constant setting relationship between oxygen saturation and oxygen concentration in artery  
 $I = 3$  (dimensionless) Range: 0 to 20  
 the parameter which describes how strongly the AMP/ATP ratio inhibits the conversion of glucose to pyruvate  
 $k_{3,0} = 2.5e + 05 \text{ mM}^{-1} \text{ s}^{-1}$  Range: 2.0e+05 to 3.0e+05  
 an apparent second-order rate constant for reaction box at zero  $\Delta p$   
 $k_{\text{AK}} = 1055 \text{ mM}^{-1} \text{ s}^{-1}$  Range: 844 to 1266  
 the forward rate constant for the conversion of two molecules of ADP to one of ATP and one of AMP [144, 180].  
 $k_{\text{aut}} = 1$  (dimensionless) Range: 0 to 1  
 control parameter allowing destruction of autoregulation  
 $\text{Keq}_{\text{MAshut}} = 10$  (dimensionless) Range: 8 to 12  
 equilibrium constant for the malate-aspartate shuttle  
 $k_{\text{glut}} = 6.20 \text{ mM}$  Range: 4.96 to 7.44  
 $k_m$  for the transport of glucose in and out of the cell [241]  
 $k_{\text{MCT},\text{H}^+} = 0.0000 \text{ mM}$  Range: 0.0000 to 0.0002  
 $k_m$  for the transport of a proton coupled with lactate in and out of the cell  
 $k_{\text{MCT}} = 2.0 \text{ mM}$  Range: 1.6 to 2.4  
 $k_m$  for the transport of lactate in and out of the cell  
 $k_{\text{lk}2} = 0.0380 \text{ mV}^{-1}$  Range: 0.0304 to 0.0456  
 second constant controlling rate of  $L_{\text{lk}}$  of  $\Delta p$   
 $k_{m,\text{ATP}} = 0.025$  (dimensionless) Range: 0.020 to 0.030  
 $k_m$  for ATP use as a fraction of normal ATP concentration [144]  
 $k_{m,\text{glycA},f} = 0.20$  (dimensionless) Range: 0.16 to 0.24  
 $k_m$  for ADP in glycolysis as a fraction of normal ADP concentration [180]  
 $k_{m,\text{glycG}} = 0.05 \text{ mM}$  Range: 0.04 to 0.06  
 $k_m$  for glucose in the caricature of glycolysis [13]  
 $k_{m,\text{glycN}} = 0.00 \text{ mM}$  Range: 0.18 to 1.00  
 $k_m$  for NAD in the caricature of glycolysis  
 $k_{m,\text{glycP},f} = 0.20$  (dimensionless) Range: 0.16 to 0.24

$k_m$  for inorganic phosphate in glycolysis as a fraction of normal phosphate concentration [180]

$k_{m,tcaN,f} = 0.6$  (dimensionless) Range: 0.0 to 10.0  
 $k_m$  for NAD in the TCA cycle as a fraction of normal NAD concentration

$k_{m,tcaP,f} = 0.005$  (dimensionless) Range: 0.000 to 10.000  
 $k_m$  for pyruvate in the TCA cycle as a fraction of normal pyruvate concentration

$k_{AK}^- = 379.0 \text{ mM}^{-1} \text{ s}^{-1}$  Range: 303.2 to 454.8  
 the backward rate constant for the conversion of two molecules of ADP to one of ATP and one of AMP [144, 180].

$K_{eq,PCr}^* = 166.0$  (dimensionless) Range: 132.8 to 199.2  
 effective equilibrium constant for the reaction in which phosphocreatine combines with ADP to give creatine and ATP [297]

$t_{1/2,PCr} = 2.0e - 05 \text{ s}$  Range: 1.6e-05 to 2.4e-05  
 halftime for the reaction in which phosphocreatine combines with ADP to give creatine and ATP

$t_{1/2,pl} = 10 \text{ mM}^{-1} \text{ s}^{-1}$  Range: 8 to 12  
 time constant for pyruvate to lactate interconversion

$K_\sigma = 10$  (dimensionless) Range: 8 to 12  
 parameter controlling sensitivity of  $\sigma_e$  to radius

$k_{unc} = 1.0$  (dimensionless) Range: 0.8 to 1.2  
 a parameter representing the action of uncouplers

$[\text{lac}]_n = 3.0 \text{ mM}$  Range: 0.1 to 5.0  
 normal concentration of lactate in the cytoplasm [298]

$[\text{lac}]_c = 1.0 \text{ mM}$  Range: 0.8 to 1.2  
 capillary lactate concentration [237]

$L_{CV,0} = 0.40$  (dimensionless) Range: 0.32 to 0.48  
 normal Complex V flux as a fraction of maximum possible flux

$L_{lk,frac} = 0.25$  (dimensionless) Range: 0.20 to 0.30  
 normal fraction of proton entry into mitochondria which is via leak channels

$\mu_{max} = 1$  (dimensionless) Not included in sensitivity analysis  
 maximum value of  $\mu$

$\mu_{min} = -1$  (dimensionless) Not included in sensitivity analysis  
 minimum value of  $\mu$

$\mu_n = 0$  (dimensionless) Not included in sensitivity analysis  
 normal value of  $\mu$

$n_a = 4.33$  (dimensionless) Range: 3.80 to 5.00  
 number of protons passing through Complex V for each ATP synthesised [299]

$[\text{NAD}_{cyt}]_n = 359 \text{ mM}$  Range: 318 to 400  
 normal concentration of NAD in the cytoplasm

$[\text{NADH}_{cyt}]_n = 50 \text{ mM}$  Range: 32 to 68

normal concentration of NADH in the cytoplasm  
 $\Delta_{\text{nadir}} = 0$  (dimensionless) Not included in sensitivity analysis  
 a switch parameter introduced to allow parameter changes at the nadir  
 of hypoxia-ischaemia  
 $[\text{NAD}]_n/[\text{NADH}]_n = 9.0$  (dimensionless) Range: 0.1 to 20.0  
 normal NAD/NADH ratio  
 $N_t = 3.0$  mM Range: 2.4 to 3.6  
 total mitochondrial NAD and NADH concentration  
 $n_h = 2.5$  (dimensionless) Range: 2.0 to 3.0  
 Hill coefficient for haemoglobin saturation  
 $n_m = 1.830$  (dimensionless) Range: 1.464 to 2.196  
 exponent in the muscular tension relationship  
 $[\text{O}_2]_n = 0.0240$  mM Range: 0.0192 to 0.0288  
 normal oxygen concentration in mitochondria  
 $P_a = 50$  mmHg Range: 30 to 80  
 arterial blood pressure  
 $P_a\text{CO}_2 = 40$  mmHg Range: 20 to 60  
 arterial partial pressure of  $\text{CO}_2$   
 $P_a\text{CO}_{2,n} = 40$  mmHg Range: 32 to 48  
 normal arterial partial pressure of  $\text{CO}_2$   
 $P_{a,n} = 50$  mmHg Range: 45 to 60  
 normal value of ABP  
 $[\text{PCr}]_n = 2.6$  mM Range: 0.1 to 10.0  
 normal concentration of phosphocreatine in cell cytoplasm [295]  
 $[\text{PCr}]_n/[\text{P}_i]_n = 2.73$  (dimensionless) Range: 0.10 to 10.00  
 normal PCr/ $\text{P}_i$  concentration in the cytoplasm  
 $\phi = 0.0360$  mM Range: 0.0288 to 0.0432  
 value of  $\text{O}_2$  concentration at half maximal saturation  
 $\text{pH}_{m,n} = 7.4$  (dimensionless) Range: 7.2 to 7.6  
 normal mitochondrial pH  
 $\text{pH}_{o,n} = 7.0$  (dimensionless) Range: 6.8 to 7.2  
 normal extra-mitochondrial pH  
 $P_{ic} = 4.5$  mmHg Range: 3.6 to 5.4  
 intracranial blood pressure  
 $P_{ic,n} = 4.5$  mmHg Range: 3.6 to 5.4  
 normal intracranial blood pressure  
 $p_{\text{tot}} = 18.4$  (dimensionless) Range: 18.0 to 20.0  
 total protons pumped by reactions ared, aox and box  
 $P_{vs} = 1.5$  mmHg Range: 1.2 to 1.8  
 pressure in the venous sinuses [300]  
 $[\text{Py}]_n = 0.10$  mM Range: 0.08 to 0.12  
 normal concentration of pyruvate ions in the cytoplasm [301]  
 $r_0 = 0.01260$  cm Range: 0.01008 to 0.01512  
 a special radius in the elastic tension relationship

$R_C = 2.2$  (dimensionless) Range: 0.0 to 10.0  
 parameter controlling sensitivity of  $\eta$  to  $P_a\text{CO}_2$

$R_O = 1.5$  (dimensionless) Range: 0.0 to 10.0  
 parameter controlling sensitivity of  $\eta$  to  $[\text{O}_{2,c}]$

$R_P = 4$  (dimensionless) Range: 0 to 10  
 parameter controlling sensitivity of  $\eta$  to  $P_a$

$R_u = 0$  (dimensionless) Not included in sensitivity analysis  
 parameter controlling sensitivity of  $\eta$  to  $u$

$r_{CV} = 5$  (dimensionless) Range: 4 to 6  
 a parameter controlling the ratio of maximal to minimal rates of oxidative phosphorylation

$r_m = 0.0270$  cm Range: 0.0216 to 0.0324  
 value of vessel radius giving maximum muscular tension

$r_n = 0.01870$  cm Range: 0.01496 to 0.02244  
 normal radius of blood vessels

$r_{occ} = 0$  (dimensionless) Range: 0 to 1  
 fraction by which the radius of the carotid arteries has been reduced

$r_t = 0.0180$  cm Range: 0.0144 to 0.0216  
 parameter in the muscular tension relationship

$\text{SaO}_{2,n} = 0.96$  (dimensionless) Range: 0.90 to 1.00  
 normal saturation of the arterial haemoglobin

$\text{SaO}_2 = 0.96$  (dimensionless) Range: 0.50 to 1.00  
 saturation of the arterial haemoglobin

$\sigma_{\text{coll}} = 62.79$  mmHg Range: 50.23 to 75.35  
 value of pressure at which vessels collapse

$\sigma_{e0} = 0.1425$  mmHg Range: 0.1140 to 0.1710  
 parameter in relationship determining  $\sigma_e$

$\tau_{\text{CO}_2} = 5$  s Range: 4 to 6  
 the time constant associated with  $v_{\text{CO}_2}$

$\tau_{\text{O}_2} = 20$  s Range: 16 to 24  
 the time constant associated with  $v_{\text{O}_2}$

$\tau_{P_a} = 5$  s Range: 4 to 6  
 the time constant associated with  $v_{P_a}$

$\tau_u = 0.5$  s Range: 0.4 to 0.6  
 the time constant associated with  $v_u$

$u_n = 1$  (dimensionless) Not included in sensitivity analysis  
 resting “demand”

$\text{VArat}_n = 3.0$  (dimensionless) Range: 2.4 to 3.6  
 the normal ratio of the volume of the veins to the volume of the arteries

$V_{\text{mit}} = 0.0670$  (dimensionless) Range: 0.0536 to 0.0804  
 fraction of brain water which is mitochondria

$V_{t,n} = 1.0$  (dimensionless) Range: 0.8 to 1.2  
 normal total blood volume

$[\text{Hbtot}]_n = 5.4$  mM Range: 3.5 to 8.0

normal total concentration of haemoglobin O<sub>2</sub> binding sites in the arteries and veins (four times haemoglobin concentration)

$Z = 59.03 \text{ mV}$  Not included in sensitivity analysis

$2.303 \times RT/F$  where  $R$  is the ideal gas constant ( $8300 \text{ mJ K}^{-1} \text{ mol}^{-1}$ ),  $T$  is the temperature ( $298 \text{ K}$ ),  $F$  is the Faraday constant ( $9.65 \times 10^4 \text{ C mol}^{-1}$ ) and  $2.303$  arises from  $1/\log_{10} e$ .

## D.7 Derived Parameters

$$\text{Cu}_{A,o,\text{init}} = \text{Cu}_{A,o,n} = 0.022 \text{ mM} \quad (\text{D.146})$$

initial oxidized Cu<sub>A</sub>

$$[\text{AMP}]_n = \frac{K_{\text{eq,ADPATP}}[\text{ADP}]_n^2}{[\text{ATP}]_n} = 0.000334 \text{ mM} \quad (\text{D.147})$$

normal AMP concentration in cytoplasm

$$\text{Cu}_{A,o,n} = [\text{CCO}]_{\text{mit}} \text{Cu}_{A,\text{frac},n} = 0.022 \text{ mM} \quad (\text{D.148})$$

normal oxidized Cu<sub>A</sub>

$$\text{Cu}_{A,r,n} = [\text{CCO}]_{\text{mit}} - \text{Cu}_{A,o,n} = 0.01084 \text{ mM} \quad (\text{D.149})$$

the resting amount of reduced cytochrome-c-oxidase

$$a_{3,\text{frac},n} = 1 - \frac{\text{cyt } a_{3,r,n}}{[\text{CCO}]_{\text{mit}}} = 0.9748 \text{ (dimensionless)} \quad (\text{D.150})$$

normal oxidised fraction of cytochrome a<sub>3</sub>

$$\text{cyt } a_{3,o,n} = [\text{CCO}]_{\text{mit}} - \text{cyt } a_{3,r,n} = 0.03201 \text{ mM} \quad (\text{D.151})$$

normal oxidised cytochrome a<sub>3</sub>

$$\text{cyt } a_{3,r,\text{init}} = \text{cyt } a_{3,r,n} = 0.000828 \text{ mM} \quad (\text{D.152})$$

initial reduced cytochrome a<sub>3</sub>

$$\text{cyt } a_{3,r,n} = \frac{f_n \left( 1 + \exp(-c_3(\Delta p_n - \Delta p_{30})) \right)}{k_3[\text{O}_2]_n \exp(-c_3(\Delta p_n - \Delta p_{30}))} = 0.000828 \text{ mM} \quad (\text{D.153})$$

normal reduced cytochrome a<sub>3</sub>

$$C_{\text{NADH},n} = \frac{Z}{2} \log \left( \frac{1}{[\text{NAD}]_n / [\text{NADH}]_n} \right) = -28.16 \text{ mV} \quad (\text{D.154})$$

normal value of  $C_{\text{NADH}}$

$$[\text{Cr}]_n = \frac{K_{\text{eq,PCr}}^* [\text{ADP}]_n [\text{PCr}]_n}{[\text{ATP}]_n} = 4.316 \text{ mM} \quad (\text{D.155})$$

normal concentration of creatine in cytoplasm

$$[\text{CCO}]_{\text{mit}} = \frac{[\text{CCO}]_{\text{tis}}}{V_{\text{mit}}} = 0.03284 \text{ mM} \quad (\text{D.156})$$

concentration of cytochrome c oxidase in mitochondria

$$d_f = d\Delta_{\text{nadir}} = 0 \text{ (dimensionless)} \quad (\text{D.157})$$

the fraction of cells which are considered as dead

$$\Delta G_{1,n} = -4 \left( E_{1,n} + Z \log \left( \frac{\text{Cu}_{\text{A},\text{o},n}}{\text{Cu}_{\text{A},\text{r},n}} \right) \right) + p_1 \Delta p_n = -474.4 \text{ mV} \quad (\text{D.158})$$

normal free energy associated with reaction ared

$$\Delta G_{2,n} = -4 \left( E_2 + Z \left( \log \left( \frac{\text{Cu}_{\text{A},\text{r},n}}{\text{Cu}_{\text{A},\text{o},n}} \right) - \log \left( \frac{\text{cyt } a_{3,\text{r},n}}{\text{cyt } a_{3,\text{o},n}} \right) \right) \right) + p_2 \Delta p_n = -39.7 \text{ mV} \quad (\text{D.159})$$

normal free energy associated with reaction aox

$$\Delta G_n = \Delta G^\circ + ZF \log(g_{p,n}) = -5.91e + 04 \text{ J mol}^{-1} \quad (\text{D.160})$$

normal Gibbs free energy of ATP hydrolysis

$$D_{\text{O}_2} = \frac{J_{\text{O}_2,n}}{[\text{O}_{2,\text{c}}]_n - [\text{O}_2]_n} = 0.6796 \text{ s}^{-1} \quad (\text{D.161})$$

diffusion rate between capillaries and mitochondria

$$\Delta p_{30} = \Delta p_n + \Delta p_{3,\text{corr}} = 143.6 \text{ mV} \quad (\text{D.162})$$

value of PMF at which reaction box is maximally sensitive to  $\Delta p$

$$\Delta p_{\text{CV0}} = \frac{-\Delta G_n}{n_a F} = 141.5 \text{ mV} \quad (\text{D.163})$$

a constant in the rate of Complex V

$$\Delta \text{pH}_n = \text{pH}_{\text{m},n} - \text{pH}_{\text{o},n} = 0.4 \text{ (dimensionless)} \quad (\text{D.164})$$

the resting value of pH difference across mitochondrial inner membrane

$$\Delta p_n = \Delta \Psi_n + Z \Delta \text{pH}_n = 168.6 \text{ mV} \quad (\text{D.165})$$

the resting value of the proton motive force

$$\Delta \Psi_{\text{init}} = \Delta \Psi_n = 145 \text{ mV} \quad (\text{D.166})$$

initial value of mitochondrial inner membrane potential

$$E_{1,n} = E_{1,\text{NADH},n} = 538.8 \text{ mV} \quad (\text{D.167})$$

the normal value of  $E_1$

$$E_{1,\text{NADH},n} = \mathcal{E}_0(\text{Cu}_A) - \mathcal{E}_0(\text{NADH}) + C_{\text{NADH},n} = 538.8 \text{ mV} \quad (\text{D.168})$$

normal value of  $E_{1,\text{NADH}}$

$$E_2 = \mathcal{E}_0(\text{cyt } a_3) - \mathcal{E}_0(\text{Cu}_A) = 103 \text{ mV} \quad (\text{D.169})$$

the energy provided by transfer of four electrons from  $\text{Cu}_{\text{A},\text{r}}$  to  $\text{cyt } a_{3,\text{o}}$

$$\text{EPP} = 2[\text{ATP}]_n + [\text{ADP}]_n + [\text{PCr}]_n + [\text{P}]_n = 5.964 \text{ mM} \quad (\text{D.170})$$

the total exchangeable phosphate pool

$$f_n = \frac{\text{CMRO}_{2,n}}{V_{\text{mit}}} = 0.2985 \text{ mM s}^{-1} \quad (\text{D.171})$$

normal resting rate of  $f_1$  and  $f_2$

$$G_0 = G_{0,n} r_0^4 = 0.001196 \text{ ml}_{\text{blood}} \text{ ml}_{\text{brain}}^{-1} \text{ mmHg}^{-1} \text{ s}^{-1} \quad (\text{D.172})$$

conductance of the supplying artery compartment

$$G_{0,n} = G_{0,\text{frac}} G_n = 0.001196 \text{ ml}_{\text{blood}} \text{ ml}_{\text{brain}}^{-1} \text{ mmHg}^{-1} \text{ s}^{-1} \quad (\text{D.173})$$

normal conductance of the supplying artery compartment

$$\text{glyc}_{\text{a,n}} = \frac{[\text{ADP}]_n^2}{k_{m,\text{glycA}}^2 + [\text{ADP}]_n^2} = 0.9615 \text{ (dimensionless)} \quad (\text{D.174})$$

term in the expression for normal glycolysis rate

$$\text{glyc}_{\text{g,n}} = \frac{[\text{gluc}]_n}{k_{m,\text{glycG}} + [\text{gluc}]_n} = 0.96 \text{ (dimensionless)} \quad (\text{D.175})$$

term in the expression for normal glycolysis rate

$$\text{glyc}_{\text{p,n}} = \frac{[\text{P}]_n^2}{k_{m,\text{glycP}}^2 + [\text{P}]_n^2} = 0.9615 \text{ (dimensionless)} \quad (\text{D.176})$$

term in the expression for normal glycolysis rate

$$G_n = \frac{\text{CBF}_n}{P_{\text{a,n}} - P_{\text{vs}}} \left( 1 + \frac{1}{G_{0,\text{frac}}} + \frac{1}{G_{\text{VArat,n}}} \right) = 0.0002392 \text{ ml}_{\text{blood}} \text{ ml}_{\text{brain}}^{-1} \text{ mmHg}^{-1} \text{ s}^{-1} \quad (\text{D.177})$$

normal resistance of cerebral circulation

$$g_{\text{p,n}} = \frac{[\text{ADP}]_n [\text{P}]_n}{1000 [\text{ATP}]_n} = 9.524e - 06 \text{ (dimensionless)} \quad (\text{D.178})$$

normal phosphorylation potential

$$G_{\text{t,n}} = \frac{G_n G_{0,n} G_v}{G_n G_{0,n} + G_n G_v + G_v G_{0,n}} = 0.0001649 \text{ ml}_{\text{blood}} \text{ ml}_{\text{brain}}^{-1} \text{ mmHg}^{-1} \text{ s}^{-1} \quad (\text{D.179})$$

normal value of the total conductance of all blood vessel compartments

$$G_v = G_{\text{VArat,n}} G_n = 0.0009567 \text{ ml}_{\text{blood}} \text{ ml}_{\text{brain}}^{-1} \text{ mmHg}^{-1} \text{ s}^{-1} \quad (\text{D.180})$$

conductance of the veins

$$\text{HbO}_{2,\text{n}} = 1000 \frac{V_{\text{a,n}} [\text{HbO}_{2,\text{a}}]_n + V_{\text{v,n}} [\text{HbO}_{2,\text{v}}]_n}{4} V_{\text{blood,n}} = 26.89 \mu\text{M} \quad (\text{D.181})$$

normal total oxygenated haemoglobin (NIRS)

$$\text{Hbt}_n = 1000 \frac{(V_{\text{a,n}} + V_{\text{v,n}}) [\text{Hbtot}]_n}{4} V_{\text{blood,n}} = 43.88 \mu\text{M} \quad (\text{D.182})$$

normal total haemoglobin (NIRS)

$$\text{HHb}_n = 1000 \frac{V_{\text{a,n}} [\text{HHb}_\text{a}]_n + V_{\text{v,n}} [\text{HHb}_\text{v}]_n}{4} V_{\text{blood,n}} = 16.99 \mu\text{M} \quad (\text{D.183})$$

normal total deoxygenated haemoglobin (NIRS)

$$\text{H}_{\text{m,init}}^+ = \text{H}_{\text{m,n}}^+ = 3.981e - 05 \text{ mM} \quad (\text{D.184})$$

initial hydrogen ion concentration in mitochondria

$$H_{m,n}^+ = 10^{3-pH_{m,n}} = 3.981e - 05 \text{ mM} \quad (\text{D.185})$$

normal hydrogen ion concentration in mitochondria

$$h_n = -r_n + \sqrt{r_n^2 + 2r_0h_0 + h_0h_0} = 0.00214 \text{ cm} \quad (\text{D.186})$$

normal wall thickness of cerebral vessels

$$[H^+]_n = 1000 \times 10^{-pH_{o,n}} = 0.0001 \text{ mM} \quad (\text{D.187})$$

normal hydrogen ion concentration in the cytoplasm

$$J_{O_2,n} = CMRO_{2,n} = 0.02 \text{ mM s}^{-1} \quad (\text{D.188})$$

the resting rate of supply of oxygen to the mitochondria

$$k_{1,n} = \frac{f_n}{Cu_{A,o,n} - \frac{1}{Keq_{1,n}}Cu_{A,r,n}} = 13.7 \text{ s}^{-1} \quad (\text{D.189})$$

the value of  $k_1$  at normal  $\Delta p$  and [NADH]

$$k_{2,n} = \frac{f_n}{Cu_{A,r,n}cyt a_{3,o,n} - \frac{1}{Keq_{2,n}}Cu_{A,o,n}cyt a_{3,r,n}} = 2681 \text{ mM}^{-1} \text{ s}^{-1} \quad (\text{D.190})$$

normal forward rate constant for reaction aox

$$k_3 = \frac{k_{3,0} \left( 1 + \exp(-c_3(0 - \Delta p_{30})) \right)}{\exp(-c_3(0 - \Delta p_{30}))} = 2.5e + 05 \text{ mM}^{-1} \text{ s}^{-1} \quad (\text{D.191})$$

rate constant for reaction box

$$Keq_{ADPATP} = \frac{k_{AK}}{k_{AK}^-} = 2.784 \text{ (dimensionless)} \quad (\text{D.192})$$

equilibrium constant for the conversion of ADP to ATP and AMP

$$k_{CV} = \frac{-1}{\Delta p_n - \Delta p_{CV0}} \ln \left( \frac{1 - L_{CV,0}}{1 + r_{CV}L_{CV,0}} \right) = 0.05927 \text{ mV}^{-1} \quad (\text{D.193})$$

a parameter controlling the sensitivity of Complex V flux to driving force

$$Keq_{1,n} = 10^{(-1/Z)(p_1 \Delta p_n / 4 - E_{1,n})} = 50.31 \text{ (dimensionless)} \quad (\text{D.194})$$

normal equilibrium constant for reaction ared

$$Keq_{2,n} = 10^{(-1/Z)(p_2 \Delta p_n / 4 - E_2)} = 0.07735 \text{ (dimensionless)} \quad (\text{D.195})$$

normal equilibrium constant for reaction aox

$$K_G = \frac{G_n}{r_n^4} = 1956 \text{ ml}_{\text{blood}} \text{ ml}_{\text{brain}}^{-1} \text{ mmHg}^{-1} \text{ s}^{-1} \text{ cm}^{-4} \quad (\text{D.196})$$

constant of proportionality relating pressure drop to flow

$$k_m = [ATP]_n k_{m,ATP} = 0.03 \text{ mM} \quad (\text{D.197})$$

$k_m$  for ATP use

$$k_{m,\text{glycA}} = k_{m,\text{glycA},f} [ADP]_n = 0.0024 \text{ mM} \quad (\text{D.198})$$

$k_m$  for ADP in the caricature of glycolysis

$$k_{m,\text{glycP}} = k_{m,\text{glycP},f}[\text{P}]_n = 0.1905 \text{ mM} \quad (\text{D.199})$$

$k_m$  for inorganic phosphate in the caricature of glycolysis

$$k_{m,\text{tcaN}} = k_{m,\text{tcaN},f}[\text{NAD}]_n = 1.62 \text{ mM} \quad (\text{D.200})$$

$k_m$  for NAD in the TCA cycle

$$k_{m,\text{tcaP}} = k_{m,\text{tcaP},f}[\text{Py}]_n = 0.0005 \text{ mM} \quad (\text{D.201})$$

$k_m$  for pyruvate in the TCA cycle

$$k_{\text{PCr}}^- = \frac{\ln(2)}{\left( K_{\text{eq,PCr}}[\text{PCr}]_n[\text{ADP}]_n + [\text{Cr}]_n + [\text{ATP}]_n \right) t_{1/2,\text{PCr}}} = 0.6691 \text{ mM}^{-1} \text{ s}^{-1} \quad (\text{D.202})$$

the backward rate of reaction for the reaction in which phosphocreatine combines with ADP to give creatine and ATP

$$k_{\text{pl}}^- = t_{1/2,\text{pl}} = 10 \text{ mM}^{-1} \text{ s}^{-1} \quad (\text{D.203})$$

rate of backwards reaction in the pyruvate lactate equilibrium

$$k_{\text{PCr}} = \frac{\ln(2)}{\left( [\text{PCr}]_n[\text{ADP}]_n + \frac{[\text{Cr}]_n + [\text{ATP}]_n}{K_{\text{eq,PCr}}} \right) t_{1/2,\text{PCr}}} = 1.111e + 06 \text{ mM}^{-2} \text{ s}^{-1} \quad (\text{D.204})$$

the forward rate of reaction for the reaction in which phosphocreatine combines with ADP to give creatine and ATP

$$K_{\text{eq,PCr}} = \frac{K_{\text{eq,PCr}}^*}{[\text{H}^+]_n} = 1.66e + 06 \text{ mM}^{-1} \quad (\text{D.205})$$

equilibrium of the reaction in which phosphocreatine combines with ADP to give creatine and ATP

$$k_{\text{TCA}_n} = \frac{1}{3} \frac{\text{CMRO}_{2,n}}{V_{\text{mit}}} = 0.0995 \text{ mM s}^{-1} \quad (\text{D.206})$$

normal rate of the TCA cycle

$$L_{\text{CV,frac}} = 1 - L_{\text{lk,frac}} = 0.75 \text{ (dimensionless)} \quad (\text{D.207})$$

normal fraction of proton entry into mitochondria associated with ADP phosphorylation

$$L_{\text{CV,max}} = \frac{L_{\text{CV,n}}}{L_{\text{CV,0}}} = 10.3 \text{ mM s}^{-1} \quad (\text{D.208})$$

the maximum rate of proton flow through Complex V

$$L_{\text{CV,n}} = L_n L_{\text{CV,frac}} = 4.119 \text{ mM s}^{-1} \quad (\text{D.209})$$

the resting flow of protons into the matrix through Complex V

$$L_{\text{lk0}} = \frac{L_{\text{lk,n}}}{\exp(\Delta p_n k_{\text{lk2}}) - 1} = 0.002269 \text{ mM s}^{-1} \quad (\text{D.210})$$

first constant controlling rate of  $L_{\text{lk}}$  of  $\Delta p$

$$L_{\text{lk,n}} = L_n L_{\text{lk,frac}} = 1.373 \text{ mM s}^{-1} \quad (\text{D.211})$$

the resting flow of protons into the matrix via leak channels

$$L_n = p_{tot}f_n = 5.492 \text{ mM s}^{-1} \quad (\text{D.212})$$

the total flow of protons back into mitochondria

$$\text{NADH}_n = N_t - [\text{NAD}]_n = 0.3 \text{ mM} \quad (\text{D.213})$$

normal concentration of NADH in the mitochondria

$$[\text{NAD}]_n = \frac{N_t}{1 + \frac{[\text{NAD}]_n/[\text{NADH}]_n}{1}} = 2.7 \text{ mM} \quad (\text{D.214})$$

normal concentration of NAD in the mitochondria

$$[\text{O}_{2,a}] = \phi \left( \frac{\text{SaO}_2}{1 - \text{SaO}_2} \right)^{1/n_h} = 0.1283 \text{ mM} \quad (\text{D.215})$$

arterial dissolved oxygen concentration

$$[\text{O}_{2,c}]_{\text{init}} = [\text{O}_{2,c}]_n = 0.05343 \text{ mM} \quad (\text{D.216})$$

initial concentration of dissolved oxygen in the capillary

$$[\text{O}_{2,c}]_n = \phi \left( \frac{\text{ScO}_{2,n}}{1 - \text{ScO}_{2,n}} \right)^{1/n_h} = 0.05343 \text{ mM} \quad (\text{D.217})$$

normal concentration of dissolved oxygen in the capillary

$$[\text{O}_2]_{\text{init}} = [\text{O}_2]_n = 0.024 \text{ mM} \quad (\text{D.218})$$

initial oxygen concentration in mitochondria

$$p_1 = p_{tot} - p_{23} = 10.4 \text{ (dimensionless)} \quad (\text{D.219})$$

the number of protons pumped by reaction aed

$$P_{1,n} = \frac{P_{a2,n} + P_{v,n}}{2} = 26.59 \text{ mmHg} \quad (\text{D.220})$$

normal average blood pressure in vessels

$$p_2 = 4 \times 1 = 4 \text{ (dimensionless)} \quad (\text{D.221})$$

total protons pumped by reaction aox

$$p_{23} = 4 \times 2 = 8 \text{ (dimensionless)} \quad (\text{D.222})$$

total protons pumped by reactions aox and box

$$p_3 = p_{23} - p_2 = 4 \text{ (dimensionless)} \quad (\text{D.223})$$

total protons pumped by reaction box

$$P_{a2,n} = \frac{G_{0,n}P_{a,n} + G_nP_{v,n}}{G_n + G_{0,n}} = 43.31 \text{ mmHg} \quad (\text{D.224})$$

normal arterial blood pressure at the start of the cerebral arteries

$$\text{PaO}_2 = \frac{[\text{O}_{2,a}]}{k_{\text{H},\text{O}_2}} = 91.68 \text{ mmHg} \quad (\text{D.225})$$

partial pressure of oxygen in the arteries

$$[P]_n = \frac{[PCr]_n}{[PCr]_n/[P_i]_n} = 0.9524 \text{ mM} \quad (\text{D.226})$$

the normal concentration of inorganic phosphate in the cytoplasm

$$P_{v,n} = \frac{G_{t,n}}{G_v} (P_{a,n} - P_{vs}) + P_{vs} = 9.862 \text{ mmHg} \quad (\text{D.227})$$

normal venous blood pressure

$$r_0 = 1 - r_{\text{frac}} r_{\text{occ}} = 1 \text{ (dimensionless)} \quad (\text{D.228})$$

radius of the supplying artery compartment

$$r_{\text{frac}} = 1 - (1 - \text{occ}_{\text{frac}})^{1/4} = 0.3313 \text{ (dimensionless)} \quad (\text{D.229})$$

fraction by which the radius of the supplying artery compartment is reduced if the carotid arteries are fully occluded

$$\text{ScO}_{2,n} = \frac{\text{SaO}_{2,n} + \text{SvO}_{2,n}}{2} = 0.7285 \text{ (dimensionless)} \quad (\text{D.230})$$

normal capillary oxygen saturation

$$\sigma_{e,n} = \sigma_{e0} \left( \exp \left( \frac{K_\sigma (r_n - r_0)}{r_0} \right) - 1 \right) - \sigma_{\text{coll}} = -44.89 \text{ mmHg} \quad (\text{D.231})$$

normal elastic stress in vessel walls

$$\text{SvO}_{2,n} = \frac{[\text{HbO}_{2,v}]_n}{[\text{Hbtot}]_n} = 0.497 \text{ (dimensionless)} \quad (\text{D.232})$$

normal venous oxygen saturation

$$T_{e,n} = \sigma_{e,n} h_n = -0.09604 \text{ mmHg cm} \quad (\text{D.233})$$

normal elastic tension in vessel walls

$$T_{\text{max}0} = \frac{T_{\text{max},n}}{1 + k_{\text{aut}} \mu_n} = 1.206 \text{ mmHg cm} \quad (\text{D.234})$$

$T_{\text{max}}$  at normal  $\mu$

$$T_{\text{max},n} = \frac{T_{m,n}}{\exp \left( - \left( \frac{r_n - r_m}{r_t - r_m} \right)^{n_m} \right)} = 1.206 \text{ mmHg cm} \quad (\text{D.235})$$

normal maximum muscular tension developed by circulation

$$T_{m,n} = (P_{1,n} - P_{ic,n}) r_n - T_{e,n} = 0.5091 \text{ mmHg cm} \quad (\text{D.236})$$

normal muscular tension in vessel walls

$$u = u_n = 1 \text{ (dimensionless)} \quad (\text{D.237})$$

the representation of “demand” in the model

$$\nu_{\text{CO}_2,n} = P_a \text{CO}_{2,n} = 40 \text{ mmHg} \quad (\text{D.238})$$

normal value of  $\nu_{\text{CO}_2}$  ( $P_a \text{CO}_2$  passed through a first order filter)

$$V_{\text{glucosein}} = \frac{[\text{gluc}_c]}{k_{\text{glut}} + [\text{gluc}_c]} = 0.4609 \text{ (dimensionless)} \quad (\text{D.239})$$

rate term for glucose transported into the cell; this is a michaelis menten

term, but fixed because blood glucose concentration is fixed

$$v_{\text{glut}} = \frac{\text{CMR}_{\text{gluc},n}}{V_{\text{glucosein}} - \frac{[\text{gluc}]_n}{[\text{gluc}]_n + k_{\text{glut}}}} = 0.01473 \text{ mM s}^{-1} \quad (\text{D.240})$$

Vmax for glucose transport both in and out of the cell from the capillary

$$V_{\text{lacin}} = \frac{[\text{lac}_c][\text{H}^+]_n}{(k_{\text{MCT}} + [\text{lac}_c])([\text{H}^+]_n + k_{\text{MCT},\text{H}^+})} = 0.3333 \text{ (dimensionless)} \quad (\text{D.241})$$

rate of lactate transport into the cell

$$v_{\text{MCT}} = \begin{cases} v_{\text{MCT, val}} & \text{if } v_{\text{MCT, val}} > 0 \\ \text{NaN} & \text{otherwise} \end{cases} = 0.008 \text{ mM s}^{-1} \quad (\text{D.242})$$

rate constant for lactate transport

$$v_{\text{MCT, val}} = \frac{2\text{CMR}_{\text{gluc},n} - \frac{\text{CMRO}_{2,n}}{3}}{\frac{[\text{lac}]_n[\text{H}^+]_n}{([\text{lac}]_n + k_{\text{MCT}})([\text{H}^+]_n + k_{\text{MCT},\text{H}^+})} - V_{\text{lacin}}} = 0.008 \text{ mM s}^{-1} \quad (\text{D.243})$$

Calculated value for  $v_{\text{MCT}}$ . If this is not greater than zero, parameter set is invalid.

$$v_{\text{glyc},n} = \frac{\text{CMR}_{\text{gluc},n}}{\text{glyc}_{g,n}\text{glyc}_{p,n}\text{glyc}_{a,n}} = 0.004957 \text{ mM s}^{-1} \quad (\text{D.244})$$

normal Vmax for glycolysis which is assumed to be modified by the ratio of AMP to ATP

$$V_{a,n} = \frac{V_{t,n}}{1 + \text{VArat}_n} = 0.25 \text{ (dimensionless)} \quad (\text{D.245})$$

normal arterial blood volume as a fraction of total blood volume

$$V_{v,n} = V_{t,n} \frac{\text{VArat}_n}{1 + \text{VArat}_n} = 0.75 \text{ (dimensionless)} \quad (\text{D.246})$$

normal venous volume

$$v_{\text{O}_2,n} = [\text{O}_{2,c}]_n = 0.05343 \text{ mM} \quad (\text{D.247})$$

normal value of  $v_{\text{O}_2}$  ( $[\text{O}_{2,c}]$  passed through a first order filter)

$$v_{P_{a,n}} = P_{a2,n} = 43.31 \text{ mmHg} \quad (\text{D.248})$$

normal value of  $v_{P_a}$  ( $P_{a2}$  passed through a first order filter)

$$v_{\text{TCA}} = \frac{k_{\text{TCA},n}}{[\text{Py}]_n[\text{NAD}]_n} (k_{m,\text{tcaN}} + [\text{NAD}]_n) (k_{m,\text{tcaP}} + [\text{Py}]_n) = 0.16 \text{ mM s}^{-1} \quad (\text{D.249})$$

Vmax for the TCA cycle

$$v_{u,n} = u_n = 1 \text{ (dimensionless)} \quad (\text{D.250})$$

normal value of  $v_u$  ( $u$  passed through a first order filter)

$$[\text{HHb}_a] = [\text{Hbtot}] (1 - \text{SaO}_2) = 0.216 \text{ mM} \quad (\text{D.251})$$

concentration of haemoglobin  $\text{O}_2$  binding sites not occupied by  $\text{O}_2$  (four

times deoxyhaemoglobin concentration) in the arteries

$$[\text{HHb}_a]_n = [\text{Hbtot}]_n (1 - \text{SaO}_{2,n}) = 0.216 \text{ mM} \quad (\text{D.252})$$

normal concentration of haemoglobin O<sub>2</sub> binding sites not occupied by O<sub>2</sub> (four times deoxyhaemoglobin concentration) in the arteries

$$[\text{HbO}_{2,a}] = [\text{Hbtot}]\text{SaO}_2 = 5.184 \text{ mM} \quad (\text{D.253})$$

concentration of O<sub>2</sub> bound to arterial haemoglobin (four times oxyhaemoglobin concentration)

$$[\text{HbO}_{2,a}]_n = [\text{Hbtot}]_n \text{SaO}_{2,n} = 5.184 \text{ mM} \quad (\text{D.254})$$

normal concentration of O<sub>2</sub> bound to arterial haemoglobin (four times oxyhaemoglobin concentration)

$$[\text{HbO}_{2,v}]_{\text{init}} = [\text{HbO}_{2,v}]_n = 2.684 \text{ mM} \quad (\text{D.255})$$

initial concentration of O<sub>2</sub> bound to venous haemoglobin (four times oxyhaemoglobin concentration)

$$[\text{HbO}_{2,v}]_n = \frac{\text{CBF}_n [\text{HbO}_{2,a}]_n - J_{\text{O}_2,n}}{\text{CBF}_n} = 2.684 \text{ mM} \quad (\text{D.256})$$

normal concentration of O<sub>2</sub> bound to venous haemoglobin (four times oxyhaemoglobin concentration)

$$[\text{Hbtot}] = [\text{Hbtot}]_n = 5.4 \text{ mM} \quad (\text{D.257})$$

total concentration of haemoglobin O<sub>2</sub> binding sites in the arteries and veins (four times haemoglobin concentration)

$$[\text{HHb}_v]_n = [\text{Hbtot}]_n - [\text{HbO}_{2,v}]_n = 2.716 \text{ mM} \quad (\text{D.258})$$

normal concentration of haemoglobin O<sub>2</sub> binding sites not occupied by O<sub>2</sub> (four times deoxyhaemoglobin concentration) in the veins

# Bibliography

- [1] P. S. Shah, A. Ohlsson, and M. Perlman. Hypothermia to treat neonatal hypoxic ischemic encephalopathy: Systematic review. *Arch. Pediatr. Adolesc. Med.*, 161(10):951–958, 2007.
- [2] S. J. Vannucci and H. Hagberg. Hypoxia-ischemia in the immature brain. *J. Exp. Biol.*, 207(Pt 18):3149–54, 2004.
- [3] R. C. Vannucci. Experimental biology of cerebral hypoxia-ischemia: relation to perinatal brain damage. *Pediatr. Res.*, 27(4):317–326, 1990.
- [4] M. Thoresen, J. Penrice, A. Lorek, E. B. Cady, M. Wylezinska, V. Kirkbride, C. E. Cooper, G. C. Brown, A. D. Edwards, J. S. Wyatt, and Others. Mild hypothermia after severe transient hypoxia-ischemia ameliorates delayed cerebral energy failure in the newborn piglet. *Pediatr. Res.*, 37(5):667–670, 1995.
- [5] S. Roth, A. Edwards, E. Cady, D. Delpy, J. Wyatt, D. Azzopardi, J. Baudin, J. Townsend, A. Stewart, and E. Reynolds. Relation between cerebral oxidative metabolism following birth asphyxia and neurodevelopmental outcome and brain growth at one year. *Dev. Med. Child Neurol.*, 34(4):285–295, 1992.
- [6] A. D. Edwards, P. Brocklehurst, A. J. Gunn, H. Halliday, E. Juszczak, M. Levene, B. Strohm, M. Thoresen, A. Whitelaw, and D. Azzopardi. Neurological outcomes at 18 months of age after moderate hypothermia for perinatal hypoxic ischaemic encephalopathy: synthesis and meta-analysis of trial data. *BMJ*, 340(feb09 3):c363, 2010.
- [7] O. Iwata and S. Iwata. Filling the evidence gap: How can we improve the outcome of neonatal encephalopathy in the next 10 years? *Brain Dev.*, 33(3):221–228, 2011.
- [8] M. I. Levene. Cool treatment for birth asphyxia, but what’s next? *Arch. Dis.*

*Child.*, 95(3):F154–F157, 2010.

- [9] D. Azzopardi, J. S. Wyatt, E. B. Cady, D. T. Delpy, J. Baudin, A. L. Stewart, P. L. Hope, P. A. Hamilton, and E. O. R. Reynolds. Prognosis of newborn infants with hypoxic-ischemic brain injury assessed by phosphorus magnetic resonance spectroscopy. *Pediatr. Res.*, 25(5):445–451, 1989.
- [10] P. J. Doormaal, L. C. Meiners, H. J. Horst, C. N. Veere, and P. E. Sijens. The prognostic value of multivoxel magnetic resonance spectroscopy determined metabolite levels in white and grey matter brain tissue for adverse outcome in term newborns following perinatal asphyxia. *Eur. Radiol.*, 22(4):772–778, 2011.
- [11] G. Ancora, E. Maranella, S. Grandi, F. Sbravati, E. Coccolini, S. Savini, and G. Faldella. Early predictors of short term neurodevelopmental outcome in asphyxiated cooled infants. a combined brain amplitude integrated electroencephalography and near infrared spectroscopy study. *Brain Dev.*, 2011.
- [12] M. Banaji, A. Mallet, C. E. Elwell, P. Nicholls, and C. E. Cooper. A model of brain circulation and metabolism: Nirs signal changes during physiological challenges. *PLoS Comput. Biol.*, 4(11):e1000212, 2008.
- [13] L. Edvinsson, E. T. Mackenzie, and J. McCulloch. *Cerebral Blood Flow and Metabolism*. Raven Pr, 1992.
- [14] C. Blakemore and S. Jennett. *The Oxford companion to the body*. Oxford University Press, 2001.
- [15] A. F. Folino. Cerebral autoregulation and syncope. *Prog. Cardiovasc. Dis.*, 50(1):49–80, 2007.
- [16] J. Astrup. Thresholds in cerebral ischemia—the ischemic penumbra. *Stroke*, 12(6):723, 1981.
- [17] E. C. Peterson, Z. Wang, and G. Britz. Regulation of cerebral blood flow. *Int. J. Vasc. Med.*, 2011, 2011.
- [18] M. J. Cipolla. *The Cerebral Circulation*. Integrated Systems Physiology: From Molecule to Function. Morgan & Claypool Life Sciences, San Rafael (CA), 2009.
- [19] A. H. van Beek, J. A. Claassen, M. G. O. Rikkert, and R. W. Jansen. Cerebral autoregulation: an overview of current concepts and methodology with special

- focus on the elderly. *J. Cereb. Blood Flow Metab.*, 28(6):1071–1085, 2008.
- [20] S. Strandgaard. Autoregulation of cerebral blood flow in hypertensive patients. the modifying influence of prolonged antihypertensive treatment on the tolerance to acute, drug-induced hypotension. *Circulation*, 53(4):720–727, 1976.
- [21] G. Greisen. Autoregulation of cerebral blood flow in newborn babies. *Early Hum. Dev.*, 81(5):423–428, 2005.
- [22] L. Tyszczuk, J. Meek, C. Elwell, and J. S. Wyatt. Cerebral blood flow is independent of mean arterial blood pressure in preterm infants undergoing intensive care. *Pediatrics*, 102(2 Pt 1):337–341, 1998.
- [23] O. Pryds, G. Greisen, H. Lou, and B. Friis-Hansen. Vasoparalysis associated with brain damage in asphyxiated term infants. *J. Pediatr.*, 117(1 Pt 1):119–125, 1990.
- [24] H. Jóhannsson and B. K. Siesjö. Cerebral blood flow and oxygen consumption in the rat in hypoxic hypoxia. *Acta Physiol. Scand.*, 93(2):269–276, 1975.
- [25] M. Reivich. Arterial PCO<sub>2</sub> and cerebral hemodynamics. *Am. J. Physiol.*, 206:25–35, 1964.
- [26] B. K. Siesjö. *Brain energy metabolism*. John Wiley & Sons, 1978.
- [27] P. Mitchell. Coupling of phosphorylation to electron and hydrogen transfer by a chemi-osmotic type of mechanism. *Nature*, 191(4784):144–148, 1961.
- [28] C. E. Cooper. Nitric oxide and cytochrome oxidase: substrate, inhibitor or effector? *Trends Biochem. Sci.*, 27(1):33–39, 2002.
- [29] P. D. Boyer. The ATP synthase—a splendid molecular machine. *Annu. Rev. Biochem.*, 66:717–749, 1997.
- [30] D. F. Rolfe and M. D. Brand. The physiological significance of mitochondrial proton leak in animal cells and tissues. *Biosci. Rep.*, 17(1):9–16, 1997.
- [31] P. C. Hinkle. P/O ratios of mitochondrial oxidative phosphorylation. *Biochim. Biophys. Acta*, 1706(1-2):1–11, 2005.
- [32] B. Korzeniewski and W. Froncisz. An extended dynamic model of oxidative phosphorylation. *Biochim. Biophys. Acta*, 1060(2):210–223, 1991.

- [33] D. E. Atkinson. The energy charge of the adenylate pool as a regulatory parameter. interaction with feedback modifiers. *Biochemistry*, 7(11):4030–4034, 1968.
- [34] B. Ludwig, E. Bender, S. Arnold, M. Hüttemann, I. Lee, and B. Kadenbach. Cytochrome c oxidase and the regulation of oxidative phosphorylation. *Chem-biochem*, 2(6):392–403, 2001.
- [35] R. S. Balaban. Regulation of oxidative phosphorylation in the mammalian cell. *Am. J. Physiol.*, 258(3 Pt 1):C377–C389, 1990.
- [36] I. A. Simpson, A. Carruthers, and S. J. Vannucci. Supply and demand in cerebral energy metabolism: the role of nutrient transporters. *J. Cereb. Blood Flow Metab.*, 27(11):1766–1791, 2007.
- [37] A. G. Lowe and A. R. Walmsley. The kinetics of glucose transport in human red blood cells. *Biochim. Biophys. Acta*, 857(2):146–154, 1986.
- [38] L. Pellerin and P. J. Magistretti. Glutamate uptake into astrocytes stimulates aerobic glycolysis: a mechanism coupling neuronal activity to glucose utilization. *Proc. Natl. Acad. Sci. U. S. A.*, 91(22):10625–10629, 1994.
- [39] M. Bélanger, I. Allaman, and P. Magistretti. Brain energy metabolism: Focus on astrocyte-neuron metabolic cooperation. *Cell Metab.*, 14(6):724–738, 2011.
- [40] R. Jolivet, I. Allaman, L. Pellerin, P. J. Magistretti, and B. Weber. Comment on recent modeling studies of astrocyte-neuron metabolic interactions. *J. Cereb. Blood Flow Metab.*, 30(12):1982–1986, 2010.
- [41] S. Mangia, M. DiNuzzo, F. Giove, A. Carruthers, I. A. Simpson, and S. J. Vannucci. Response to ‘comment on recent modeling studies of astrocyte-neuron metabolic interactions’: much ado about nothing. *J. Cereb. Blood Flow Metab.*, 31(6):1346–1353, 2011.
- [42] G. C. Brown and J. J. Neher. Eaten alive! cell death by primary phagocytosis: “phagoptosis”. *Trends Biochem. Sci.*, 37(8):325–332, 2012.
- [43] F. J. Northington, R. Chavez-Valdez, and L. J. Martin. Neuronal cell death in neonatal hypoxia-ischemia. *Ann. Neurol.*, 69(5):743–758, 2011.
- [44] Z. S. Vexler and D. M. Ferriero. Molecular and biochemical mechanisms of perinatal brain injury. *Semin. Neonatol.*, 6(2):99–108, 2001.

- [45] M. V. Johnston. Excitotoxicity in neonatal hypoxia. *Ment. Retard. Dev. Disabil. Res. Rev.*, 7(4):229–234, 2001.
- [46] C. Ikonomidou, J. L. Mosinger, K. S. Salles, J. Labruyere, and J. W. Olney. Sensitivity of the developing rat brain to hypobaric/ischemic damage parallels sensitivity to N-methyl-aspartate neurotoxicity. *J. Neurosci.*, 9(8):2809–2818, 1989.
- [47] K. Blomgren and H. Hagberg. Free radicals, mitochondria, and hypoxia-ischemia in the developing brain. *Free Radic. Biol. Med.*, 40(3):388–397, 2006.
- [48] J. P. Bolaños and A. Almeida. Roles of nitric oxide in brain hypoxia-ischemia. *Biochim. Biophys. Acta, Bioenerg.*, 1411(23):415–436, 1999.
- [49] D. M. Ferriero, D. M. Holtzman, S. M. Black, and R. A. Sheldon. Neonatal mice lacking neuronal nitric oxide synthase are less vulnerable to hypoxic-ischemic injury. *Neurobiol. Dis.*, 3(1):64–71, 1996.
- [50] N. A. Terpolilli, S.-W. Kim, S. C. Thal, W. M. Kuebler, and N. Plesnila. Inhaled nitric oxide reduces secondary brain damage after traumatic brain injury in mice. *J. Cereb. Blood Flow Metab.*, 33(2):311–318, 2013.
- [51] S. S. Kety and C. F. Schmidt. The nitrous oxide method for the quantitative determination of cerebral blood flow in man: Theory, procedure and normal values. *J. Clin. Invest.*, 27(4):476–483, 1948.
- [52] M. A. McLean and J. J. Cross. Magnetic resonance spectroscopy: principles and applications in neurosurgery. *Br. J. Neurosurg.*, 23(1):5–13, 2009.
- [53] M. E. Phelps. PET: A biological imaging technique. *Neurochem. Res.*, 16(9):929–940, 1991.
- [54] P. Nandi and S. M. Lunte. Recent trends in microdialysis sampling integrated with conventional and microanalytical systems for monitoring biological events: a review. *Anal. Chim. Acta*, 651(1):1–14, 2009.
- [55] G. M. Hale and M. R. Querry. Optical constants of water in the 200 nm to 200 micron wavelength region. *Applied Optics*, 12(3):555–563, 1973.
- [56] C. Elwell. *A Practical Users Guide to NIRS*. UCL Reprographics, London, 1995.
- [57] M. Wolf, M. Ferrari, and V. Quaresima. Progress of near-infrared spectroscopy

and topography for brain and muscle clinical applications. *J. Biomed. Opt.*, 12(6):062104–14, 2007.

- [58] J. E. Brazy. Cerebral oxygen monitoring with near infrared spectroscopy: Clinical application to neonates. *J. Clin. Monit.*, 7(4):325–334, 1991.
- [59] R. Springett, Y. Sakata, and D. T. Delpy. Precise measurement of cerebral blood flow in newborn piglets from the bolus passage of indocyanine green. *Phys. Med. Biol.*, 46(8):2209–25, 2001.
- [60] A. D. Edwards, J. S. Wyatt, C. Richardson, D. T. Delpy, M. Cope, and E. O. Reynolds. Cotside measurement of cerebral blood flow in ill newborn infants by near infrared spectroscopy. *Lancet*, 2(8614):770–771, 1988.
- [61] J. S. Wyatt, M. Cope, D. T. Delpy, S. Wray, and E. O. Reynolds. Quantification of cerebral oxygenation and haemodynamics in sick newborn infants by near infrared spectrophotometry. *Lancet*, 2(8515):1063–1066, 1986.
- [62] F. F. Jobsis. Noninvasive, infrared monitoring of cerebral and myocardial oxygen sufficiency and circulatory parameters. *Science*, 198(4323):1264–1267, 1977.
- [63] R. E. Gagnon, F. A. Gagnon, A. J. Macnab, R. E. Gagnon, F. A. Gagnon, and A. J. Macnab. Comparison of 13 published cytochrome c oxidase near-infrared spectroscopy algorithms. *Eur. J. Appl. Physiol.*, 74(6):487–495, 1996.
- [64] S. J. Matcher, C. E. Elwell, C. E. Cooper, M. Cope, and D. T. Delpy. Performance comparison of several published tissue near-infrared spectroscopy algorithms. *Anal. Biochem.*, 227(1):54–68, 1995.
- [65] R. Springett and H. M. Swartz. Measurements of oxygen in vivo: overview and perspectives on methods to measure oxygen within cells and tissues. *Antioxid. Redox Signaling*, 9(8):1295–1302, 2007.
- [66] M. Ferrari, D. F. Hanley, D. A. Wilson, and R. J. Traystman. Redox changes in cat brain cytochrome-c oxidase after blood-fluorocarbon exchange. *Am. J. Physiol.*, 258(6):H1706–H1713, 1990.
- [67] Y. Hoshi, O. Hazeki, Y. Kakihana, and M. Tamura. Redox behavior of cytochrome oxidase in the rat brain measured by near-infrared spectroscopy. *J. Appl. Physiol.*, 83(6):1842–1848, 1997.
- [68] M. Tamura. Non-invasive monitoring of the redox state of cytochrome oxidase in

- living tissue using near-infrared laser lights. *Jpn. Circ. J.*, 57(8):817–824, 1993.
- [69] S. Wray, M. Cope, D. T. Delpy, J. S. Wyatt, and E. O. Reynolds. Characterization of the near infrared absorption spectra of cytochrome aa<sub>3</sub> and haemoglobin for the non-invasive monitoring of cerebral oxygenation. *Biochim. Biophys. Acta*, 933(1):184–192, 1988.
- [70] A. L. Sylvia and C. A. Piantadosi. O<sub>2</sub> dependence of in vivo brain cytochrome redox responses and energy metabolism in bloodless rats. *J. Cereb. Blood Flow Metab.*, 8(2):163–172, 1988.
- [71] C. E. Cooper, D. T. Delpy, and E. M. Nemoto. The relationship of oxygen delivery to absolute haemoglobin oxygenation and mitochondrial cytochrome oxidase redox state in the adult brain: a near-infrared spectroscopy study. *Biochem. J.*, 332(Pt 3):627–632, 1998.
- [72] C. E. Cooper, M. Cope, R. Springett, P. N. Amess, J. Penrice, L. Tyszczuk, S. Punwani, R. Ordidge, J. Wyatt, and D. T. Delpy. Use of mitochondrial inhibitors to demonstrate that cytochrome oxidase near-infrared spectroscopy can measure mitochondrial dysfunction noninvasively in the brain. *J. Cereb. Blood Flow Metab.*, 19(1):27–38, 1999.
- [73] J. P. Newman, D. M. Peebles, S. R. G. Harding, R. Springett, and M. A. Hanson. Hemodynamic and metabolic responses to moderate asphyxia in brain and skeletal muscle of late-gestation fetal sheep. *J. Appl. Physiol.*, 88(1):82–90, 2000.
- [74] L. Bennet, V. Roelfsema, J. M. Dean, G. Wassink, G. G. Power, E. C. Jensen, and A. J. Gunn. Regulation of cytochrome oxidase redox state during umbilical cord occlusion in preterm fetal sheep. *Am. J. Physiol.-Reg. I*, 292(4):R1569–R1576, 2007.
- [75] C. E. Cooper and R. Springett. Measurement of cytochrome oxidase and mitochondrial energetics by near-infrared spectroscopy. *Philos. Trans. R. Soc. Lond. B. Biol. Sci.*, 352(1354):669–676, 1997.
- [76] A. D. Edwards, G. C. Brown, M. Cope, J. S. Wyatt, D. C. McCormick, S. C. Roth, D. T. Delpy, and E. O. Reynolds. Quantification of concentration changes in neonatal human cerebral oxidized cytochrome oxidase. *J. Appl. Physiol.*, 71(5):1907–1913, 1991.
- [77] M. M. Tisdall, I. Tachtsidis, T. S. Leung, C. E. Elwell, and M. Smith. Near-

- infrared spectroscopic quantification of changes in the concentration of oxidized cytochrome c oxidase in the healthy human brain during hypoxemia. *J. Biomed. Opt.*, 12(2):024002, 2007.
- [78] A. D. McGown, H. Makker, C. Elwell, P. G. Al Rawi, A. Valipour, and S. G. Spiro. Measurement of changes in cytochrome oxidase redox state during obstructive sleep apnea using near-infrared spectroscopy. *Sleep*, 26(6):710–716, 2003.
- [79] H. R. Heekeren, M. Kohl, H. Obrig, R. Wenzel, W. v. Pannwitz, S. J. Matcher, U. Dirnagl, C. E. Cooper, and A. Villringer. Noninvasive assessment of changes in cytochrome-c-oxidase oxidation in human subjects during visual stimulation. *J. Cereb. Blood Flow Metab.*, 19(6):592–603, 1999.
- [80] H. Obrig, R. Wenzel, M. Kohl, S. Horst, P. Wobst, J. Steinbrink, F. Thomas, and A. Villringer. Near-infrared spectroscopy: does it function in functional activation studies of the adult brain? *Int. J. Psychophysiol.*, 35(2–3):125–42, 2000.
- [81] K. Uludağ, J. Steinbrink, M. Kohl-Bareis, R. Wenzel, A. Villringer, and H. Obrig. Cytochrome-c-oxidase redox changes during visual stimulation measured by near-infrared spectroscopy cannot be explained by a mere cross talk artefact. *Neuroimage*, 22(1):109–119, 2004.
- [82] C. Kolyva, I. Tachtsidis, A. Ghosh, T. Moroz, C. E. Cooper, M. Smith, and C. E. Elwell. Systematic investigation of changes in oxidized cerebral cytochrome c oxidase concentration during frontal lobe activation in healthy adults. *Biomed. Opt. Express*, 3(10):2550–2566, 2012.
- [83] I. Tachtsidis, M. M. Tisdall, T. S. Leung, C. Pritchard, C. E. Cooper, M. Smith, and C. E. Elwell. Relationship between brain tissue haemodynamics, oxygenation and metabolism in the healthy human adult brain during hyperoxia and hypercapnea. *Adv. Exp. Med. Biol.*, 645:315–320, 2009.
- [84] M. Wolf, G. Naulaers, F. van Bel, S. Kleiser, and G. Griesen. A review of near infrared spectroscopy for term and preterm newborns. *J. Near Infrared Spectrosc.*, 20(1):43–55, 2012.
- [85] S. Suzuki, S. Takasaki, T. Ozaki, and Y. Kobayashiu. A tissue oxygenation monitor using NIR spatially resolved spectroscopy. In *Proceedings of optical tomography and spectroscopy of tissue III*, volume 3597, pages 582–592, 1999.

- [86] R. E. Gagnon, A. J. Macnab, F. A. Gagnon, D. Blackstock, and J. G. LeBlanc. Comparison of two spatially resolved NIRS oxygenation indices. *J. Clin. Monit. Comput.*, 17(7):385–391, 2002.
- [87] K. Yoshitani, M. Kawaguchi, K. Tatsumi, K. Kitaguchi, and H. Furuya. A comparison of the INVOS 4100 and the NIRO 300 near-infrared spectrophotometers. *Anesth. Analg.*, 94(3):586–590, 2002.
- [88] M. Thavasoathy, M. Broadhead, C. Elwell, M. Peters, and M. Smith. A comparison of cerebral oxygenation as measured by the NIRO 300 and the INVOS 5100 near-infrared spectrophotometers. *Anaesthesia*, 57(10):999–1006, 2002.
- [89] N. Nagdyman, P. Ewert, B. Peters, O. Miera, T. Fleck, and F. Berger. Comparison of different near-infrared spectroscopic cerebral oxygenation indices with central venous and jugular venous oxygenation saturation in children. *Paediatr. Anaesth.*, 18(2):160–166, 2008.
- [90] I. Tachtsidis. *Experimental Measurements of Cerebral Haemodynamics and Oxygenation and Comparisons with a Computational Model: a Near-Infrared Spectroscopy Investigation*. PhD thesis, Univeristy College London, 2005.
- [91] K. Kishi, M. Kawaguchi, K. Yoshitani, T. Nagahata, and H. Furuya. Influence of patient variables and sensor location on regional cerebral oxygen saturation measured by INVOS 4100 near-infrared spectrophotometers. *J. Neurosurg. Anesthesiol.*, 15(4):302–306, 2003.
- [92] P. G. Al-Rawi, P. Smielewski, and P. J. Kirkpatrick. Evaluation of a near-infrared spectrometer (NIRO 300) for the detection of intracranial oxygenation changes in the adult head. *Stroke*, 32(11):2492–2500, 2001.
- [93] K. Yoshitani, M. Kawaguchi, N. Miura, T. Okuno, T. Kanoda, Y. Ohnishi, and M. Kuro. Effects of hemoglobin concentration, skull thickness, and the area of the cerebrospinal fluid layer on near-infrared spectroscopy measurements. *Anesthesiology*, 106(3):458–462, 2007.
- [94] M. Smith and C. Elwell. Near-infrared spectroscopy: shedding light on the injured brain. *Anesth. Analg.*, 108(4):1055–1057, 2009.
- [95] M. M. Tisdall and M. Smith. Multimodal monitoring in traumatic brain injury: current status and future directions. *Br. J. Anaesth.*, 99(1):61–67, 2007.
- [96] J. M. Murkin, S. J. Adams, R. J. Novick, M. Quantz, D. Bainbridge, I. Iglesias,

- A. Cleland, B. Schaefer, B. Irwin, and S. Fox. Monitoring brain oxygen saturation during coronary bypass surgery: a randomized, prospective study. *Anesth. Analg.*, 104(1):51–8, 2007.
- [97] M. M. Tisdall, C. Taylor, I. Tachtsidis, T. S. Leung, C. E. Elwell, and M. Smith. The effect on cerebral tissue oxygenation index of changes in the concentrations of inspired oxygen and end-tidal carbon dioxide in healthy adult volunteers. *Anesth. Analg.*, 109(3):906–913, 2009.
- [98] E. E. Benarroch. N-acetylaspartate and N-acetylaspartylglutamate: neurobiology and clinical significance. *Neurology*, 70(16):1353–7, 2008.
- [99] S. D. Friedman, J. E. Jensen, B. B. Frederick, A. A. Artru, P. F. Renshaw, and S. R. Dager. Brain changes to hypocapnia using rapidly interleaved phosphorus-proton magnetic resonance spectroscopy at 4 T. *J. Cereb. Blood Flow Metab.*, 27(3):646–653, 2007.
- [100] M. van der Graaf. In vivo magnetic resonance spectroscopy: basic methodology and clinical applications. *Eur. Biophys. J.*, 39(4):527–540, 2010.
- [101] D. P. Soares and M. Law. Magnetic resonance spectroscopy of the brain: review of metabolites and clinical applications. *Clin. Radiol.*, 64(1):12–21, 2009.
- [102] A. Holdcroft, L. Hall, G. Hamilton, S. J. Counsell, G. M. Bydder, and J. D. Bell. Phosphorus-31 brain MR spectroscopy in women during and after pregnancy compared with nonpregnant control subjects. *Am. J. Neuroradiol.*, 26(2):352–356, 2005.
- [103] B. Ross and S. Bluml. Magnetic resonance spectroscopy of the human brain. *Anat. Rec.*, 265(2):54–84, 2001.
- [104] M. Stubbs, Z. M. Bhujwala, G. M. Tozer, L. M. Rodrigues, R. J. Maxwell, R. Morgan, F. A. Howe, and J. R. Griffiths. An assessment of  $^{31}\text{P}$  mrs as a method of measuring pH in rat tumours. *NMR Biomed.*, 5(6):351–359, 1992.
- [105] R. Aaslid, T. M. Markwalder, and H. Nornes. Noninvasive transcranial doppler ultrasound recording of flow velocity in basal cerebral arteries. *J. Neurosurg.*, 57(6):769–774, 1982.
- [106] H. S. Markus. Transcranial doppler ultrasound. *Br. Med. Bull.*, 56(2):378–388, 2000.

- [107] M. Y. Kassab, A. Majid, M. U. Farooq, H. Azhary, L. A. Hershey, E. M. Bednarczyk, D. F. Graybeal, and M. D. Johnson. Transcranial doppler: An introduction for primary care physicians. *J. Am. Board Fam. Med.*, 20(1):65–71, 2007.
- [108] H. White and B. Venkatesh. Applications of transcranial doppler in the ICU: a review. *Intensive Care Med.*, 32(7):981–994, 2006.
- [109] T. Aoyagi, M. Kishi, K. Yamaguchi, and S. Watanabe. Improvement of the ear-piece oximeter. *Japanese Society of Medical Electronics and Biological Engineering*, 974:90–91, 1974.
- [110] G. A. Millikan. The oximeter, an instrument for measuring continuously the oxygen saturation of arterial blood in man. *Rev. Sci. Instrum.*, 13(10):434–444, 1942.
- [111] T. Aoyagi. Pulse oximetry: its invention, theory, and future. *J. Anesth.*, 17(4):259–266, 2003.
- [112] M. W. Wukitsch, M. T. Petterson, D. R. Tobler, and J. A. Pologe. Pulse oximetry: analysis of theory, technology, and practice. *J. Clin. Monit. Comput.*, 4(4):290–301, 1987.
- [113] K. R. Ward and D. M. Yealy. End-tidal carbon dioxide monitoring in emergency medicine, part 1: Basic principles. *Acad. Emerg. Med.*, 5(6):628–636, 1998.
- [114] B. S. Kodali. Capnography. <http://www.capnography.com/>.
- [115] P. Eberhard. The design, use, and results of transcutaneous carbon dioxide analysis: current and future directions. *Anesth. Analg.*, 105(6 Suppl):S48–52, 2007.
- [116] N. H. Naqvi and M. D. Blafox. *Blood pressure measurement: an illustrated history*. Parthenon Pub. Group, 1998.
- [117] E. Meaney. Formula and nomogram for the sphygmomanometric calculation of the mean arterial pressure. *Heart*, 84(1):64–64, 2000.
- [118] G. A. Lodygensky, T. E. Inder, and J. J. Neil. Application of magnetic resonance imaging in animal models of perinatal hypoxic-ischemic cerebral injury. *Int. J. Dev. Neurosci.*, 26(1):13–25, 2008.
- [119] M. J. Painter. Animal models of perinatal asphyxia: contributions, contradictions, clinical relevance. In *Seminars in pediatric neurology*, volume 2, pages

37–56, 1995.

- [120] T. Roohey, T. N. Raju, and A. N. Moustogiannis. Animal models for the study of perinatal hypoxic-ischemic encephalopathy: a critical analysis. *Early Hum. Dev.*, 47(2):115–146, 1997.
- [121] E. Cady, M. Joan Dawson, P. Hope, P. Tofts, A. De L. Costello, D. Delpy, E. Reynolds, and D. Wilkie. Non-invasive investigation of cerebral metabolism in newborn infants by phosphorus nuclear magnetic resonance spectroscopy. *Lancet*, 321(8333):1059–1062, 1983.
- [122] A. Lorek, Y. Takei, E. B. Cady, J. S. Wyatt, J. Penrice, A. D. Edwards, D. Peebles, M. Wylezinska, H. Owen-Reece, V. Kirkbride, C. E. Cooper, R. F. Aldridge, S. C. Roth, G. Brown, D. T. Delpy, and E. O. R. Reynolds. Delayed (“secondary”) cerebral energy failure after acute hypoxia-ischemia in the newborn piglet: Continuous 48-hour studies by phosphorus magnetic resonance spectroscopy. *Pediatr. Res.*, 36(6):699–706, 1994.
- [123] H. Mehmet, X. Yue, M. Squier, A. Lorek, E. Cady, J. Penrice, C. Sarraf, M. Wylezinska, V. Kirkbride, C. Cooper, G. Brown, J. Wyatt, E. Reynolds, and A. Edwards. Increased apoptosis in the cingulate sulcus of newborn piglets following transient hypoxia-ischaemia is related to the degree of high energy phosphate depletion during the insult. *Neurosci. Lett.*, 181(1–2):121–125, 1994.
- [124] J. Penrice, A. Lorek, E. B. Cady, P. N. Amess, M. Wylezinska, C. E. Cooper, P. D’Souza, G. C. Brown, V. Kirkbride, A. D. Edwards, J. S. Wyatt, and E. O. R. Reynolds. Proton magnetic resonance spectroscopy of the brain during acute hypoxia-ischemia and delayed cerebral energy failure in the newborn piglet. *Pediatr. Res.*, 41(6):795–802, 1997.
- [125] M. Tsuji, H. Naruse, J. Volpe, and D. Holtzman. Reduction of cytochrome aa3 measured by near-infrared spectroscopy predicts cerebral energy loss in hypoxic piglets. *Pediatr. Res.*, 37(3):253–259, 1995.
- [126] M. Tamura, O. Hazeki, S. Nioka, B. Chance, and D. S. Smith. The simultaneous measurements of tissue oxygen concentration and energy state by near-infrared and nuclear magnetic resonance spectroscopy. *Adv. Exp. Med. Biol.*, 222:359–363, 1988.
- [127] K. M. Tichauer, D. W. Brown, J. Hadway, T.-Y. Lee, and K. S. Lawrence. Near-infrared spectroscopy measurements of cerebral blood flow and oxygen con-

- sumption following hypoxia-ischemia in newborn piglets. *J. Appl. Physiol.*, 100(3):850–857, 2006.
- [128] M. Shadid, R. Moison, P. Steendijk, L. Hiltermann, H. M. Berger, and F. Van Bel. The effect of antioxidative combination therapy on post hypoxic-ischemic perfusion, metabolism, and electrical activity of the newborn brain. *Pediatr. Res.*, 44(1):119–124, 1998.
- [129] A. A. Rosenberg. Cerebral blood flow and o<sub>2</sub> metabolism after asphyxia in neonatal lambs. *Pediatr. Res.*, 20(8):778–782, 1986.
- [130] A. Solås, B. H. Munkeby, and O. D. Saugstad. Comparison of short- and long-duration oxygen treatment after cerebral asphyxia in newborn piglets. *Pediatr. Res.*, 56(1):125–131, 2004.
- [131] Y. S. Chang, W. S. Park, M. Lee, K. S. Kim, S. M. Shin, and J. H. Choi. Near infrared spectroscopic monitoring of secondary cerebral energy failure after transient global hypoxia-ischemia in the newborn piglet. *Neurol. Res.*, 21(2):216–224, 1999.
- [132] P. E. Grant, N. Roche-Labarbe, A. Surova, G. Themelis, J. Selb, E. K. Warren, K. S. Krishnamoorthy, D. A. Boas, and M. A. Franceschini. Increased cerebral blood volume and oxygen consumption in neonatal brain injury. *J. Cereb. Blood Flow Metab.*, 29(10):1704–1713, 2009.
- [133] T. Ioroi, C. Peeters-Scholte, I. Post, C. Leusink, F. Groenendaal, and F. van Bel. Changes in cerebral haemodynamics, regional oxygen saturation and amplitude-integrated continuous EEG during hypoxia-ischaemia and reperfusion in newborn piglets. *Exp. Brain Res.*, 144(2):172–177, 2002.
- [134] M. Toet, L. Hellstrom-Westas, F. Groenendaal, P. Eken, and L. S. de Vries. Amplitude integrated EEG 3 and 6 hours after birth in full term neonates with hypoxic-ischaemic encephalopathy. *Arch. Dis. Child. Fetal Neonatal Ed.*, 81(1):F19–F23, 1999.
- [135] P. Hunter, P. V. Coveney, B. de Bono, V. Diaz, J. Fenner, A. F. Frangi, P. Harris, R. Hose, P. Kohl, P. Lawford, K. McCormack, M. Mendes, S. Omholt, A. Quarteroni, J. Skår, J. Tegner, S. Randall Thomas, I. Tollis, I. Tsamardinos, J. H. G. M. van Beek, and M. Viceconti. A vision and strategy for the virtual physiological human in 2010 and beyond. *Phil. Trans. R. Soc. A*, 368(1920):2595–2614, 2010.

- [136] E. J. Crampin. Computational physiology and the physiome project. *Exp. Physiol.*, 89(1):1–26, 2004.
- [137] H.-Y. Chuang, M. Hofree, and T. Ideker. A decade of systems biology. *Annu. Rev. Cell Dev. Biol.*, 26(1):721–744, 2010.
- [138] J. Southern, J. Pitt-Francis, J. Whiteley, D. Stokeley, H. Kobashi, R. Nobes, Y. Kadooka, and D. Gavaghan. Multi-scale computational modelling in biology and physiology. *Prog. Biophys. Mol. Biol.*, 96(1–3):60–89, 2008.
- [139] P. J. Hunter and T. K. Borg. Integration from proteins to organs: the physiome project. *Nat. Rev. Mol. Cell Biol.*, 4(3):237–243, 2003.
- [140] M. Czosnyka, N. G. Harris, J. D. Pickard, and S. Piechnik. CO<sub>2</sub> cerebrovascular reactivity as a function of perfusion pressure—a modelling study. *Acta Neurochir. (Wien)*, 121(3-4):159–165, 1993.
- [141] F. Hyder, R. G. Shulman, and D. L. Rothman. A model for the regulation of cerebral oxygen delivery. *J. Appl. Physiol.*, 85(2):554–564, 1998.
- [142] M. Ursino and C. A. Lodi. Interaction among autoregulation, CO<sub>2</sub> reactivity, and intracranial pressure: a mathematical model. *Am. J. Physiol.*, 274(5 Pt 2):H1715–H1728, 1998.
- [143] A. Aubert and R. Costalat. Modelling of the coupling between brain electrical activity and metabolism. *Acta Biotheor.*, 49(4):301–326, 2001.
- [144] B. Korzeniewski and J. A. Zoladz. A model of oxidative phosphorylation in mammalian skeletal muscle. *Biophys. Chem.*, 92(1-2):17–34, 2001.
- [145] A. Gjedde. Cerebral blood flow change in arterial hypoxemia is consistent with negligible oxygen tension in brain mitochondria. *Neuroimage*, 17(4):1876–1881, 2002.
- [146] S. Cortassa, M. A. Aon, E. Marbán, R. L. Winslow, and B. O’Rourke. An integrated model of cardiac mitochondrial energy metabolism and calcium dynamics. *Biophys. J.*, 84(4):2734–2755, 2003.
- [147] A. Aubert and R. Costalat. Interaction between astrocytes and neurons studied using a mathematical model of compartmentalized energy metabolism. *J. Cereb. Blood Flow Metab.*, 25(11):1476–90, 2005.

- [148] A. Jung, R. Faltermeier, R. Rothoerl, and A. Brawanski. A mathematical model of cerebral circulation and oxygen supply. *J. Math. Biol.*, 51(5):491–507, 2005.
- [149] D. A. Beard. Modeling of oxygen transport and cellular energetics explains observations on in vivo cardiac energy metabolism. *PLoS Comput. Biol.*, 2(9):e107, 2006.
- [150] L. Vatov, Z. Kizner, E. Ruppin, S. Meilin, T. Manor, and A. Mayevsky. Modeling brain energy metabolism and function: a multiparametric monitoring approach. *Bull. Math. Biol.*, 68(2):275–291, 2006.
- [151] J. Alastruey, S. M. Moore, K. H. Parker, T. David, J. Peiró, and S. J. Sherwin. Reduced modelling of blood flow in the cerebral circulation: Coupling 1-D, 0-D and cerebral auto-regulation models. *Int. J. Numer. Meth. Fluids*, 56(8):1061–1067, 2008.
- [152] M. Cloutier, F. B. Bolger, J. P. Lowry, and P. Wellstead. An integrative dynamic model of brain energy metabolism using in vivo neurochemical measurements. *J. Comput. Neurosci.*, 27(3):391–414, 2009.
- [153] A. A. Linninger, M. Xenos, B. Sweetman, S. Ponkshe, X. Guo, and R. Penn. A mathematical model of blood, cerebrospinal fluid and brain dynamics. *J. Math. Biol.*, 59(6):729–759, 2009.
- [154] M. DiNuzzo, S. Mangia, B. Maraviglia, and F. Giove. Changes in glucose uptake rather than lactate shuttle take center stage in subserving neuroenergetics: evidence from mathematical modeling. *J. Cereb. Blood Flow Metab.*, 30(3):586–602, 2010.
- [155] S. Mangia, I. A. Simpson, S. J. Vannucci, and A. Carruthers. The in vivo neuron-to-astrocyte lactate shuttle in human brain: evidence from modeling of measured lactate levels during visual stimulation. *J. Neurochem.*, 109:55–62, 2009.
- [156] P. Orłowski, M. Chappell, C. S. Park, V. Grau, and S. Payne. Modelling of ph dynamics in brain cells after stroke. *J. R. Soc. Interface*, 1(3):408–416, 2011.
- [157] G. Kellie. An account with some reflections on the pathology of the brain. *Edinburgh Med. Chir. Soc. Trans.*, 1:84–169, 1824.
- [158] J. Reichold, M. Stampanoni, A. L. Keller, A. Buck, P. Jenny, and B. Weber. Vascular graph model to simulate the cerebral blood flow in realistic vascular networks. *J. Cereb. Blood Flow Metab.*, 29(8):1429–1443, 2009.

- [159] L. Grinberg, T. Anor, J. Madsen, A. Yakhot, and G. Karniadakis. Large-scale simulation of the human arterial tree. *Clin. Exp. Pharmacol. Physiol.*, 36(2):194–205, 2009.
- [160] R. B. Panerai, S. L. Dawson, and J. F. Potter. Linear and nonlinear analysis of human dynamic cerebral autoregulation. *Am. J. Physiol.*, 277(3 Pt 2):H1089–1099, 1999.
- [161] A. P. Blaber, R. L. Bondar, F. Stein, P. T. Dunphy, P. Moradshahi, M. S. Kassam, and R. Freeman. Transfer function analysis of cerebral autoregulation dynamics in autonomic failure patients. *Stroke*, 28(9):1686–1692, 1997.
- [162] S. J. Payne and L. Tarassenko. Combined transfer function analysis and modelling of cerebral autoregulation. *Ann. Biomed. Eng.*, 34(5):847–858, 2006.
- [163] R. B. Buxton and L. R. Frank. A model for the coupling between cerebral blood flow and oxygen metabolism during neural stimulation. *J. Cereb. Blood Flow Metab.*, 17(1):64–72, 1997.
- [164] K. Krab, H. Kempe, and M. Wikström. Explaining the enigmatic  $K_M$  for oxygen in cytochrome c oxidase: a kinetic model. *Biochim. Biophys. Acta*, 1807(3):348–58, 2011.
- [165] B. Teusink, J. Passarge, C. A. Reijenga, E. Esgalhadó, C. C. van der Weijden, M. Schepper, M. C. Walsh, B. M. Bakker, K. van Dam, H. V. Westerhoff, and J. L. Snoep. Can yeast glycolysis be understood in terms of in vitro kinetics of the constituent enzymes? testing biochemistry. *Eur. J. Biochem.*, 267(17):5313–5329, 2000.
- [166] F. Hynne, S. Danø, and P. G. Sørensen. Full-scale model of glycolysis in *Saccharomyces cerevisiae*. *Biophys. Chem.*, 94(1-2):121–163, 2001.
- [167] A. Joshi and B. O. Palsson. Metabolic dynamics in the human red cell: Part I—comprehensive kinetic model. *J. Theor. Biol.*, 141(4):515–528, 1989.
- [168] A. Joshi and B. O. Palsson. Metabolic dynamics in the human red cell. part III—metabolic reaction rates. *J. Theor. Biol.*, 142(1):41–68, 1990.
- [169] E. Mogilevskaya, O. Demin, and I. Goryanin. Kinetic model of mitochondrial krebs cycle: Unraveling the mechanism of salicylate hepatotoxic effects. *J. Biol. Phys.*, 32(3-4):245–271, 2006.

- [170] F. Wu, F. Yang, K. C. Vinnakota, and D. A. Beard. Computer modeling of mitochondrial tricarboxylic acid cycle, oxidative phosphorylation, metabolite transport, and electrophysiology. *J. Biol. Chem.*, 282(34):24525–37, 2007.
- [171] M. C. Kohn, M. J. Achs, and D. Garfinkel. Computer simulation of metabolism in pyruvate-perfused rat heart. II. krebs cycle. *Am. J. Physiol.-Reg. I*, 237(3):R159–R166, 1979.
- [172] G. Magnus and J. Keizer. Minimal model of beta-cell mitochondrial  $\text{Ca}^{2+}$  handling. *Am. J. Physiol.*, 273(2 Pt 1):C717–C733, 1997.
- [173] R. Heinrich and T. Rapoport. Mathematical analysis of multienzyme systems. II. steady state and transient control. *Biosystems*, 7(1):130–136, 1975.
- [174] A. Aubert and R. Costalat. A model of the coupling between brain electrical activity, metabolism, and hemodynamics: Application to the interpretation of functional neuroimaging. *Neuroimage*, 17(3):1162–1181, 2002.
- [175] R. Buxton, K. Miller, L. Frank, and E. Wong. Bold signal dynamics: the balloon model with viscoelastic effects. *Proc. Int. Mag. Reson. Med.*, 6:1401, 1998.
- [176] A. Aubert, L. Pellerin, P. J. Magistretti, and R. Costalat. A coherent neurobiological framework for functional neuroimaging provided by a model integrating compartmentalized energy metabolism. *Proc. Natl. Acad. Sci. U. S. A.*, 104(10):4188–4193, 2007.
- [177] P. Orlowski, D. O’Neill, V. Grau, Y. Ventikos, and S. Payne. Modelling of the physiological response of the brain to ischaemic stroke. *Interface Focus*, 3(2):20120079, 2013.
- [178] BioModels database. <http://www.ebi.ac.uk/biomodels-main/>.
- [179] F. Wu, J. A. L. Jeneson, and D. A. Beard. Oxidative ATP synthesis in skeletal muscle is controlled by substrate feedback. *Am. J. Physiol. Cell Physiol.*, 292(1):C115–C124, 2006.
- [180] M. Banaji, I. Tachtsidis, D. Delpy, and S. Baigent. A physiological model of cerebral blood flow control. *Math. Biosci.*, 194(2):125–173, 2005.
- [181] M. Banaji. BRAINCIRC Home Page. <http://braincirc.sourceforge.net/>.

- [182] The HDF group. hierarchical data format version 5. <http://www.hdfgroup.org/HDF5/>.
- [183] M. Hucka, A. Finney, H. M. Sauro, H. Bolouri, J. C. Doyle, H. Kitano, A. P. Arkin, B. J. Bornstein, D. Bray, A. Cornish-Bowden, A. A. Cuellar, S. Dronov, E. D. Gilles, M. Ginkel, V. Gor, I. I. Goryanin, W. J. Hedley, T. C. Hodgman, J. Hofmeyr, P. J. Hunter, N. S. Juty, J. L. Kasberger, A. Kremling, U. Kummer, N. Le Novère, L. M. Loew, D. Lucio, P. Mendes, E. Minch, E. D. Mjolsness, Y. Nakayama, M. R. Nelson, P. F. Nielsen, T. Sakurada, J. C. Schaff, B. E. Shapiro, T. S. Shimizu, H. D. Spence, J. Stelling, K. Takahashi, M. Tomita, J. Wagner, and J. Wang. The systems biology markup language (SBML): a medium for representation and exchange of biochemical network models. *Bioinformatics*, 19(4):524–531, 2003.
- [184] A. Finney and M. Hucka. Systems biology markup language: Level 2 and beyond. *Biochem. Soc. Trans.*, 31(Pt 6):1472–1473, 2003.
- [185] The CellML project. <http://www.cellml.org/>.
- [186] CellML model repository. <http://models.cellml.org/cellml>.
- [187] SBML. <http://sbml.org>.
- [188] OpenCell. <http://sourceforge.net/projects/cellml-opencell>.
- [189] OpenCOR. <http://www.opencor.ws>.
- [190] B. J. Bornstein, S. M. Keating, A. Jouraku, and M. Hucka. LibSBML: an API library for SBML. *Bioinformatics*, 24(6):880–881, 2008.
- [191] W3C math home. <http://www.w3.org/Math/>.
- [192] MATLAB. The MathWorks, Inc., Natick, Massachusetts, United States.
- [193] PottersWheel. <http://www.potterswheel.de/index.html>.
- [194] SimBiology. <http://www.mathworks.co.uk/products/simbiology/>.
- [195] Free Software Foundation. <http://www.fsf.org/about/>.
- [196] Scientific computing tools for python — numpy. <http://numpy.scipy.org/>.
- [197] D. Kroshko. OpenOpt: Free scientific-engineering software for mathematical

modeling and optimization, 2007–.

- [198] S. Kirkpatrick, C. D. Gelatt, and M. P. Vecchi. Optimization by simulated annealing. *Science*, 220(4598):671–680, 1983.
- [199] D. E. Goldberg. *Genetic algorithms in search, optimization, and machine learning*. Addison-Wesley publishing company, inc., Reading (Massachusetts), 1989.
- [200] J. Kennedy and R. Eberhart. Particle swarm optimization. In *IEEE International Conference on Neural Networks, 1995. Proceedings*, volume 4, pages 1942–1948, 1995.
- [201] E. Jones, T. Oliphant, P. Peterson, et al. SciPy: Open source scientific tools for Python.
- [202] PSwarm Solver. <http://www.norg.uminho.pt/aivaz/pswarm/>.
- [203] A. I. F. Vaz and L. N. Vicente. A particle swarm pattern search method for bound constrained global optimization. *J. Global Optim.*, 39(2):197–219, 2007.
- [204] M. J. D. Powell. An efficient method for finding the minimum of a function of several variables without calculating derivatives. *Comput. J.*, 7(2):155–162, 1964.
- [205] R. P. Brent. *Algorithms for Minimization Without Derivatives*, chapter 5. Dover Publications, 1973.
- [206] M. D. Morris. Factorial sampling plans for preliminary computational experiments. *Technometrics*, 33(2):161–174, 1991.
- [207] I. M. Sobol'. On sensitivity estimation for nonlinear mathematical models. *Matematicheskoe Modelirovanie*, 2(1):112–118, 1990.
- [208] G. Pujol. *sensitivity: Sensitivity Analysis*, 2008.
- [209] T. Moroz, M. Banaji, M. Tisdall, C. E. Cooper, C. E. Elwell, and I. Tachtsidis. Development of a model to aid NIRS data interpretation: Results from a hypercapnia study in healthy adults. *Adv. Exp. Med. Biol.*, 2011.
- [210] J. E. Brian. Carbon dioxide and the cerebral circulation. *Anesthesiology*, 88(5):1365–1386, 1998.
- [211] H. Ito, I. Kanno, M. Ibaraki, J. Hatazawa, and S. Miura. Changes in human

- cerebral blood flow and cerebral blood volume during hypercapnia and hypocapnia measured by positron emission tomography. *J. Cereb. Blood Flow Metab.*, 23(6):665–670, 2003.
- [212] H. A. Kontos, A. J. Raper, and J. L. Patterson. Analysis of vasoactivity of local pH, PCO<sub>2</sub> and bicarbonate on pial vessels. *Stroke*, 8(3):358–360, 1977.
- [213] R. Tian, P. Vogel, N. A. Lassen, M. J. Mulvany, F. Andreassen, and C. Aalkjaer. Role of extracellular and intracellular acidosis for hypercapnia-induced inhibition of tension of isolated rat cerebral arteries. *Circ. Res.*, 76(2):269–275, 1995.
- [214] J. P. You, Q. Wang, W. Zhang, I. Jansen-Olesen, O. B. Paulson, N. A. Lassen, and L. Edvinsson. Hypercapnic vasodilatation in is. *Acta Physiol. Scand.*, 152(4):391–397, 1994.
- [215] S. Navón and a. Agrest. ATP content in the central nervous system of rats exposed to chronic hypercapnea. *Am. J. Physiol.*, 205(5):957–8, 1963.
- [216] L. Borgström, K. Norberg, and B. K. Siesjö. Glucose consumption in rat cerebral cortex in normoxia, hypoxia and hypercapnia. *Acta Physiol. Scand.*, 96(4):569–574, 1976.
- [217] J. Folbergrová, K. Norberg, B. Quistorff, and B. K. Siesjö. Carbohydrate and amino acid metabolism in rat cerebral cortex in moderate and extreme hypercapnia. *J. Neurochem.*, 25(4):457–462, 1975.
- [218] A. I. Arieff, A. Kerian, S. G. Massry, and J. DeLima. Intracellular pH of brain: alterations in acute respiratory acidosis and alkalosis. *Am. J. Physiol.*, 230(3):804–812, 1976.
- [219] B. K. Siesjö. Cerebral metabolic rate in hypercarbia—a controversy. *Anesthesiology*, 52(6):461–465, 1980.
- [220] I. Horvath, N. T. Sandor, Z. Ruttner, and A. C. McLaughlin. Role of nitric oxide in regulating cerebrocortical oxygen consumption and blood flow during hypercapnia. *J. Cereb. Blood Flow Metab.*, 14(3):503–509, 1994.
- [221] S. P. Yang and J. A. Krasney. Cerebral blood flow and metabolic responses to sustained hypercapnia in awake sheep. *J. Cereb. Blood Flow Metab.*, 15(1):115–123, 1995.
- [222] A. B. Kliefoth, R. L. Grubb, and M. E. Raichle. Depression of cerebral oxygen

- utilization by hypercapnia in the rhesus monkey. *J. Neurochem.*, 32(2):661–663, 1979.
- [223] L. Ligeti, K. Hines, E. Dora, T. Sinnwell, M. T. Huang, and A. C. McLaughlin. Cerebral blood flow and metabolic rate in the conscious, freely moving rat: the effects of hypercapnia, and acute ethanol administration. *Alcohol. Clin. Exp. Res.*, 15(5):766–770, 1991.
- [224] T. L. Davis, K. K. Kwong, R. M. Weisskoff, and B. R. Rosen. Calibrated functional MRI: mapping the dynamics of oxidative metabolism. *Proc. Natl. Acad. Sci. U. S. A.*, 95(4):1834–1839, 1998.
- [225] A. C. Zappe, K. Uludağ, A. Oeltermann, K. Uğurbil, and N. K. Logothetis. The influence of moderate hypercapnia on neural activity in the anesthetized nonhuman primate. *Cereb. Cortex*, 18(11):2666–2673, 2008.
- [226] F. Xu, J. Uh, M. R. Brier, J. Hart, U. S. Yezhuvath, H. Gu, Y. Yang, and H. Lu. The influence of carbon dioxide on brain activity and metabolism in conscious humans. *J. Cereb. Blood Flow Metab.*, 31(1):58–67, 2011.
- [227] H. Cho, E. M. Nemoto, M. Sanders, K. Fernandez, and H. Yonas. Comparison of two commercially available near-infrared spectroscopy instruments for cerebral oximetry. technical note. *J. Neurosurg.*, 93(2):351–354, 2000.
- [228] P. Smielewski, P. Kirkpatrick, P. Minhas, J. D. Pickard, and M. Czosnyka. Can cerebrovascular reactivity be measured with near-infrared spectroscopy? *Stroke*, 26(12):2285–2292, 1995.
- [229] T. J. Germon, P. D. Evans, A. R. Manara, N. J. Barnett, P. Wall, and R. J. Nelson. Sensitivity of near infrared spectroscopy to cerebral and extra-cerebral oxygenation changes is determined by emitter-detector separation. *J. Clin. Monit. Comput.*, 14(5):353–360, 1998.
- [230] E. Rostrup, I. Law, F. Pott, K. Ide, and G. M. Knudsen. Cerebral hemodynamics measured with simultaneous PET and near-infrared spectroscopy in humans. *Brain Res.*, 954(2):183–193, 2002.
- [231] H. Ito, M. Ibaraki, I. Kanno, H. Fukuda, and S. Miura. Changes in the arterial fraction of human cerebral blood volume during hypercapnia and hypocapnia measured by positron emission tomography. *J. Cereb. Blood Flow Metab.*, 25(7):852–857, 2005.

- [232] S. P. Lee, T. Q. Duong, G. Yang, C. Iadecola, and S. G. Kim. Relative changes of cerebral arterial and venous blood volumes during increased cerebral blood flow: implications for BOLD fMRI. *Magn. Reson. Med.*, 45(5):791–800, 2001.
- [233] G. Greisen, T. Leung, and M. Wolf. Has the time come to use near-infrared spectroscopy as a routine clinical tool in preterm infants undergoing intensive care? *Phil. Trans. R. Soc. A*, 369(1955):4440–4451, 2011.
- [234] M. Firbank, C. E. Elwell, C. E. Cooper, and D. T. Delpy. Experimental and theoretical comparison of NIR spectroscopy measurements of cerebral hemoglobin changes. *J. Appl. Physiol.*, 85(5):1915–1921, 1998.
- [235] B. Jelfs, M. Banaji, I. Tachtsidis, C. E. Cooper, and C. E. Elwell. Modelling noninvasively measured cerebral signals during a hypoxemia challenge: steps towards individualised modelling. *PLoS one*, 7(6):e38297, 2012.
- [236] T. Moroz, M. Banaji, N. J. Robertson, C. E. Cooper, and I. Tachtsidis. Computational modelling of the piglet brain to simulate near-infrared spectroscopy and magnetic resonance spectroscopy data collected during oxygen deprivation. *J. R. Soc. Interface*, 2012.
- [237] R. Springett, J. Newman, M. Cope, and D. T. Delpy. Oxygen dependency and precision of cytochrome oxidase signal from full spectral NIRS of the piglet brain. *Am J. Physiol. Heart Physiol.*, 279(5):H2202–H2209, 2000.
- [238] D. W. Brown, J. Hadway, and T.-Y. Lee. Near-infrared spectroscopy measurement of oxygen extraction fraction and cerebral metabolic rate of oxygen in newborn piglets. *Pediatr. Res.*, 54(6):861–867, 2003.
- [239] G. Lossec, Y. Lebreton, J. C. Hulin, M. Fillaut, and P. Herpin. Age-related changes in oxygen and nutrient uptake by hindquarters in newborn pigs during cold-induced shivering. *Exp. Physiol.*, 83(6):793–807, 1998.
- [240] J. S. Soul, G. A. Taylor, D. Wypij, A. J. Duplessis, and J. J. Volpe. Noninvasive detection of changes in cerebral blood flow by near-infrared spectroscopy in a piglet model of hydrocephalus. *Pediatr. Res.*, 48(4):445–449, 2000.
- [241] R. Gruetter, E. J. Novotny, S. D. Boulware, D. L. Rothman, G. F. Mason, G. I. Shulman, R. G. Shulman, and W. V. Tamborlane. Direct measurement of brain glucose concentrations in humans by  $^{13}\text{C}$  NMR spectroscopy. *Proc. Natl. Acad. Sci. U. S. A.*, 89(3):1109–1112, 1992.

- [242] K. LaNoue, W. J. Nicklas, and J. R. Williamson. Control of citric acid cycle activity in rat heart mitochondria. *J. Biol. Chem.*, 245(1):102–111, 1970.
- [243] A. Lupton, B. S. Stonestreet, and W. Oh. Autoregulation of brain blood flow in the newborn piglet: regional differences in flow reduction during hypotension. *Early Hum. Dev.*, 6(1):99–107, 1982.
- [244] S. Chemtob, K. Beharry, J. Rex, D. Varma, and J. Aranda. Prostanoids determine the range of cerebral blood flow autoregulation of newborn piglets. *Stroke*, 21(5):777–784, 1990.
- [245] K. M. Brady, J. K. Lee, K. K. Kibler, R. B. Easley, R. C. Koehler, and D. H. Shaffner. Continuous measurement of autoregulation by spontaneous fluctuations in cerebral perfusion pressure: comparison of 3 methods. *Stroke*, 39(9):2531–7, 2008.
- [246] D. W. Brown, P. A. Picot, J. G. Naeini, R. Springett, D. T. Delpy, and T.-Y. Lee. Quantitative near infrared spectroscopy measurement of cerebral hemodynamics in newborn piglets. *Pediatr. Res.*, 51(5):564–570, 2002.
- [247] R. Springett, M. Wylezinska, E. B. Cady, M. Cope, and D. T. Delpy. Oxygen dependency of cerebral oxidative phosphorylation in newborn piglets. *J. Cereb. Blood Flow Metab.*, 20(2):280–289, 2000.
- [248] K. Haaland, B. Karlsson, E. Skovlund, H. Lagercrantz, and M. Thoresen. Post-natal development of the cerebral blood flow velocity response to changes in CO<sub>2</sub> and mean arterial blood pressure in the piglet. *Acta Paediatr.*, 84(12):1414–1420, 1995.
- [249] T. E. Duffy. Carbohydrate and energy metabolism in perinatal rat brain: relation to survival in anoxia. *J. Neurochem.*, 24(2):271–276, 1975.
- [250] C. E. Cooper, S. J. Matcher, J. S. Wyatt, M. Cope, G. C. Brown, E. M. Nemoto, and D. T. Delpy. Near-infrared spectroscopy of the brain: relevance to cytochrome oxidase bioenergetics. *Biochem. Soc. Trans.*, 22:974–980, 1994.
- [251] V. Quaresima, R. Springett, M. Cope, J. T. Wyatt, D. T. Delpy, M. Ferrari, and C. E. Cooper. Oxidation and reduction of cytochrome oxidase in the neonatal brain observed by in vivo near-infrared spectroscopy. *Biochim. Biophys. Acta*, 1366:291–300, 1998.
- [252] A. Mayevsky and B. Chance. Oxidation-reduction states of NADH in vivo :

From animals to clinical use. *Mitochondrion*, 7(5):330–339, 2007.

- [253] D. H. Williamson, P. Lund, and H. A. Krebs. The redox state of free nicotinamide-adenine dinucleotide in the cytoplasm and mitochondria of rat liver. *Biochem. J.*, 103(2):514–527, 1967.
- [254] B. E. Livingston, R. A. Altschuld, and C. M. Hohl. Metabolic compartmentalization in neonatal swine myocytes. *Pediatr. Res.*, 40(1):59–65, 1996.
- [255] T. Moroz, T. Hapuarachchi, A. Bainbridge, D. Price, E. Cady, E. Baer, I. Tachtsidis, K. Broad, M. Ezzati, N. J. Robertson, D. Thomas, X. Golay, and C. E. Cooper. Modelling blood flow and metabolism in the piglet brain during hypoxia-ischaemia: simulating brain energetics. *Adv. Exp. Med. Biol.*, 789:339–344, 2013.
- [256] C. D. Kurth, W. J. Levy, and J. McCann. Near-infrared spectroscopy cerebral oxygen saturation thresholds for hypoxia-ischemia in piglets. *J. Cereb. Blood Flow Metab.*, 22(3):335–41, 2002.
- [257] D. Oriot, K. Beharry, J. B. Gordon, and J. V. Aranda. Ascorbic acid during cerebral ischemia in newborn piglets. *Acta Paediatr.*, 84(6):621–626, 1995.
- [258] A. Bainbridge, I. Tachtsidis, S. D. Faulkner, D. Price, T. Zhu, E. Baer, K. D. Broad, D. L. Thomas, E. B. Cady, N. J. Robertson, and X. Golay. Brain mitochondrial oxidative metabolism during and after cerebral hypoxia-ischemia studied by simultaneous phosphorus magnetic-resonance and broadband near-infrared spectroscopy. *Neuroimage*, 2013.
- [259] S. J. Matcher, P. Kirkpatrick, K. Nahid, M. Cope, and D. T. Delpy. Absolute quantification methods in tissue near-infrared spectroscopy. In *Proc Spie*, volume 2389, pages 486–495, 1995.
- [260] M. Essenpreis, M. Cope, C. E. Elwell, S. R. Arridge, P. van der Zee, and D. T. Delpy. Wavelength dependence of the differential pathlength factor and the log slope in time-resolved tissue spectroscopy. *Adv. Exp. Med. Biol.*, 333:9–20, 1993.
- [261] L. Vanhamme, A. van den Boogaart, and S. Van Huffel. Improved method for accurate and efficient quantification of MRS data with use of prior knowledge. *J. Magn. Reson.*, 129(1):35–43, 1997.
- [262] A. Saltelli, S. Tarantola, F. Campolongo, and M. Ratto. *Sensitivity Analysis in Practice: A Guide to Assessing Scientific Models*. John Wiley & Sons, 2004.

- [263] J. J. Lemasters, A. L. Nieminen, T. Qian, L. C. Trost, and B. Herman. The mitochondrial permeability transition in toxic, hypoxic and reperfusion injury. *Mol. Cell. Biochem.*, 174(1-2):159–165, 1997.
- [264] A. R. Cross and A. W. Segal. The NADPH oxidase of professional phagocytes—prototype of the NOX electron transport chain systems. *Biochim. Biophys. Acta*, 1657(1):1–22, 2004.
- [265] R. Springett, J. Newman, D. T. Delpy, and M. Cope. Oxygen dependency of cerebral CuA redox state during increased oxygen consumption produced by infusion of a mitochondrial uncoupler in newborn piglets. *Adv. Exp. Med. Biol.*, 471:181–188, 1999.
- [266] M. Banaji. A generic model of electron transport in mitochondria. *J. Theor. Biol.*, 243(4):501–16, 2006.
- [267] C. E. Cooper and J. S. Wyatt. NMR spectroscopy and imaging of the neonatal brain. *Biochem. Soc. Trans.*, 28(2):121–126, 2000.
- [268] M. Qiao, P. Latta, S. Meng, B. Tomanek, and U. I. Tuor. Development of acute edema following cerebral hypoxia-ischemia in neonatal compared with juvenile rats using magnetic resonance imaging. *Pediatr. Res.*, 55(1):101–106, 2004.
- [269] F. C. Coelho, C. T. Codeço, and M. G. M. Gomes. A bayesian framework for parameter estimation in dynamical models. *PLoS ONE*, 6(5):e19616, 2011.
- [270] T. Toni, D. Welch, N. Strelkowa, A. Ipsen, and M. P. H. Stumpf. Approximate bayesian computation scheme for parameter inference and model selection in dynamical systems. *J. R. Soc. Interface*, 6(31):187–202, 2009.
- [271] T. Toni and M. P. H. Stumpf. Parameter inference and model selection in signaling pathway models. In *Computational Biology*, number 673 in Methods in Molecular Biology, pages 283–295. Humana Press, 2010.
- [272] ABC-SysBio. <http://www.theosysbio.bio.ic.ac.uk/resources/abc-sysbio/>.
- [273] H. M. Sauro, M. Hucka, A. Finney, C. Wellock, H. Bolouri, J. Doyle, and H. Kitano. Next generation simulation tools: the systems biology workbench and BioSPICE integration. *Omics*, 7(4):355–372, 2003.
- [274] M. H. Baslow. Evidence that the tri-cellular metabolism of N-acetylaspartate

functions as the brain's "operating system": how NAA metabolism supports meaningful intercellular frequency-encoded communications. *Amino Acids*, 39:1139–1145, 2010.

- [275] X. Yue, H. Mehmet, J. Penrice, C. Cooper, E. Cady, J. S. Wyatt, E. O. R. Reynolds, A. D. Edwards, and M. V. Squier. Apoptosis and necrosis in the newborn piglet brain following transient cerebral hypoxia-ischaemia. *Neuropathol. Appl. Neurobiol.*, 23(1):16–25, 1997.
- [276] P. Orłowski, D. O'Neill, V. Grau, V. Y., and S. Payne. Modelling of the physiological response of the brain to stroke. *Virtual Physiological Human*, 2012.
- [277] T. Hapuarachchi, T. Moroz, A. Bainbridge, D. Price, E. Cady, K. Baer, K. Broad, M. Ezzati, D. Thomas, X. Golay, N. J. Robertson, and I. Tachtsidis. Modelling blood flow and metabolism in the piglet brain during hypoxic-ischaemia: simulating brain energetics. *Adv. Exp. Med. Biol.*, In press.
- [278] N. J. Robertson, F. M. Cowan, I. J. Cox, and A. D. Edwards. Brain alkaline intracellular pH after neonatal encephalopathy. *Ann. Neurol.*, 52(6):732–742, 2002.
- [279] E. B. Cady, O. Iwata, A. Bainbridge, J. S. Wyatt, and N. J. Robertson. Phosphorus magnetic resonance spectroscopy 2 h after perinatal cerebral hypoxia-ischemia prognosticates outcome in the newborn piglet. *J. Neurochem.*, 107(4):1027–1035, 2008.
- [280] A. L. Hodgkin and A. F. Huxley. Currents carried by sodium and potassium ions through the membrane of the giant axon of loligo. *J. Physiol. (Lond.)*, 116(4):449, 1952.
- [281] E. Bullmore and O. Sporns. Complex brain networks: graph theoretical analysis of structural and functional systems. *Nat. Rev. Neurosci.*, 10(3):186–198, 2009.
- [282] O. David and K. J. Friston. A neural mass model for MEG/EEG: coupling and neuronal dynamics. *Neuroimage*, 20(3):1743–1755, 2003.
- [283] R. C. Sotero, N. J. Trujillo-Barreto, Y. Iturria-Medina, F. Carbonell, and J. C. Jimenez. Realistically coupled neural mass models can generate EEG rhythms. *Neural Comput.*, 19(2):478–512, 2007.
- [284] R. C. Sotero and N. J. Trujillo-Barreto. Biophysical model for integrating neuronal activity, EEG, fMRI and metabolism. *Neuroimage*, 39(1):290–309, 2008.

- [285] O. Pryds and A. D. Edwards. Cerebral blood flow in the newborn infant. *Arch. Dis. Child. Fetal Neonatal Ed.*, 74(1):F63–F69, 1996.
- [286] M. P. Ehrlich, J. N. McCullough, N. Zhang, D. J. Weisz, T. Juvonen, C. A. Bodian, and R. B. Griep. Effect of hypothermia on cerebral blood flow and metabolism in the pig. *Ann. Thorac. Surg.*, 73(1):191–197, 2002.
- [287] C. E. Elwell, J. R. Henty, T. S. Leung, T. Austin, J. H. Meek, D. T. Delpy, and J. S. Wyatt. Measurement of CMRO<sub>2</sub> in neonates undergoing intensive care using near infrared spectroscopy. *Adv. Exp. Med. Biol.*, 566:263–268, 2005.
- [288] M. A. Mintun, M. E. Raichle, W. R. Martin, and P. Herscovitch. Brain oxygen utilization measured with O-15 radiotracers and positron emission tomography. *J. Nucl. Med.*, 25(2):177–187, 1984.
- [289] P. Poulsen, D. Smith, L. Østergaard, E. Danielsen, A. Gee, S. Hansen, J. Astrup, and A. Gjedde. In vivo estimation of cerebral blood flow, oxygen consumption and glucose metabolism in the pig by [<sup>15</sup>O]water injection, [<sup>15</sup>O]oxygen inhalation and dual injections of [<sup>18</sup>F]fluorodeoxyglucose. *J. Neurosci. Methods*, 77(2):199–209, 1997.
- [290] L. Algotsson, K. Messeter, C. H. Nordstrom, and E. Ryding. Cerebral blood flow and oxygen consumption during isoflurane and halothane anesthesia in man. *Acta Anaesthesiol. Scand.*, 32:15–20, 1988.
- [291] T. Oshima, F. Karasawa, Y. Okazaki, H. Wada, and T. Satoh. Effects of sevoflurane on cerebral blood flow and cerebral metabolic rate of oxygen in human beings: A comparison with isoflurane. *Eur. J. Anaesthesiol.*, 20(7):543–547, 2003.
- [292] P. J. Hanley, J. Ray, U. Brandt, and J. Daut. Halothane, isoflurane and sevoflurane inhibit NADH: ubiquinone oxidoreductase (complex I) of cardiac mitochondria. *J. Physiol. (Lond.)*, 544(3):687–693, 2002.
- [293] Z. Rong, M. Banaji, T. Moroz, and C. E. Cooper. Can mitochondrial cytochrome oxidase mediate hypoxic vasodilation via nitric oxide metabolism? *Adv. Exp. Med. Biol.*, 765:231–238, 2013.
- [294] K. Roth and M. W. Weiner. Determination of cytosolic ADP and AMP concentrations and the free energy of ATP hydrolysis in human muscle and brain tissues with <sup>31</sup>P NMR spectroscopy. *Magn. Reson. Med.*, 22(2):505–511, 1991.

- [295] R. J. Corbett, A. R. Lupton, D. Garcia, and J. I. Ruley. Energy reserves and utilization rates in developing brain measured in vivo by  $^{31}\text{P}$  and  $^1\text{H}$  nuclear magnetic resonance spectroscopy. *J. Cereb. Blood Flow Metab.*, 13(2):235–246, 1993.
- [296] P. A. Flecknell, R. Wootton, and M. John. Cerebral blood flow and cerebral metabolism in normal and intrauterine growth retarded neonatal piglets. *Clin. Sci.*, 64(2):161–165, 1983.
- [297] J. W. Lawson and R. L. Veech. Effects of pH and free  $\text{Mg}^{2+}$  on the  $K_{\text{eq}}$  of the creatine kinase reaction and other phosphate hydrolyses and phosphate transfer reactions. *J. Biol. Chem.*, 254(14):6528–6537, 1979.
- [298] T. S. Rosenkrantz, J. Kubin, O. P. Mishra, D. Smith, and M. Delivoria-Papadopoulos. Brain cell membrane  $\text{Na}^+$ ,  $\text{K}^+$ -ATPase activity following severe hypoxic injury in the newborn piglet. *Brain Res.*, 730(1–2):52–57, 1996.
- [299] M. Brand, J. L. Pakay, A. Ocloo, J. Kokoszka, D. Wallace, P. Brookes, and E. Cornwall. The basal proton conductance of mitochondria depends on adenine nucleotide translocase content. *Biochem. J.*, 392(2):353, 2005.
- [300] M. Pourcyrous, C. W. Leffler, H. S. Bada, S. B. Korones, and D. W. Busija. Cerebral blood flow responses to indomethacin in awake newborn pigs. *Pediatr. Res.*, 35(5):565–570, 1994.
- [301] M. Erecinska, S. Cherian, and I. A. Silver. Energy metabolism in mammalian brain during development. *Prog. Neurobiol.*, 73(6):397–445, 2004.